Delft University of Technology

Compliant Full Film Lubricated Bearings

Concept Design & Development

Nijssen, J.P.A.

DOI

Publication date

2022

Document Version

Final published version

Important note

To cite this publication, please use the final published version (if applicable).
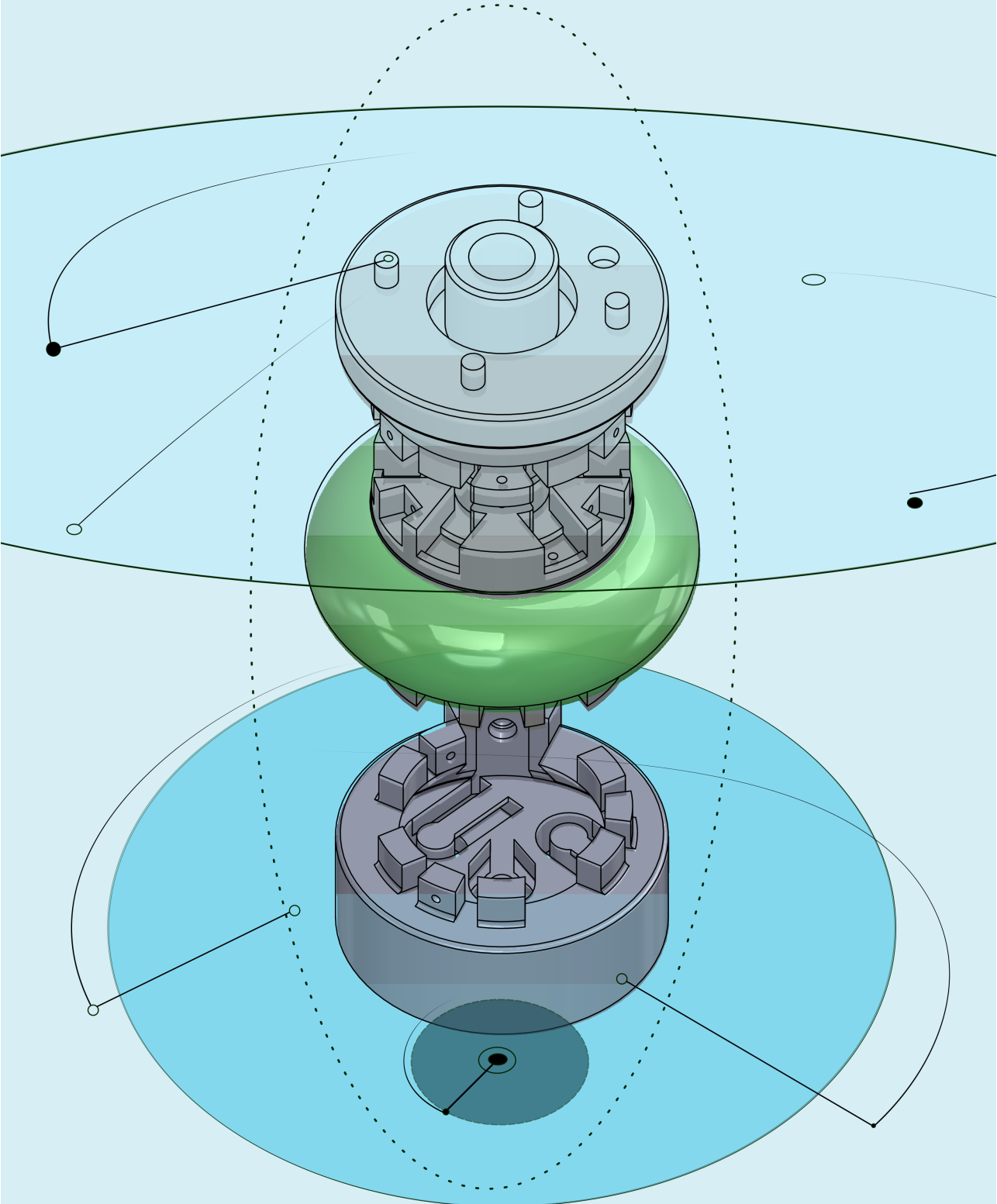Please check the document version above.

Compliant Full Film Lubricated Bearings

Concept Design & Development

Joep P.A. Nijssen

COMPLIANT FULL FILM LUBRICATED BEARINGS
CONCEPT DESIGN & DEVELOPMENT

Dissertation

For the purpose of obtaining the degree of doctor
at Delft University of Technology,
by the authority of the Rector Magnificus Prof.dr.ir. T.H.J.J. van der Hagen,
chair of the Board for Doctorates,
to be defended publicly on Friday, 25 February 2022 at 12.30 hours

by

Joep Peter Abram NIJSSEN

Master of Science in Mechanical Engineering,
Delft University of Technology, The Netherlands,
Born in Groningen, The Netherlands.

This dissertation has been approved by the promotors

Dr.ir. R.A.J. van Ostayen
Prof.dr.ir. J.L. Herder

Composition of the doctoral committee:

Rector Magnificus,	chairperson
Dr.ir. R.A.J. van Ostayen	
	Delft University of Technology, promotor
Prof.dr.ir. J.L. Herder	Delft University of Technology, Promotor

Independent members:
Prof.dr.ir. M.B. de Rooij	
	University of Twente
Prof.dr.ir. P. de Baets	Ghent University
Prof.dr.ir. C.A. Bakker	
	Delft University of Technology
Prof.dr.ir. P. Breedveld	
	Delft University of Technology
Prof.dr.ir. A. Keulen	Delft University of Technology

An electronic version of this dissertation is available at
http://repository.tudelft.nl/.

A good model starts from assumptions that simplify but are not surprising, yet reaches surprising results.

Paul Collier

CONTENTS

SUMMARY

Full film lubricated bearings are machine components that excel in their ability to carry high loads with very little friction. Their main archetypes, passive hydrodynamic and active hydrostatic bearings, are used in a wide variety of applications, ranging from hydraulic pumps to high precision machine benches. They are most commonly lubricated using oil-based lubricants and have been a staple in improving machine performance for many decades.

The continuous search for higher performing and more sustainable designs has given ample opportunity to revisit these machine components, and to investigate their possible implementation into machines and fields that so far have not been able to make use of their superior performance characteristics. This lack of increased implementation is often due to fundamental limitations of these components. Both the performance of hydrostatic and hydrodynamic bearings is directly coupled to their need for a thin lubricant film to provide stiffness and load capacity. For hydrostatic bearings in particular, this requirement can more accurately be defined as the need for the bearing surfaces to remain parallel to its counter-surface, separated by a thin film of lubricant in the order of 100 micrometer. Not only the performance, but also ecological constraints have been more dominant in recent years. The conventional use of oil-based lubricants has given researchers the motivation to look for cleaner and more sustainable lubricants. The engineering community keeps on moving forward to a higher performing and more sustainable future.

This thesis investigates one fundamental design direction to obtain higher performance and increase the implementation field of full film bearings. By implementing compliant design, or the use of elastic elements, several facets of in particular hydrostatic bearing limitations are investigated. Two fundamental limitations are dominant throughout this dissertation: the design for changing counter surfaces and the design for multiple operating conditions. Several principles are introduced that improve the use of hydrostatic bearings for non-constant counter surfaces. These principles are the use of functionally graded materials to minimize the pre-loading effect the hydrostatic pressure has on the elastic bearing support, distributed whiffletree support-systems to increase bearing deformability, and the introduction of a compliant water-filled universal joint with superior stiffness characteristics compared to the state of the art. The universal joint makes use of the principle of closed-form pressure balancing, which is pressurizing an enclosed body of fluid to obtain low rotation stiffness while maintaining high support stiffness. All these principles are described through design models and are further investigated with the use of finite element models.

The second dominant subject that is investigated in this dissertation is developing hydrostatic bearings that function for multiple operating conditions with the use of compliant elements. This principle, defined in this work as passive shape shifting, gives hydrostatic bearings more flexibility when it comes to designing for more discrete load

cases, such as the one that can be found in hydraulic pumps. Besides describing this concept design principle with finite element models, a step towards real life application is also made in a scaled case study. By combining the previously mentioned compliant universal joint and a hydrostatic bearing using the principle of passive shape shifting, a contact-mechanics free alternative for axial piston pumps is proposed. This mechanism is designed for a scaled case study and validated through experimental work and finite element modelling.

This thesis, which is conceptual in nature, combines these different design directions and therefor shows design directions that broaden the field of use for full film lubricated bearings by using elastic elements.

SAMENVATTING

Volle filmlagers zijn machine onderdelen die uitstekende wrijving en draagkracht karakteristieken bezitten. Ze kunnen grofweg onderverdeeld worden in twee subtypes: de passieve hydrodynamische en actieve hydrostatische lagers. Deze worden in een groot spectrum aan applicaties gebruikt, waaronder hydraulische pompen en draai en freesbanken. Doorgaans wordt een olie-gebaseerd smeermiddel gebruikt, en zijn ze een veel gebruikt machine onderdeel om machine eigenschappen te verbeteren.

De zoektocht naar steeds beter functionerende en duurzame machines heeft ruimte gegeven voor verdere ontwikkeling van deze specifieke machine onderdelen, ook in apparaten waar deze voorheen niet gebruikt werden. Fundamentele beperkingen van volle filmlagers zorgen doorgaans voor hun afwezigheid, en vooral de koppeling tussen de film laag dikte en lager prestatie zijn hierbij cruciaal. Specifiek voor hydrostatische lagers is er de limitatie veroorzaakt door de noodzaak om een parallel lager oppervlak te hebben met het tegenloop vlak. Zeker omdat deze filmlagen klein zijn, doorgaans 100 micrometer, is dit voor bepaalde ontwerpen een knelpunt. Daarnaast is niet alleen prestatie maar zijn ook duurzaamheid karakteristieken steeds meer een punt van aandacht, zeker nu de wereld een grotere focus legt op de klimaatdoelen. Olie, wat doorgaans gezien word als een niet-duurzame grondstof, word steeds vaker in kwaad daglicht gezet en voedt daarmee de zoektocht naar duurzame alternatieven. Het kan dus gezegd worden dat de ingenieurs van vandaag de dag constant bezig zijn met innoveren en stappen te maken in zowel de zoektocht naar betere prestaties als duurzaamheid.

Dit proefschrift onderzoekt een specifieke ontwerprichting om tot deze verbeterde prestaties te kunnen komen: het gebruik van elastische elementen. Door middel van het ontwerpen van elastische volle filmlagers kunnen meerdere facetten van hun beperkingen worden aangepakt. Specifiek focust dit werk zich op twee dominante beperkingen: het ontwerpen voor veranderende tegenloopvlakken en het ontwerpen voor meerdere operatie condities. Voor deze twee beperkingen zijn verschillende principes ontwikkelt die deelproblemen oplossen die belangrijk zijn voor het ontwikkelen van een volledige oplossing. Als eerste is het principe van functioneel gegradeerde materialen bekeken om daarmee het elastisch-voorspanning effect dat word veroorzaakt door de hydrostatische druk op elastische lagers te minimaliseren. Ten tweede is gekeken naar het gebruik van een discreet ophangingsysteem genaamd een 'Whiffletree', en om daarmee vervorming karakteristieken op te delen in daarvoor specifiek ontwerpen mechanismen. Ten derde is er gekeken naar een alternatief voor elastische twee graden van vrijheid scharnieren, die bestaat uit een elastisch lichaam die een vloeistof insluit en daarmee sterke prestaties levert als het gaat om stijfheid. Deze principes zijn alle bekeken door middel van het ontwikkelen van ontwerp methodes en het gebruik van eindige elementen modellen.

De tweede dominante limitatie van hydrostatische lagers dat is bekeken in dit proefschrift is het ontwerpen voor verschillende operatiecondities door middel van elastische elementen. Dit ontwerpprincipe, wat het passief vormverandering principe is ge-

noemd in dit werk, geeft hydrostatische lagers de mogelijkheid ontworpen te worden voor discrete condities. Een voorbeeld van een dergelijke discrete operatieconditie kan worden gevonden in hydraulische cilinderpompen, waar een groot drukverschil ontstaat tussen de compressie en vul-slag. Naast het introduceren van de ontwerpmethode en een validatiestap door middel van eindige elementen methoden, is ook een voorbeeld ontwerpcasus bekeken. In axiale zuigerpompen bevindt zich een zogenaamd zuiger-slipper mechanisme, wat de koppeling van rotatie naar translatie bewerkstelligt. Het combineren van de eerder genoemde elastische twee graden van vrijheid scharnier en een hydrostatische lager die gebruik maakt van het passief vormveranderingsprincipe is voor deze casus ontworpen om daarmee een stap richting industriële implementatie van de concepten te maken.

Dit proefschrift is conceptueel van aard, en combineert verschillende ontwerprichtingen om daarmee de mogelijkheden te laten zien hoe het gebruik van elastische elementen de mogelijkheden binnen volle filmlager ontwerp vergroten.

ACKNOWLEDGEMENTS

It was in 2009, the final year of my high school education, that I had a conversation with my math teacher concerning the following steps in my education. The conclusion from that talk was clear: "don't go for a study where a lot, if any, math is involved". The fact that I finished high school with the bare minimum in math also didn't help. But I was, and always have been, very stubborn and there was one thing I really wanted to do, which was to create new things. In my case that meant either continuing my love for music, which at that time I was heavily involved in with my friends, or pursue an engineering degree. The final push of my mother notched me towards the latter, and I started with the bachelor Industrial Design Engineering in Delft. This was not without it's challenges, especially with the course 'Product in Werking', which I had the pleasure of re-doing the exam a total of 5 times. However, I managed and at the end of 3 years I was staring at the finish line. Together with my friend Bas Heming, I decided that designing was only interesting as long as we were also involved in the technical aspects, which in our case meant a switch towards mechanical engineering. This meant courses full of math, long hours at 3mE and the constant feeling of "What have I gotten myself into". However, once again, I managed to work myself through all the courses 3mE and then PME had to offer. I completed my masters in the United States, where Charles Kim together with Just Herder and Giuseppe Radaelli back in Delft showed me how inspiring research was. And so again, at the end of my master Precision and Microsystem Engineering I was left thinking what I wanted to do next. This didn't take long, as Ron van Ostayen send me an email not even a week after my graduation with the question if I was interested in a PhD position. Fast forward another 4 and a bit years, and here we are at the end of the PhD and at the end of an amazing journey that spanned more than 10 years of my life. Before diving into this work, I want to take the time to show all the people who are part of my life how gratefull I am of their support in this journey.

First I want to thank all the guys and girls at Delft Offshore Turbine and the DOB-academy. In the first year of my PhD I spent mostly at the 'Oude Bibliotheek' and the 'Hal', which was a great learning experience. Especially I want to thank Anton and Niels, who I had the pleasure to learn from both professionally and personally. Niels, thank you not only for the reviewing of parts of this thesis, but also for being a great mentor. The majority of my time as a PhD candidate however, was spent at the university, and therefore there is a large group of people I want to thank. First I would like to thank Just Herder for reviewing this work and being my second supervisor throughout these years. You are a great source of inspiration. Next, my direct PhD and postdoc colleagues Ali, Nima, Niranjan, Reinier, Werner, Jelle, Ad, Davood, Jelle and Ali. A special thanks to Thijs and Freek who I had the pleasure of working together with during the first pandemic months, and in particular my greatest thanks to Stefan Lampaert. We have been close colleagues throughout the years and I could not have wished for a better collleague

and friend to help me out when I could not see all the possibilities. Also I want to thank Patrick, Bradley, Spiridon, Gideon and Rob for all their technical support and expertise. I do not know how many times I came with questions for orders or things I needed from the workshops. Besides the colleagues from the university I have had the pleasure of working closely with a number of students, which I would like to express my great gratitude. Jan, Thibaud, Johan, Robin, Vincent, Sebas, Pieter and Dave, thank you all for helping this dissertation forward with your enthousiasm and skills. The work of both Vincent and Dave have been particularly of interest, and can be seen as chapters in this disseration. Besides all master students, I would like to thank all bachelor final project groups that I supervised for their contributions, and in particular Thobias, Stef, Matthijs, Jelte and Daan, who are responsible for one of the examples in the 6th chapter.

Next to the support of colleagues, I want to thank a group of close friends in particular. I met Steven, Hidde, Sander & Leroy all at the start of my bachelor and we have been good friends ever since. The weekends of going to the gym, watching movies, going out for drinks (or having drinks at the Statenweg), playing games/boardgames, going on holiday and doing our absolute best to make fun of each other have been some of the best ways of taking my mind of the problems encountered throughout the PhD. Besides my friends, it has been my family and my girlfriend that have listened to me complain the most and supported me at all times of the day. Mom and Dad, thank you for always being there for support. Between Groningen and Delft there is quite some distance (for dutch standards), and therefor the phone has been our most common way of communicating. You both have always been there for me, and I could not wish for better parents. My sister Jorien, Ricardo and their little one, my nephew Daan, thank you for always cheering me up when I was back at home. And of course I want to thank you, Stefania. We met in a Bachata class at the sport centre in Delft, so without me sticking around for the PhD in Delft we might have never met, but I am more happy than anything we did. I know I can be difficult and stubborn, and you have the patience to always listen and help me whenever and however you can. I'm looking forward to spent all of our years together.

Lastly there is one person I would like to thank in particular. Ron, we have worked closely together throughout these past years. There is no other person I have learned as much from throughout the past 10 years when it comes to engineering, research and perseverance. You have a wonderful way of inspiring and collaborating with people, and you have always been there to help. I hope this is not the end, but the beginning of a long period where we will stay in touch about life and work, and keep on collaborating. Thank you Ron for being a true mentor.

1

INTRODUCTION

"Screw it, let's do it".

Richard Branson

1

When most engineers think of a bearing, they usually think of the components we find in our bikes and cars: small steel balls or cylinders encapsulated in a steel housing, lubricated with grease or oil. They are often not considered the most exiting or innovative machine component. Yet, they often define some of the most critical machine characteristics through performance and lifetime. There is a wide variety of bearing embodiments, and the performance between them varies significantly. Of all bearing types, full film bearings are known to combine some excellent performance characteristics with some serious drawbacks [159, 192, 212]. Full film bearings are bearings using a thin-film lubricant between the two moving surfaces to minimize friction and obtain high load-carrying capacities. Full film bearings can traditionally be divided into hydrostatic and hydrodynamic variants. Hydrodynamic bearings are passive components which require non-parallel counter surfaces and a sufficient sliding velocity in order for their lubrication and load carrying capacity to form [192]. They are used in generators, reactors, car engines or ship propeller shafts [94, 139, 140], and have excellent lubrication and load carrying capacities. The alternative is the so-called hydrostatic bearings, which are active machine components used in systems where high load capacity, low friction and high precision are desired [210]. The conventional hydrostatic bearing and its counter surface are rigid and well defined with a constant, usually zero curvature. This, besides the requirement of a pump, is necessary, since the performance of hydrostatic bearings is directly related to a well defined and small film height between bearing and its counter surface.

Although both these machine components are bearings with significant potential to improve machine life and performance, their application range is somewhat limited by thin film aspects. In particular for the hydrostatic embodiment, the addition of the possibility to slide against surfaces with a spatially varying curvature, would proof useful in systems such as radial pumps and motors [68], and in the field of civil engineering. The costs of making surfaces flat enough for the desired specifications of conventional hydrostatic bearings can be significant, and in some cases such as for very large surfaces the machinability might be costly and increasingly difficult to obtain [199]. The question thus arises what can be done to improve such a bearing so that a new set of potential applications can benefit from the inherent performance characteristics.

The solution might lie in the inherent property of a hydrostatic bearing, requiring it to be parallel to its counter surface. Since the counter surface is often defined by the application, the solution should be found in the bearing design itself. By allowing for compliance of the bearing, we could maintain this inherent parallel film requirement. The bearing surface and support would thus be required to deform, which could be done passively by making the bearing elastic. The idea of elasticity or compliance in hydrostatic bearings has been used before. The most common approach is the use of a solid, elastic material in the form of a rubber support. This has been used to deal with counter track waviness [209, 214], to increase load capacity while the bearing is tilted [10], to function as elastic pivots in hydrodynamic bearings [136] or in journal bearing pad design with an integrated compliant foil structure [15]. All of these examples however have one thing in common: they have been solely implemented for small deformations. The unknown territory lies in the extension of this idea to large deformations of bearing supports. This is where the use case of new applications such as radial pumps and motors

could truly benefit from the superior performance of full film lubricated bearings. There are however several aspects that require careful consideration in a research project that focusses on the development of large deformations of compliant bearings. Designing a bearing that is both highly deformable (a desired characteristic), and has a high-load capacity (an inherent benefit of hydrostatic bearings), is at its core a contradiction and a challenge. Besides this, there are additional effects such as the deformation that a highly compliant bearing will obtains through the pressurized thin film. Can we thus develop and design components, principles and systems that move us towards this goal?

1.1. THESIS OBJECTIVE AND APPROACH

This thesis investigates the potential prospect of deformable hydrostatic bearings from a design engineering perspective. A design engineering perspective means that the focus of this work lies on developing design principles and embodiments that will be validated through computational and scaled case studies, which show the promise of functional deformable hydrostatic bearings. The goal of this thesis has been summarized as follows:

Thesis objective: *The implementation of compliance into water lubricated hydrostatic bearings resulting in improved performance and new design methodologies.*

To make this goal more tangible, a set of sub-objectives are proposed. These are based on defining the *why*, *how* and *what* of the research objective. Although both hydrostatic and hydrodynamic bearings are the subject of this dissertation, the majority of the methods, as will be seen in this dissertation, are of particular interest for hydrostatic bearings. The previous section introduced us to the potential of compliant hydrostatic bearing development in terms of some applications. The following three research objectives will form the basis to further motivate and define the challenges proposed in this introduction, by providing an outlook on the potential of these combined principles. These objectives are as follows:

I: *Determine the relevance of compliant bearing design in terms of engineering, environmental and innovation needs.*

II: *Adress existing limitations in hydrostatic bearing design by using state of the art techniques found in compliant design.*

III: *Develop design cases and analyse the performance of developed principles.*

1.1.1. HOW TO READ THIS THESIS

The structure of this thesis is based on the research goal and the subsequent presented sub-objectives. The three objectives are discussed by the content of the following parts: Motivation (*why*), Principles (*how*) and Implementation (*what*).The three objectives are addressed in the three main parts of this thesis, and each part builds on the previous one. This structure can be seen in figure 1.1. We first motivate why we have done this

research through examples from multiple perspectives. Following this motivation, the principles developed as part of this research direction are introduced. All principles are either novel designs, novel design perspectives, or novel design methods, and form the technical body of this thesis. In the last part several design principles developed in this research are combined and implemented in a specific case study. As this thesis concerns a mechanical engineering subject, this step of providing a physical example further validates our conceptual ideas and principles by giving them footing. The content of the three parts of this dissertation can be described as follows.
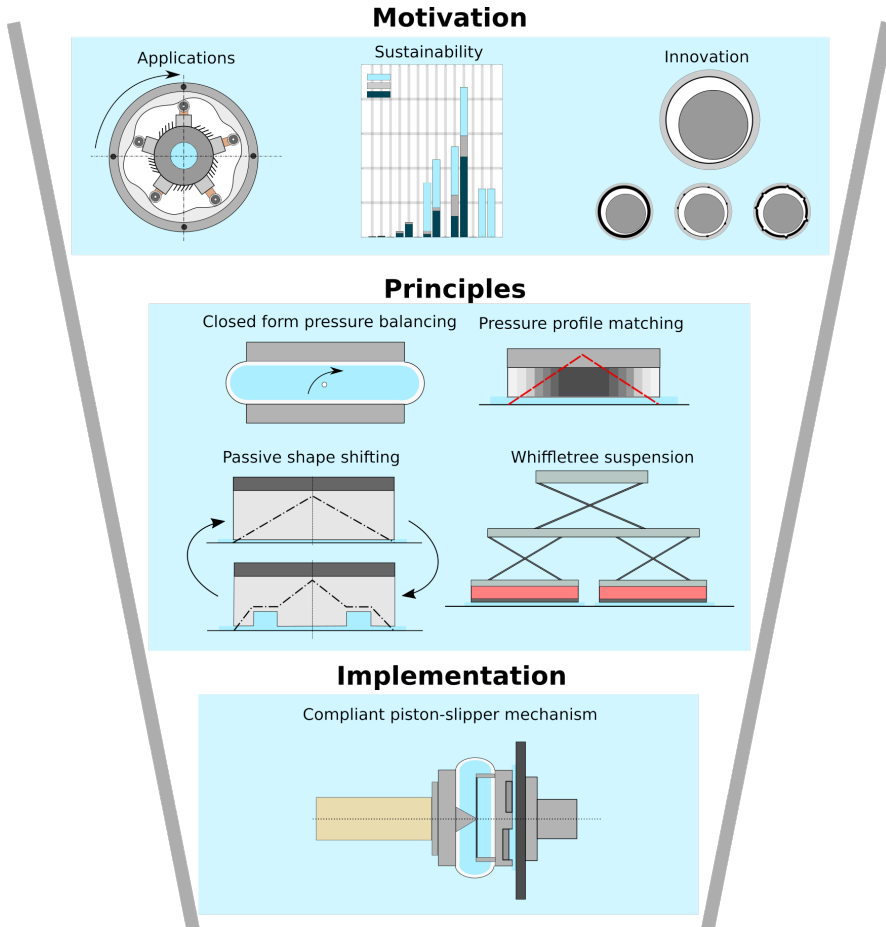
Figure 1.1: The backbone structure of this dissertation and the subjects found in its 8 chapters. All parts build on the preceding part, and thus funnel the results of this thesis from a principles to a practical implementation.

Part 1: Motivation, consists of chapters 2, 3 and 4 respectively. All these chapters discuss a different perspective of the research motivation for compliant full film bearing design. In chapter 2 performance motivations in a potential system are discussed. Chap-

ter 3 looks at the sustainability perspective and how this increasingly becomes a more important measure for all new developments. Finally, chapter 4 discusses the need for innovation within the field of full film bearing development, and how compliant design can prove beneficial. Subsequently, it proposes a set of development directions.

Part 2: Principles, consists in total of 4 chapters. These chapters all present a design principle where compliant design is used to directly or indirectly improve a full film bearing characteristic. Chapter 5 introduces the principle of pressure profile matching, where clever design of the bearing support can eliminate some properties inherent in compliant full film bearings. Chapter 6 presents the design approach of passive shape shifting. By using compliant elements, a full film bearing can deform between different primary bearing topologies, at different points of the operating range. Chapter 7 studies the possibilitie to improve the deformability of full film bearings through the introduction of a whiffletree system. This system divides the bearing into discrete compliant rotational elements. Finally, chapter 8 introduces a novel compliant joint based on the principle of closed form pressure balancing. By encapsulating a fluid inside an elastic body, a joint can be created that has excellent rotational-to-support stiffness properties. These could potentially be implemented in the previously proposed whiffletree based bearing, or as stand alone bearing supports.

Part 3: Implementation consists of a single chapter. This part provides an example of how some of the proposed principles can be implemented in a demonstrator to show its potential. The compliant alternative of the piston-slipper mechanism found in many axial piston pumps is presented. The compliant alternative combines the principles of closed form pressure balancing and passive shape shifting, and creates a contact-mechanics free solution.

1.1.2. CHAPTER CONVERSION

All chapters are in this dissertation are either fully or partially based on one or more articles. The list of all publications used for this dissertation, can be found at the end of this work. To clarify which chapters are based on which articles, or which sections of articles, they are briefly detailed here.

CHAPTER 2: HYDRAULIC POWERTRAINS FOR WIND TURBINES

This chapter is original content, specifically written for this dissertation. Its content is inspired by research statements that were the subject of the conference article *Nijssen, J.P.A., Kempenaar, A. and Diepeveen, N., Development of an Interface between a Plunger and an Eccentric Running Track for a Low-speed Seawater Pump*, which was presented at the 11th International Fluid Power Conference Aachen in 2018 [163].

CHAPTER 3: THE ECO-IMPACT OF FULL FILM LUBRICATED BEARINGS

This chapter is an abridged version of the article *Nijssen, J.P.A., Van Ostayen, R.A.J., Faludi, J., An Eco-impact Design Metric for Water Lubricated Bearings based on Anticipatory Life Cycle Assessment, published in the journal of Cleaner Production, volume 321 2021*. Parts of the introduction have been removed to improve integration in this thesis. Addition-

ally, the results of the identified bearing geometries in literature have been moved to chapter 4 of this thesis.

Chapter 4: Full Film Bearing Design Innovation using Compliance

This chapter is a combination of original content specifically created for this dissertation and the introduction parts of several articles. The chapter integrates the identified bearing geometries results in literature from the article *Nijssen, J.P.A., Van Ostayen, R.A.J., Faludi, J., An Eco-impact Design Metric for Water Lubricated Bearings based on Anticipatory Life Cycle Assessment, published in the Journal of Cleaner Production, volume 321, 2021* with the introduction sections of that same article and the articles *Nijssen, J.P.A., Van Ostayen, R.A.J., Compliant Hydrostatic Bearings Utilizing Functionally Graded Materials, Journal of Tribology, 2020, 142(11)* and *Nijssen, J.P.A. , van Ostayen, R.A.J, Passive Shape Shifting: A Compliant Design Approach for Full Film Bearings, Published in Proceedings of the Institution of Mechanical Engineers, Part C: Journal of Mechanical Engineering Science (2021).*

Chapter 5: Pressure Profile Matching for Compliant Hydrostatic Bearings

This chapter is a shorter version of the article *Nijssen, J.P.A., Van Ostayen, R.A.J., Compliant Hydrostatic Bearings Utilizing Functionally Graded Materials, Journal of Tribology, 2020, 142(11).* Part of the introduction is removed and used in chapter 4 to improve integration within this thesis.

Chapter 6: Passive Shape Shifting Design Strategy for Full Film Bearings

This chapter is an abridged version of the article *Nijssen, J.P.A. , van Ostayen, R.A.J, Passive Shape Shifting: A Compliant Design Approach for Full Film Bearings, Published in Proceedings of the Institution of Mechanical Engineers, Part C: Journal of Mechanical Engineering Science (2021).* Part of the introduction is removed and used in chapter 4 to improve integration within this dissertation.

Chapter 7: Whiffletree-based Hydrostatic Bearing Supports

This chapter is an abridged version on the article *van Parijs, V., Nijssen, J.P.A., Van Ostayen, R.A.J.,Whiffletree Based Supports for Self-Adjustable Hydrostatic Bearings, published in Advances in Mechanical Engineering, 2021.* Vincent van Parijs is the first author of the article, coached by the author of this thesis. The introduction of this chapter has been re-written to better integrate it within this dissertation.

Chapter 8: Compliant Joints using the Principle of Closed Form Pressure Balancing

This chapter is a shorter version of the article *Sonneveld, D.D, Nijssen, J.P.A., Van Ostayen, R.A.J., Compliant joints using the principle of closed form pressure balancing, To be submitted to Mechanisms and Machine Theory, 2022.* Dave Sonneveld is the first author of this article, coached by the author of this thesis. The introduction of this chapter has been re-written for better integration in this work.

1

Chapter 9: Compliant Piston-Slipper Mechanism for Axial Piston Pumps
This chapter is the full version of the article in preparation *Nijssen, J.P.A., Sonneveld, D., Van Ostayen, R.A.J., Design of Compliant Piston-Slipper Mechanisms for Wobble Plate Piston Pumps.*

I

MOTIVATION

2

HYDRAULIC POWERTRAINS FOR WIND TURBINES

This chapter provides motivation for the use of water lubricated full film bearings in one of the most promising fields of sustainable energy technology: wind turbine technology. In conventional wind turbine design some form of electric generator is placed high above ground or sea level in the nacelle of the wind turbine. An alternative to these is the use of a hydraulic transmission, generating high pressure fluid in the nacelle through the use of an hydraulic pump, and then transporting this high pressure fluid to ground level to drive an hydraulic motor coupled to an electric generator. The potential improvements in weight reduction, lower capital costs and potentially improved reliability makes this an attractive alternative. One promising development comprises a hydraulic system that makes use of seawater as the hydraulic fluid and lubricant. Currently no functional hydraulic water-based drivetrains exist that are commercially widely implemented. One of the key components that has been identified as a failure component is the interface between the eccentric surface, seen in radial piston pumps, and the piston. This chapter shows what the fundamental limitations are of conventional solutions, and what is required to move towards a promising alternative.

With the effects of global warming becoming ever clearer, the engineering community is slowly increasing its commitment to the development of clean energy source alternatives. One of the most popular alternative energy sources is one of abundance: wind. The wind energy industry has steadily grown over the years, and is reaching the point in which it can provide a clear portion of the worlds energy consumption needs. That wind energy is a more sustainable energy source then coal and oil, becomes evident when looking at the environmental impact of turbines through their life cycle assessment. A typical wind turbine pays off its carbon and energy 'debt' in around 6 to 12 months [50, 93]. After this payback period, the turbine becomes carbon negative, meaning it becomes an environmentally friendly energy source. This makes it an excellent option, especially since its carbon and energy payback period is also significantly shorter then that of other clean sources such as nuclear and hydro power [93]. Several generations of wind turbine systems exist and in some countries they provide a significant portion of the energy source. In Denmark, 47 % of its domestic energy supply came from wind in 2019 [3]. This was generated by large wind farms, which will reach a total output of 4900 MW in 2030 [3]. Although this is a great prospect and a reason for optimism, worldwide significant steps still need to be made. This becomes clearer when comparing Denmark to a country which on paper is very similar: The Netherlands. In the Netherlands, only 8.7 % of all energy use was obtained through sustainable energy sources. Of this 8.7%, only 21.4% came from land and sea-based wind energy [218]. This difference between two very similar countries shows how much still needs to be done. One of the ways the engineering community is doing this, is by providing constant inno-

Figure 2.1: The Danish wind turbine farm Anholt, the third largest wind turbine farm in the world.

vation. This need becomes clear when looking into the state of the art of wind turbine technology [165, 188]. 'Classic' wind turbines consist of a rotor which converts wind power into kinetic energy through torque and rotational velocity [68]. The big majority of turbines placed so far are either turbines with a gearbox which lowers torque and increases rotational velocity, or direct drive generators. Although both are widely used, as

with every machine, they are subject to some fundamental limitations. The most common turbine used worldwide makes use of a three-stage gearbox to obtain the desired rotational velocity [17]. Gearboxes are one of the most frequent failure components [36], because of the highly dynamic loads they are subject to [68]. This causes systems that are originally designed for 20 year lifetime to fail in a significantly shorter time [68], which causes significant downtime and costs. Direct drivetrains lack these mechanical transmissions but require significant amounts of rare earth metals, something widely seen as unsustainable [68]. Next to that, they have a higher mass [177], and require more stiff constructions to support this weight. With the trend of continuously increasing size, this will continue to provide a more significant design challenge in terms of reliability [17] and costs [152].

2.1. HYDRAULIC WIND TURBINES

Beside the previously mentioned 'conventional' turbine embodiments, significant amounts of research and development is also performed in novel designs. These alternatives try to limit one of the mentioned limitations through either replacement of components or complete overhauls of classic designs. One of the alternatives that is getting increased attention is the use of hydraulic components [58, 68, 165, 174] to replace the electronics based drivetrain. They have the following fundamental advantages:

- They have a high torque to weight ratio [68].

- Simpler fundamental construction materials for the turbine itself, rare earth materials are only required at a central point (central generator) [68].

- Hydraulic components are highly reliable [187], and could eliminate all forms of failure as seen in current gearbox-based embodiements.

These advantages fueled the development by companies to provide a promising alternative system. Delft Offshore Turbine (DOT) is a company that has taken this design philosophy, and proposed a wind turbine concept based on hydraulics. In Figure 2.2, the general lay-out of the proposed system can be seen. Multiple wind turbines with each their own hydraulic drivetrain are coupled to a collective power generation system in the shape of a Pelton wheel [68, 174]. The main challenge that they face with their system is the wish to use seawater as the hydraulic liquid, and the use of an open loop system. Multiple arguments can be made for the use of water, and in particular seawater. The use of oil would force the system to be a closed loop system, since any spilling of oil into the environment from a green energy source would prove disastrous from a social and economical standpoint. A closed oil loop system of this scale would also create significant heat which would prove to be insufficiently removed through the natural convection of the environment [156, 174]. Besides this, the amount of hydraulic fluid in even a closed system would be significant and therefor costly. The use of water as an hydraulic medium would alleviate these problems entirely. Spilling water into the ocean, the desired location of the proposed system, would not have negative consequences. This allows the use of an open loop system, which coupled with the fact that water is a superior hydraulic fluid in terms of thermal properties, could also negate any
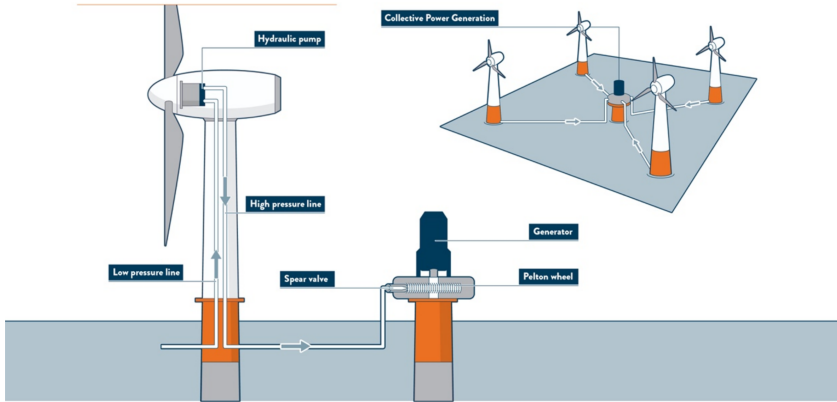
Figure 2.2: The basic lay-out of the Delft offshore Turbine wind farm. Several wind turbines with each an hydraulic pump are connected to a single large generator through a pelton wheel.

form of system cooling problems. Combine this with the previously defined advantages of hydraulics and the proposed system could prove to be a highly scalable green energy source.

2.2. RADIAL PISTON PUMPS

The hydraulic pump is the center component when it comes to replacing electric with hydraulic transmissions. The potential in mass reduction becomes evident when directly putting a generator and equal power hydraulic pump side by side in the same nacelle, seen in Figure 2.3. Hydraulic pumps are well developed machine components, and significant amounts of literature can be found concerning their performance. A wind

Figure 2.3: Image obtained from [174]. (Left) A conventional lay-out of a gearbox generator wind turbine. (Right) The setup proposed by Delft Offshore Turbine, with its potential weight and space reduction.

turbine however is a peculiar case, because of the low rotational speed and high torque input generated. Industry has shown its potential of designing low rotational speed, high torque pumps with high efficiency. An example, seen in figure 2.4, is the CB1120 radial piston motor/pump by Hagglunds/ Bosch Rexroth [91]. This motor/pump is able to generate a max power output of almost 1MW, while rotating at only 27 RPM. The main advantage of this pump archetype is its efficient footprint and its inherent ability to have a gear ratio through a cam ring, without the use of conventional gearboxes. This en-
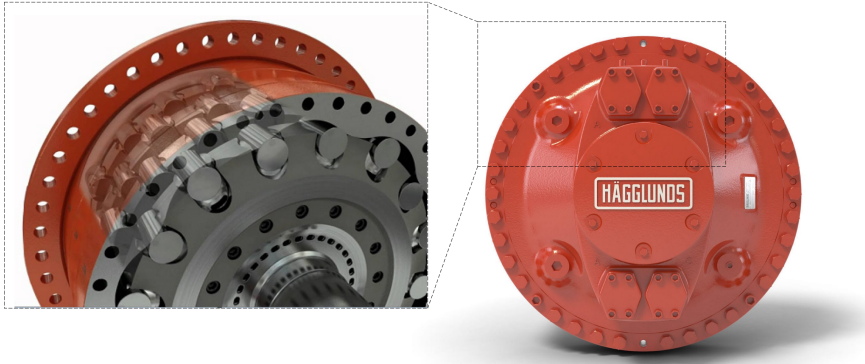
Figure 2.4: The basic layout of the Hagglunds CB radial piston. Several versions with varying power, volumetric output and operating pressures are available.

sures relatively high volumetric output and, since its a piston based pump, high output pressures [68]. These pumps are also typically high reliable [262], and thus are used in systems where long lifetimes are required.

The challenge comes from using water as the desired hydraulic medium. There are several companies that are able to provide high pressure/ high flow water pumps. An example is the Kamat K120000-5G [122], with pressures up to 3500 Bar and flows up to 3939 L/min for a maximum power output of 1.2 MW. The disadvantage for the large majority of providers, including the previously mentioned Kamat pump, is the need for a high input rotational speed. This fundamentally comes from the industrial standard of electric motors operating at 50Hz (60 Hz in the U.S.A.) and thereby defining 1500 RPM as the standard rotational speed. The challenge for Delft Offshore Turbine and thus for such a open loop water hydraulic turbine system is obtaining a low input speed, high pressure and high volumetric flow water pump.

The load case increases in difficulty when further investigating the fundamental properties of a radial piston pump. A radial piston pump can obtain an inherent gear ratio through the use of a so-called camring, as seen in Figure 2.5.A. By letting the camring rotate while holding the piston housing stationary, a stroke of the piston can be obtained. The piston is continuously pressurized, meaning it always will try to stay in contact with the camring. It will translate equally to the number of waves on the camring per rotation. The interface between the piston and camring transforms a rotation into a translation and is one of the main tribological interfaces present in the pump.

2.3. TRIBOLOGY INTERFACES
A bearing is required within this previously mentioned interface in order to constrain motions to only the desired motion and reduce the friction between the moving parts. The reason for the focus on this element is because of its importance in not only fun-

(A)   (B)
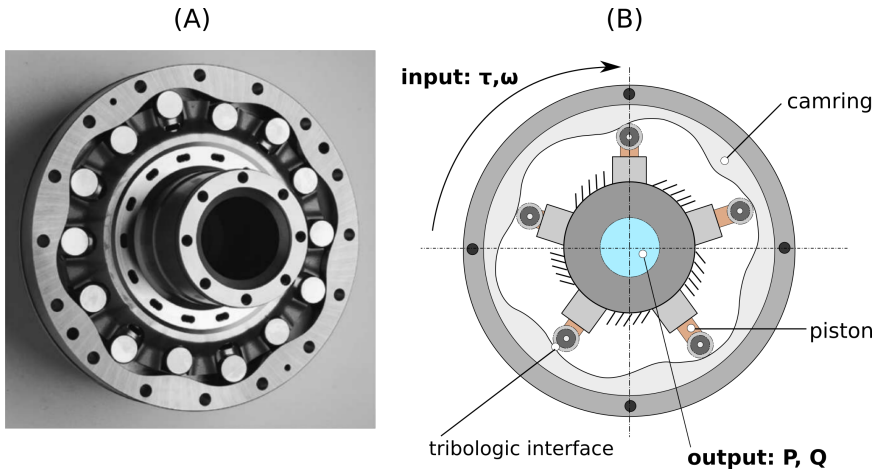
Figure 2.5: (Left)The basic lay-out of a radial piston pump utilizing a camring to obtain a higher gear ratio. (Right) The basic input and output for a radial piston pump, specifically defining the crucial tribology interface.

damental functioning of the pump, but also the limitation it gives to the pump design. The camring design seen in the Hagglunds pump [122] causes the large load to be transported through an increasingly smaller surface area, since the pistons point inwards. This means the high torques generated by the wind turbine have to be transferred into high pressures of the pump output through this interface. The development trend of ever-increasing force-density will further strain this limitation. Together with the fact that the camring is fundamentally a counter surface with a continuously varying curvature makes these interfaces a challenging design case.

The characteristic that makes this desgin case even more challenging is the use of water as the hydraulic fluid. The Hagglunds CB 1120, one of the pumps used in this work as a benchmark of performance, both uses oil as its hydraulic fluid as well as its lubricant. Although having some significant downsides as a hydraulic fluid, as a lubricant oil is generally superior. Oil is significantly more viscous then water, a property fundamental to the lubrication properties of a fluid. The typical viscosity of water at room temperature is 1 [mPa · s], while that of oil can vary from 10 to 100 times more. This lubrication property is in pumps advantageous for the piston-housing bearing interface. Also since oil in general does not invoke any negative effects on other tribological interfaces such as the camring-piston interface, sealing is less crucial. The most common view on water in tribology however, is that it is seen as an undesired pollution of the lubricant [149, 189]. A second undesired characteristic is the corrosive effects on metals, which are one of the most commonly used materials in tribological material pairs such as found in hydrostatic and hydrodynamic bearings [107].

Taking all these challenges into account, the following fundamental design characteristics can be defined for the piston-camring interface:

- Low friction to minimize mechanical losses.

- High lifetime.

- A high load capacity-to-bearing footprint ratio.

- Functional for counter surfaces with a non-constant or varying curvature.

In terms of design options, only a few bearing archetypes are known in literature [159, 192] that would function for the presented interface. These archetypes will be discussed briefly, since they form an important step in comparing design alternatives.

2.3.1. PLAIN BEARINGS

Plain bearings are widely seen as the simplest type of bearings and are one of the most common archetypes used in a variety of, often less demanding, applications. They can be generally divided into dry rubbing and self-lubricating. Because dry rubbing plain bearings do not make use of any lubricant, they are limited by dynamic friction and material properties. Several embodiements can be seen in figure 2.6. Usually a non-metal
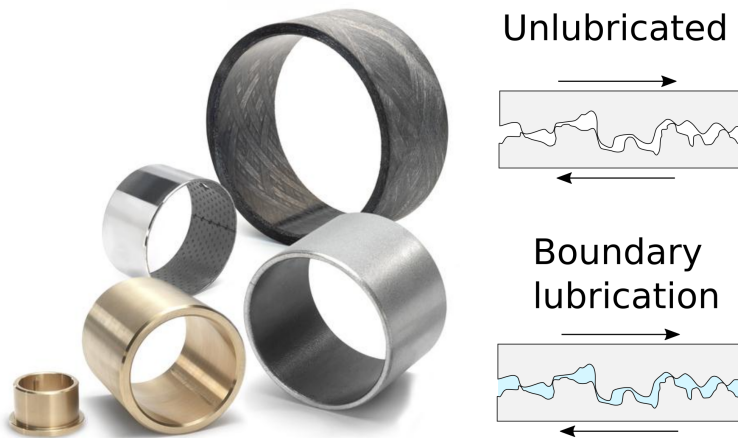
Figure 2.6: A variety of plain bearings and their lubrication cases.

is used as bearing material, with a metal counter surface. Their performance, being limited by temperature performance of the material, thus has a limited allowable velocity. This is generally described by a PV value (pressure times velocity) [210]. Lubricated plain bearings include self-lubricating porous metals, which are impregnated with a lubricant. This lubricant, conventionally some form of mineral oil, is stored within interconnected voids. These type of bearings operate somewhere in the boundary lubrication regime, where the lubricant creates part of the load carrying capabilities.

2

2.3.2. ROLLING-ELEMENT BEARINGS

The rolling type bearing is for many engineering applications the gold standard, especially when higher performance is required. They fundamentally consist of a repeating series of rolling elements stacked between an inner and outer housing. These rolling elements have several embodiments, from single ball rows, to cylinders, conical and spherical rollers. They have a wide range of load and velocity ranges. Because of the geometries used, motion is primarily generated by rolling, and very little sliding. Rolling resistance is generally significantly lower then the resistance of sliding elements. They are usually lubricated by either oil or grease, which significantly improves their lifetime. Although elasto-hydrodynamic lubrication effects [192] does give them full film characteristics, they still experience wear. Next to this, degradation of their often closed system lubricant results in limited lifetime.

2.3.3. FLUID FILM BEARINGS

The final primary archetype that could be implemented are fluid film bearings. A thin film of fluid is able to completely lift bearing and counter surfaces from each other. This has two resulting advantages: the lack of contact eliminates wear and it introduces very low friction. This type of lubrication is called full film lubrication and can be seen in Figure 2.7 as the optimum use of lubricant. Full film lubrication can be achieved through
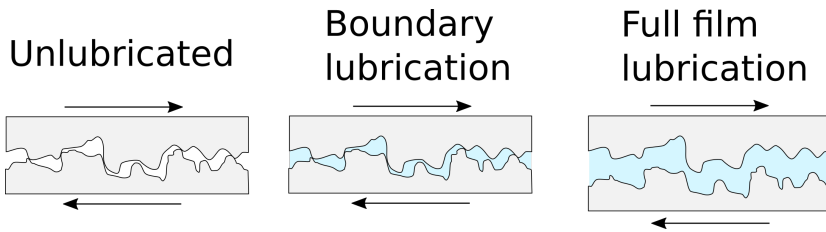
Figure 2.7: How the different regions in the lubrication regime can be defined. In case of full film lubrication, a complete fluid layers seperates the two moving surfaces.

two principles, hydrostatic and hydrodynamic lubrication. With hydrodynamic lubrication, two surfaces are moving relatively to each other with sufficient velocity for a load-carrying lubricating film to be generated [192]. A fundamental constraint is that these two surfaces should be inclined at some angle to each other, since a parallel configuration will not form a pressure field that supports any load. The load capacity of this type of bearings is thus directly related to the velocity of the bearing system. A fundamental limitation of this bearing type, compared to roller bearings, is that it suffers from performance similar to plain bearings when the velocity is low. An alternative to overcome this limitation is through the implementation of a hydrostatic power source. Instead of relying on motion and geometry to create the required fluid pressure, an external pressure source such as a pump is used. The advantage of this is, as long as the pressure source is able to create enough pressure, the potential load capacity is infinite! This means that any potential load case can be met with low friction characteristics. However, the need for an external pressure source automatically discards this bearing options in many cases.
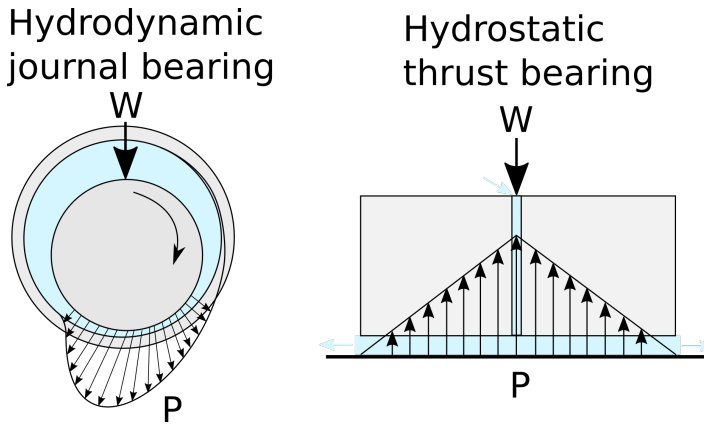
Figure 2.8: (Left) A hydrodynamic journal bearing and its functional pressure profile. (Right) A hydrostatic thrust bearing and its functional pressure profile, assuming a smooth bearing surface.
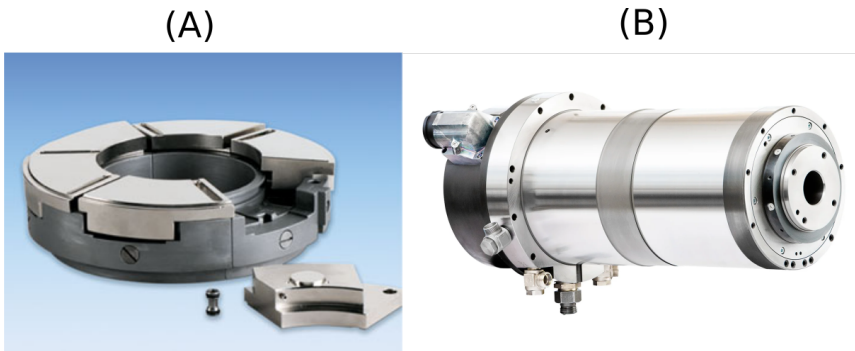
Figure 2.9: (A) A Kingsbury Tilting pad hydrodynamic thrust bearing. (B) A hydrostatic journal bearing by Zollern.

2.3.4. PERFORMANCE & LIMITATIONS

The field of tribology is a well investigated field, and the performance of these previously mentioned archetypes has been well researched. To give a comparison between the types of performance that can be obtained for each different bearing type, the data presented by [159] is used for both journal bearings and thrust bearings. The comparison for oil-lubricated embodiments can be seen in Figure 2.10 and 2.11 respectively. What the two figures represent is the limitation in performance that all bearing archetypes have.

It shows how the different bearing archetypes are fundamentally limited in performance both by load and velocity, two key input characteristics of bearings. The limitation of plain bearings, both dry and lubricated, become apparent through both figures. Compared to these simpler embodiments, roller bearings have superior performance over a larger operation range. They are however fundamentally limited by their frequency of rotation, which is caused by a number of different characteristics. This lim-

2
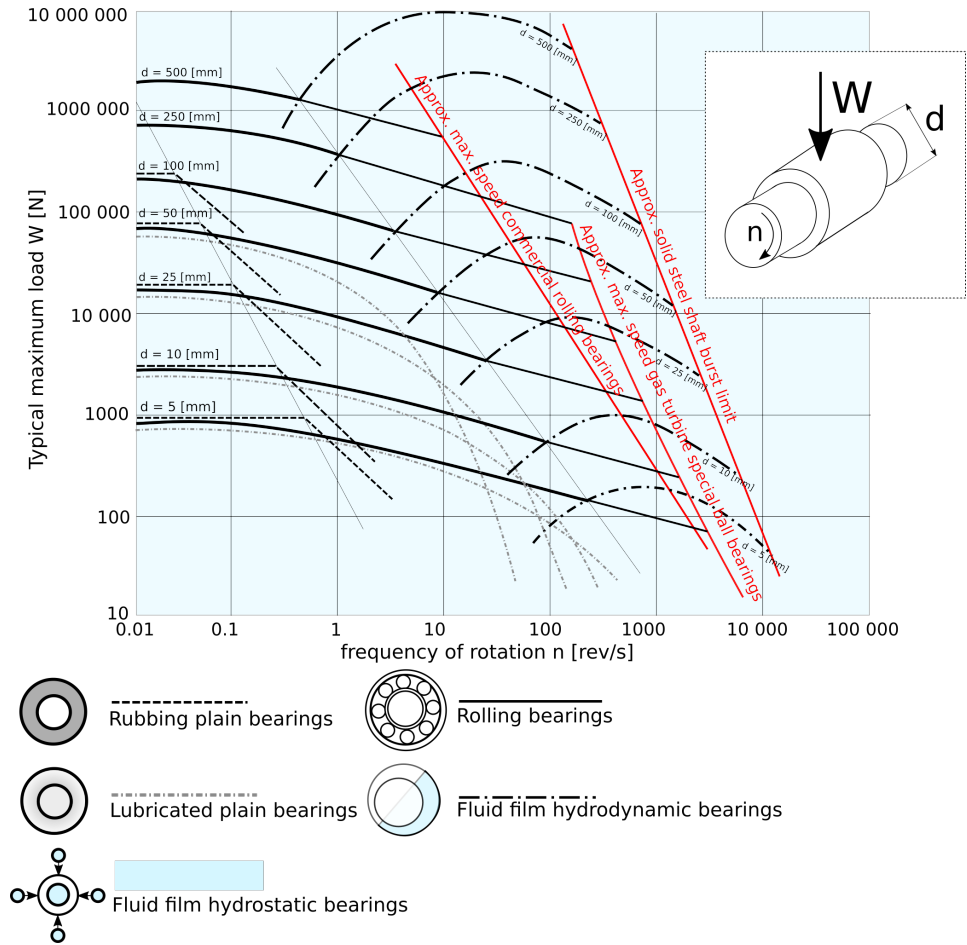
Figure 2.10: The operation range of different journal bearing types, based on the data and tables presented in [159]. The fluid film hydrostatic bearing has a theoretical indefinite work-range, as long as enough input pressure is provided.

itation is defined by the bearing cage and its guiding surfaces, lubricant, centrifugal and gyratory forces acting on the rolling elements and additional component limitation such as seals. Roller bearing used for gas turbines are utilized at extreme rotational velocities, and are used at the limits of this type of bearing capabilities [99]. The main failure mechanism in roller bearings is material fatigue, a failure mode not found in full film bearings.

The two remaining alternatives are the hydrodynamic and hydrostatic fluid film bearings. As previously discussed, these bearing types are defined by their superior performance, which also is visualized in both Figure 2.10 and 2.11. They not only have the highest load carrying capacity given the smallest footprint, hydrostatic versions have a theoretical infinite application area, given the limitation of sufficient input pressure.

For the design of increasingly larger water piston pumps for wind turbines, a set of
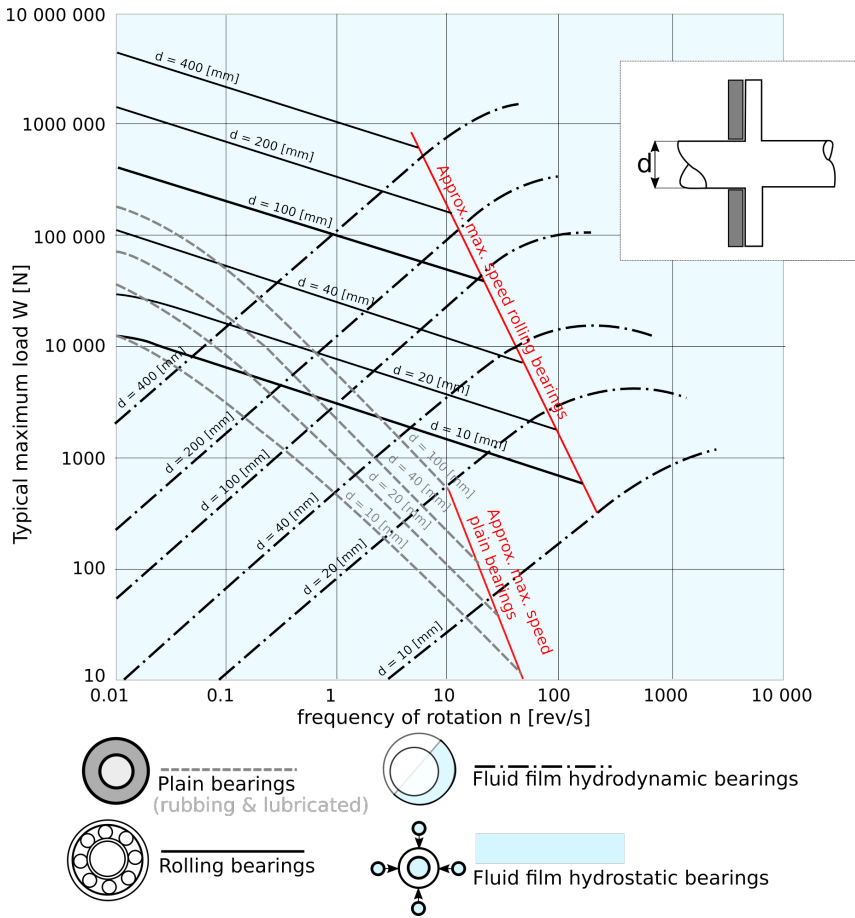
Figure 2.11: The operation range of different thrust bearings, based on the data and table found in [159].

five desired fundamental characteristics have been defined before as:

- Low friction to minimize mechanical losses.

- 'Infinite' lifetime.

- A high load capacity-to-bearing footprint ratio.

- Water lubricated.

- Functional for non-constant curvature counter surfaces.

These figures and the fundamental limitations of all bearings help us navigate through the decision making process. Rubbing and lubricated plain bearings fall short in terms of load-carrying performance as well as the friction and lifetime characteristics, since these bearings are inherently subject to wear. Rolling bearings, have a direct coupling

between footprint and load carrying capacity, have limitations in terms of velocity, are difficult to be combined with water lubricated systems due to corrosion, and are subject to wear.

Compared to these bearing archetypes, hydrodynamic fluid bearings have higher load capacity-to-bearing footprint ratios and low friction characteristics. They however have their own limitations, since they function as plain bearings at low velocity, meaning they do experience some form of wear, and have fundamentally limited load capacities coupled to both bearing footprint and velocity. Finally, hydrostatic bearings show the most promise in the majority of the required characteristics. They have low friction, do not experience wear and can be designed with water lubrication in mind. They also have a crucial characteristic that the other archetypes lack, through the use of the external pressure source, their load capacity can be decoupled from their footprint. They however, also have a limitation: they are conventionally designed for constant curvature counter surfaces.

2.4. CONCLUSION

The development of water hydraulic piston pump driven wind turbines is a step towards a more sustainable future, which is still full of engineering challenges. The higher power to weight, high reliability and low costs of hydraulic drivetrains means their potential improvements compared to the state of the art can prove to be significant. The use of water as hydraulic and lubricant as well as the desire for low friction and 'infinite' lifetime however puts significant strain on one of the crucial design components: the piston-camring bearing interface. Looking at the fundamental characteristics of all bearing archetypes, its observed that they all posses some form of limitation on the pump performance, be that through dimensional constraints, limited load-capacity, or lifetime limitations. It thus becomes clear that direct implementation of existing bearing embodiments would significantly limit performance.

3

THE ECO-IMPACT OF FULL FILM LUBRICATED BEARINGS

Water lubricated bearings have been named in literature as a sustainable alternative to their oil-based counterparts but is this always the case? Sustainable machine design has been named as one of the motivators of this work, and therefor this chapter investigates the impact of full film water lubricated bearings. In order to clarify when water lubricated bearings are or are not a sustainable alternative, and inform design decisions, an eco-impact metric is created for bearing concept design. The model is based on data from the materials, geometries and material combinations that have been the subject of research attention in the past 20 years in water lubricated bearing design. The model provides simple equations, fed with data from literature on materials, production and their tribological combination to provide initial insight on the sustainability of these types of bearings and future designs. A case study illustrates that quantifying environmental impacts can help determine when lubricant loss is more important than material choice, or vice-versa.

The previous chapter shortly investigated the motivation for sustainable sources and talked about the principle, but mostly expanded on the reasons for choosing full film lubricated bearings from the standpoint of performance. Mechanical systems themselves and their operation lifetime, material use and production processes however also greatly impact our planet. It is then also no surprise that beside the continuous search for increased performance, improving sustainable machine design is another increasingly important topic. Tribology is one of the key components when it comes to the continuous search for sustainability improvements within engineering [168]. Water as a lubricant has a rich history in the field of full film tribology. Going back as early as 1840 [171] it has been used in many systems where water is the logical choice, such as many marine applications and water-hydraulic systems [107]. The general view for the majority of history in tribology has been that water is more of a nuisance, than a sustainable alternative to oil-based lubrication. This becomes more clear when looking at Figure 3.1. Here, scientific journal publications from 1955 to 2020 focusing on bearing design with water were investigated for their mention of water as a environmentally friendly solution, mentioning either 'environmentally friendly' OR 'pollution free' OR 'eco friendly' OR 'ecological' OR 'sustainability'. This resulted in the first mentions of sustainability being found starting around the 1990's. Until the 1990's no mention of
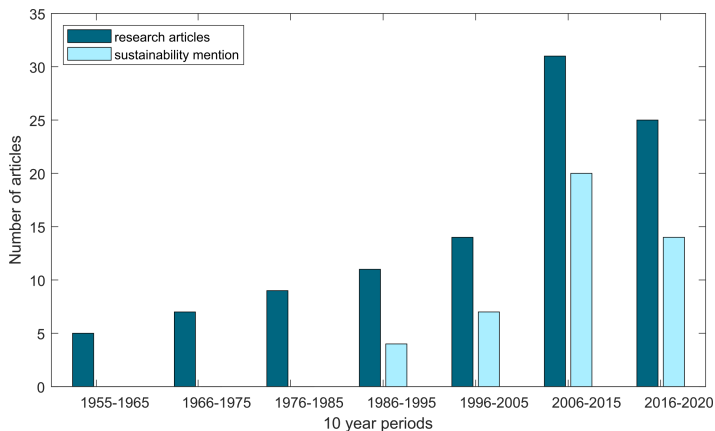
Figure 3.1: Mentions of sustainability of articles on bearing designs with water lubrication. The last period, only being 4 years of length, already has almost similar sustainability mentions as the decade before.

any of these synonyms for sustainability were found. It was not until Clarke [37] mentioned sustainability, mostly from the perspective of the hydraulic medium instead of the lubricant. The influence of tribology on sustainability of engineering can be seen in several ways. An estimated 103 EJ and 7,040 Mt CO_2 is spend on friction losses on a global level [104]. Some other key impact factors are the losses of oil-based lubricants into the environment[181],[169] or their end of life disposal [38]. Improvements within these fields in terms of sustainability can result in valuable improvements. The concept of sustainable or 'green tribology' has been defined specifically with this this in mind as 'the science and technology of tribological aspects of ecological balance and of environmental and biological impacts' [168]. Green tribology has been suggested to potentially

lead to energy savings, environmental benefits, cost reduction and social progress [205]. To achieve this, Nosonosky and Bhusian [168] noted twelve principles of green tribology. Amongst them are (1) Minimization of heat and energy dissipation, (2) Minimization of wear, (3) Natural lubrication, (4) Biodegradable lubrication, and (5) Sustainable energy applications. These objectives align to those presented by Tzanakis et al. [205], and provide tribology researchers a clear set of objectives to aim for. The minimization of heat and energy dissipation as well as the minimization of wear align perfectly with the inherent properties of full film lubricated bearings. However, when looking at present literature and its statements concerning water, it is used synonymous with a sustainable lubricant alternative [149]. At first glance this might indeed seem like a valid statement, the general perception of water is of course that water is a more sustainable medium then any form of oil. This can also been seen in the Carbon footprint of water [184] being very low compared to that of lubricant oil [113]. There are however other critical components that define the sustainability of a bearing system, including embodiment, material combination and wear performance. In order to make well founded arguments concerning sustainability of a particular bearing design, these components have to be taken into account. Given the worldwide engineering trends, it will become part of engineers, designers and researchers to take into account sustainability when developing novel system at the earliest convenience. These types of sustainability analyses are currently performed solely at the end of the design cycle, when more data is available, but the choices have already been made and the 'damage' is done. Having a method available for the sustainability analysis early in the design process can greatly improve the motivation for choosing water lubricated bearings and the decision for the most sustainable design. An anticipatory sustainability metric could thus be used to improve the motivation on sustainable water lubricated bearing design.

As observed in literature [39, 81], several metrics can be used to define sustainability. The problem that generally arises with Life Cycle Assessment (LCA) approaches is the lack of reliable data, especially when more exotic materials and production processes are involved. One could thus look at metrics which are more generally available, namely:

1. global warming potential (GWP), defined by the carbon dioxide equivalent [CO_2eq].

2. primary energy use [MJ].

These metrics are widely available for the far majority components necessary for analysis and are widely understood by a large spectrum of the engineering field. They are thus favored over other important impact categories such as acidification, eutrophication, particulate emissions, or resource depletion that would have required estimations and are usually compared to each other with given weight factors. Since the materials analyzed here are not likely to have extreme differences in their impact category profiles (such as one material having very high GWP impacts but very low acidification, with another material having the reverse), the metric of GWP should provide reasonable comparisons, even if it is an incomplete picture.

This chapter investigates the possibility of defining a metric for sustainability for full film lubricated bearing design based on anticipatory life cycle assessment [240]. In the

form of simple equations, the environmental impacts of different design options can be calculated. The data needed for the calculations come from literature on full film water lubricated bearings, based on primary topologies, production steps and material combinations, observed in the past 20 years of research literature. A design case is used to compare how water lubricated bearings can perform compared to their classic oil-based counterparts in terms of sustainability, further motivating the proposed need.

3.1. METHODS

An LCA is a validated approach for sustainability analyses. The approach has been described in detail in the ISO14040 standard [194]. The problem with conventional LCA approaches, is that they usually require data from mature industries, supply chains and products. They are therefore usually performed in retrospect. A different approach is to use this type of analysis as an anticipatory metric as presented by [240]. This anticipatory approach allows for the LCA resulting metric to be used during development to make more quantitative based statements concerning the sustainability of a certain design. The construction of the metric follows initial identification steps performed in. Of these steps, the most fundamental is how to define sustainability for the type of system under consideration, which can vary greatly.

Taking into account the primary scope of the assessment, a general system boundary has been determined [194]. The visualization of the general bearing system used in this work can be seen in Figure 3.2. The system consists of the two main components crucial to full film lubricated bearing design, the bearing system and lubricant. The lubricant directly influences the material choices and thereby also the production of the bearing system. Its presence directly influences the performance obtained in operation, and therefore the lifetime of the system. Resulting decommissioning of the bearing system is linked to the time-to-maintenance of the bearing [100]. The following assumptions are made for the analysis of different types full film lubricated systems:

1. Transport, water and energy used between all processes are not taken into account for this analysis. Motivation for this choice is two-fold. Firstly, these steps are necessary for all bearings independent of their type (water or oil-based), and thus the impact for these steps will be more or less equal. This means that their impact will only effect the total magnitude, but hardly influence relative differences between bearing types. The difference between lubricants will be taken into account in the raw material acquisition comparison. Secondly, based on an extensive description of a roller bearing LCA [53] which are comparable systems in comparable applications, it was concluded that the influence of transport on the total system is small compared to the significantly more dominant effects of materials and production. Waste management is not taken into account because it again is assumed to be similar for all bearing types.

2. Operation, maintenance and decommissioning depend primarily on bearing lifetime and lubricant leakage. For bearings this can directly be expressed using the wear of the bearing and the leakage from the bearing. The higher the wear of the bearing, the sooner maintenance will have to be provided or decommissioning
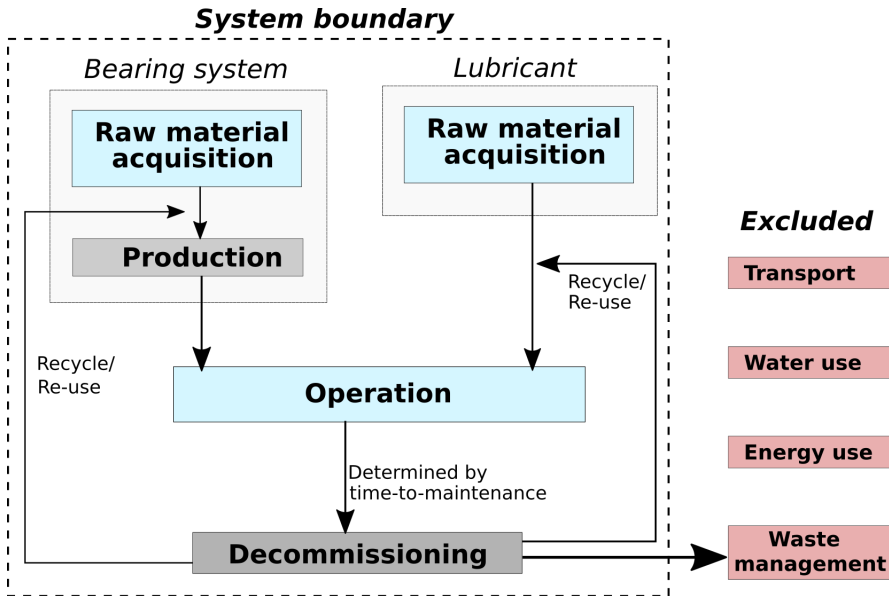
Figure 3.2: Visualization of the boundary system used for the analysis. Transport is not taken into account, and water use is not taken into account except in the form of lubricant leakage when water lubricated systems are considered.

occurs. Simultaneously, the higher the leakage from the bearing, the larger the relevance of the lubricant on the sustainability of the system. Both wear and leakage are dependent on several factors including velocity, load and temperature.

The environmental impact contributions are thus captured in the following 4 attributes: The bearing, lubricant, lifetime and leakage. The system visualized in Figure 3.2 is therefore redefined using these main factors. Please note that the model thus simplifies a more complex system in favor of a model consisting of a limited set of well defined parameters.

3.1.1. ECO-IMPACT METRIC

The functional unit used in this work is the eco-impact of a given bearing design for a given service life. Because of the desire for an anticipatory assessment, the impact contributors have been simplified to the following main components: Bearing mass and production, lubricant use and loss, and bearing lifetime. These components are relatively easily identified, but still describe the system with an acceptable degree of accuracy. Secondly, environmental impact parameters are usually expressed as function of weight, further motivating the choice of using bearing mass compared to alternatives. Mass also is also directly dependable on bearing structure, size and shape and thus take these characteristics into account. Figure 3.3 visualizes the main contributors and their system components needed for determining an impact assessment. The bearing and lubricant impacts are used to represent a bearing design at the start of its operation life.
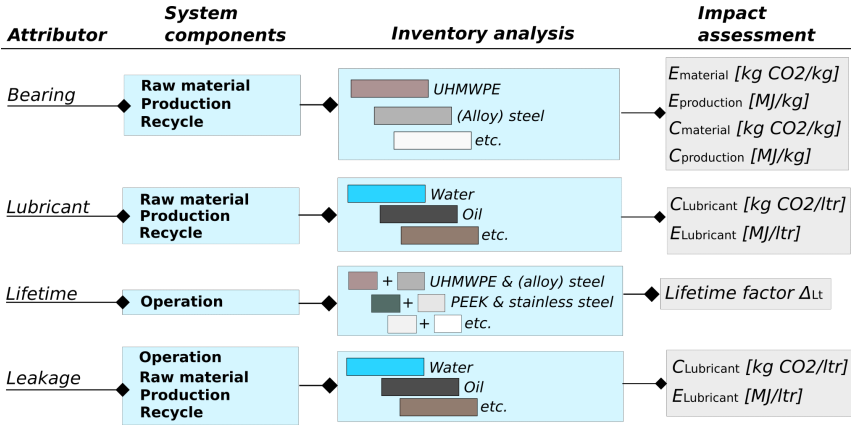
Figure 3.3: A visual representation of the impact assessment parameters as related to the bearing system.

The second component is defining the effects of operation. This effect is dominated by the wear of the bearing and the loss of lubricant through leakage. The wear of the bearing is determined by its material combination, lubricant and load condition, while the leakage is primarily based by the design of the bearing and its operation condition. Based on these system components, the following relations are proposed:

$$C_{\text{Bear}} = \frac{M_{\text{total}} \cdot (c_{\text{mat}} + c_{\text{prod}})}{\Delta_o} \tag{3.1}$$

$$C_{\text{Lub}} = c_{\text{lub}} \cdot (V_0 + \dot{V}_{\text{day}} \cdot t) \tag{3.2}$$

$$E_{\text{Bear}} = \frac{M_{\text{total}} \cdot (e_{\text{mat}} + e_{\text{prod}}))}{\Delta_o} \tag{3.3}$$

$$E_{\text{Lub}} = e_{\text{lub}} \cdot (V_0 + \dot{V}_{\text{day}} \cdot t) \tag{3.4}$$

where M_{total} is the total bearing mass [kg], c_{mat} the specific CO_2 impact of the bearing material [kg CO_2/kg], c_{prod} the specific production contribution of the bearing [kg CO_2/kg], Δ_o the operation factor defined by the material combination. V_0 is initial lubrication volume [ltr], $\dot{V}_{\text{day}}$ is the daily leakage volume rate [ltr/day], t [days] is time scaling factor coupled to the leakage and c_{lub} the CO_2 impact per liter of the lubricant. The lubricant is defined in carbon equivalent per volume expressed in liter, since this is more common practice in literature. Lastly e_{mat}, e_{prod} and E_{Lub} are the primary energy equivalents. The impact of lubricant loss through degradation and leakage is effectively captured in the defined volume rate $\dot{V}_{\text{day}}$ and the initial volume V_0. Because the leakage volume rate $\dot{V}_{\text{lub}}$ has to be replaced in order to guarantee operation, and replacing the entire lubricant volume V_0 is required when degradation has occurred, they effectively capture both effects. The lifetime factor Δ_o [-] presented in equation 1 and 3 is a measure of incorporating wear effects of the bearing, and is meant as a comparative method between material combinations. The use of this lifetime factor is based on the following assumptions to provide a fair comparison.

1. When comparing material combinations, the same load case has to be considered.

2. The mass M_{total} is only defined by the one part of the bearing that is susceptible to wear in the material combination, as it is assumed that the counter surface has effectively infinite lifetime by comparison.

To objectively make a anticipatory comparison, it is needed to simplify a general bearing system. By determining the sustainability component of only that specific component of the bearing that wears, a more general comparison can be made. The addition of other components of the bearing system might make the model more complete, but would also introduce additional uncertainties. The mass M_{total} will thus be defined solely by the mass of the wearing material, as seen in figure 3.4. Using equations 1 to 4, a CO_2
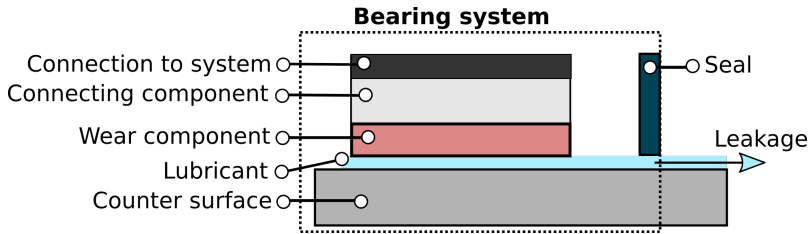
Figure 3.4: Basic embodiment representation of bearing system, where the wear component dominates the sustainability analysis. The seal is only modeled through its effect on limiting the daily leakage volume $\dot{V}_{\text{day}}$.

equivalent and primary energy representative impact metrics can be defined:

$$C_{\text{Total}} = C_{\text{Bear}} + C_{\text{Lub}} \tag{3.5}$$

$$E_{\text{Total}} = E_{\text{Bear}} + E_{\text{Lub}} \tag{3.6}$$

Where C_{Total} and E_{Total} are the CO_2 equivalent and primary energy representative impact factors respectively. These two metrics can be used to give an anticipatory impact assessment for a given bearing configuration. It can thus be used to compare bearing systems with different lubricants and material choices.

For different bearing materials and lubricants, material combinations, and manufacturing methods used to produce these bearings and lubricants, input data is required in order to be able to perform this analysis.

3.1.2. DATA COLLECTION

Previously, the approach to define an impact metric has been defined. The metrics defined in equations 3.6 and 3.6 are dependent on various material properties and bearing dimensions. This work focuses on water lubricated full film bearings. Bearing designers can also use this work to directly evaluate the differences of a water lubricated design with an oil lubricated alternative. However, the wide variety in materials combinations used for water lubricated bearings makes them the primary focus of this work.

To find the required input data, a literature analysis on bearing development of the past 20 years has been performed. Articles focused on water lubricated bearings from the past 20 years are collected, characterized by design, principal materials and material combinations. The materials are then described in terms of their sustainability and

performance characteristics such that they can be implemented in the introduced sustainability metric. This analysis is performed in three steps, namely:

1. The identification and categorization of literature focusing on water lubricated bearings.

2. Identify used materials, material combinations and bearing designs.

3. Determine characteristics required for sustainability metric.

An analysis framework was constructed for the first step, being identification and categorization of literature. This approach is similar to the approach performed in [198].

The choice was made to analyze water lubricated bearing development from the year 2000 onward in which sustainability was explicitly mentioned. The literature investigation has been divided into a search for work focused on design and performance, and a search for work focused on materials. This in order to get an overview on the relative focus performed on both components within the full film bearing design. The literature analysis strategy can be seen in Table 3.1.

Only English written sources were analysed. As for other inclusion criteria, all papers concerning water lubrication with additional additives in the lubricant were excluded. Roller bearings were excluded as well. In case of duplicates, such as for instance in work presented in both a dissertation and a journal publication, only the journal publication is included. The approach is visualized in Figure 3.5.
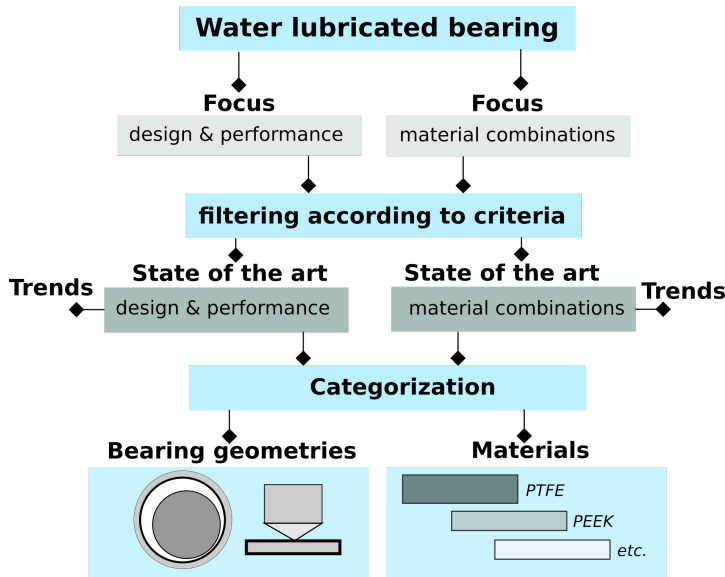
Figure 3.5: Approach used to differentiate between geometry and material focused literature.

Table 3.1: Data collection strategy.

Literature data collection strategy	
Search keywords (focus on design)	1) "WW" AND "lubricated" AND "bearing" 2) "WW" AND "hydrostatic" AND "bearing" 3) "WW" AND "hydrodynamic" AND "bearing" 4) "WW" AND "slider" AND "bearing" 5) "WW" AND "lubricated" AND "XXX" 6) "WW" AND "slipper" 7) "WW" AND "journal" AND "bearing" Where "XXX" is a range of applications: Spindle, pump, motor, systems, and "WW" is water
Search keywords (focus on material)	1) "WW" AND "lubricated" AND "Bearing" AND "materials" 2) "WW" AND "lubricated" AND "material" AND "combinations" 3) "WW" AND "lubricated" AND "materials" 4) "WW" AND "lubricated" AND "YYY" Where "YYY" is a material archetype: plastic, metal, composite, ceramic, and "WW" is water
Used Databases	Elsevier, ASME, Sagepub, Springer, Google Scholar, Scopus
Year range	2000-2020
Language	English
Included Publications	Original research article, conference article, review article, book, reports
Inclusion criteria	1) In English language 2) water without additives as lubricant 3) sliding contact at boundary or mixed lubrication
Exclusion criteria	1) duplicates

3.1.3. INVENTORY ANALYSIS

The analysis strategy is thus used to identify the materials, material combinations and bearing designs used in full film water lubricated bearing design. It therefore differs from a conventional review, in that the focus is not to broadly identify the field in different aspects, but instead to map only these crucial parameters:

- The c_{mat} and e_{mat} parameters for the bearing materials found using the analysis.

- The c_{prod} and c_{prod} parameters, specified for the material archetypes found in the analysis. The archetypes are defined as polymers, metals, ceramics and compos-

ites.

- The Δ_o factor, depending on material combinations found in literature.

- The c_{lub} and e_{lub} parameters for the lubricant.

After identification of the materials, the production steps and subsequent environmental impacts are determined.

The impact parameters for bearing materials, production processes, material combinations and lubricant are obtained by the combination of available literature, CES Edupack [18] and ecoinvent 3.6 [241]. These parameters are generally expressed as a function of weight. To model the environmental impact per kg of final formed material as a result of specific manufacturing processes, the Eco Audit tool in CES edupack has been used. In case of manufacturing methods that require the removal of material, it has been assumed that 20 % has been removed. Because this removal is heavily dependent on design, the examples here can only be used as an indication to show the share of manufacturing on the sustainability of a system. This however is acceptable because in general the contribution of production is low in contrast to the virgin material and time-to-maintenance effects captured by the lifetime factor Δ_o. For this reason, the effect of production is modeled as a function of the material archetypes. Finally, the material combination impact value is determined through the use of the so-called 'triboregister', which is a library by the Dutch ministry of traffic and water management [183]. It provides an extensive overview of tribological material combinations loaded under equal conditions, with most of the data in this reference being obtained in water lubricated systems.

3.2. Analysis results

A total of 127 articles was found matching the previously identified criteria. The review resulted in 53 articles with a focus on design or performance, and 74 with a focus on material combinations. Because this list of articles found is already fairly small, no articles were discarded based on journal ranking or (lack of) citations. In accordance with the review approach visualized in Figure 3.3, a categorization of both bearing geometries and materials present in both groups was performed. It is important to note that in the case of a material focused research, a functional bearing geometry is often not necessary. This means that in the majority of cases, research is performed using either a pin-on-disc or ball/pin-on-ring type tribometer. The articles with a focus on design and performance are [5, 12, 16, 33, 40, 61, 62, 71, 74, 82, 89, 97, 103, 110, 111, 124, 131, 133–135, 137, 138, 140, 141, 143, 145, 147, 150, 157, 161, 166, 170, 172, 173, 175, 180, 190, 213, 223, 225, 226, 234, 244, 245, 250, 252–254, 256–259, 263, 264]. Respectively, all articles with a focus on materials are [1, 4, 20–32, 41, 42, 45–49, 63, 69, 70, 73, 76–78, 83–86, 94, 112, 117–119, 121, 132, 133, 139, 142, 144, 154, 155, 160, 167, 179, 196, 197, 201, 207, 208, 219–222, 227–230, 232, 233, 235–239, 243, 248, 249, 255, 261].

3.2.1. Materials

Both categories of articles were investigated in terms of presented materials. It has to be noted, that for articles focusing on design a material combination was often not

expressed, since this is not crucial for certain topics. Since a wide variety of material are used in bearing design, a characterization was made based on the following previously mentioned archetypes: metals, ceramics, polymers and composites. All materials present in literature have been mapped within these archetypes in terms of their recurrence. The resulting overview of materials can be seen in figure 3.6. Materials with only a single occurrence in literature, have a combined representation stated in the archetypes as 'other'. Also, certain variations of the same material are all combined into a single representation into the overview. This means certain types of stainless steel are all captured under the same representation "stainless steel". This generalization is chosen to favor overview over detail. Secondly, a certain specific version of the same primary material only influences the eco-impact properties in a limited way, and these properties for very specific versions of a material are usually not identified in literature.
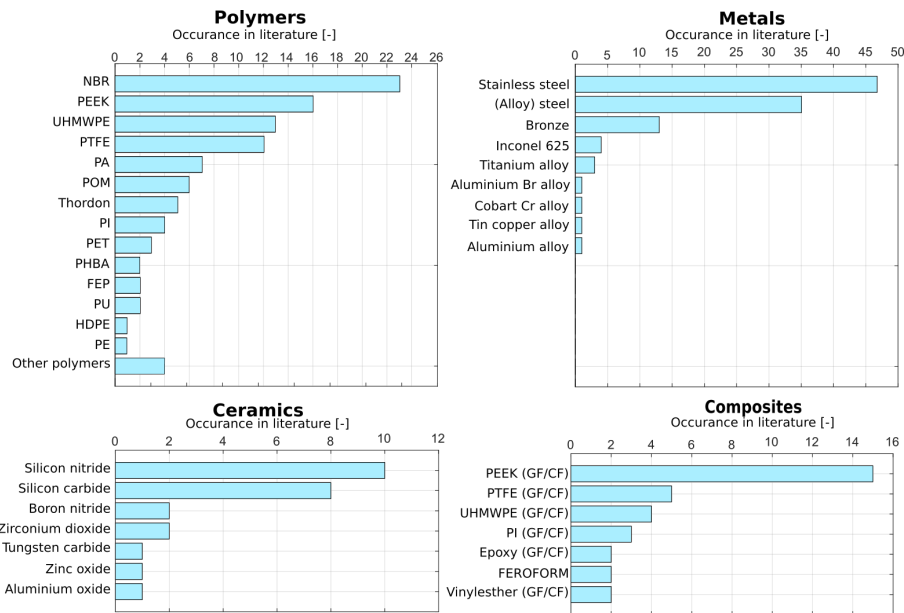
Figure 3.6: Materials found in literature and their occurrence. For the polymer archetype presented in this figure, the full names of the presentated materials are: Nitrile Butadiene Rubber (NBR), Polyether ether ketone (PEEK), Ultra-high-molecular-weight polyethylene (UHMWPE), Polytetrafluoroethylene (PTFE), Polyamide (PA), Polyoxymethylene (POM), Polyimide (PI), Polyethylene terephthalate (PET), polyhydroxybenzoic acid (PHBA), fluorinated ethylene propylene (FEP), Polyurethane (PU), High-density polyethylene (HDPE) and polyethylene (PE). For the composite archetypes, GF and CF stands for glass fiber and carbon fiber respectively. The full names for the abbreviated metals are aluminium bronze alloy and cobalt chrome alloy.

The most common polymers present in literature are PEEK, Nitrile Butadiene rubber (NBR) and Ultra High Molecular Weight PolyEthelyne (UHMWPE) respectively. The single occurrence polymers found in [83] have been combined into a single representation defined as 'other'. The most common materials present are stainless steels, steel alloys and bronze. There have been several different types of stainless steels presented in literature, with the most common being type 316 with 17 occurrences. The group steel alloys

covers a wide variety of different steels, including tool steel, type 45 structural carbon steel and 34CrMo1. Often however in design focused articles, the specific steel type is not given. To obtain an improved overview and because the exact metal is not required for later sustainability impact assessment, the different steels have been grouped. This archetype is also often in literature, because it is the most common counter surface. Furthermore, the unique present metals in literature are tin-copper alloy [261] and Cobalt Chrome alloy [86]. By far the most common ceramics for water lubricated bearings are silicon carbide and silicon nitride. The additional unique present ceramics in literature is tungsten carbide [167]. These material type is most self paired archetype, meaning either a combination of the same materials or the same material archetype is used. Finally, composites commonly presented in literature are a form of filled PEEK, followed by filled UHMWPE and filled PTFE. This closely follows the trend of most common polymers present in literature. The additional uniquely presented materials in literature are filled vinyl ester and filled PPS. These are usually compared with respect to their virgin/unfilled counterparts in literature to determine where the performance increase is obtained.
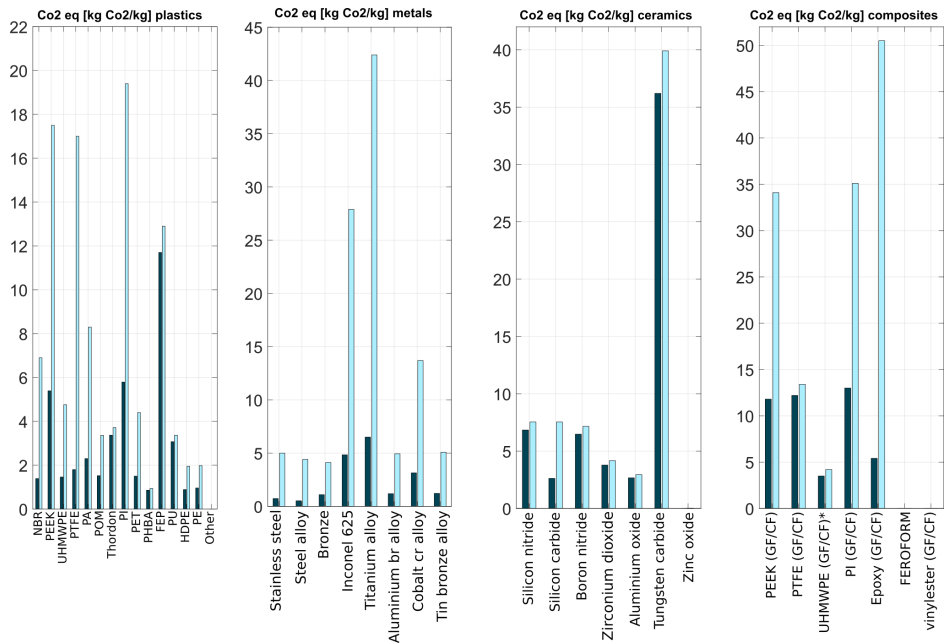
Figure 3.7: CO_2 equivalent for all materials presented in this work. The dark and light bars are the worst and best case scenarios in terms of recycling. The CO_2 equivalents for materials FEROFORM and fiber filled vinylester were not observed in literature and therefor not determined.

MATERIAL IMPACT

To obtain the necessary data required for the use of the equivalent impact factors as assessment tools, the previously presented materials in figure 3.6 are used. The CO_2 equivalent is presented in Figure 3.7, while the primary energy is presented in Figure
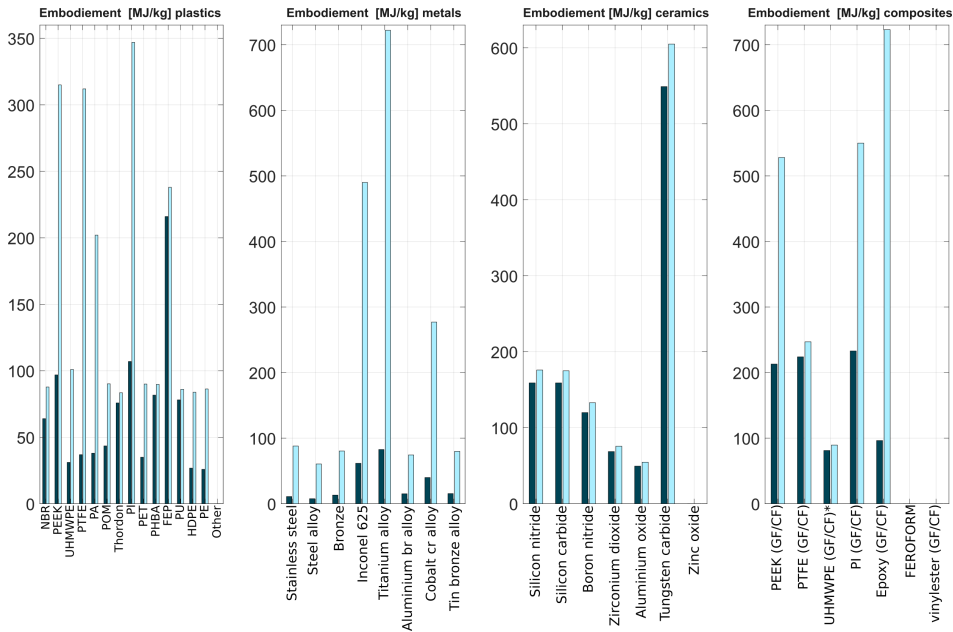
Figure 3.8: Primary energy for all materials found in this work. The dark and light bars are the worst and best case scenarios in terms of recycling. The CO_2 equivalents for materials FEROFORM and fiber filled vinylester were not observed in literature and therefor not determined.

3.8. In all cases both a best and worst case scenario have been presented. The best case means the embodiment energy and CO_2 equivalent have been determined for material that will be recycled, while the worst case scenario is determined by its virgin production without any recycling, down cycling or landfill procedures.

3.2.2. MATERIAL COMBINATIONS

To visualize the occurrence of certain material combinations, an overview is presented in figure 3.9. 83 unique material type combinations have been observed in literature. The choice is made to cluster material combinations consisting of metals or ceramics with a specific counter surface material that occur only once in literature in their respective "other" groups. As seen also in the presence of materials in literature, primarily polymers-metals and composite-metal combinations have been observed. Virgin and filled PEEK in combination with stainless steel is by far the most common material combination observed. Silicon carbide is the most self-mated material combination in literature.

LIFETIME FACTOR

In case of a comparison between material combinations, the load case is crucial for the subsequent analysis. To provide the reader with material for such a comparison, a library of different tribological material combinations has been analysed based on those found in the triboregister [183].

	Stainless steel	(Alloy) Steel	Bronze	Inconel 625	Other metals	Silicon nitride	Silicon carbide	Boron nitride	Zirconium dioxide	Other ceramics
NBR	5	5	3	0	1	0	0	0	0	0
PEEK	10	4	0	1	0	1	0	0	0	0
UHMWPE	5	2	3	3	0	0	0	0	0	0
PTFE	5	5	1	1	0	0	0	0	0	0
PA	2	2	0	0	1	0	0	0	0	0
POM	3	2	0	0	0	0	0	0	0	0
Thordon	3	2	0	0	1	0	0	0	0	0
PI	3	1	0	0	0	0	0	0	1	0
PET	1	0	0	2	0	0	0	0	0	0
PHBA	2	1	0	0	0	0	0	0	0	0
FEP	2	0	0	0	0	0	0	0	0	0
PU	0	0	0	0	1	0	0	0	0	0
HDPE	0	0	1	0	0	0	0	0	0	0
PE	0	1	0	0	0	0	0	0	0	0
PMMA	1	0	0	0	0	0	0	0	0	0
Stainless steel	0	0	3	0	1	1	1	0	0	0
(Alloy) steel	0	0	1	0	1	2	1	0	0	2
Bronze	3	1	0	0	0	0	0	0	0	0
Inconel 625	0	0	0	0	0	0	0	0	0	0
Titanium alloy	0	0	0	0	0	0	0	0	0	1
Copper Al alloy	1	0	0	0	0	0	0	0	0	0
Cobalt Cr alloy	0	0	0	0	0	0	0	0	0	0
Zinc copper alloy	0	0	0	0	0	0	0	0	0	0
Silicon nitride	1	2	0	0	0	0	2	1	0	1
Silicon carbide	1	1	1	0	0	3	4	0	1	2
Boron nitride	0	0	0	0	0	1	0	1	0	0
Zirconium dioxide	0	0	0	0	0	0	1	0	0	0
Aluminium oxide	0	0	0	0	0	0	1	0	0	0
Tungsten carbide	0	0	0	0	1	0	0	0	0	0
Zinc oxide	0	0	0	0	0	0	0	0	0	0
PEEK (GF/CF)	10	4	0	0	0	1	0	0	0	0
PTFE (GF/CF)	4	3	0	0	0	0	0	0	0	0
UHMWPE (GF/CF)	1	1	0	1	1	0	0	0	0	0
PI (GF/CF)	2	1	0	0	0	0	0	0	0	0
Epoxy (GF/CF)	2	0	0	0	0	0	0	0	0	0
FEROFORM	1	1	0	0	0	0	0	0	0	0
Vinylester (GF/CF)	0	2	0	0	0	0	0	0	0	0

Figure 3.9: Overview of material combinations found in literature. The number is a representation of the material combination occurance in literature.

In table 3.2, several water lubricated material combinations and their load-conditions have been presented. The amount of wear is used to determine the lifetime factor for these material combinations. In the table presented, material 1 is the one that wears down, while material 2 is the counter-surface. Operation factor Δ_o is based on determining the effectiveness of the material combination. This has been done by normalizing the wear relative to the most effective water-lubricated material combination. Any material with a $\Delta_o < 1$ indirectly means the time-to-maintenance would be lower with respect to the reference material combination, which is UHMWPE to Stainless steel (SS). Simultaneously, a value $\Delta_o > 1$ would be an increase of time-to-maintenance of the same bearing sleeve. To give an example of how this could be implemented, a comparison be-

tween UHMWPE to stainless steel and HDPE to stainless steel in table 3.2 can be made. If a system has been designed such that the lifetime is dictated by the lifetime of UHMWPE to stainless steel ($\Delta_t = 1$), using a HDPE bearing sleeve instead would mean that in that given lifespan, the HDPE sleeve would have to be replaced more then 44 times, because the material combination is less effective against wear. Although a simplification of the real life situation, which is dependent on significantly more variables, this lifetime factor Δ_o allows for a systematic comparison of the effects of different material combinations.

3.2.3. PRODUCTION IMPACT

Figure 3.10 shows the overview of production methods analyzed in this work. The presented figure is based on using 4 materials per material archetype found in literature to define an average production cost per archetype group and production method. The plot shows both the median in all cases, as well as the outliers to determine the range. For the archetypal material of polymers, PEEK, UHMWPE, PTFE, and POM have been used as typical examples. For the metals, stainless steel, bronze, medium carbon steel, and inconel 625 have been used. For the ceramics, silicon nitride, silicon carbide, boron nitride, and zirconium dioxide have been utilized. Finally, GF PEEK, GF PTFE, CF PI and GF UHMWPE has been analyzed to obtain the typical values for the composite manu-

Table 3.2: Lifetime factor for several material combinations.

Mat 1	Mat 2	Ra	[MPa]	[mm/s]	[C]	wear	Δ_0
Water lubr.						$*10^{-9}$ $[mm^2/N]$	
UHMWPE (CF)	SS	0.8	2.7	10	20	0.429	1
UHMWPE	SS	0.4	2.5	10	20	1	0.429
PEEK	SS	0.1	2.5	500	20	1.5	0.286
PA 6	SS	0.8	2.4	10	20	4.4	0.0975
PTFE (CF)	SS	0.8	2.5	10	20	7.0	0.06128
UHMWPE	Steel	2.5	2.7	10	20	9.7	0.044
HDPE	SS	0.5	2.5	10	20	19	0.0226
PET	SS	0.8	2.5	10	20	20.1	0.021
PTFE	SS	0.8	2.5	10	20	37	0.0116
PTFE (GF)	SS	0.8	2.5	10	20	45	0.0095
POM	SS	0.8	2.5	10	20	46	0.0093
Bronze	Steel	1.6	2.5	10	20	34	0.0088
Thordon	SS	0.8	2.5	10	20	93.1	0.0046
Aluminium br.	SS	0.8	2	10	20	219	0.00195
SBR	SS	0.8	2	10	20	451	0.0009
Oil Lubr.							
UHMWPE	SS	1.8	2.5	10	<70	0.001	429
UHMWPE	Steel	2.5	2.5	10	<70	0.01	42.9
Steel	Steel	2.5	2.5	10	20	2	0.214
Bronze	SS	0.8	2.5	10	20	5.7	0.0753
Aluminium br.	SS	2.5	2.5	10	<70	6	0.0715

facturing archetype. For polymer fine machining, the medians are 0.18 [kg Co2/kg] and 1.905 [MJ/kg].

For Polymer molding, these are 2.125 [kg CO_2/kg] and 30.5 [MJ/kg]. Polymer grinding has medians of 12 [kg CO_2/kg] and 2.67 [MJ/kg]. For forging and casting these are 0.325 [kg CO_2/kg], 4.36 [MJ/kg] and 1.02 [kg CO_2/kg], 13.55 [MJ/kg] respectively. Metal fine machining has medians of 0.075 [kg CO_2/kg], 1.14 [MJ/kg]. Composite molding has medians of 2.07 [kg CO_2/kg] and 30.39 [MJ/kg]. Finally, composite fine machining and ceramic grinding have medians of 0.24 [kg CO_2/kg], 2.35 [MJ/kg] and 1.76 [kg CO_2/kg], 23.5 [MJ/kg] respectively.
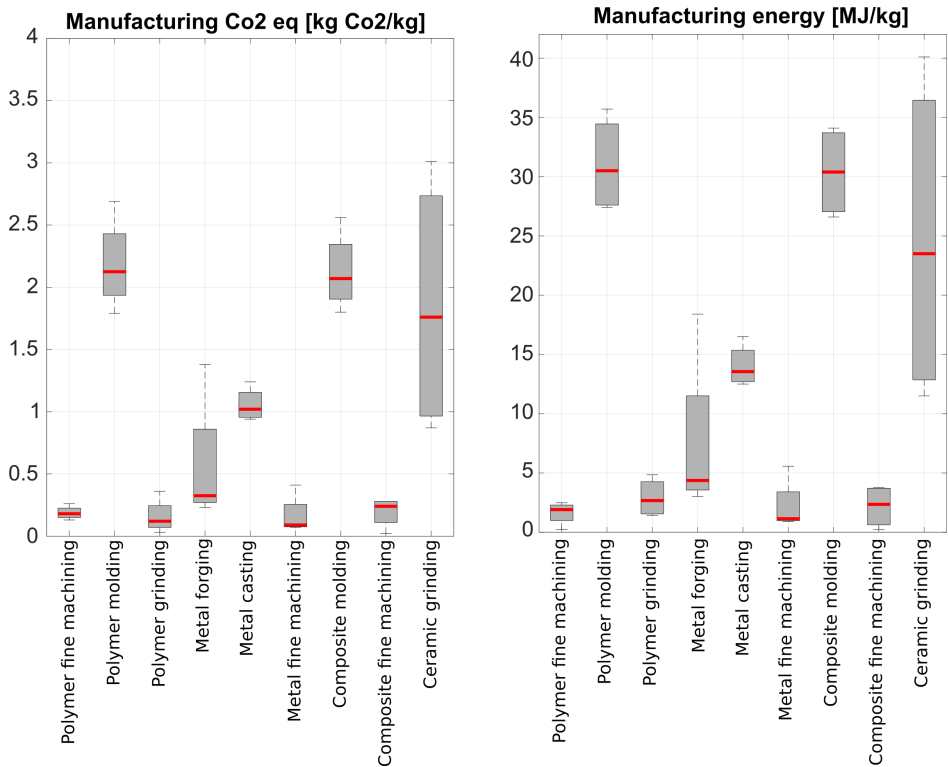
Figure 3.10: Overview of the primary energy and CO_2 equivalent of several manufacturing processes for the different material archetypes.

3.2.4. Lubricant impact

The lubricant is an integral part of the sustainability determination of the bearing system. Although the main focus in this work is water, several types of oil have also been presented in order to make the comparison between these different lubricant systems. The ecological impact of water is dependant on its treatment processes, and a wide variety of sources can be found in literature [195]. In total three relatively expensive water sources have been identified for comparison, being desalinated groundwater, desalinated sea-

water and recycled water, all presented in the previously mentioned article. It is directly compared with mineral [178], synthetic [113] and a hydraulic rapeseed oil [153]. The resulting values can be found in Figure 3.11. A description of the embodied energy of synthetic oil has not been observed in literature. Therefore an estimate value of synthetic oil has presented based on the relative similarity between synthetic and mineral oil. It is important to note that the lubricant impact only looks at the direct environmental impact of the lubricant production. The lifetime factor addresses the effect of the lubricant on the lifetime properties. Because of the similar impact of the different presented type of water sources, recycled drinking water is used to represent the lubricant in the model.

3
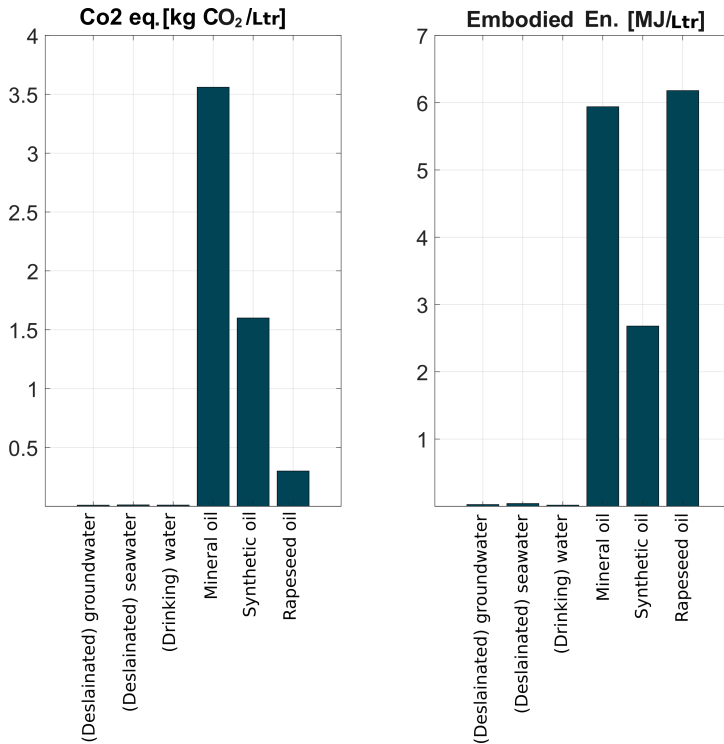
Figure 3.11: CO_2 equivalent and Embodiment energy of several lubricants. Note that for desalinated groundwater at 0.0016 [kg/CO_2/ltr] & 0.027 [MJ/ltr], desalinated seawater at 0.0025 water [kg/CO_2/ltr] & 0.042 [MJ/ltr] and recylced drinking water at 0.0011 [kg/CO_2/ltr] & 0.018[MJ/ltr] is significantly lower than any oil alternative.

.

3.3. ANTICIPATORY IMPACT ANALYSIS

In this work an analytical sustainability metric has been presented that can be used as a design tool when designing water lubricated bearings. To show the potential use of the approach, an example case is presented.

3.3.1. CASE: SHIP JOURNAL BEARING

In ship propulsion systems journal bearings are widely used, and known for leaking lubricant even though continuous efforts are being made to limit this leakage. To prevent (sea)water from entering the ship's hull, the system is designed such that the lubricant is pressurized, thus preventing leakage of the environment into the ship. Even though seals are widely used to limit this, an estimated yearly 4.6 to 28.6 million liters of lubricant leaks from stern tubes [55]. And although water lubricated systems are present in this industry, many more are still oil lubricated because of better lifetime performance. The presented sustainability metric can prove a valuable tool when weighing what the benefit of water lubrication could be. Dimensions presented in [181] have been used for this design case to determine the difference. The majority of these initial dimensions could otherwise be determined with the initial models used in the design process.

Table 3.3: Data for anticipatory sustainability analysis using framework presented in this article.

Sleeve ma.	M_{total} [kg]	V_0 [L]	Production 1	Production 2	Lubr.
UHMWPE	22.065	1.1	Poly. molding	Poly. fine mach.	water
PEEK	30.81	1.1	Poly. molding	Poly. fine mach.	water
Steel	184.86	0.6	Metal forging	Metal fine mach.	oil
Bronze	208.56	0.6	Metal casting	Metal fine mach.	oil
UHMWPE	22.065	1.1	Polymer molding	Metal fine mach.	oil

The dimensions of bearings for so-called bulk carrier ships will be used for this example comparative analysis. For this analysis, the A.0 conventional journal bearing geometry has been used, consisting of bearing sleeve and counter surface axle. Also as previously stated, only the component susceptible to wear, which in this case is the bearing sleeve, will be used for the impact assessment. The inner bearing diameter is 469 mm, with a thickness of 25 mm and a bearing length of 960 mm [181]. This results in a total volume of 0.0237 m^3. In all cases the propulsion shaft is made of a steel alloy. This analysis will compare UHMWPE, PEEK, Steel and bronze as possible bearing sleeve materials. Using the densities of 931 kg/m^3 for UHWMPE, 1300 kg/m^3 for PEEK, 7800 kg/m^3 for steel and 8800 kg/m^3 for bronze results in bearing sleeve masses of 22.065 kg, 30.81 kg, 184.86 kg and 208.56 kg respectively. In order to determine the initial bearing lubrication volume, the bearing clearance presented in [181] will be used, being 0.8 mm and 1.59 mm for metal and polymer bearings respectively. The daily stern tube leakage is also presented in the previously mentioned, and is equal to 6 liters per day for bulk carrier ships. This leakage may be significant, and it is assumed that all lubricant is effectively replaced by replenishment of this loss. The lubricant volume V_0 is thus modeled solely by the initial volume of lubricant present in the bearing gap, and not the volume of any additional lubricant reservoir. Two production steps have been taken into account in accordance with the material archetypes that have been used. For all materials and production processes, the median values of Figure 3.7, 3.8 and 3.10 have been used. Finally, for UHMWPE and PEEK the lubricant is assumed to be water, while for steel and bronze its assumed to be synthetic oil as stated in Figure 3.11. The operation time (time-to-maintenance) t is assumed to be equal to 24 months, meaning 730 days, and is the time
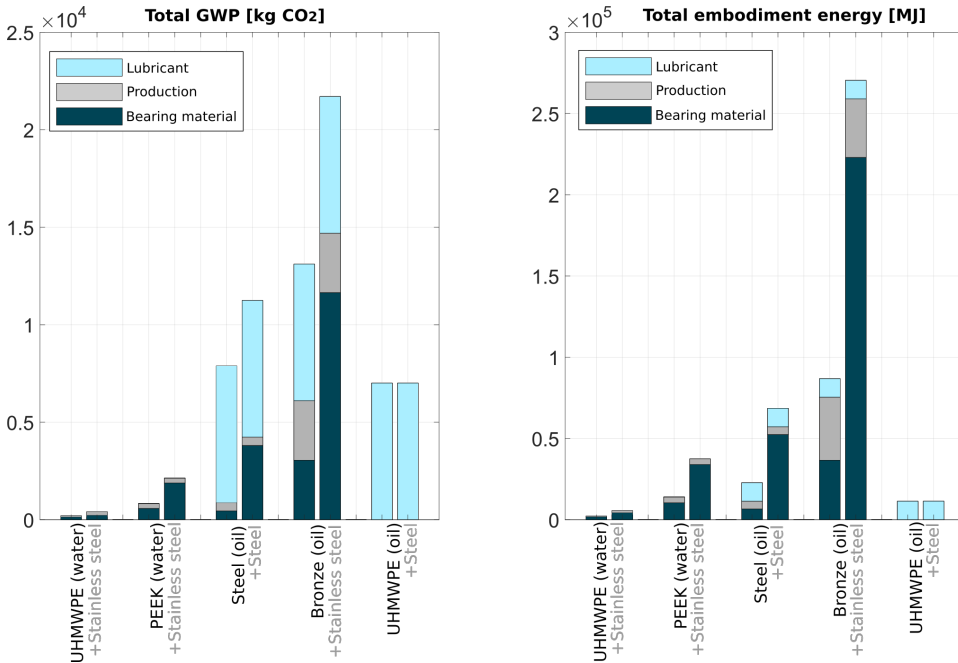
Figure 3.12: Total GWP and embodiment energy for the 5 material/lubricant combinations analyzed in the case study. In all cases, both the worst and best case material scenario's (recycled or virgin) have been presented. The total GWP for water lubricated UHMWPE-stainless steel is 191.44 and 360.72 kg CO_2, and the total embodiment energy equals 3335.72 and 6920.33 MJ respectively.

between subsequent instances of dry docking and maintenance/renewal of the bearing system. Finally, in order to take the effect of material scenario (recycled or virgin) into account, two cases will be presented for all material combinations accordingly. The resulting impact factors can be calculated using equations 3.5 and 3.6 respectively, resulting in the comparison between cases as seen in Figure 3.12. Figure 3.12 shows that in this case, the total GWP impacts of oil-lubricated bearings are much worse than the total impacts of water-lubricated bearings for all material combinations, even when the impacts of manufacturing the bearings are smaller. It also shows when the environmental impacts of oil lubricant are larger than the impacts of bearing material and production, versus when they are smaller. Note that, in addition to the climate change impacts calculated here, oil leakage into water would also cause ecotoxicity. Such impacts could be calculated with LCA using the same methods as shown here for GWP, and could be weighed against the impacts of climate change using single score LCA methodologies such as Eco-Cost or ReCiPe[81]. Such analyses are outside the scope of this study, but would come to similar conclusions regarding what bearings are better for what applications.

3.4. DISCUSSION

In this work a method is proposed that allows bearing designers to make initial decisions concerning the sustainability of their design concepts. The focus is to propose an analytical approach, minimizing uncertainty, while a secondary focus is to provide all data necessary to perform the analysis for water lubricated bearings. The model uses anticipatory LCA, with the analytical equations fed by data from literature to enable environmental impact analysis. Details on these three parts of the results follow.

3.4.1. ECO-IMPACT METRIC BASED ON ANTICIPATORY LCA

The proposed model has two dominant choices that greatly influence the performance: The bearing system and bearing load case, both of which will be discussed.

First is the choice of bearing system, defined in figure 3.4. This means the proposed method is not suitable for some cases to define the eco-impact of the bearing system. For example, the effect of water leakage of bearings in water pumps, where the hydraulic liquid is simultaneously also used as lubricant, can be neglected for a closed system. Rather it should be used as a tool in design cases where the choice between water or oil-based alternatives can be made. Pumps and motors of various sizes as well as the previously presented ship's propeller shafts are examples of these. Because of the intended generality of the approach and the list of assumptions for the bearing system, the modeling approach already contains several simplifications. However, because of this generality, not many assumptions need to be made for bearing designers to implement the analysis, allowing for fast initial sustainability statements. As with other anticipatory LCA methods, it should be used to make comparisons and identify the largest impacts, to support decision making and prioritization. The case study shows, using the supplementary calculator, how this analysis can be performed.

Secondly the load case can greatly change depending on the type of lubricant used and the subsequent change in bearing geometry and performance characteristics. This effect is neglected in the proposed model, in favor of consistency between all combinations, thus limiting uncertainty. More specifically, since these types of data are in general not available for engineers in initial design stages, this type of uniform comparison often results in a more reliable comparison. The alternative would be to test several materials for the given load case of the proposed application, an action which is labor intensive, as well as requiring potentially significant initial investment.

3.4.2. DATA FROM LITERATURE

To enable the impact calculation, much data has been gathered from literature. The analysis showed that a wide variety of material combinations has been used for water lubricated bearing applications, but only a few have been reported in high numbers. Within this range of materials, there is however a significant difference in eco-impact, and it thus worthwhile for bearing designers to investigate the scope of possibilities. As is often expected in LCA types of analyses, the impact of the primary material plays a dominant role in the eco-impact of the system. What is interesting to not is that little innovation has occured in terms of materials, where mostly PEEK or its composite forms have been analyzed extensively by multiple researchers over the past two decades.

3.4.3. IMPACT ANALYSIS

The modelling equations show that the highest impact comes from the material combination, and its wear rate, as well as the lubricant leakage. The example case shows the significant effect of the lubricant in particular, showing that a material combination which is superior in lifetime can still be a far inferior choice when it comes to sustainable design. An interesting observation to note in the case study is that water lubricated PEEK proves to be a superior choice to oil-lubricated PEEK when looking at CO_2, but can be inferior when analyzing the primary energy values.

The case study shows that in some cases the replacement of an inferior material combination would be preferable because of the lubricant use. This is counter intuitive for many design cases, where often the system with the highest lifetime is chosen because of its superior performance. There are however situations where the most sustainable option is one of increased replacement, especially when the time-to-maintenance is dominated by other components in the mechanical system. The proposed method allows for this metric to be taken into account similar to mechanical performance and cost during decision making. This approach of course only partially allows for the engineer to makes these conclusions based on solely two parameters, and as such has its limitations.

Engineers may choose to use more comprehensive LCA metrics that measure many impact categories such as ReCiPe [81]. However, even the basic quantification of environmental impacts presented in this work clearly shows the importance of lubricant loss on the bearing system's sustainability.

3.5. CONCLUSION

The presented method allows designers of water lubricated bearings to calculate the environmental impact of their designs during concept design stages through the use of the anticipatory LCA based approach. The work provides a extensive data-set for water lubricated bearings in particular, where the past 20 year state of the art has been identified and collected in a dataset. Several of these material combinations possess impressive performance characteristics even in comparison with some oil-lubricated alternatives. The presented case study shows how this anticipatory LCA base approach can be used to give initial indications on sustainability of bearing designs considering certain materials and combinations. The provided supplementary material accompanying this paper can be used to perform this calculation. It indicates the crucial effect the lubricant has on statements concerning sustainability, even when bearing embodiment is an order of magnitude better in terms of wear, as can be seen between water-lubricated UHMWPE on steel and oil-lubricated UHMWPE on steel. As long as uncertainty and possible ranges of different values are accounted for in different scenarios, anticipatory LCAs can greatly aid in decision making.

Thus, the statement often seen in literature that water lubricated bearings are a green alternative to oil-lubricated bearings, depends heavily on the design case. Especially when a closed system is used, it might be a significantly more sustainable option to take the more conventional oil-lubricated bearing. This way, sustainability can be used as a design criteria, similar to the way costs and performance are used currently for decision making in these types of systems.

4

FULL FILM BEARING DESIGN INNOVATION USING COMPLIANCE

The previous chapters have looked at the need for innovation in full film bearing design based on engineering and ecological aspects. This chapter looks into how compliant design can prove to be a valuable design tool in order to obtain these aspects. The main objectives that this dissertation focusses on are discussed and the different ways of solving limitations that are present in full film bearing design are introduced.

We have seen in the previous two chapters two important reasons that drive engineering innovation: unsolved technical challenges in combination with the move towards sustainability. The two chapters also discussed how full film lubricated bearings can potentially play an important role in this objective. In case of the presented water hydraulic transmissions in chapter 2, the bearing interface is one of the most challenges design components. The addition of full film lubricated bearings would not only mean the possibility to obtain higher load capacities and lower track friction at smaller bearing footprints. The implementation of hydrostatic lubrication could also remove all contact mechanics from these interfaces. In the case presented, the use of water as a lubricant is an overall system requirement. Water lubrication, as investigated in chapter 3, could also lower the eco-impact of full film bearings, compared to oil-lubricated alternatives. What could greatly improve the performance of the system presented in chapter 2 is a new type of water lubricated hydrostatic bearing. This design is however not without its challenges. Water performs poorly as a lubricant and has corrosive characteristics, bearing loads are significant and variable, design spaces are limited, and the to-be-followed counter surface has a continuously varying curvature. The objective is thus ambitious. In order to developed a viable alternative, we have to investigate what type if innovations have presented themselves in the field, what the community has been focussing on and which challenges remain. Analyzing the literature data of chapter 3 in terms of
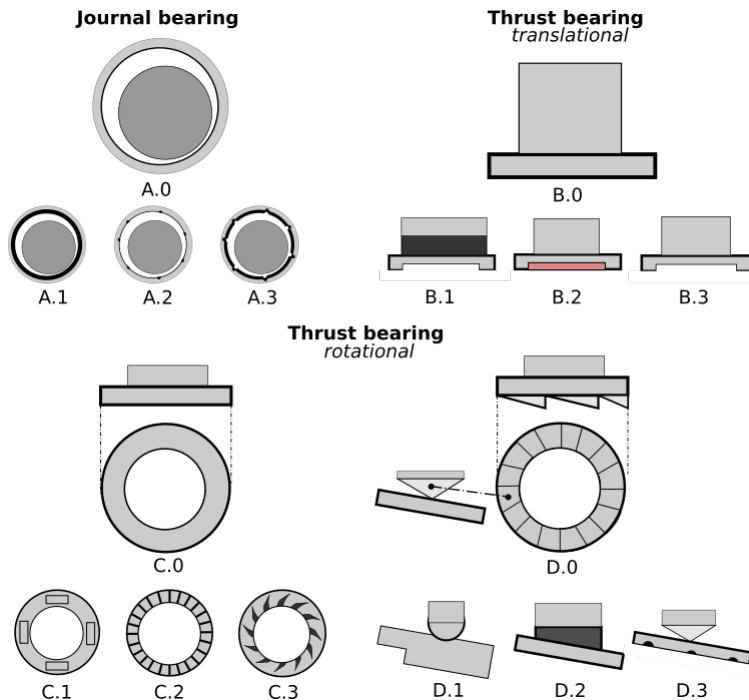

Figure 4.1: Primary geometries of bearings observed in literature, as well as their specialized embodiment.

used bearing designs gives us a clearer picture on the state of design that has been sub-

Table 4.1: Overview of literature research with a focus on geometry. The literature is organized relative to their main bearing geometry.

A.0	A.1	A.2	A.3
Andersson [5]	Litwin [133]	Majumdar [150]	Cabrera [16]
Hirani [103]	Liu [145]	Pai [172] [173]	Orndorff [170]
Litwin [140]	Liu [143]	Wang [224]	Hua [110]
Wang [226]		Feng [61]	Peng [175]
Litwin [141]		Cheng [33]	Wang [223]
Genyuang [74]		Lu [147]	Wang [225]
Gao [71]		Gong [89]	Zhou [264]
Zhang [257]		Li [131]	Zhou [263]
Ye [252]			Yang [250]
Zhang [259]			
Xie [137]			
Feng [62]			
B.0	**B.1**	**B.2**	**B.3**
	van Ostayen [213]	Hanawa [97]	Nie [161]
			Huanglong [111]
			Kang [124]
			Yin [253]
			Xu [245]
C.0	**C.1**	**C.2**	**C.3**
	Gohara [82]	Xiang [244]	Yoshimoto [254]
	Andres [180]		Lin [138]
D.0	**D.1**	**D.2**	**D.3**
Dabrovski [40]	Nakano [157]	Liang [134]	Boonlong [12]
Song [190]	Zhang [258]	Liang [135]	
	Zhang [256]	Ning [166]	

4

ject of research in water lubricated systems. The divisions of these articles is presented in detail in table 4.1, and the visualization of the bearing archetypes can be seen in figure 4.1. Bearing geometries found in the past 20 years of literature are divided into one of three main groups: journal bearings, (translational) thrust bearings and (rotational) thrust bearings. Within these main categories, 14 different embodiments of bearing geometries were found in literature of the past 20 years. The majority of the literature found focuses on the conventional journal bearing geometry, with a rotating rod (A.0). Other geometries are the rubber housing (A.1), stave bearing (A.2) and rubber stave bearing (A.3). This geometry group is the one with the most attention in research, and is one of the most commonly used bearing designs. The most investigated bearing in the thrust bearing category is that with a pocket embodiment (B.3). Other occurring embodiments are those with a rubber support (B.1) and a hybrid bearing with a porous land area (B.2). Rotational thrust bearings come in two main categories: those with fixed geometries (C.0) and those with tilting pads (D.0). For the fixed geometry, different embodiments were found in the shape of multiple pockets (C.1), radial microgrooves (C.2) and spiral

microgrooves (C.3). For the tilting pad embodiment (D.0), a step tilting pad variant (D.1), rubber supported (D.2) and grooved pad (D.3) have been observed.

A clear visible trend here is that the large majority of researched and implemented bearing designs are conventional well known topologies. This however quite often makes sense, since they are implemented in systems that have historically benefited from their potential. The main approach in this respect remains to create a geometry out of solid material and optimize that geometry for one certain operation condition [66]. What the design case presented in chapter 2 shows us however, is that there are systems that would benefit from not rigid, but deformable bearing surfaces. This is mainly motivated by the non-uniformity of the curvature of the counter surface. When looking into full film bearing designs for coping with counter surface deformations, we see that a number of designs are presented. [10, 215] used rubber supports to cope with counter surface irregularities. Other uses are the compliant embodiment of a hinge used for tilting [136, 209] or to change the dimensions of features in the bearing surface [114, 115]. These examples make use of elastic or compliant elements, but all have one limitation:

Statement 1: *Compliance is traditionally used to cope with small deformations, usually in the order of magnitude of the film thickness.*

This limitation automatically means that a significant number of potential applications cannot implement the available design alternatives, where deformations with respect to the film height or bearing dimensions need to be larger. The example of chapter 2 would be an impossible design case, since the counter surface eccentricity is significant compared to the design dimensions of the conventional bearings that can be used. Based on the motivation for many of these earlier presented articles that take into account deformability, we come to the following statement:

Statement 2: *Elasticity in full film bearing design is traditionally seen as an error that has to be accounted for.*

Literature in that sense mostly sees elasticity of full film bearings as something that can explain a difference between the desired performance of a model and the eventual performance of a prototype, rather then an additional design option in the toolbox that can be used to obtain improved performance.

4.1. Revisiting compliant design

In this thesis we therefore want to revisit this design philosophy of compliant bearing design, revisit existing ideas and develop new methods. Previous chapters motivate that the step towards a sustainable future requires us to design systems with a greener footprint and improved performance. We believe that further innovating hydrostatic bearings using compliant design would contribute to reach this ideal.

This believe is not without merit. Developments in the field of compliant mechanism design have been continuously moving forwards [109]. Advancements in new production methods such as advanced additive manufacturing approaches have allowed for the production of significantly more exotic designs then were thought to be previously possi-

ble. Advancements in material development [54, 206] allows for characteristics that were previously not possible with conventional bulk materials. In this dissertation we thus revisit compliant design, its desired objectives and which innovations found in compliant design can be used to improve and innovate with. Figure 4.2 shows us a number of potential innovation directions in the form of design tools and design objectives which have been identified for this work. The potential implementation of full film lubricated
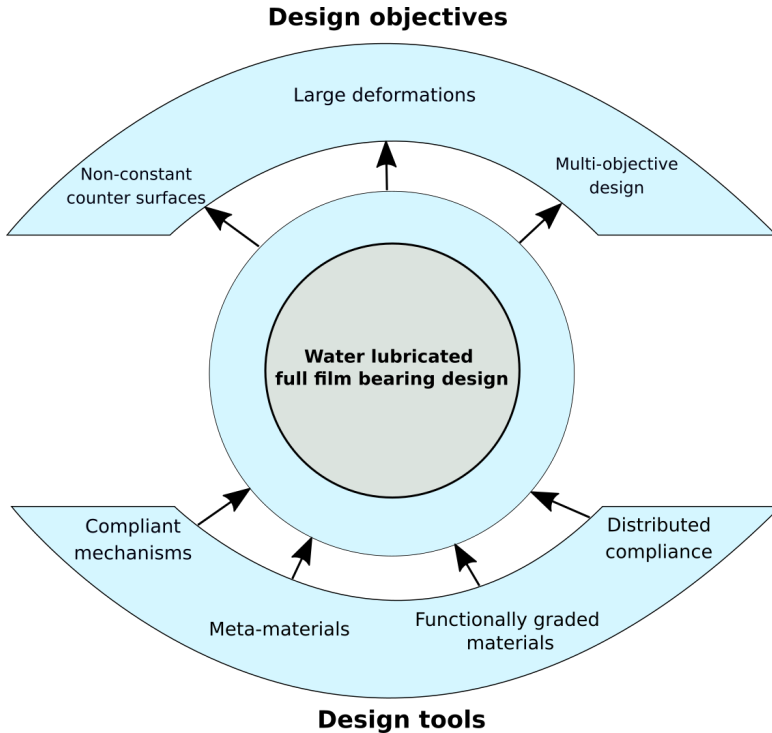
Figure 4.2: Identified innovation principles in compliant design literature that might prove to be valuable design tools for water lubricated full film bearing design. The design objectives that are the main subject of this thesis are defined here as well.

bearings in systems such as the water hydraulic transmission of chapter 2 opens up new possibilities. Those cases specified are about developing bearings that cope with non-constant curvature counter surfaces. Because of the lack of literature on the subject subject, it is important to define first what is meant with a highly deformable hydrostatic bearing. The definition of large elastic deformation is usually expressed in relation to whether or not geometric non-linearity has to be taken into account[109]. To define highly deformable full film bearings, a definition can be made starting from this dependence on the amount of deformation:

Statement 3: *Highly deformable fluid bearings are able to deform to $\geq 10\% \cdot H$, where H is defined as height of the bearing in its undeformed configuration.*

Another crucial aspect in fluid film bearings, is the presence of the lubricant film. Conventional elastic fluid bearings have been described in terms of their deformation capabilities relative to the nominal fluid film height. This convention is summarized in the second statement:

Statement 4: *Highly deformable fluid bearings are able to deform $\geq 100 \cdot h_0$, where h_0 is defined as the average film height of the fluid film.*

Together, statements 3 and 4 provide the definition of highly deformable fluid bearings as used in this work. However, this idea of 'design with compliance' can be taken even further. More often than not, the geometry of the bearing is the limiting factor for the performance when variable operating conditions are considered, because not every bearing geometry excels in every aspect. This means the bearing designer usually resorts to designing for an average or maximum operating point in the full operating range. In that sense the limitations of conventional hydrostatic bearings lie not only in their lack deformability to cope with counter surfaces with a non-uniform curvature, but also with changing operation conditions. The hydraulic cylinder pump seen in chapter two is a de-
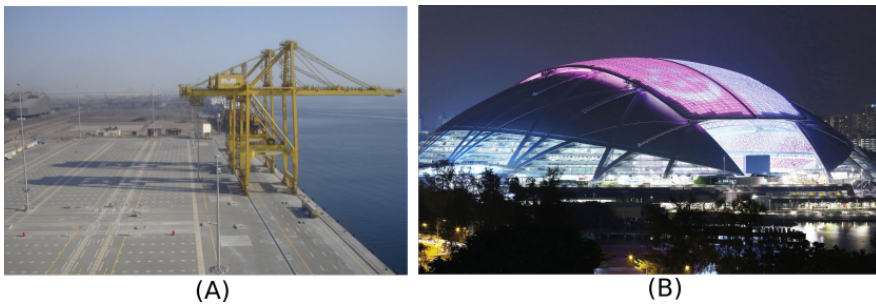
Figure 4.3: Primary geometries of bearings observed in literature, as well as their specialized embodiment.

sign case where not only the counter surface has a non-uniform curvature, also its load condition changes significantly between the suction and compression stroke. Besides the previously mentioned application in chapter 2, several other applications with varying load cases can be devised [159]. Harbour cranes can be seen as an example where the velocity over the operating range might change, but where the load remains close to constant. An example of an operating condition where the velocity remains at a low constant velocity but where the load changes significantly, are for instance stadium rooftops with a varying load. There are different methods of coping with these changes. One is the use of mechatronic components, as is the design vision of tribotronics [79]. A viable, low cost, passive alternative is the implementation of compliant elements [64, 115]. The potential of revisiting compliant full film bearing design thus not only lies in design for deformation, but changing operating conditions in general. The design tools presented in figure 4.2 are implemented to overcome several of the limitations found in full film bearing design. The chapters in part 2 all focus on a particular limitation to be solved.

4.2. RESEARCHED PRINCIPLES

In order to address the design challenges mentioned earlier, a number of principles have been researched in this thesis. These principles are fundamentally based on solving existing limitations present in conventional hydrostatic bearings, by using state of the art techniques found in compliant design, as seen in figure 4.2. There is always a coupling between the design tool used and the design objective as specified in this figure. In all cases compliant elements are used, and water is assumed to be the lubricant of choice. These challenges and subsequent methods are the following:

1. **Pressure profile matching**: The use of an **elastic** *functionally graded material* to eliminate the effects of compliant-hydrostatic pre-loading. This effect is the elastic deformation of the bearing caused by the pressure profile of hydrostatic bearings and is important for designing bearings to *track non-uniform counter surface curvature using large deformations* (chapter 5).

2. **Passive shape shifting**: The introduction of **compliant** elements to design passive bearings that can operate for two specific operation points in the operation range (*multi-objective design*), seen in chapter 6.

3. **Whiffletree-based bearing supports**: The use of a *distributed **compliant** system* to combine discrete compliant mechanisms and bearing pads and optimize their functional use in order to design a *large deforming* hydrostatic bearing (chapter 7).

4. **Closed form pressure balancing**: The principle behind *large deforming* fluid filled **compliant** rotational mechanisms with an excellent axial-to-rotation stiffness ratio (chapter 8).

The resulting methods will be the content of the following part of this thesis and its included chapters.

II

PRINCIPLES

5

PRESSURE PROFILE MATCHING FOR COMPLIANT HYDROSTATIC BEARINGS

When a bearing is made compliant, the film pressure starts to influence the deformation of the support itself. This effect, called compliant-hydrostatic pre-loading, is especially crucial to take into account when designing highly deformable hydrostatic bearings. In this chapter the principle of pressure profile matching to minimize the effect of this pre-loading is explained. A 2D design model introduced is used to determine the performance of such an elastic bearing utilizing stiffness profile matching. Additionally, an extension to the model is presented to analyse the basic bearing performance of these type of bearings over small counter surface eccentricities. Finally, an embodiment of such a material distribution is presented utilizing functionally graded materials. These embodiments are analysed with respect to their failure behaviour, showing an improved shear stress and strain energy density distribution with the functionally graded supports compared to conventional elastic supports.

One of the fundamental statements valid for conventional hydrostatic bearings, seen in chapter 1, is that the bearing surface and counter surface remain close to parallel [192]. The effective bearing situation seen in Figure 5.1.(A) is expected. This changes
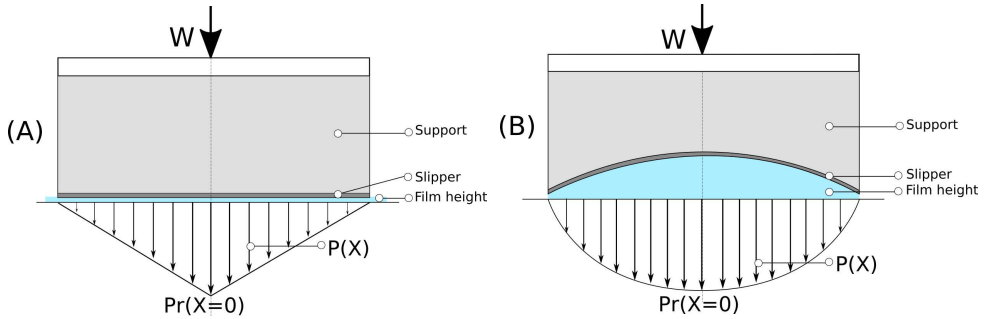

Figure 5.1: (A) An 'infinitely long' high stiffness parallel slider on a flat running track. (B) The same slider with a compliant support. The deformation of the support influences the obtained pressure profile.

when bearing support compliance is introduced, either through geometry, material or a combination of these two. The pressure profile affects the deformation of the bearing as seen in Figure 5.1.(B). Here, the deformation of the bearing influences the pressure, and vice versa. If the stiffness of the bearing support is uniform, this will result in a non-constant deformation and therefore non-parallel film height. This could be used to increase load capacity by introducing virtual recesses. It can however also negatively influence the bearing in terms of volumetric flow, damping and mechanical failure. Here lies one of the challenges observed when designing highly deformable hydrostatic bearings. When non-constant curvature counter surfaces need to be followed, the pressure profile creates a pre-loaded bearing configuration. The bearing inherently has a pre-disposition for a certain deformed state, caused by this pre-loading. When designing bearings meant for large variable curvature counter-surfaces, this is an undesired characteristic. The question therefore arises if an elastic bearing support can be designed in a neutral position in terms of deformation, therefore minimizing the pre-loading effects.

5.1. METHOD OF PRESSURE PROFILE MATCHING

The approach of pressure profile matching is based on knowing the hydrostatic pressure profile of a given bearing geometry. For thin film bearing geometries the Reynolds equation yields the pressure distribution in the thin lubricating film[192]. In a compliant hydrostatic bearing this fluid pressure causes so-called hydrostatic pre-loading:

Compliant-hydrostatic pre-loading: *Pre-load condition created by the fluid film pressure on the elastic bearing support in initial operating condition.*

In more detail, with compliant-hydrostatic effects we mean the influence of global deformation of the support on the pressure build-up. The presence of a compliant support can however also be used advantageously to negate this effect, by tuning the bearing

support stiffness from a constant stiffness to spatially varying stiffness. It creates possibilities for the bearing designer, who can now design for the bearing configuration, when loaded by the nominal load and sliding on the nominal counter surface curvature. In this work we limit the embodiment of this approach to solely use elastic material properties. The approach of pressure profile matching is defined in this work as follows:

Pressure profile matching: *Designing the bulk material properties of the bearing support such that the reaction pressure profile of the bearing support for a nominal compression is equal in shape to that of the pressure profile generated by the fluid film.*

The initial configuration becomes significantly more important when the counter surface has a non-uniform curvature in the sliding direction. This becomes clear when looking at tracks having both convex and concave curvatures. The average deformation between an equal magnitude convex and concave curvature $H_{avg} = U$ is the middle line between these maxima as seen in Figure 5.2. In this average configuration, no preloading other then uniform compression is desired, since any other would result in a preference towards either of the primary curved directions. This would limit the symmetric bearing deformation performance. To obtain a parallel bearing in this averaged
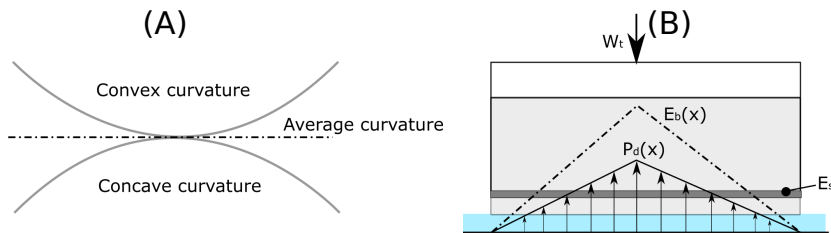
Figure 5.2: (A) Average 'curvature', when both convex and concave curvatures are present in eccentric counter surfaces. (B) 'Infinite' Parallel hydrostatic bearing geometry on a flat running track.

deformation configuration a non-uniform material profile is needed, because the pressure profile is non-uniform as well. When designing the bearing support, only one material configuration can be created and must thus be chosen carefully. By utilizing pressure profile matching it is possible to design for this initial condition using solely the material distribution of the bearing support. This approach has been implemented in a 2D infinitely long design model to show the possibilities.

5.1.1. DESIGN MODEL
In literature, a wide number of basic bearings models are presented that accurately describe the behaviour of specific bearing geometries [185, 192]. However, the models becomes significantly more tedious when the effects of elasticity are introduced. Although the advance of computational numerics has improved and Elastohydrodynamic Lubrication (EHL) problems are now significantly easier, these techniques can rarely be used as an efficient design tool. Therefore in this chapter a design model utilizing the simple bearing models as presented in literature [185], is introduced to predict the compression created by compliant-hydrostatic pre-loading. The model consists of a 2D model

to determine displacement, while solving a 1D inverse Reynolds equation on the pressure film boundary. A representation of the model can be seen in Fig. 5.3. The model assumes there is a slipper present as seen in Fig. 5.1, which is a plate-like component that allows for free bending of the bearing surface but prevents any deformations in the in-plane direction. The slipper can be seen as a roller constraint as seen in Fig. 5.3.

Similar to the flexible supports found in literature [209, 214], in this work rubber-like materials are used. The model utilizes the principle of stiffness matching, meaning that it starts with the assumption of an expected displacement field, i.e. a uniform compression (Figure 5.2). The displacement field is assumed to be described by:

$$\begin{bmatrix} u_x \\ u_y \end{bmatrix} = \begin{bmatrix} \frac{2x}{L}\left(\sqrt{1-\frac{4y^2}{H^2a^2}} - \sqrt{1-\frac{1}{a^2}}\right)C \\ \left(\frac{1}{2}-\frac{y}{H}\right)U \end{bmatrix} \tag{5.1}$$

where H and L are the height and length of the symmetric support respectively. C is the amplitude of curvature at the edge and U the uniform compression magnitude. Finally, a is a scaling parameter used to soften the boundary condition of the displacement field. This is necessary because the basic geometry used to describe the deformation in x direction is a semi-ellipse. Since this has an infinite gradient at $y = 0.5L$, it will thus not allow for an alaytical solution. The softening parameter a is used to prevent this. The components of the 2D linearised Green-Lagrange deformation tensor [105] can then be defined as:

$$\begin{bmatrix} \epsilon_{xx} \\ \epsilon_{yy} \\ \epsilon_{xy} \end{bmatrix} = \begin{bmatrix} \frac{\partial u_x}{\partial x} \\ \frac{\partial u_y}{\partial y} \\ \frac{1}{2}\left(\frac{\partial u_x}{\partial y}+\frac{\partial u_y}{\partial x}\right) \end{bmatrix} \tag{5.2}$$

A linear-elastic material model is used, defined by Hooke's law [105]. Assuming plane strain, the material stiffness matrix $\mathbf{S}$ can be defined as:

$$\mathbf{S} = \frac{E_b(x)}{(1+v)(1-2v)}\begin{bmatrix} 1-v & v & 0 \\ v & 1-v & 0 \\ 0 & 0 & \frac{1-2v}{2} \end{bmatrix} \tag{5.3}$$

where v is the Poisson's ratio of the material and $E_b(x)$ the Young's modulus which is assumed to be non-constant in the x-direction. The principle of virtual work can be applied to determine the values of uniform compression U and curve amplitude C as function of material properties and load condition. The virtual displacement field as function of δU and δC can be defined as:

$$\begin{bmatrix} \delta u_x \\ \delta u_y \end{bmatrix} = \begin{bmatrix} \frac{2x}{L}\left(\sqrt{1-\frac{4y^2}{H^2a^2}} - \sqrt{1-\frac{1}{a^2}}\right)\delta C \\ \left(\frac{1}{2}-\frac{y}{H}\right)\delta U \end{bmatrix} \tag{5.4}$$

Assuming small displacement gradients, the components of the virtual strain field $\delta\epsilon$ can be defined by replacing u_x and u_y with δu_x and δu_y within the linearized Green-Lagrange deformation tensor. The total virtual work W_t corresponding to static equilibrium, can then be defined as:

$$W_t = \int_x \int_{ay} \delta\vec{\epsilon}^T \vec{\sigma} \cdot \mathrm{d}y\mathrm{d}x - \int_x \delta U P(x)\mathrm{d}x \tag{5.5}$$
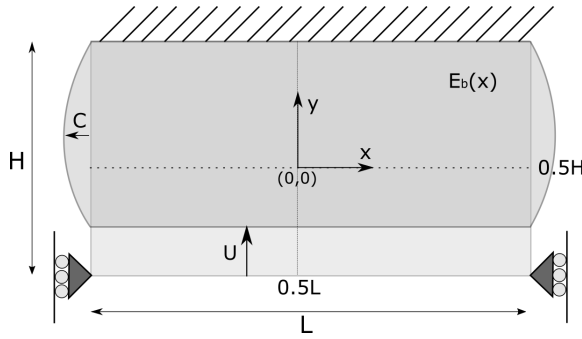
Figure 5.3: Model definition used to determine compression magnitude.

where $P(x)$ is the bearing pressure profile. The parameter α is used to neglect a part of the boundary of the elliptic displacement field causing stiffening. This effect becomes more pronounced with incompressible materials. Thus for equilibrium, the virtual work of admissible deformation will equal the virtual work of external loads:

$$\begin{bmatrix} \frac{\mathrm{d}W_t}{\mathrm{d}\delta U} \\ \frac{\mathrm{d}W_t}{\mathrm{d}\delta C} \end{bmatrix} = \begin{bmatrix} K_{11} & K_{12} \\ K_{21} & K_{22} \end{bmatrix} \begin{bmatrix} U \\ C \end{bmatrix} \tag{5.6}$$

This results in two linear equations independant of the virtual displacements δU and δC. These can be re-written in matrix notation to define the stiffness matrix **K**:

$$\begin{bmatrix} \int_x P_p(x)dx \\ 0 \end{bmatrix} = \begin{bmatrix} K_{11} & K_{12} \\ K_{21} & K_{22} \end{bmatrix} \begin{bmatrix} U \\ C \end{bmatrix} \tag{5.7}$$

This result defines a relationship between the material distribution defined by the Young's modulus, the pressure profile and the uniform compression U. This relation can be used to determine the approximate uniform compression $w_0(x) = U$ for the bearing support given a certain material distribution $E_b(x)$, pressure profile $P_p(x)$ and support dimensions H and L. The height of the lubricating fluid film resulting in this pressure profile can then be determined using an inverse elasto-hydrostatic approach [11, 56, 186]. The pressure distribution in a hydrostatic bearing is characterized by the maximum pressure at the supply inlet $P_{p,0}$ located at $x = 0$, and the drop-off in pressure to ambient at the bearing edges in the two areas opposite the supply, the left section ($-\frac{L}{2} \le x < 0$), and the right section ($0 < x \le \frac{L}{2}$). The flow through the supply restrictor Q_s is modelled as:

$$Q_s = G_s(P_s - P_{p,0}) \tag{5.8}$$

where P_s is the constant supply pressure input for the bearing, and G_s the hydraulic resistance of the restrictor. For the examples in this chapter a linear restrictor has been implemented, modelled as follows:

$$G_s = \frac{\pi d_r^4}{128\eta l_r} \tag{5.9}$$

Table 5.1: bearing general dimension and load conditions

Parameter	Description	Value
P_s	supply pressure	8 MPa
P_r	desired recess pressure	3 MPa
H	support height	1 m
L	support length	2 m
H_s	slipper height	5 mm
d_r	restrictor diameter	1 mm
l_r	restrictor length	20 mm
η	viscosity (water)	1 mPa · s
a	softening factor	1.001
α	Boundary factor	0.88

where d_r is the diameter of the restrictor, η the viscosity of the lubricant and l_r the restrictor length. The total flow through the inlet restrictor Q_s is divided in two parts.

$$Q_s = -Q_L + Q_R \tag{5.10}$$

where Q_L and Q_R are the flows through the left and right section, respectively. The flow in any point in the lubricating film is given by:

$$Q = -\frac{h^3}{12\eta} P_{,x} \tag{5.11}$$

where $P_{,x}$ is the gradient in x-direction of the pressure distribution. Thus for any point in the film the height can be determined:

$$-\frac{h^3}{12\eta} = \begin{cases} Q_L/P_{,x} & \text{if } (-\frac{L}{2} \le x < 0) \\ Q_s/\left(P_{,xL} + P_{,xR}\right) & \text{if } x = 0 \\ Q_R/P_{,x} & \text{if } (0 < x \le \frac{L}{2}) \end{cases} \tag{5.12}$$

where $P_{,xL}$ and $P_{,xR}$ stand for the left and right value of the discontinuous pressure gradient at the supply point $x = 0$, respectively.

5.1.2. DESIGN EXAMPLE: PRE-LOADED PARALLEL BEARING

The method is used to design for the compliant-hydrostatic pre-loading of a hydrostatic slider. A parallel flat pad bearing as seen in Fig. 5.2 is used as bearing geometry, of which the pressure shape is well known [185]. By placing the coordinate system of this bearing at $x = y = 0$, the idealized pressure profile can be defined as:

$$P_{\mathrm{p}}(x) = P_{\mathrm{initial}}(x) = P_{p,0}\left(1 - \left|\frac{2x}{L}\right|\right) \tag{5.13}$$

This is the idealized pressure profile of a perfectly parallel 'infinitely' long flat pad bearing. In this example, the parameters presented in table 5.1 are used. To analyse the performance of the model, it is compared with a Finite Element Method (FEM) model using

Comsol Multiphysics. In the FEM model, a solid embodiment of the support and slipper are used.The slipper is made of titanium-like material, modelled with $E_s = 100$ [GPa] and $\nu_s = 0.25$ [-]. The finite element analysis is performed as an compliant-hydrostatic model. This means same load condition is used as seen in Fig. 5.3, with the exception that the Reynolds equation is defined on the boundary $y = -H/2$. The other difference is that the FEM based model computes the Reynolds equation conventionally, meaning it calculates the pressure for a given film height, and then iterates until the deformation of the support matches the load. The film height is defined as follows:

$$h_C = h_0 + d_C \tag{5.14}$$

Where h_0 is the film height at the supply point and d_C the deformation of the bearing surface in y direction. To obtain the correct value for h_0 the model iterates for this variable to obtain an equilibrium between a constant external load W_0 and the load capacity of the film defined by $W_1 = \int_L P(x)\,dx$. A linear elastic material model is used, with a constant Poisson's ratio for the support in both the numerical and analytical model. The previously presented design model defines the material distribution as:

$$E_b(x) = E_A \left(1 - \left| \frac{2x}{L} \right| \right) \tag{5.15}$$

With E_A the material stiffness amplitude,chosen as $E_A = 3.5E7$ [Pa] in this example. The deformation of the support as well as the film height and pressure profile are compared between the design model and the FEM model. The resulting comparison can be seen in Fig. 5.4. The boundary factor for the displacement was defined to be $\alpha = 0.88$, to prevent the stiffening effect caused by the ellipsoid displacement field. The effective stiffness matrix was calculated to be the following:

$$\mathbf{K} = \begin{bmatrix} 1.3527E8 & -0.4754E8 \\ -0.4754E8 & 0.213E8 \end{bmatrix} \tag{5.16}$$

5.1.3. EFFECTS OF NON-CONSTANT COUNTER SURFACES

The design model can be extended for the analysis of track curvatures, which are of interest for highly compliant bearings. Such a periodic surface waviness can be modelled using a wave function:

$$H_{\text{track}}(x) = -H_a \cos(\frac{2\pi x}{L_t}) \tag{5.17}$$

where H_a is the track waviness amplitude, x the position of the track and L_t the track length. This periodic function has also been seen in literature [214], and is a good first order approach to modelling non-flat surfaces. Using the previously presented approach based on the approximate solutions using virtual work is limited for analysing these type of deformations. For different locations on the curvature a different approximate displacement is needed, and the deformation in the x-direction becomes assymetric. These actions would become tedious for analysing an sinusiodal track and would loose their practicallity. In order to be able to analyse these type For now it is assumed that this counter surface waviness is limited to small amplitudes in the order of $H_a = H/100$,
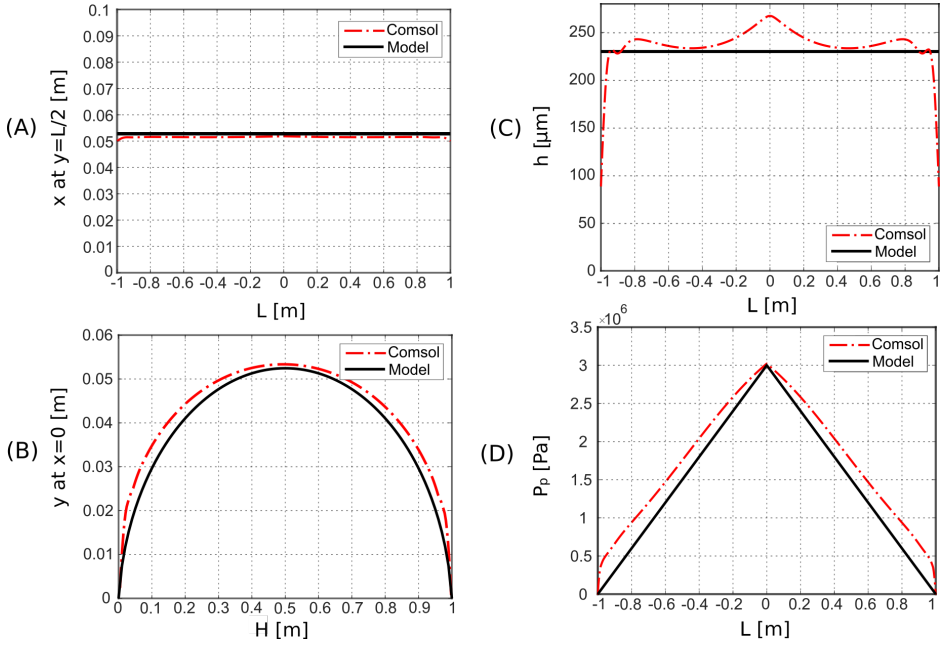
Figure 5.4: (A) uniform compression U. (B) deformation in x-direction with C at $H = 0.5$ [m]. (C) Film height. (D) Pressure profile.

with H being the support height. This way, the additional effect of track curvature can be modelled as a linear addition to the nominal compression of the support with an acceptable error. Using this method for larger track waviness would result in an underestimation of the stiffness and overestimate the resulting support compression. A scaled representation of the load case can be seen in Fig. 5.5. Assuming pure axial compression, the pressure profile as function of non-uniform track compression is defined as:

$$P_{\text{support}}(x) = \frac{E_b(x) H_t(x)}{H} \tag{5.18}$$

where H is the support height, $E_b(x)$ the Young's modulus of the support which may vary in x-direction, and $H_t(x)$ the description of the waviness of the counter surface. The additional pressure needed to deform the elastic slipper can be modelled in a similar approach. Assuming that the slipper can be modelled as a plate [203], the necessary pressure profile can be modelled as:

$$P_{\text{slipper}}(x) = E_s \frac{H_s^3}{12} \frac{\text{d}^4 H_{\text{track}}(x)}{\text{d}x^4} \tag{5.19}$$

With the H_s equal to the slipper height and E_s the Young's modulus of the slipper, which is assumed to be constant. This way a simplified cumulative effect of both the compression of the bearing due to the pressure profile as well as the counter surface eccentricities is taken into account. The hydrostatic pressure profile can then be defined by the

Figure 5.5: Deformation of track with respect to bearing support. Please note that the scale of deformation caused by the track is increased for better understanding.

following relation:

$$P_{\text{wavy}}(x) = P_{\text{slipper}}(x) + P_{\text{support}}(x) \tag{5.20}$$

which states the wavy hydrostatic pressure can be defined by the pressure required to deform the bearing support and the bearing slipper on the non-constant curved counter surface. Since the pressure profile changes due to changes in curvature, the actual uniform compression required to balance the load can be defined as:

$$U_{\text{eccentric}} = \frac{\left(\int_x P_{\text{initial}}(x)\mathrm{d}x - \int_x P_{\text{eccentric}}(x)\mathrm{d}x\right)}{\left(\int_x P_{\text{initial}}(x)\mathrm{d}x\right)\mathrm{U}} \tag{5.21}$$

where U is the initial uniform compression determined before. Using this relation, we can define the approximated compression U_1. This finally allows us to define the total approximated pressure profile present in the fluid film as:

$$P_{\text{total}} = P_{\text{eccentric}} + \frac{U_{\text{eccentric}}}{\mathrm{U}} P_{\text{initial}} \tag{5.22}$$

which can be used in the inverse Reynolds model extension to determine the film height. Note that in this case the error the model has at $h(x = 0)$ will become more prominent because of larger slope changes between the left and right side relative to $h(x = 0)$. The pressure on the effective bearing surface A'_{b} will continuously change due to the effects of the track waviness.

5.1.4. Design example: pre-loading and non-constant curvature

The same bearing support and load condition from Example 1 are used again here. Now, a counter surface with surface waviness is added defined by equation 5.17. The track amplitude $H_A = 0.01$ [m] and the wave length $L_t = 5\pi$. The compression value of U = 0.056 [m] from Example 1 is used again. The bearing surface passes the entire track length L_t in both the FEM and analytical model. To compare both the FEM model and analytical model their envelopes are compared. The envelope consists of all values obtained by the film and pressure profile moving over the track. The envelope of the model shows
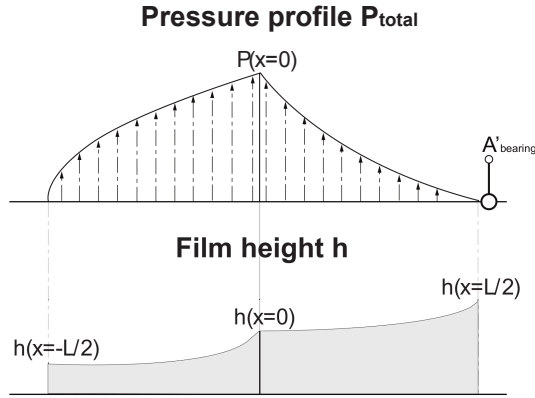
Figure 5.6: Visualization of the swinging effect in the pressure and film height caused by the additional pressure contributions of the eccentric counter surface. Please note both are increased in scale for better understanding.
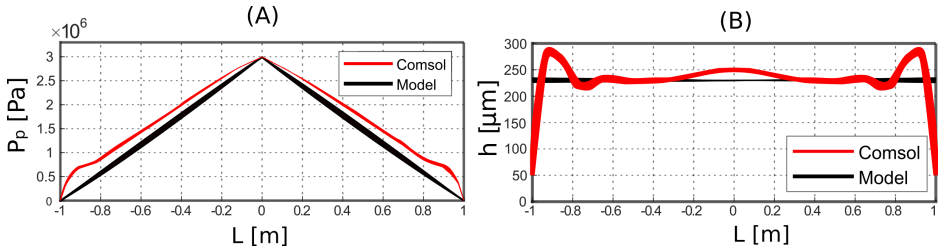

Figure 5.7: (A) pressure envelope of the FEM model and design model for an eccentric counter surface with $H_a = 0.01$ [m]. (B) Film height envelope of both models.

the expected 'swinging' behaviour of the pressure and film height, see Fig. 5.6. Since the counter surface is always in some form of sinusoidal curve, the FEM model has a slightly different film and pressure profile compared to its counterpart in Example 1. This is most clearly seen in the higher peak values found in the film height.

5.2. PROFILE MATCHING THROUGH FUNCTIONALLY GRADED MATERIALS

Having a distributed material lies at the basis of profile matching. These types of materials in literature are typically called 'functionally graded' materials [34, 44, 54, 57, 206]. Motivated by compliant bearing supports seen in literature, the entire model is based on using rubber-like materials. Rubber-like materials have also been used in literature as functionally graded (FG) material [44, 57] and are relatively easy to produce using casting techniques, which is a known production approach for FG materials [54]. Although a continuous material distribution is desired, production difficulties in actually obtaining such a support might prove limiting. It is therefore of interest to investigate the additional effects of discretisation seen in Fig. 5.8, which is one of the more conventional

approaches to realizing functionally graded materials [206].

With the introduction of elasticity in the bearing designs an important failure mode is introduced, that affects conventional hydrostatic bearings less: mechanical failure. Mechanical failure in rubber often occurs due to cracks or tearing [13], or at the interfaces with other materials [6]. The significant difference in Poisson's ratio and material stiffness causes high shear stresses at these boundaries. Tearing or cracks on the other hand, can be analysed by looking at strain energy density [95, 132]. The analysis of these failure modes provides insight in possible further improvements of the graded material support in addition to the minimization of the hydrostatic pre-loading. This difference between a constant material and functionally graded material support are investigated using a FEM model. The model takes into account the slipper plate by modelling it as
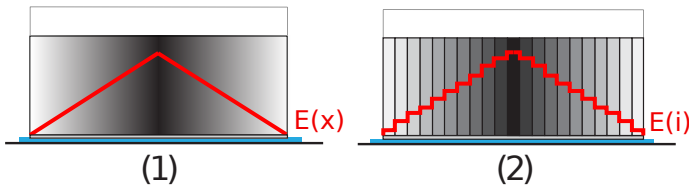

Figure 5.8: (1) Theoretically desired functionally graded material support. (2) Discrete alternative to obtain similar performance.

a pure roller constraint on the boundary $[y = -\frac{H}{2}, -\frac{W}{2} \geq x \geq \frac{W}{2}]$. This is equal as seen in Fig 5.3. On this boundary in y-direction a uniform compression equal to $U = \frac{H}{10}$ is applied. The design parameters are $H = 1$, $\nu = 0.49$, $L = 2$. For the graded material support the Young's modulus can be defined using equation 5.15, where $E_A = 1$. The model effectively normalizes the Young's modulus value. As has been observed in literature for FG materials [34, 106], the Poisson's ratio is kept constant. For a constant material support with an equal effective material stiffness, this means a Young's modulus $E_s = 0.5$. The comparison between the two material distributions can be seen in Fig. 5.9. By grading the material down to 0 at the edge of the support, the peak shear stress expected at this location [214], which is usually observed in these type of supports is removed. This typical peak stress at the corners is a direct result from the gradient in the displacement field, even though no external load is observed on this location. The maximum occurring stress concentration has moved more towards the centre of the support. This new distribution of stresses can be seen in Fig. 5.10. To provide insight into the improvement in failure criteria, two failure sets are investigated. One is the average shear stress $(\sigma_{xy})_{\text{avg}}$ and the strain energy density W_{avg} over the constraint line seen in Fig. 5.9. This represents the average stress and strain energy over the edge where the support is bonded to the rigid world. The second failure criterion is the average occurring peak stress $(\sigma_{xy})_{\text{peak}}$ and strain energy density W_{peak} at the edge of the constraint line, seen in Fig. 5.9. Since the latter is notoriously inaccurate in FEM, an approach based on that of [90] and [80] is used, where a peak region is used to determine this value. Here, this region is a semi circle with a radius $r_s = H/1E4$. The resulting values can be seen in table 5.2. The fundamental limitation of the optimal distribution is that the outer boundary value of the Young's modulus approaches 0, which has no physical representation in a
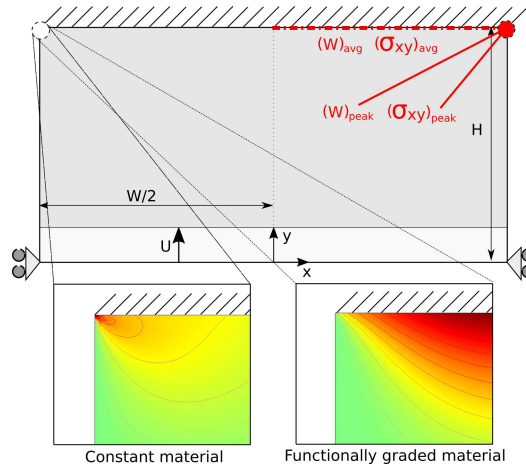
Figure 5.9: FEM model shows the average stress given along half the constraint line as well as at the corner. The resulting effect is a loss of peak value concentration at the corners. Note that the support is presented in its undeformed configuration.

solid material.

5.2.1. MATERIAL DISCRETIZATION EFFECTS

A realistic embodiment of the continuously distributed material, is one such as seen in Fig. 5.8.2. Discrete constant material property elements can be used to design a functionally graded support. In this work these discretised supports will be analysed using an uneven amount of elements, and thus there is always a center element present. Assuming symmetry with respect to this center element, the most basic Young's modulus distribution, being linear per element, can be defined as:

$$E_{\text{element}}(i) = \frac{E_s}{(d+1)} i \tag{5.23}$$

Where i is the element number , d the total number of unique discrete elements, and $E_s = 1$ the centre Young's modulus value. For a discretisation of 11 the value of $d = 6$. Figure 5.11 shows the effect of discretisation on the distribution of shear stress and strain energy respectively. Figure 5.11 shows a general trend of convergence towards the performance found in the continuous functionally graded support. When utilizing mixing and casting as production methods for the functionally graded rubbers, the combining of two materials in different fractions can suffice. This means the outer element will always have the properties of the more compliant material, meaning the Young's modulus per element can be defined as:

$$E_{\text{element}}(i) = \frac{E_s - E_o}{(d-1)} (i-1) + E_o \tag{5.24}$$

The increased failure performance is thus determined by the following parameters:
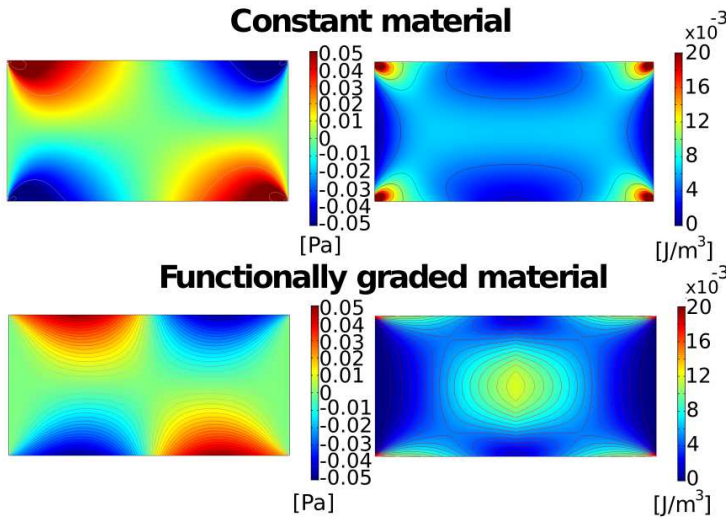
1. The total number of unique discrete elements d.

Figure 5.10: distribution of shear stress σ_{xy} and strain energy density W for a constant material support and functionally graded support. Note that the supports are presented in undeformed configuration, and the range of both parameters has been made equal.

Table 5.2: Analysis of failure modes for both supports.

Parameter	Constant material	FG material
$(\sigma_{xy})_{\text{avg}}$	0.0385 [Pa]	0.0345 [Pa]
W_{avg}	0.0087 [J/m^3]	0.0073 [J/m^3]
$(\sigma_{xy})_{\text{peak}}$	0.468 [Pa]	0.000822 [Pa]
W_{peak}	1.8 [J/m^3]	0.014 [J/m^3]

2. The ratio of Young's modulus between The inner element E_o and the outer element E_s defined as $\lambda_E = \frac{E_s}{E_o}$.

The dependency on these parameters can be illustrated by determining the effect on occurring shear stress σ_{xy} and the strain energy density W. Of the failure analysis methods presented in Fig. 5.10, the average shear and strain energy density over the constraint line $(\sigma_{xy})_{\text{avg}}$ and W_{avg} are utilized. These are preferred over the peak values, mainly because in discretisation the peak value does not necessarily remain in the same location. To have a uniform comparison between different distributions the average contact line values are therefore used. The ratio of material λ_E is analysed by comparing different values of E_0 with respect to $E_s = 1$. This is presented in Fig. 5.12.

5.3. DISCUSSION

5.3.1. DESIGN MODEL
The design model presented in section 5.1.1 is limited by three important factors. Firstly, it does not consider geometric non-linearities, being limited to a linear strain field. The
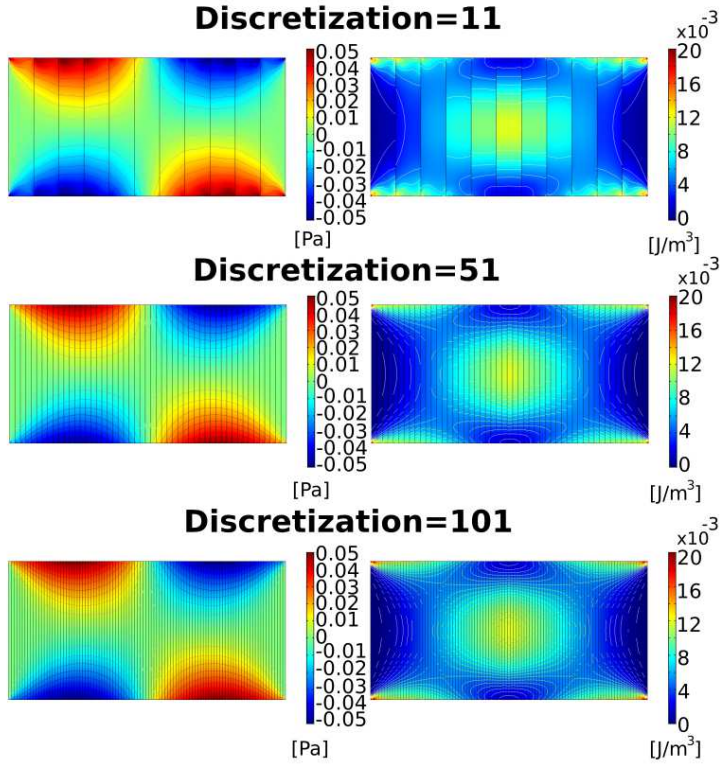
Figure 5.11: Distribution of shear stress σ_{xy} and strain energy density W for different discretised supports. Note that all deformations are scaled to 0, and the range of both parameters has been made equal.
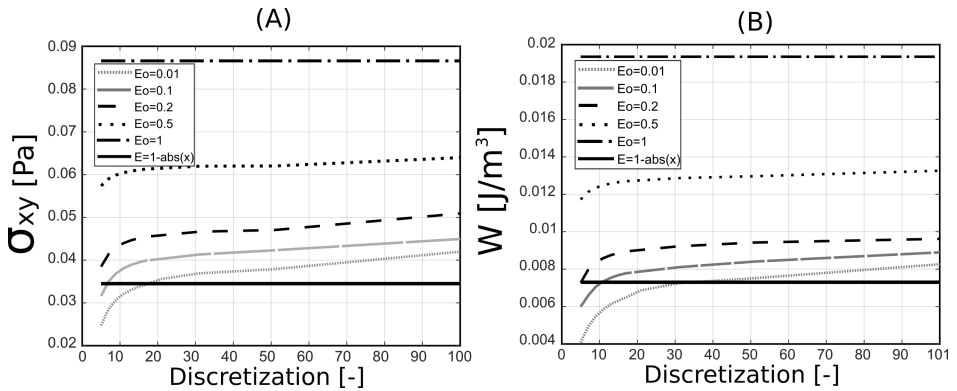

Figure 5.12: Shear stress and strain energy densities for different material ratios, over a range of increased discretisation. The results of a support using equation 5.15 as material distribution is added for reference.

second limitation is the displacement field presented in equations 1 and 2 needing a correction factor to prevent a singularity in the stiffness determination, as a result of

the selected displacement field being elliptical. This limitation is directly visible in the performance of the model, and is one of two main contributors to the error between FEM and model in Fig. 5.4. The other main contributor to the difference of the two models is the basic assumption used in stiffness matching. As seen in Fig. 5.4.D, there is a slight deviation between the expected shape of the pressure profile (and thus the assumed material distribution) and the actual pressure profile for this material distribution. Since the example presented is not a pure compression element, but has coupling between deformation in x and y direction, a deviation from this theoretical shape is expected. The final assumption of the slipper being a pure roller constraint prevents any higher order effects from being taken into account when determining the film height, thus limiting its accuracy.

5.3.2. NON-CONSTANT COUNTER SURFACES

An extension to the design model for the use in analysing the effect of non-constant curvature counter surfaces is presented in section 5.1.3, where an example was used to present the performance of this extension to the model. The main limitation of this extension to the model is the assumption of pure compression without any cross coupling to the deformation in the other directions. This means that the use of this extension for analysis of highly deformable bearings, considering statements 1 and 2, is limited. The alternative would be a similar approach performed to that of the hydrostatic pre-loading model. The main argument against this, is that the displacement field defining the bearing deformation will continuously change asymmetrically given every position on a counter surface. Although significantly more accurate, this would be a computationally intensive model. The use of this model with respect to FEM based approaches then becomes questionable. The main objective of the presented model extension is that it provides insight into the 'swinging' behaviour on film and pressure caused by the continuously varying curvature, which can be captured using the pressure and film height envelope.

5.3.3. FUNCTIONALLY GRADED MATERIAL

In section 5.2, the use of functionally graded materials to obtain the desired material distribution used in stiffness profile matching is presented. A FEM model using a normalized material is used to investigate the effect on failure modes between a constant material support and its functionally graded counterpart. This re-distribution of the support material has significant effect on the stress and strain energy distribution seen on the boundary constraint. Primarily, the stress and strain energy concentration normally observed in these kind of supports [214], can be significantly be decreased in magnitude as seen in table 5.2 using this material grading. What is interesting to note is that the average shear stress and strain energy density along the constraint between both support configurations does not change significantly. This suggest, as can be also seen in the distribution of both parameters in Fig. 5.11, that the stress concentrations are more distributed across the bearing surface.

5.3.4. Discretization of support

A possible embodiment of applying functionally material grading is through discretisation of the support in elements with a varying Young's modulus. Figure 5.11 shows that this approach converges towards the theoretically optimum distribution seen in Fig. 5.10. The main assumption that is made here, is assuming there are castable material combinations with very large differences in Young's modulus which can be observed in the difference between the inner element E_s and outer element E_o. The effect on this ratio λ_E is therefore also investigated as seen in Fig. 5.12. The main effect noticed here, is that there is a convergence occurring given a certain material ratio, while increasing the number of discrete elements. This is caused by the method of analysing this value. By averaging the stresses and strain densities, the weight of all elements is equal. With higher discretisation values, this effect averages out similar to that observed in Fig. 5.11. It does also show that there is only a slight increase of performance between ratio $\Lambda_E = 100$ and $\lambda_E = 10$ when looking at a higher discretisation numbers.

5.4. Conclusion

In this chapter a design approach is presented to minimize one of the attributions to performance limitation found in compliant-hydrostatic bearings. By using profile matching, the effects of compliant-hydrostatic pre-loading can be minimized to result in a favourable compression condition. The design model presented can be used to determine this compression given an expected pressure profile during design. Please note that this approach is not limited to only uniform compression as the required displacement field, or to flat pad bearing geometries. In fact, this principle of stiffness profile matching can be used for other geometries and other desired hydrodynamic or hydrostatic pressure profiles. Others presented in literature, such as in [185], can be used in similar fashion. The extension for analysis of non constant curvature surfaces is limited in applicability to small amplitudes, but does provide insight in the expected behaviour. Finally, functionally graded supports exhibit a more equally distributed load condition, thus lowering the effects of peak stresses, which are known to cause failure in these type of rubber to other material interfaces [6].

6

PASSIVE SHAPE SHIFTING DESIGN STRATEGY FOR FULL FILM BEARINGS

In tribotronic bearing design active components are used to adapt the bearing perfor-mance to the operating conditions. The principle of self-adaptive bearings has also been presented in literature using a passive approach to design for variation in operating con-ditions. This chapter presents an alternative design approach for self-adaptive bearings. The approach focuses on the shift between two known bearing geometries, both favorable within a part of the operating regime. Using compliant elements in the bearing design al-lows for passive shape shifting. Four examples are presented which present this behavior for variable velocity and load conditions. The design approach could possibly provide a cheaper alternative for simple active bearing designs, or could be combined with active components in a tribotronics design to improve existing performance.

A different approach is to consider how changes in operating conditions can be handled passively, that is without additional sensors, actuators, or control unit. The use of compliance can also be implemented in the design of a passive bearing that can cope with change in operation conditions. This has been seen to some degree in the work of [114], naming it self-adapting surfaces. In these types of bearings, the features such as pockets change in depth in order to adapt to the operation condition. This has been seen to some degree in the work by Jackson et. al [52, 114, 115], where it was referred to as self-adapting surfaces. A second detailed body of work on shape adaptability of bearing using compliance has been performed by Fesanghary et. al [64–66]. In these types of bearings, the features such as pockets or grooves change in depth in order to adapt to the operation condition. These properties have been utilized both in thrust and journal bearings. This principle of self-adapting however can be taken further. By switching between bearing geometries which are known to excel given a certain operation condition, additional performance could potentially be unlocked. In this research we present a method where the bearing is not designed to be optimal in one operating point, but in two selected points in the operating range. This design principle of switching between known bearing shapes, is introduced as the principle of passive shape shifting. This chapter further goes into the potential of this approach to obtain bearings for multi-objective load and velocity operation conditions that can potentially enhance or replace tribotronics. It will be shown how existing bearing geometries can be combined through elastic elements to capture the essence of the principle in a set of examples.

6

6.1. Method of shape shifting

In this chapter we consider the bearing design problem from a multi-objective perspective. This lies at the basis of the passive shape shifting approach, which is to cope with changing operating conditions passively, i.e. without active mechatronic components. It therefore can be used to change the bearing's performance depending on the specific point in the operating condition range. Performance for full film bearings is a broad concept, but usually consist of aspects such as the minimum allowed film height, load capacity, volumetric flow, friction, normal and tilt stiffness. An example of such a switch can be seen in figure 6.1. The determination of these performance characteristics requires the evaluation of the pressure profile in the bearing, and thus the solution of the Reynolds equation [51], which in 1D form is equal to:

$$\frac{d}{dx}\left(-\frac{h^3}{12\eta}\frac{dP}{dx} + \frac{h}{2}U\right) = 0 \tag{6.1}$$

where h is the film height, P the pressure distribution, η the viscosity and U the velocity of the counter surface. The Reynolds equation inherently captures the coupling between film height, load capacity and volumetric lubricant flow. Depending on the bearing geometry, this results in differences in the aforementioned performance criteria [9]. With passive shape shifting, the bearing uses changes in operating condition, i.e. load and velocity, to change between bearing geometries and thereby obtains a difference in performance. For this approach to be effective, a set of bearing geometries must be identified between which the actual bearing geometry will switch. Literature [9, 185]
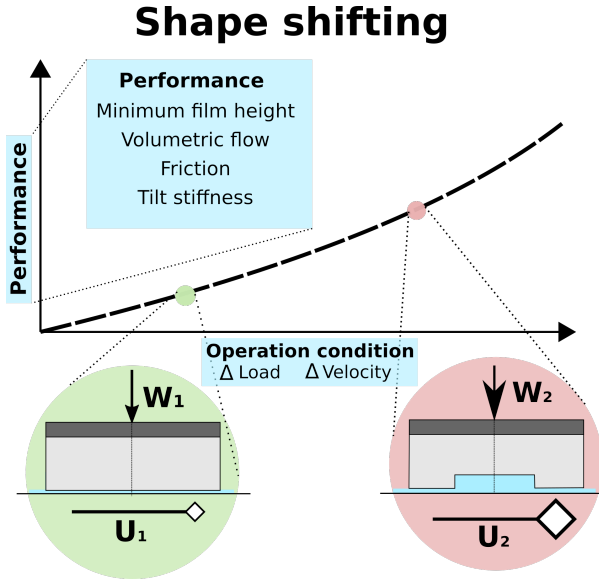
Shape shifting

Figure 6.1: Different operation conditions that can be utilized during passive shape shifting, resulting in changes in possible performance criteria.

can provide an extensive overview of different geometries and their subsequent performance, of which several have been implemented in this work. The following parameters are used as dimensionless expressions of bearing performance:

$$\bar{h} = \frac{h_{\min}}{L} \tag{6.2}$$

$$\bar{B} = \frac{q\eta}{P_r h_{\min}^3} \tag{6.3}$$

$$\bar{\mu} = \frac{1}{UW} \int_0^L \left(\frac{h^3}{12\eta} \left(\frac{dP}{dx} \right)^2 + \frac{\eta U^2}{h} \right) dx \tag{6.4}$$

which are the dimensionless minimum film height $\bar{h}$ [-], the flow shape factor $\bar{B}$ [-] and friction coefficient $\bar{\mu}$ [-] in accordance with [185]. They are defined by the minimum film height $h_{\min}$ [m], the bearing length L [m], bearing load $W = \int_0^L P dx$ [N], viscosity η [Pa·s], output flux q and velocity U [m/s]. The operation conditions are defined by the dimensionless parameters:

$$\bar{W} = \frac{W}{P_s A} \tag{6.5}$$

$$\bar{\zeta} = \frac{U\eta}{W} \tag{6.6}$$

$$\tag{6.7}$$

where $\bar{W}$ is the dimensionless load, ζ [-] the characteristic bearing number, P_s [Pa] the supply pressure and A [m²] the bearing area. In case of a hydrostatic bearing that is not
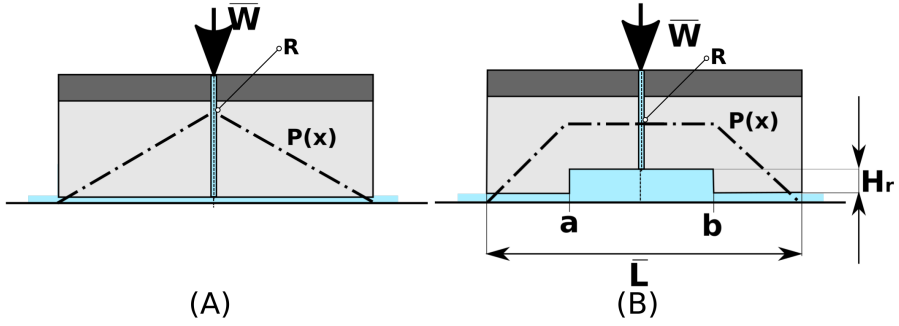
Figure 6.2: (A) Parallel hydrostatic bearing. (B) Hydrostatic bearing with recess.
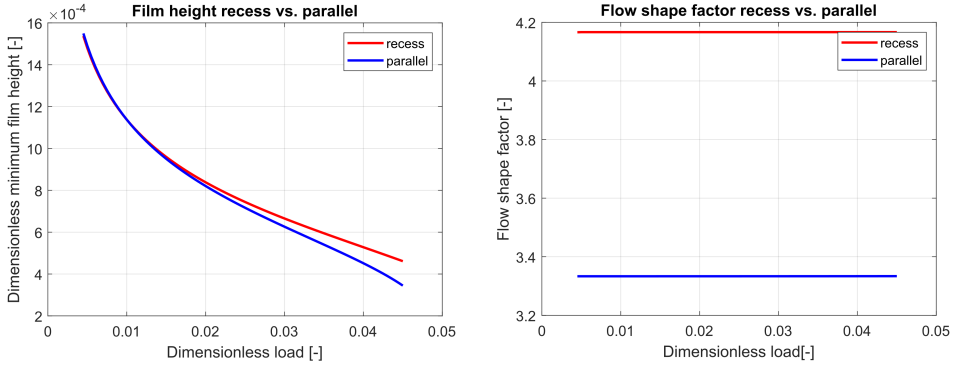

Figure 6.3: Hydrostatic parallel versus recess bearing in terms of their minimum film height and flow shape factor.

subjected to velocity variations, these dimensionless numbers can be used to define the operation condition. The bearing geometry directly influences the performance that is realized depending on the load and velocity operation condition. This becomes more clear when looking at a possible switchable bearing geometry pair as seen in Figure 6.2. These bearing geometries exhibit distinct differences in pressure profile and therefore load capacity. Given an operation range in which the dimensionless load parameter varies, two performance criteria are utilized, that is the minimum film height $\bar{h}$ [-] and the flow shape factor $\bar{B}$ [-]. Both bearings can be modeled using the 1D Reynolds equation defined in Equation 6.1. The recess of figure 6.2.B. is modeled as having a $L_r = L/10$ in size located symmetrically in the centre of the bearing, with a height $H_r = L/100$. An external pressure source is used with a constant source pressure equal to P_s. A linear restrictor (R) is used, which is modeled as:

$$Q_r = \frac{\pi r_r^4}{128\eta} \frac{(P_s - P_r)}{l_r} \tag{6.8}$$

where $r_r = 0.001L$ and $l_r = 0.02L$. The dimensions of the restrictor are based on having a similar minimum film at the lower bound of the range. The resulting performance for one order of magnitude varying load can be seen in Figure 6.3. The resulting comparison shows the superiority of the two bearings at different points in the operation range. The parallel bearing, having lower load capacity, has a superior overall flow shape factor and therefore lower volumetric loss. This comes at the cost of having an inferior minimum film height at lower operational loads. This might be crucial in for instance shock loads, causing the bearing to lose its full film capabilities. In that case the recess bearing, with its superior load capacity might be preferred at the cost of a higher temporary flow shape factor.

This fundamentally is the objective of shape shifting, where a varying load case benefits from a change in performance without the use of active components. By moving between the two geometries, the desired performance at both ends of the operational range can be obtained. The following two approaches have been identified as fundamental shape shifting strategies, as visualized in Figure 6.4. The approaches can be de-

Shape shifting strategies

Shift of outer geometry
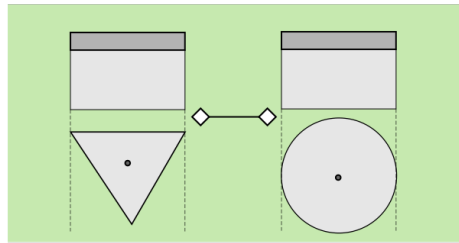
Shift of Feature

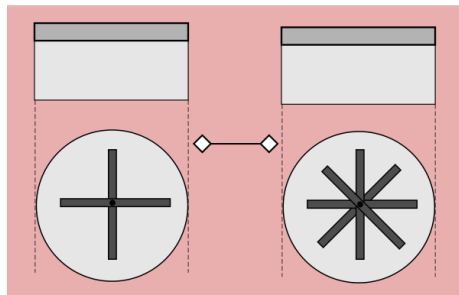

Figure 6.4: Identified shape shifting strategies. Focus in this work is solely on the shift of feature strategy.

fined as follow:

- *Shift of outer geometry*: Changing the bearing outer boundary or the dominant bearing boundary.

- *shift of feature*: Adding or changing the features of bearing surface.

The approaches do not necessarily differentiate in their final objective, but rather possibilities to obtain the same result.

6.1.1. APPROACH TO OBTAINING PASSIVE SHAPE SHIFTING

The primary approach presented in this work to obtain passive shape shifting is through the use of elastic components. The change in operating conditions, i.e. load and velocity, causes changes in the resulting pressure profiles that is acting on the bearing geometry. These changes in location and magnitude of the pressure distribution cause deformation, which in turn can change the bearing geometry and therefore its performance. The implementation of compliant elements to cope with change is analogous to what has been seen in literature [65, 114, 115], where linear compliant bearing elements cope with changes in the load condition. Passive shape shifting is a conceptually different design approach in its explicit switch between two different bearing geometries at two locations in the operation range, rather then having features adjust to changes in operation. An example of a compliant shape shifting implementation of Figure 6.2 can be seen in Figure 6.5. When $\bar{W}_2 > \bar{W}_1$, the increased load can be used to compress the
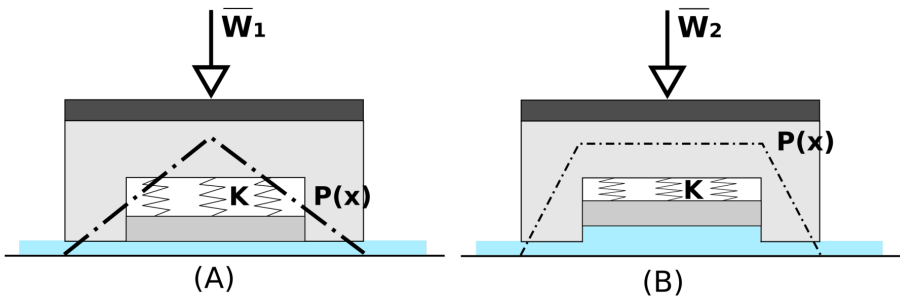

Figure 6.5: (A) parallel hydrostatic bearing with an elastic element defined by stiffness K. (B) Hydrostatic bearing with recess after shape shift. The implementation is presented here in the form of a spring supported separate element in the center of the bearing. A functional embodiment of such an elastic implementation could be similar to the suspended compliant beams that have been observed in [52, 64], a monolithic structure without sliding friction between the pocket and its internal wall.

elastic element and therefore passively change the bearing geometry. Implementation of the elastic component thus determines how the shape shifting will occur. Through the use of a number of examples, the potential and design approach will be presented. This work exclusively focuses on using the second design approach, the so-called shift in feature. This design approach takes the preference in this because of its intuitive implementation in existing bearing designs.

6.2. MODELING DESIGN EXAMPLES

To show the potential of passive shape shifting, the second design presented in Figure 6.4 will be used to obtain different shape shifting bearing designs. The examples will either be load or velocity dependent, meaning the operation range will either be represented by

the dimensionless load $\bar{W}$ for hydrostatic bearings or the characteristic bearing number $\bar{\zeta}$ for hydrodynamic bearings. The examples will share the following common traits:

1. The main dimension will be expressed by a characteristic bearing length $\bar{L} = 1$ [-].

2. Any elastic elements used within the bearing surface are modeled as both geometrically linear as well as possessing a linear elastic material model.

3. The examples will be presented in their lowest possible geometrical embodiment. This means they will modeled in 1D if possible.

The modeling of the primary bearing examples using the finite element method has been studied and described in literature extensively over the past 40 years [7]. In addition, the focus in this work is the design approach, and thus a finite element approach generally suffices for first concept validity. The examples are all modeled using Comsol Multiphysics V5.5. Here the Reynolds equation is defined using the general form partial differential equation toolbox. In the examples the geometrical embodiment is used with the smallest dimension. And thus the majority of examples are defined purely as a line, with the space between nodes defining pockets. This is done as such since solely the domain between the fluid and bearing is modeled. All examples are modeled as quasi static, meaning time dependent effects such as squeeze are not taken into account. This means the Reynolds equation on the majority of examples is defined as described in equation 1. In case of a 2D geometry, the Reynolds equation is defined as follows:

$$\frac{\partial}{\partial x}\left(-\frac{h^3}{12\eta}\frac{\partial P}{\partial x} + \frac{h}{2}U\right) + \frac{\partial}{\partial y}\left(-\frac{h^3}{12\eta}\frac{\partial P}{\partial y} + \frac{h}{2}V\right) = 0 \tag{6.9}$$

Where U and V are the velocities in x and y direction, respectively. The film height h can be described using a function that includes all possible potential groove shapes and that will be specified for each example that follows. For all examples the solution for the film height will be found by solving to find load equilibrium:

$$W = \int_A P\mathrm{d}A \tag{6.10}$$

Where A is either a surface (x, y) or a region (x) depending on the dimension of the geometrical embodiment. This means both the general form PDE and global ODE physics of Comsol have been implemented. Note that the models are not necessarily optimized. Instead the objective of this work is to provide a viewpoint on the potential of passive shape-shifting as a design approach. Four examples are presented in the next section, each with a specific set of operating point combinations and therefore bearing design concepts to be merged in one shape shifting design.

6.2.1. EXAMPLE 1: TILTING RAYLEIGH STEP
This example is based on the change of dominant bearing geometry and consists of the combination of the well known Rayleigh step bearing and tilting pad bearing seen in Figure 6.6. The Rayleigh step is known as the bearing geometry with the highest hydrodynamic load capacity of all bearing geometries [96]. It is thus highly suited as a geometry
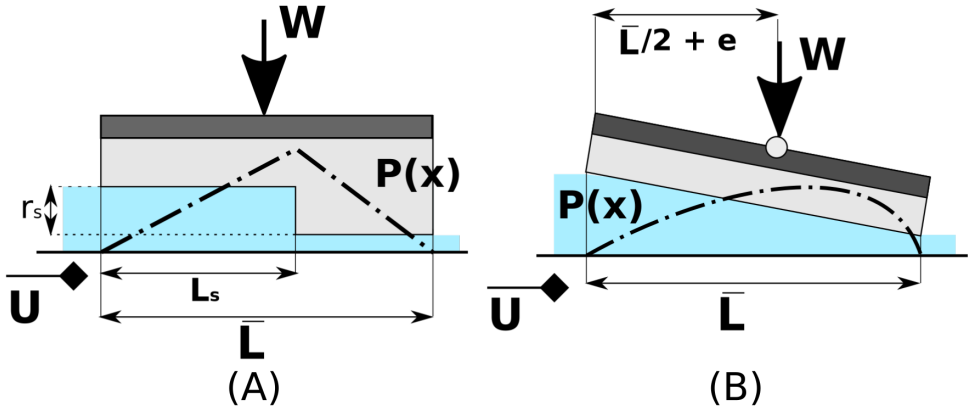
Figure 6.6: (A) Rayleigh step with all design parameters denoted. (B) a conventional tilting pad. with all design parameters denoted.

to be used for good hydrodynamic lift-off properties. The Rayleigh step is a fixed sized bearing geometry as seen in figure 6.6. The tilting pad, on the other hand is a geometry that is dependent on the relative film height and therefore changes depending on the load condition. Both bearing geometries are analyzed using the 1D Reynolds equation. In the case of the Rayleigh step the film height h_r is defined as:

$$h_r = h_0 + f(x) \tag{6.11}$$

where $f(x)$ is a step function with location of the step at L_s and with a step height of r_s. The optimal values for such a geometry are known [210].m The film height of the tilting pad h_t can be defined as follows:

$$h_t = h_0 \left(1 + a(1 - x)\right) \tag{6.12}$$

with a the dimensionless angle parameter. This parameter can be solved by determining the equilibrium of load and of moment and by setting the eccentricity value e equal to the optimal value of $0.077L$ [210]. This moment equilibrium needs to be solved simultaneously with the load equilibrium and can be defined as:

$$W\left(\frac{L}{2} + \epsilon\right) = L^2 \int_x (Px)\mathrm{d}x \tag{6.13}$$

Because the Rayleigh step has a fixed geometry, it does not conform to the new load condition as a result of the increased counter surface velocity. At higher velocity, where the minimum film height is usually of less importance compared to the friction, its performance falls behind compared to the tilting pad. By combining the Rayleigh step and the tilting pad in one bearing using the passive shape shifting approach, both the superior friction aspect of the tilting pad at high velocity as well as the higher minimum film height of the Rayleigh step at low velocity can be realized. The resulting combination can be seen in Figure 6.7. This combination has already been investigated before in literature
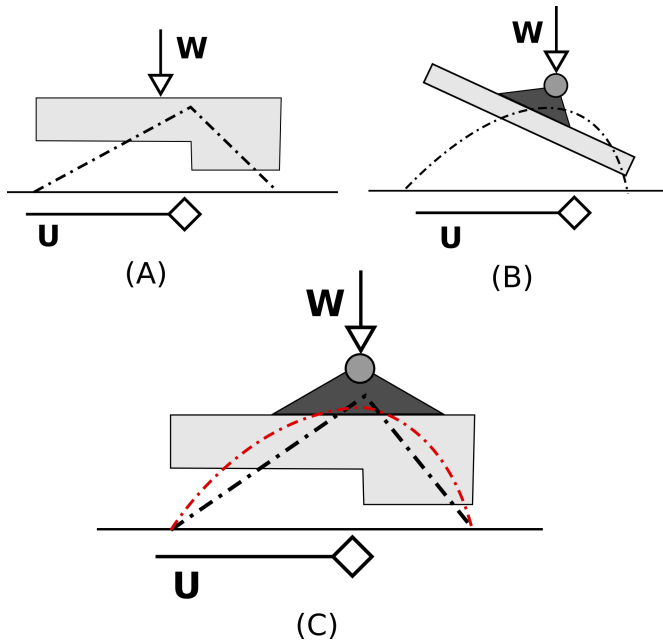
Figure 6.7: (A) Rayleigh step and (B) conventional tilting pad. They have been combined in (C) as the tilting Rayleigh step concept.

[101] in order to reduce friction over the operating range, but it is also an excellent example that shows the promise of passive shape shifting behavior. The principle behind this bearing is that it behaves like a Rayleigh step at low characteristic bearing values, while acting like a tilting pad at higher characteristic values. Note that this tilting of the Rayleigh step may result in wear of the feature and eventual loss of potential improved performance. The hinge in the tilting center, which conventionally has been realized in a knife-edge configuration, can also be made using a compliant element. This has been found in literature in different designs, such as flexure based [101, 114] and through elastic rubber material [136]. The main advantage of the second embodiment is its use in water-hydraulic systems [136].

6.2.2. EXAMPLE 2: PARALLEL TO RECESS BEARING

In the second example the previously presented parallel and recess bearing geometries are combined with the implementation of an elastic component as seen in Figure 6.5. The hydrostatic bearing with an elastic recess pocket is subjected to a variable load. The bearing is again modeled using the 1D Reynolds equation. The film height in this case is defined by the following function:

$$h_h = A_r(H(x - a) - H(x - b)) + h_0 \tag{6.14}$$

where $H(x)$ is the Heaviside function, a and b are the outer locations of the virtual recess and A_r is the depth of the recess and h_0 is the minimum film height. This function is

used to imitate the bearing profile of figure 6.2.B. The boxcar function $\Pi_{bc} = H(x - a) - H(x - b)$ defines the virtual pocket, where the amplitude of the recess is directly coupled to the stiffness of the virtual spring K_r. In this example, the stiffness is coupled to the normalized load case as $K_r = (2\text{E}5 \cdot \bar{W}_1 / \bar{L})$ with $\bar{W}_1$ being the initial dimensionless load of the operation range. The remaining part of the bearing surface is considered infinitely stiff. By iteration both for the balance of global load $W - W_0$ as well as local recess load W_r, the performance of the bearing can be identified. The location of the virtual pocket is $a = -0.05L$ and $b = 0.05L$ respectively. This means the load on the recess surface can de described as:

$$W_r = \int_a^b P(x)dx \tag{6.15}$$

And the resulting virtual pocket load equilibrium as:

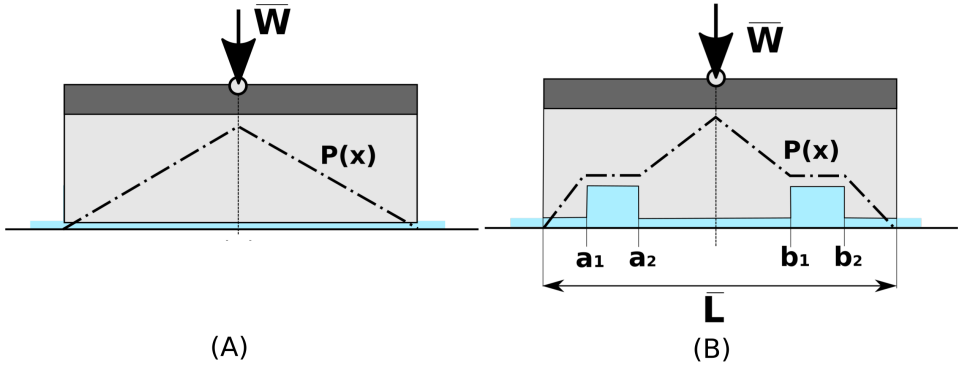$$W_r = K_r A_r \tag{6.16}$$

Figure 6.8: Pressure profile of the parallel bearing and subsequent pocket bearing that increases tilt stiffness.

6.2.3. Example 3: Parallel to tilt recess bearing

Similar to the previous example, pockets are added into the bearing surface. The newly obtained performance however is the increase of tilt stiffness at higher loads, by placing two additional pockets as seen in Figure 6.8. The film height of this 1D bearing concept can de modeled as:

$$h_h = h_{rl} + h_0 + h_{rr} \tag{6.17}$$

With h_{rl} and h_{rr} are the film height functions of the left and right pocket respectively, defined as:

$$h_{rl} = A_{rl}(H(x - a_1) - H(x - a_2)) \tag{6.18}$$
$$h_{rr} = A_{rr}(H(x - b_1) - H(x - b_2)) \tag{6.19}$$

For the example presented, $a_1 = -0.4L, a_2 = -0.3L$, $b_1 = 0.3L$ and $b_2 = 0.4L$. The same approach to determine the equilibrium between the local load and the spring stiffness

is described by equations 6.15 and 6.16 respectively. To determine the effect the pockets have on the tilt stiffness of the bearing at higher operational load, an external moment can be applied. This external moment can be defined as:

$$\bar{M}_{ex} = \bar{W}\epsilon \tag{6.20}$$

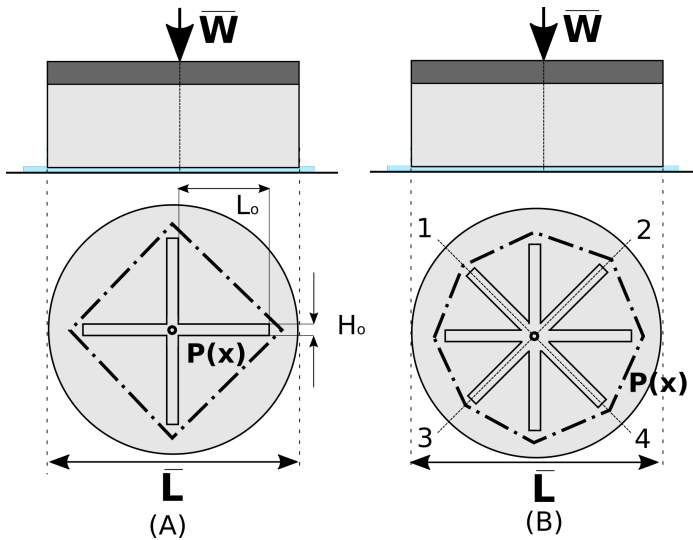Where ϵ is the relative eccentricity [-] of the load relative to the bearing center.

Figure 6.9: 2D lubricant groove bearing with its 4-groove and 8-groove configuration. The lubricant grooves that have elastic characteristics are denoted by numbers 1 to 4.

6.2.4. EXAMPLE 4: 4 TO 8 LUBRICANT GROOVE BEARING

Radial lubricant grooves have been implemented in literature as ways to feed the entire bearing surface with lubricant, in combination with an increase in load capacity. Because of the nature of the features, a 2D geometry is needed to study this concept, and the bearing is thus modeled using the 2D Reynolds equation defined in Equation 6.9. In this example the shape shifting bearing will switch between its 4 and 8 lubricant grooves embodiments. The bearing geometries as well as their pressure profiles for these two embodiments can be seen in Figure 6.9.

The dimensions of the rectangular lubricant grooves are $L_o = 5/16\bar{L}$ and $W_{groove} = 1/30\bar{L}$. The are oriented symmetrically with respect to the bearing center, with angles of 90 degrees and 45 degrees for the 4 and 8 groove embodiment respectively. The depth of the rigid grooves are given by $H_o = \bar{L}/100 + h_0$. The depth of the elastic grooves is defined by the equilibrium of the spring force W_r and the integral of the pressure over the groove surface, similar to the steps performed in the previous examples. Finally, stiffness of the elastic grooves equals $K_r = 1E5\bar{W}_1/\bar{L}$.
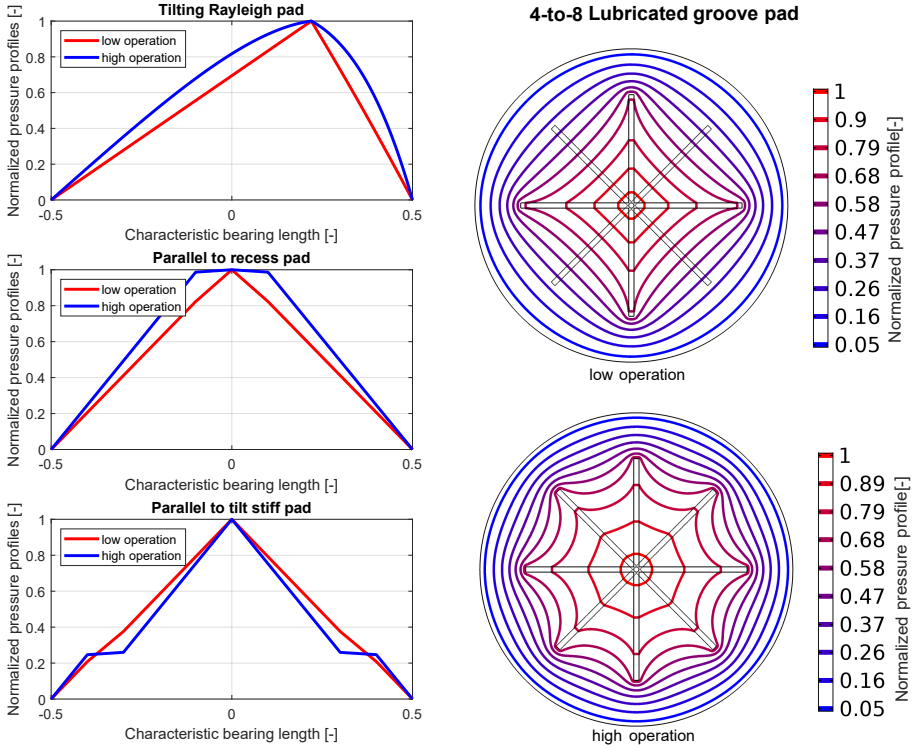
Figure 6.10: The normalized pressure profiles of all 4 concepts at both ends of their operation regime.

Figure 6.11: The Rayleigh step vs. tilting pad vs. its shape shifting variant. Both the minimum film height of the bearings as well as the friction coefficient are given for an operation range varying one order of magnitude.

6.3. RESULTS

All 4 presented examples have been analyzed using the finite element analysis software Comsol Multiphysics. In all cases an operation range is chosen of at least one order

Figure 6.12: The parallel vs. recess pad vs. its shape shifting variant. Both the minimum film height of the bearings as well as the flow shape factors are given for an operation range varying one order of magnitude.
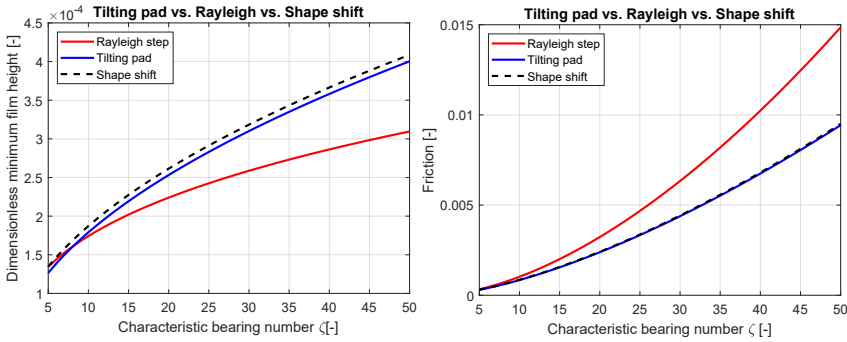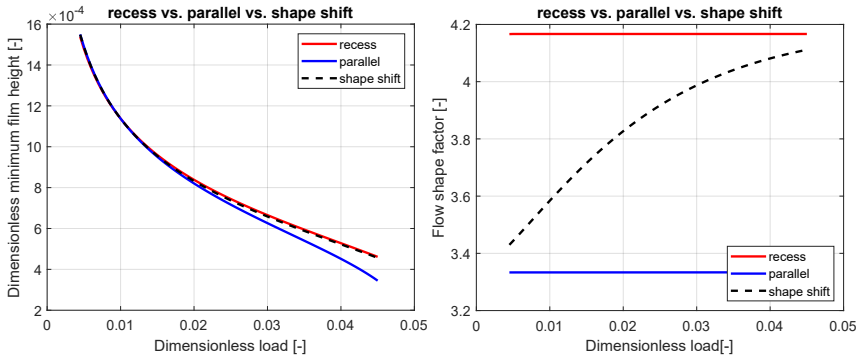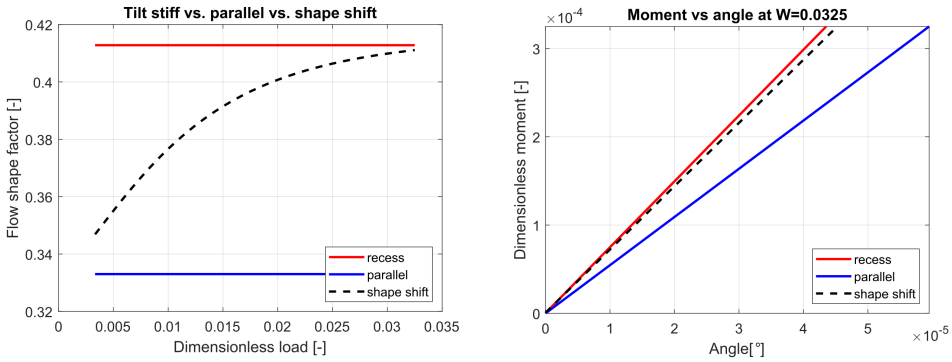

Figure 6.13: The parallel vs. tilt stiff pad vs. its shape shifting variant. Both the flow shape factors of the bearings as well as the moment-rotation curves are given for an operation range varying one order of magnitude.

of magnitude difference between the lowest and highest operation value. The pressure profiles for these two operation points in the range are presented in Figure 6.10. In all cases the rigid counterparts of shape shifting bearings are also presented to show the improvement in performance.

6.3.1. TILTING RAYLEIGH PAD

The resulting behavior can be seen in Figure 6.11. The shape shifting bearing at $\zeta = 5$ has a 0.61 % increase in minimum film height with respect to the conventional Rayleigh step, but a 12.77 % increase of film height with respect to the tilting pad. At higher operation, the shape shifting bearing follows the performance of the tilting pad with only a 0.77 % higher friction coefficient then its tilting pad counterpart. The angle parameter $a = 1.179$ for the conventional tilting pad. The shape shifting variant however has a constantly

Figure 6.14: The 4-groove vs. 8-groove vs. its shape shifting variant. Both the minimum film height of the bearings as well as the flow shape factors are given for an operation range varying one order of magnitude.
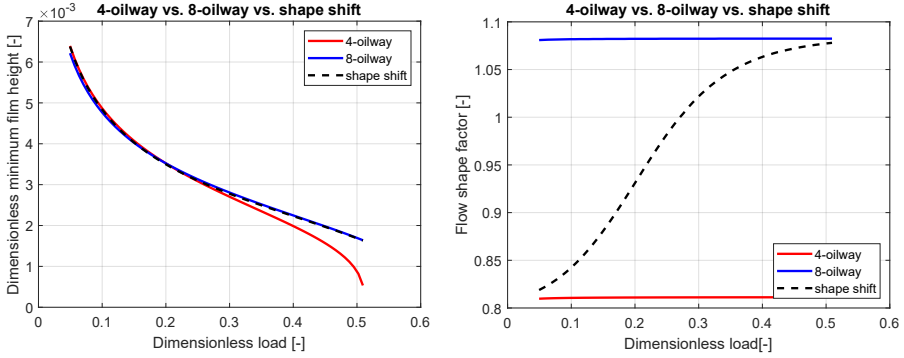
varying tilt angle, with the minimum tilt parameter being $a = 0.062$ at the lower bound of the range and $a = 0.829$ at the higher bound of the range.

6.3.2. Parallel to recess pad

In this concept the objective of the shape shifting version was to operate as a parallel bearing at low operational load, and thus low flow, and with a higher load capacity at higher operational load. Comparison between the bearings can be seen in Figure 6.12. The bearing has at low operational load $\bar{W}_1 = 0.0045$ a 2.91 % increase in flow shape factor with respect to the parallel pad. At high operational load, the shape shifting bearing has a 1.07 % lower film height then its recess counterpart.

6.3.3. Parallel to tilt stiff pad

The resulting comparison can be seen in Figure 6.13. At low operational load the difference in flow shape factor between the shape shifting bearing and its parallel counterpart is equal to 4.08 %. At higher loads the increased tilt stiffness is desired. The dimensionless rotation stiffness K_r is defined by the slope, which equals 7.46, 7.18 and 5.46 for the recess, shape shift and parallel bearings respectively. There is thus only a 3.75 % decrease in stiffness between the rigid recess and shape shifting bearings.

6.3.4. 4 to 8 lubricant groove pad

The results of the groove bearing analysis can be seen in Figure 6.14. At low operational load $\bar{W}_1 = 0.05$ the difference in flow shape factor between the 4-groove and shape shifting bearing is 1.1 %. At the high operation, the difference between the rigid 8-lubricated groove and shape shifting variant is 0.49 % respectively.

6.4. Discussion

Four examples were presented in this work to show the possibilities of passive shape shifting. The tilting Rayleigh pad bearing is the only example where the shift in shape is the result of changing pressure profile as a result of a variation in velocity. We can observe from the results that the introduction of the shape shifting variant forces us to accept some minor compromises. This is seen in the slightly higher friction for the higher end of the operating range. Note also the difference in bearing angle, in that the shape shifting variant is less tilted compared to the conventional tilting pad. As result of a velocity variation, the magnitude of the pressure does not change significantly, however the location of the pressure peak does change. It is expected that this change is less significant then a shift in pressure profile that is the result of a load change.

The other three examples exhibit shape shifting as result of a load changing operation condition. In all cases the switching results in a clear visible change in flow shape factor. Because these examples are force controlled, it is expected that the shifting properties in these bearing types are more dominant. The load variation operating condition is inherently an easier condition to utilize when working with elastic elements, because of the fundamental coupling between load and displacement through element stiffness.

This means that the design for passive shape shifting with velocity variation is inherently less intuitive, and the passive effects are less significant in terms of shifting capabilities. The examples presented in this chapter are also limited by the use of linear stiffness elements. The effective operation range could potentially be increased or decreased further through the addition of non-linear or pre-loaded stiffness elements. Non-linear stiffness elements are already widely investigated to increase the performance of other compliant mechanisms [109]. The relatively small scale of the required elements and their displacement range prove be a challenge, although micro mechanisms with comparable characteristics can also be found in Literature [129].

Finally a reflection on some of the modeling simplifications and their impact on the solutions provided is made. The introduced examples are all modeled by introducing the effects of elasticity into the Reynolds equation and by neglecting thermal effects, variations in viscosity and structural dynamics. In particular thermal effects could influence the deformation effects that are at the basis of the presented method. The reasons thermal effects have not been taken into account in the presented examples are two-fold. First, the choice for this was made based on the desire to introduce the design method and therefore solely apply simple models and the minimum required physics to show the design potential. Second, the effects thermal deformation on full film bearings is heavily dependent on the design case, dimensions and bearing topology. Thermal deformation has been seen in literature to cause significant deformation, although this is especially critical for larger hydrodynamic journal bearings where the film height is small [130, 147], and where the deformation magnitude is also seen to be around or less than the magnitude of the intended minimum film height [19, 147]. This means that these effects might effect the lower operation conditions where parallel bearing surfaces are desired, but are less critical in the high operation condition where the elastic deformation amounts to several times the minimum film height.

6.5. Conclusion

This work has presented a different design approach to design for variable operation conditions, introduced as passive shape shifting. Analogous to self-adaptive bearings, compliant elements are used to obtain movement in the bearing surface. Different to self-adaptive bearings as described in literature, here two dominant bearing geometries are chosen beforehand, making it possible to switch between them both and utilizing both dominant geometries over an operating range. This can be used to design for different objectives within the operation range, such as low ζ_f hydrodynamic lift-off, lower friction, increased tilt stiffness, or decreased volumetric flow. The preliminary insight for the method is that design for variable load conditions is more intuitive when using compliant elements compared to variable velocity conditions. Primary future objectives are the further development and validation of these type of bearings using experiments and their comparison with active bearing designs.

6

7

WHIFFLETREE-BASED HYDROSTATIC BEARING SUPPORTS

To reduce the required deformation of a single bearing pad, multiple pads can be connected through a so-called whiffletree support system. In this chapter, a symmetric whiffletree based hydrostatic bearing embodiment is introduced. A 2D model is presented that allows for determining the kinetostatic and path following properties of such a type of bearing. Design considerations are given regarding the joint rotational-, normal- and shear stiffness of each individual joint, as well as basic bearing layout. The potential of a whiffletree suspended bearing is presented through the use of a case study.

It is expected that the required deformation of the bearing, in order to maintain a parallel orientation to the counter surface, decreases as the length decreases. This is expected, as the curvature of the counter surface becomes close to linear if the length of the curvature decreases. However, a decrease in bearing length results in a decrease in load capacity which is undesirable for most applications. A solution could be to connect multiple smaller bearing pads, also called slipper, together by the use of a support structure [146]. This way, the deformation required from each slipper to maintain a close to parallel orientation with the counter surface, is reduced while load capacity could be maintained. A possible suitable support system is the whiffletree [127]. Examples of applications that use a whiffletree as support are testing setups for wind turbines and telescopes [8, 43, 127, 162]. It is important that conventional contact-based joints are not used in the support system of the hydrostatic bearing since they would re-introduce wear, friction and backlash into the system. Hydrostatic spherical joints [125] or Compliant joints [87, 202] could solve these drawbacks, providing the same motion as conventional contact joints without these negative properties, although in the case of compliant joints this generally comes at the cost of load capacity [202]. For the design of such a complete whiffletree based system, knowledge is needed about the kinematics and kinetostatics such that the potential performance can be defined. This chapter investigates the potential of such a support.

7.1. METHODS

The 2D whiffletree based large deforming hydrostatic bearing is presented in this work as an alternative to compliant support bearings as shown in Fig. 7.1. In chapter 4, large de-
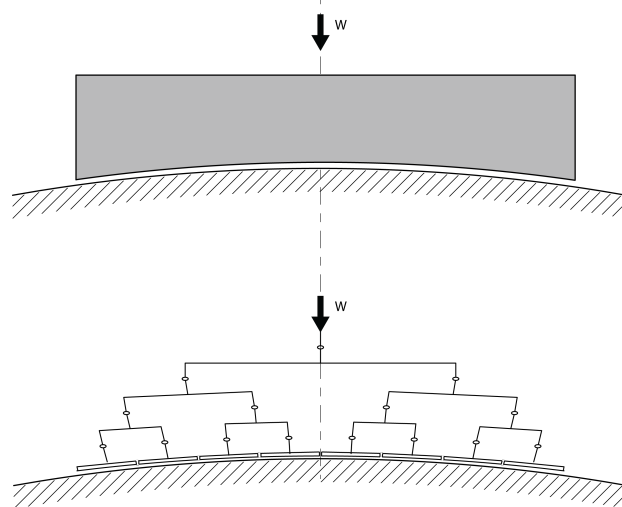

Figure 7.1: Elasto-hydrostatic bearing in its deformed configuration to remain parallel with the counter surface (Top) and a whiffletree supported hydrostatic bearing in its deformed configuration to remain parallel with the counter surface (Bottom).

formable bearings are defined as bearings that (a) are able to deform ≥ 10% of the height

of the bearing in its undeformed configuration, and (b) are able to deform ≥ 100 times the average film height of the fluid film. The implementation of compliance to obtain large deformation in full film bearings is a significantly more difficult challenge compared to their small deforming counterparts, simply because large compliance and high load capacity are not necessarily aligned design objectives. If an elastic support, called slipper in this work, is utilized for these objectives, then all required motion has to come out of a single geometry. This geometry is not necessarily designed for motion, but to obtain a certain load capacity. A whiffletree based bearing support gives a different perspective to the same design challenge. By introducing discrete components specifically designed for the load case, the load can potentially be better distributed while maintaining deformability. The whiffletree support is used to reduce the required slipper deformation by allowing each slipper to rotate, obtaining a better orientation to the counter surface. This advantage is one of the principle motivations for introducing the whiffletree support system and thus will first be analyzed in detail. Because primary motivation in this work is to introduce the whiffletree suspension as a design alternative, all modeling performed in this work will be done in 2D. In accordance with what has been observed in literature [72, 120, 211, 251], the counter surface or track of the system will be represented by a sine wave with wavelength λ and amplitude A. Bearing deforma-
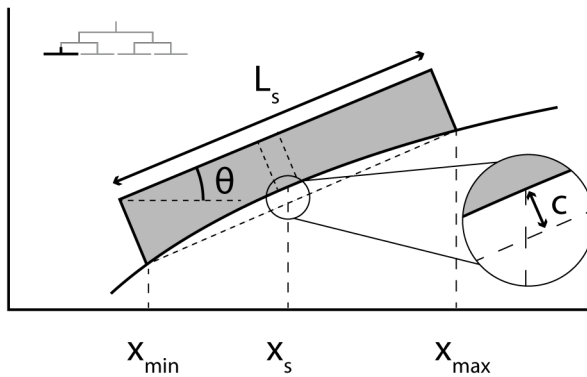
Figure 7.2: Single slipper compressed to remain parallel to the track with the corresponding parameters.

tion, as function of its length, can be expressed as the slipper compression required to maintain a parallel orientation with the track as seen in Fig. 7.1. Figure 7.2 shows a slipper in its deformed configuration while maintaining a parallel position with the gradient of the counter surface. The minimum and maximum positions of the track under the slipper, which is a specific track section in the slippers reference frame, are required for determining slipper compression. The specific track section is obtained by finding the x

position of both edges of the slipper $x_{\text{min/max}}$ described as:

$$x_{\text{min/max}} = x_{\text{s}} \pm \frac{1}{2}L_{\text{s}}\cos(\theta) \tag{7.1}$$

where x_{s} is the x position of the slipper center, L_{s} is the slipper length and θ the angle of slipper center point with respect to the horizontal. The specific track section U is now defined by:

$$U = \begin{bmatrix} x \\ y \end{bmatrix} = \begin{bmatrix} x \\ A\sin(\frac{2\pi x}{\lambda}) \end{bmatrix} \text{ for } x_{\text{min}} \le x \le x_{\text{max}} \tag{7.2}$$

where A is the amplitude of the track and λ is the wavelength of the track. The specific track section is placed at the origin defined by:

$$U_{\text{translated}} = U - T \tag{7.3}$$

where T is the translation matrix defined by:

$$T = \begin{bmatrix} x_{\text{s}} \\ A\sin(\frac{2\pi x_{\text{s}}}{\lambda}) \end{bmatrix} \tag{7.4}$$

Next, the specific track section is rotated such that the gradient of the track at position x_{s} is orientated parallel to the horizontal defined by:

$$U_{\text{final}} = R \cdot U_{\text{translated}} = \begin{bmatrix} x' \\ y' \end{bmatrix} \tag{7.5}$$

where R is the rotation matrix described by:

$$R = \begin{bmatrix} cos(\theta_{\text{s}}) & sin(\theta_{\text{s}}) \\ -sin(\theta_{\text{s}}) & cos(\theta_{\text{s}}) \end{bmatrix} \tag{7.6}$$

where θ_{s} is described by:

$$\theta_{\text{s}} = \arctan(\frac{y_{\text{s}}}{x_{\text{s}}}) \tag{7.7}$$

Finally, the compression c of the slipper to remain parallel with its track is described by:

$$c = y'_{\text{max}} - y'_{\text{min}} \tag{7.8}$$

where y'_{min} and y'_{max} are respectively the minimum and maximum y values of the rotated specific track section. The slippers maximum required compression over the whole track is obtained by following the previous steps for each x_{s} position on the track. Figure 7.3 shows the maximum compression required as a function of the slipper length for a track amplitude of 5%, 10% and 15% of the wavelength respectively. It can be seen that the relation between the compression and slipper length is approximately quadratic. This means that a decrease in slipper length of factor s will result in a decrease in compression of factor s^2. This beneficial effect can be captured through the implementation of a whiffletree in the bearing suspension and functions as one of the primary motivations for developing such a support.
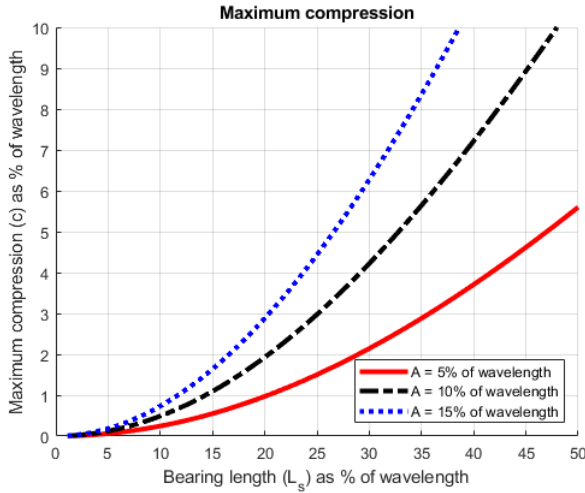
Figure 7.3: Compression required of a single slipper, as function of the slipper length for a counter track with an amplitude of 5%, 10% and 15% of the wavelength respectively.

7.1.1. Bearing Topology

Different embodiments can potentially be envisioned for these kind of support systems. The advantages for implementing these suspensions in hydrostatic bearings is that they allow for the implementation of discrete rotational components, specifically designed for the load case, while simultaneously distributing the load over the support. This, combined with the type of sinusoidal counter tracks investigated in this work, directly impact the topology. The following statements are made concerning the suspension topology investigated in this work:

1. The suspension will be used to follow symmetric variable counter surfaces.

2. The suspension will be used to fully distribute the load uniformly.

The first statement directly relates to the definition of using a sinusoidal wave as the basis for counter surfaces, and thus the expected type of deformations. Using both statements, this work introduces the symmetric whiffletree suspension that can be seen in Fig. 7.4 that will be the basis for the whiffletree support performance presented. For this topology, the height of the joint on the slipper is equal to half the slipper length and that the height of each joint in a layer is twice the length of the joint one layer below. The assumption in thus topology is that there is no distance between the slippers, which would not work in a practical embodiment. Since the focus of this work however is on the support and we minimize the impact of the slippers themselves, it is an accepted error. It is also avoidable in future practical embodiments by ensuring the slipper is smaller then L_s. This topology can be seen as the neutral design state for sinusoidal counter tracks, where the loads are equally distributed over the joints. Because of this symmetric positioning of the lower layers and all slippers design spaces being equal in size, it does

not have any inherent changes in load between the individual joints in one layer. This means all joints in the same layer will experience the same load condition, be it with a phase difference. This topology therefore has equal load distribution based on it undeformed configuration. It therefore embodies the second statement and fully distributes the load uniformly.
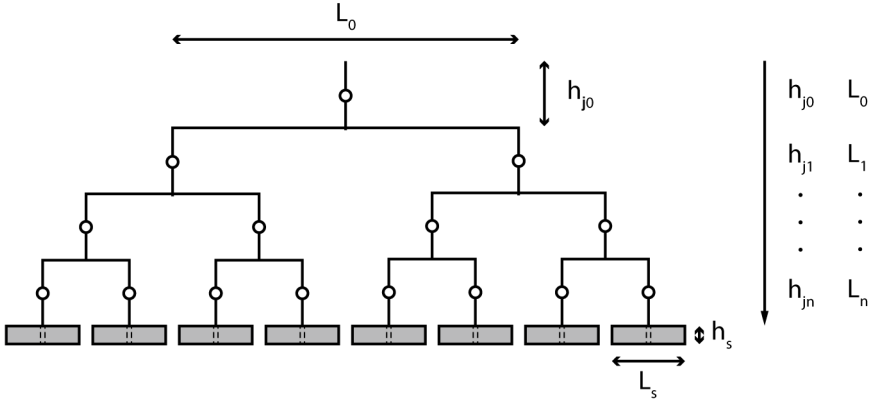
Figure 7.4: Total baring height of a triple layer whiffletree consisting of the slipper height and the joint height of each individual layer.

The next important design dimension is the bearing height. Bearing height is built up out of the slipper height and the total joint height in the system as shown in Fig. 7.4. The length of each joint L_k is defined by:

$$L_k = 2^{(n-k)} L_s \tag{7.9}$$

where L_s is the slipper length and k is the layer in which the joint is located counted from top to bottom, n being the total number of whiffletree layers and k being $n+1$ for the layer containing the slippers. The height of a single joint, depending on its location in the whiffletree, is defined as:

$$h_j = uL_k \tag{7.10}$$

where u is the joint height-to-length ratio. The total bearing height is defined by the sum of all joints as well as the total slipper height, which is dependent on the maximum allowed compression, defined as:

$$h_b = \frac{1}{e} c_{max} + \sum_{k=0}^{n} uL_k \tag{7.11}$$

where n is the number of layers in the whiffletree, u the joint height-to-length ratio, c_{max} the maximum required compression and e the maximum allowable compression of the

slippers material. Beside the general dimension of the whiffletree, both its kinematics and kinetostatics will also be defined.

7.1.2. BEARING KINEMATICS

A whiffletree based support fundamentally consists of multiple layers. Here, each layer contains a number of cells equal to the layer number, as shown in Fig. 7.5.
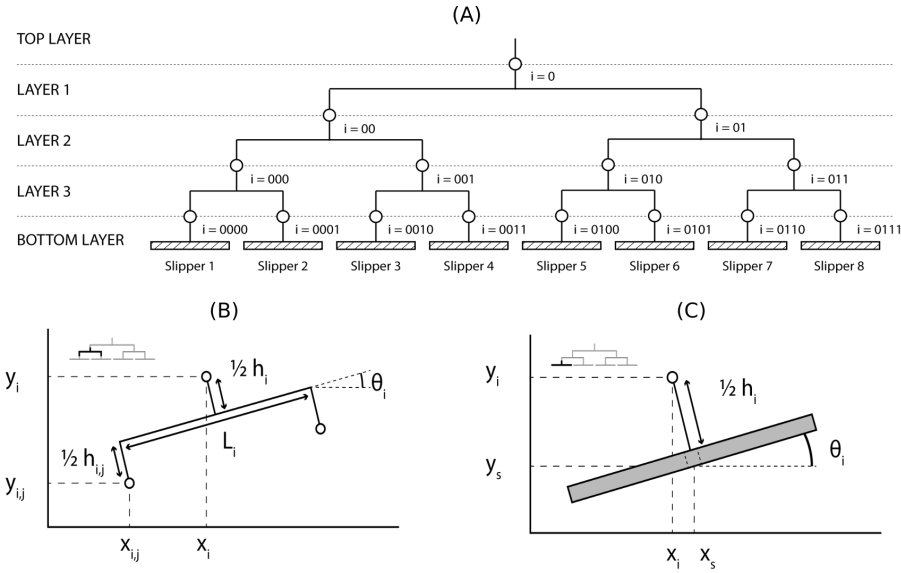
Figure 7.5: (A) Layout of a triple layer whiffletree support system with the corresponding layer and joint numbers. (B) Whiffletree layer cell configuration consisting of 3 joints connected by a rigid linkage. (C) Bottom layer cell configuration consisting of a slipper connected to a single joint by a rigid linkage.

In the proposed topology, each cell except for the bottom layer, has 3 joints connected by a rigid link as shown in Fig. 7.5B. The cells of the lowest layer consist of a slipper connected with a rigid link to a joint which is shown in Fig. 7.5C. The indexation used for the introduced topology is shown in Fig. 7.5.A. As shown, parts in the top layer of the cell are noted with an i, and parts in the bottom layer of the cell are noted with $(i, 0)$ for the left part and $(i, 1)$ for the right part or (i, j) if both parts are defined.

To allow for an analytical definition of suspension kinematics, a rigid body based model will be introduced. The whiffletree kinematics are described by the linkage dimensions, the joint angles with respect to the horizontal and the joints x and y positions. All angles with respect to the horizontal are described by θ and all pivot angles of the joints are described by ϕ as shown in Fig. 7.6. The x and y position of each joint $x_{i,j}$

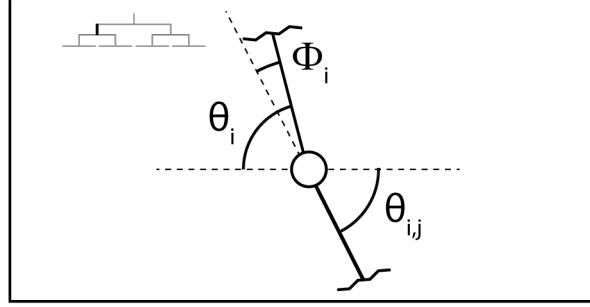Figure 7.6: The angle of each linkage with the horizontal θ and the angle with respect to the linkage one layer above ϕ.

and $y_{i,j}$, as shown in Fig. 7.5B, are defined by:

$$x_{i,j} = x_i \pm \frac{1}{2} L_i \cos(\theta_i) + \frac{1}{2}(h_i + h_{i,j}) \sin(\theta_i) \tag{7.12}$$

$$y_{i,j} = y_i \pm \frac{1}{2} L_i \sin(\theta_i) - \frac{1}{2}(h_i + h_{i,j}) \cos(\theta_i) \tag{7.13}$$

where L_i is the length of the linkage, h_i and $h_{i,j}$ are the joint heights, θ_i is the joint angle and x_i and y_i are the respective joint x and y position, one layer above. As seen in Eqn. (7.12) and (7.13), the position of each joint in a layer is described by the joints position in the ascending layer. The x and y position of the joint connected to a slipper x_i and y_i, as shown in Fig. 7.5C, are defined by:

$$x_i = x_s - \frac{1}{2} h_i \sin(\theta_i) \tag{7.14}$$

$$y_i = y_s + \frac{1}{2} h_i \cos(\theta_i) \tag{7.15}$$

where x_s and y_s are respectively the x and y position of the center of the slipper, h_i is the joint height, h_s is the slipper height and θ_i is the joint angle. This gives the x and y position of the slipper as function of the slipper angle with respect to the horizontal. Assuming that the slipper remains parallel with the gradient of the track at position x_s, the angle θ_i is defined by:

$$\theta_i = \arctan\left(2\pi A \cos(2\pi x_s)\right) \tag{7.16}$$

where A is the amplitude of the track. Furthermore, the y position of the center of the slipper is described by:

$$y_s = A \sin(2\pi x_s) \tag{7.17}$$

When setting Eqn. (7.16) and (7.17) equal to zero, so that they can be solved, the following set of equations is obtained:

$$\arctan(2\pi A\cos(2\pi x_s)) - \theta_m = 0 \tag{7.18}$$

$$A\sin(2\pi x_s) - y_s = 0 \tag{7.19}$$

If the joint in the top layer is assumed to have a prescribed x position and a variable y position, the set of equations consisting of Eqn. (7.18) and (7.19) can be obtained for each slipper. If the assumption holds that the slippers remain parallel with the gradient of the track, the system is fully constrained following Greubler's Equation resulting in a solvable system of equations [260]. If the system of equations is solved, the pivot angle ϕ of each individual joint is then defined by:

$$\phi_{i,j} = \theta_{i,j} - \theta_i \tag{7.20}$$

where $\theta_{i,j}$ is the corresponding joint angle with respect to the vertical and θ_i is the joint angle with respect to the vertical one layer above. Furthermore, the top joint y position can be obtained. So as described, the kinematics can now be obtained using the previosuly given equations. Using the top joint y position, the ratio between the peak to peak value of the top joint and the counter surface shown in Fig. 7.7A and 7.7B van be obtained. The effect of different amplitudes compared to the wavelength and the effect of increased layer numbers is presented in these figures.
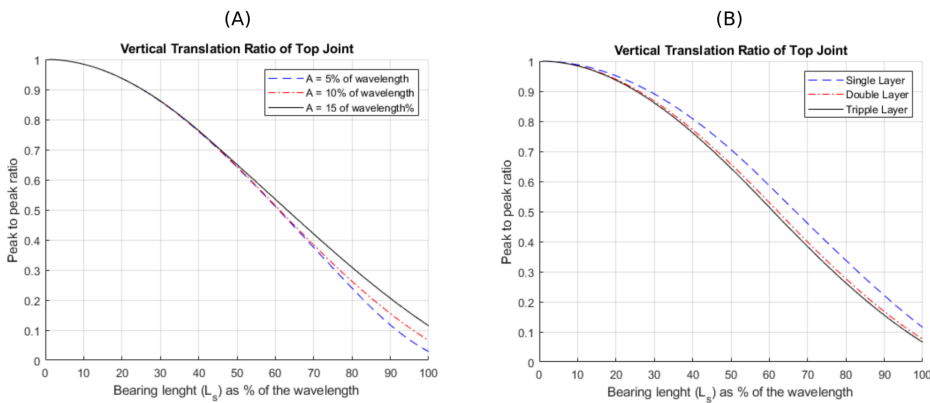
Figure 7.7: (A) Peak to peak ratio of a triple layer whiffletree with a counter surface amplitude A of 5%, 10% and 15% of the wavelength. (B) Peak to peak ratio for a single, double and triple layer whiffletree with a counter surface amplitude of 10% of the wavelength.

7.1.3. BEARING KINETOSTATICS

Kinetostatic performance of the support is directly related to the stiffness of each individual joint. The directions of the rotational-, normal- and shear stiffness of each joint are shown in Fig. 7.8. In this chapter, the linearized rotational stiffness relative to the
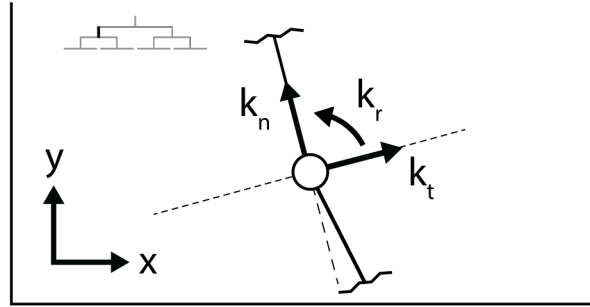
Figure 7.8: Normal-, shear- and rotational stiffness acting on each individual joint in the whiffletree.

neutral configuration of the joint k_r being defined as:

$$k_r = \frac{M_r}{\phi_r} \tag{7.21}$$

where M_r is the moment acting on the joint and ϕ_r is the pivot angle of the joint. The linearized normal stiffness relative to the neutral configuration of the joint k_n is defined as:

$$k_n = \frac{F_n}{\delta_n} \tag{7.22}$$

where F_n is the normal component of the force acting on the joint and δ_n is the allowable normal displacement of the joint. Finally, the shear stiffness of the joint k_t is defined as:

$$k_t = \frac{F_t}{\delta_t} \tag{7.23}$$

where F_t is the tangential component of the force acting on the joint and δ_t is the allowable tangential displacement of the joint. As shown, these different types of stiffness are dependent on the moments and forces acting on each joint. The forces acting on each slipper are decomposed to correspond to the fixed x and y frame connected to the upper section of the whiffletree. The forces in x and y direction acting on each slipper F_x and F_y are defined by:

$$F_x = -W_s \sin(\theta_s) \tag{7.24}$$
$$F_y = W_s \cos(\theta_s) \tag{7.25}$$

where W_s is the load capacity of the slipper and θ_s is the angle of the slipper with respect to the horizontal. The load carrying capacity of a single slipper, for an equally distributed

whiffletree support system where the load carrying capacity of the joints in each ascending layer doubles, is described by:

$$W_{\mathrm{s}} = \frac{W_{\mathrm{tot}}}{n} \tag{7.26}$$

where W_{tot} is the load carrying capacity of the system and n is the total number of slippers in the system. The forces acting on each joint $F_{\mathrm{x}(i)}$ and $F_{\mathrm{y}(i)}$ are then defined by:

$$F_{\mathrm{x}(i)} = F_{\mathrm{x}(i,1)} + F_{\mathrm{x}(i,2)} \tag{7.27}$$

$$F_{\mathrm{y}(i)} = F_{\mathrm{y}(i,1)} + F_{\mathrm{y}(i,2)} \tag{7.28}$$

To obtain the normal- and shear force acting on each joint, a second decomposition is used. The normal force F_{n} acting on each joint is defined by:

$$F_{\mathrm{n}} = F_{\mathrm{y}} \cos(\theta) - F_{\mathrm{x}} \sin(\theta) \tag{7.29}$$

where θ is the angle of the joint with respect to the horizontal. The shear force F_{t} acting on each joint is defined by:

$$F_{\mathrm{t}} = F_{\mathrm{y}} \sin(\theta) + F_{\mathrm{x}} \cos(\theta) \tag{7.30}$$

The moment M_i acting on each joint, except for the joints connected to a slipper, is defined by:

$$M_i = F_{\mathrm{a}(i)} \frac{L_i}{2} + F_{\mathrm{b}(i)} \frac{(h_i + h_{i,j})}{2} + M_{i,1} + M_{i,2} \tag{7.31}$$

where h_i and $h_{i,j}$ are the joint heights and L_i is the linkage length as shown in Fig. 7.5B and $F_{\mathrm{a}(i)}$ and $F_{\mathrm{b}(i)}$ are defined by:

$$F_{\mathrm{a}(i)} = F_{\mathrm{y}(i,1)} \cos(\theta_i) - F_{\mathrm{x}(i,2)} \sin(\theta_i) \tag{7.32}$$

$$F_{\mathrm{b}(i)} = F_{\mathrm{y}(i,1)} \sin(\theta_i) - F_{\mathrm{x}(i,2)} \cos(\theta_i) \tag{7.33}$$

where θ_i is the angle of the joint with the horizontal. The moment acting on the joints connected to the slipper is defined by:

$$M = \int x P dx \tag{7.34}$$

where P is the distributed load acting on the slipper. The rotational stiffness of each individual joint can now be obtained. Furthermore, the normal- and shear stiffness of each individual joint is given as a function of the maximum allowable displacement in the normal and tangential direction.

With the rotational stiffness of each individual joint known, the relation between the tilt stiffness of each slipper and their corresponding bottom layer joint is found. The linearized tilt stiffness relative to the neutral configuration of the slipper k_{rs} is defined by:

$$k_{\mathrm{rs}} = \frac{M_{\mathrm{s}}}{\phi_{\mathrm{s}}} \tag{7.35}$$

where M_{s} is the moment acting on the slipper and ϕ_{s} is the slipper angle with respect to the gradient of the track at position x_{s}. The tilt stiffness of the slipper is modeled as
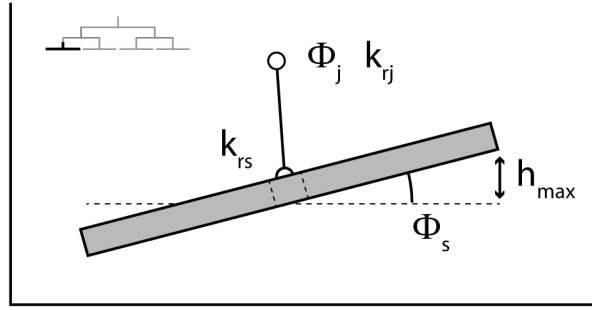
Figure 7.9: Representation of a slipper with a hinge joint connecting the slipper and bottom layer joint together and the corresponding parameters.

a hinge joint between the slipper and the bottom layer joint as seen in Fig. 7.9. The maximum tilt stiffness of the slipper is related to the maximum pivot angle of the slipper ϕ_{smax} which is defined by:

$$\phi_{\text{smax}} = \arcsin(\frac{2h_{\text{max}}}{L_{\text{s}}}) \tag{7.36}$$

where h_{max} is the maximum allowable deviation in the film height and L_{s} is the slipper length. The maximum allowable angle of the slipper prevents solid to solid contact between the slipper and track due to tilting of the slipper. However, it is desired that the influence of the tilt stiffness of the slipper on the system is negligibly small. Meaning the hinge joint between the slipper and bottom layer joint in Fig. 7.9 can be seen as a rigid connection. To assure this, a high tilt stiffness of the slipper is required with respect to the rotational stiffness of the bottom layer joint. This relation is dependent on the angle of the slipper and the angle of the bottom layer joint which is defined by:

$$k_{\text{rs}} = \frac{k_{\text{rj}}\phi_{\text{j}}}{\phi_{\text{s}}} \tag{7.37}$$

where ϕ_{j} is the bottom layer joint pivot angle and k_{rj} is the bottom layer joint rotational stiffness. With the given equations, the kinetostatic of the whiffletree can now be obtained. To position the whiffletree in every configurations that is required to follow the track, at every step a difference in load capacity on each slipper is required. The difference in load capacity on the slippers generates a moment acting on each joint, resulting in a rotation of the joint. This difference in load capacity is obtained by changing the film height under each slipper. The relation between the load capacity and film height can be found in the 1D Reynolds equation [193], showing that a decrease in film height results

in an increase in load capacity. Since the focus of this work is on the support, the modelling of the slipper load capacity is not further discussed as it falls outside of the scope. The total change in film height of each slipper is dependent on the joints that are related to the slipper and the rotational direction of these joints. For a joint to rotate counter clockwise (ccw), the corresponding slippers right of the joint should have a higher load capacity compared to the corresponding slippers left of the joint. For a joint to rotate clockwise (cw), the corresponding slippers left of the joint should in combination exert a higher force moment compared to the corresponding slippers right of the joint. As an example, looking at Fig. 7.5, for joint 11 to make a ccw rotation, slipper 3 and 4 need a decrease in film height while slipper 1 and 2 remain an equal or have an increase in film height. It is important that the total change in film height should not exceed the minimum film height under each slipper in the undeformed configuration, since this would re-introduce solid-solid contact.

7.1.4. DESIGN RULES

The sections before presented the general model for the symmetric whiffletree bearing consisting out of the following components: Bearing design dimension, kinematics and kinetostatics. Based on this model, the following rules of thumb can be introduced to aid designers in their design process, given the large degree of design freedom this whiffletree based support offers. Based on the previous models, the following rules should be followed:

1. Minimize the slipper length given the maximum slipper compression, number of whiffletree layers and bearing length for the smallest bearing design dimension.

2. Increase the number of whiffletree layers given an increase in bearing length for smallest bearing design dimension.

3. Minimize the joint rotational stiffness.

4. Maximize the joint normal- and shear stiffness.

5. Maximize the ratio between slipper tilt stiffness and bottom layer joint rotational stiffness.

For validation, the models and design rules will be implemented in a case study.

7.2. DESIGN CASE STUDY

To validate the model and show the potential of this type of support a case study is used. A potential application that currently is not able to make use of the performance characteristics of hydrostatic bearings, is the radial piston pump. Especially the variant where cam rings are implemented [163], which have counter surfaces with a sinusoidal shape, use roller bearings exclusively because of this constantly varying track. An example of such a pump topology can be seen in Fig. 7.10. A case study is presented based on the general dimension and performance criteria of an experimental water pump used in the power train of a water hydraulic wind turbine [163, 174]. The objective of this case study is to show the effect of design choices for the whiffletree support, while simultaneously
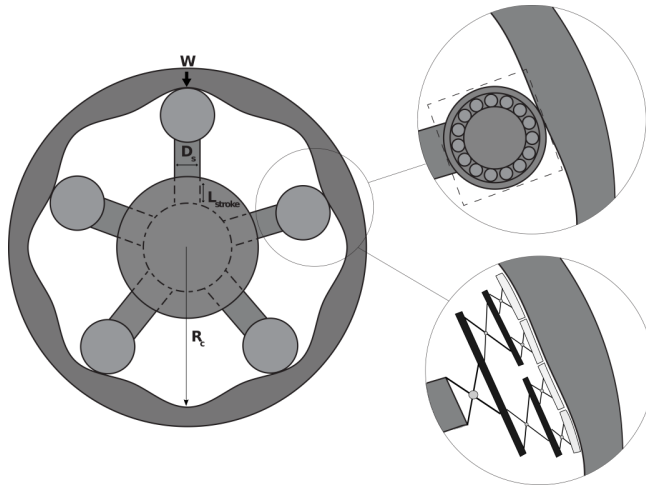
Figure 7.10: Schematic overview of the radial pump used in the case study where the conventional roller bearing and the newly obtained whiffletree supported hydrostatic bearing are shown.

providing the reader with the required kinematic and kinetostatic criteria that should be strived for when implementing this support in comparable applications. The operating conditions as well as geometrical constraints are defined in table 7.1. The main components are the cam ring, piston and pressure supply source that define this design case. As seen in Fig. 7.10, the bearing is connected to a piston and follows the path described by the cam ring surface. The fluid pressure in the piston is also used as the bearing pressure supply. To simplify this case study, the output pressure is assumed to be equal for the entire stroke cycle. This represents the highest load case. Since this is a case study that

Description	Parameter	Value	Unit
Piston diameter	D_s	0.06	[m]
Cam ring wavelength	λ	0.45	m
Piston stroke	L_{stroke}	0.03	m
Cam ring radius	R_c	0.5	m
Cam ring amplitude	A	0.023	m
Supply pressure	P_s	80E5	Pa
Bearing load	W	17	kN
Joint height to length ratio	u	1	[-]
Max compression slipper	c_{max}	0.1	[-]
Allow. normal disp. joints	δ_n	$0.01 h_j$	[m]
Allow. tangential disp. joints	δ_t	$0.01 h_j$	[m]
Total bearing length	L_{tot}	0.5λ	[m]

Table 7.1: Parametric values used in the case study.

solely investigates the kinematics and kinetostatics of the potential support, an example joint is implemented of which the joint to height ratio, the allowable normal displacement, and the tangential displacement are defined. For the slipper solely the maximum

compression criteria is defined. These characteristics are dependent on the joint used and primarily depend on its failure criteria, which fall outside the scope of this work. This example will compare a single, double and triple layer whiffletree support. The visualization of the three embodiments are presented in scale in Fig. 7.11. To obtain the desired piston stroke L_{stroke} that needs to be followed, in accordance to Fig. 7.7A, the total bearing length is chosen to be 0.5λ. The maximum allowable film height deviation allowed in this case study equals 40%. The final parameter that effects the dimension of
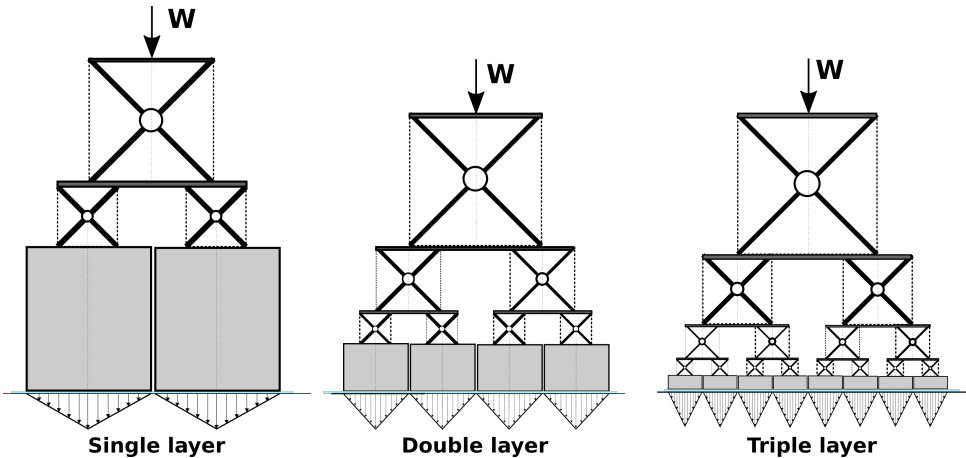

Figure 7.11: To scale dimensionless comparison between the three proposed whiffletree embodiments. The increased number of layers has a positive influence on the total bearing height, given equal bearing length.

7

the whiffletree support is the bearing to/wavelength ratio. The effect of this parameter is visualized in Fig. 7.12. A sole slipper with rotational hinge is added as reference. The way this model is set up is such that it can be used by designers to determine the maximum total bearing dimension, required joint rotations, shear and normal stiffness given this set of input parameters.

7.2.1. MODEL VALIDATION

To validate the model, a comparison is made between the analytical model and a Finite Element Model (FEM) using Comsol Multiphysics. In the FEM, the multibody dynamics toolbox is used to model the bearing. The linkages are modeled as rigid beams, using the rigid domain function and the joints are modeled as hinge joints. The top joint has a prescribed x position, a variable y position and is constrained in rotation. The slippers have a prescribed y_{s} position and angle θ as function of its x_{s} position, which are given by Eqn. (7.16) and (7.17). In the simulation, the top joint travels for a full wavelength. The validation will solely be performed on the triple layer whiffletree configuration, since this is the highest geometrical order model analyzed in this case study.
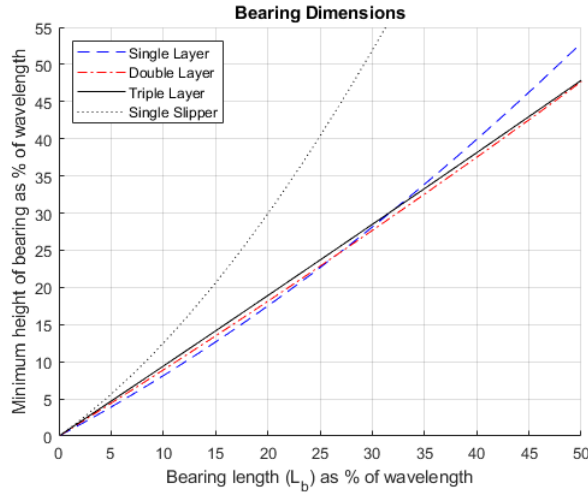
Figure 7.12: Percentage wise effect of increasing the number of whiffletree layers as function of the bearing length/wavelength has on the total bearing height.

7.3. RESULTS

Following the presented method of determining the bearing topology, the design dimension for all three embodiments of the symmetric whiffletree support can be seen in Table 7.2. Please note that any rigid connection members do not have a dimension in this work and therefore do not effect the total design dimension. Based on these dimensions, both kinematic and kinetostatic performance of all three embodiments are presented in Figure 7.13A-B. Figure 7.13A shows the comparison of the FEM model with the analytical version presented in this work for a triple layer symmetric whiffletree. Only the leftmost joint angle of each layer is shown since the remaining joints in the same layer show equal behavior with the difference of a phase shift. The comparison shows no difference between the analytical and FEM model in terms of kinematic performance, thus validating the presented model. The results of the required joint slipper rotational stiffness with respect to the rotational joint directly connected to the slipper can be seen in Fig. 7.13B. If the ratio between the rotational stiffness of the slipper and that of the first joint connecting to the slipper is high, this means the angular rotation the slipper makes can be neglected in the total performance of the system. The validated kinematic model can thus be used to determine the difference between the three different embodiments (Fig. 7.14). Again, only the leftmost joint angle of each layer is shown since the remaining joints in the same layer show equal behavior with the difference of a phase shift. The obtained kinematics are used to find the rotational stiffness, maximum normal force and maximum shear force acting on each individual joint. The resulting determination of stiffness cases for the embodiments can be seen in Table 7.3.

Type	Descr.	Param.	Value	Unit
Single	joint height (Top)	h_t	0.113	m
Layer	joint height (1)	h_1	0.056	m
	slipper length	L_s	0.113	m
	slipper height	H_s	0.154	m
	Total dim.	$L_{tot}H_{tot}$	0.073	m^2
Double	joint height (Top)	h_t	0.113	m
Layer	joint height (1)	h_1	0.056	m
	joint height (2)	h_2	0.028	m
	slipper length	L_s	0.056	m
	slipper height	H_s	0.039	m
	Total dim.	$L_{tot}H_{tot}$	0.0531	m^2
Triple	joint height (Top)	h_t	0.113	m
Layer	joint height (1)	h_1	0.056	m
	joint height (2)	h_2	0.028	m
	joint height (3)	h_3	0.014	m
	slipper length	L_s	0.028	m
	slipper height	H_s	0.01	m
	Total dim.	$L_{tot}H_{tot}$	0.497	m^2

Table 7.2: Minimum rotational stiffness and maximum normal and shear force acting on each individual joint in their corresponding layer.

Descr.	Param.	Layer	Double	Triple	Unit
rotational	k_r	Top	750	639	Nm/rad
stiffness		1	236	185	Nm/rad
		2	103	79	Nm/rad
		3	-	38	Nm/rad
normal	k_n	Top	5.92E7	5.81E7	N/m
stiffness		1	6.92E7	6.64E7	N/m
		2	8.00E7	7.43E7	N/m
		3	-	8.28E7	N/m
shear	k_s	Top	1.69E6	3.69E6	N/m
stiffness		1	0.73E6	0.68E6	N/m
		2	0	0.27E6	N/m
		3	-	0	N/m

Table 7.3: Minimum rotational stiffness and maximum normal and shear force acting on each individual joint in their corresponding layer.

7.4. DISCUSSION

The results concerning the use of the design model and results from the case study will be both discussed.
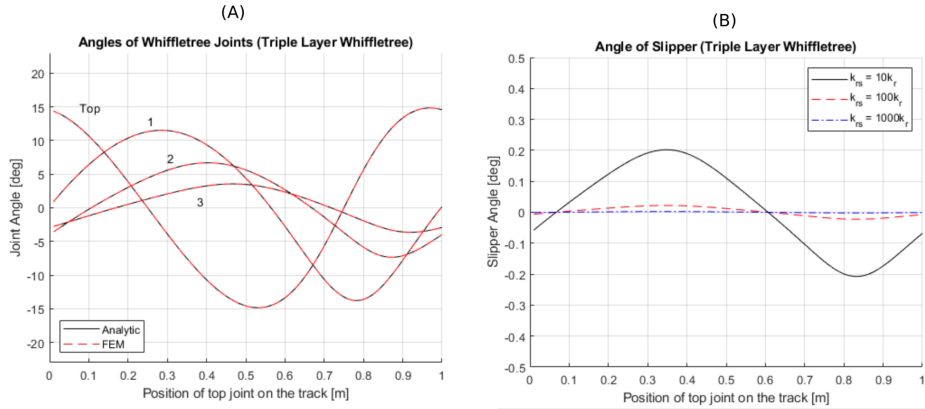
Figure 7.13: (A) Joint pivot angles of the FEM and analytical model compared for a triple layer whiffletree. (B) Slipper pivot angle of a triple layer whiffletree with a rotational stiffness ratio of 10, 100 and 1000.
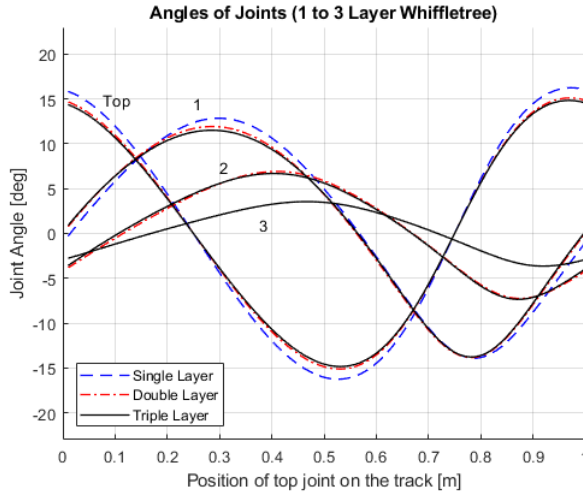

Figure 7.14: joint pivot angles of a single, double and triple layer whiffletree compared.

7.4.1. CASE STUDY

A case study has been presented to show how the design model can be implemented, and what kind of performance can be expected by adding a whiffletree as bearing support. The model consists of defining the dimensions, kinematics and kinetostatics given a certain whiffletree layer set. Given a pre-defined total bearing length of $L_{\text{tot}} = 0.5\lambda$, with λ being the cam ring wavelength, it can be seen in Fig. 7.12 and table 7.2 that the whiffletree positively influences the bearing dimension. This can be seen in the fact that the total height decreases of the bearing when increased whiffletree layers are implemented. It however also shows that in the given design case, the increase from a double

to triple layer whiffletree only marginally improves the footprint and kinematic performance. Figure 7.14 shows the joint pivot angles for the FEM and analytical model. The results obtained from the FEM and analytical models have no noticeable difference, thus validating the design model presented in Sec. 7.1.2.

From the results presented in Fig. 7.14 it can be seen that the whiffletree behaves differently when moving through the concave and convex configurations of the track. Looking at the joint pivot angles shown in Fig. 7.14, it is shown that the addition of whiffletree layers has a negligible small impact on the change in magnitude of the joint pivot angles for the different layers. This means that the top joint in a single layer whiffletree more or less rotates in a similar order of magnitude compared to a whiffletree support with several layers. This can be explained by looking at the angle of the corresponding linkage with the horizontal. The angle of the linkage is approximately equal to the angle of the gradient of the track at equal position. An increase in whiffletree layers does not change this orientation. Thus, no significant change in joint pivot angle is noted due to an increase in whiffletree angles. The top joint this retains the largest rotational angle and will always be a limiting component in a deformable bearing design. The ratio between the rotational and normal stiffness [87] gives some indication on the severity of the design challenge. These have subsequently been calculated for the different embodiments, seen in table 7.4. The results described here show that the increased number of layers in the whiffletree positively influences the top stiffness ratio, which comes at the cost of a higher required performance at the 3rd layer. Depending on the type of joints used, this stiffness requirement may prove to be critical. The required stiffness ratio described in this example would be at the limits of compliant joints as seen in literature [87], and may require the development of alternatives. On the other hand, the minimum required shear stiffness is lower then the minimum required normal stiffness.

Layer	Double layer support	Triple layer support
Top [rad/m^2]	7.89E4	9.09E4
1st [rad/m^2]	29.32E4	35.82E4
2nd [rad/m^2]	77.67E4	94.05E4
3rd [rad/m^2]	-	217.89E4

Table 7.4: dimensional normal to rotational stiffness that gives an indication of the required performance for the contact-free joint implementation.

Finally, it is shown that an increase in whiffletree layers results in a decrease in slipper length, and thus a decrease in required compression of each slipper. The slipper pivot angle is shown in Fig. 7.13 for a rotational stiffness ratio between slipper and bottom layer joint for one, two and three orders of magnitude. It is shown that for a ratio of three orders of magnitude, no noticeable change in slipper pivot angle is noted. Meaning that a rotational stiffness ratio between slipper and bottom layer joint of at least three orders of magnitude is desired.

7.4.2. Model limitations
The design model provides a method to design a 2D whiffletree supported large deforming hydrostatic bearing. There are a few limitations to this design. Firstly, conventional

hinge joints are used in the model compared to the preffered compliant joints. This is done for modelling purposes and the friction that occurs in conventional contact joints is neglected in this study. This is done since rigid body mechanics can be used in combination with the conventional hinge joints.Furhtermore, it is assumed that the center of rotation stays at the same place while using compliant joints in the system. Since the scope of this project is to find a general solution regarding the kinematics and kinetostatics, and this simplification is valid. Secondly, the total perimeter of the bearing increases when multiple smaller slippers are connected together compared to a single slipper of equal length and width. The increase in bearing perimeter results in an increase in fluid losses of the bearing. The perimeter of the bearing, and thus the fluid losses, can be reduced by connecting all slippers together thereby creating a single slipper that consists of multiple segments connected by elastic joints.. This will also change the pressure profile from the single slippers as shown in Figure 7.11 to a continues pressure profile which can be described by a higher order polynomial. It is recommended to look into the behaviour of this single continous slipper in future research. Thirdly, the total joint length is restricted by the total linkage length. This is shown in the assumption that the bottom layer joint has a length of half the slipper length and each ascending joint is twice the length of the joint one layer below, resulting in the maximum allowable bearing length on each linkage. Fourthly, this work gives an explanantion for the static and quasi-static state of a whiffletree supported hydrostatic bearing. Further research can be conducted to find the possible changes in results when perturbations and stability parameters in the dynamic state are taken into account. Finally, the slippers are geometrically not limiting the model and thus placed directly next to each other. In reality, when the bearing moves into a concave configuration, the slippers need to pass through each other which results in jamming. This can be solved by either using less of the maximum bearing design space or adding a gap between the slippers large enough such that the slipper can pass without contact. The latter option needs to follow from an extension of the model, to determine this exact gap dimension without influencing the bearing dimensions to much.

7.5. CONCLUSION

This work shows the potential of a whiffletree support system to increase the capability of 2D compliant hydrostatic bearings to follow non-constant curvature counter surfaces. An approximately quadratic relation is found between the slipper compression and length, and thus the required slipper compression is reduced for a decrease in slipper length. It is shown that an increase in whiffletree layers does not greatly affect the joint pivot angles of the ascending layers. However, the addition of extra layers in the whiffletree does lower each individual slipper length, reducing the required compression of the slipper. A ratio of at least three orders of magnitude between the slipper tilt stiffness and bottom layer joint is required to show no noticeable influence caused by the tilting of the slipper. Finally, the whiffletree can be used to rotate smaller slippers reducing their required compression while maintaining load capacity.

8

COMPLIANT JOINTS USING THE PRINCIPLE OF CLOSED FORM PRESSURE BALANCING

Compliant joints have significant advantages compared to rigid-body hinges due to a monolithic design and the absence of friction, which prevents effects like backlash and stick-slip behaviour. However, the loading capability is often limited and the support stiffness generally decreases during rotation. A new design principle called closed form pressure balancing has been proposed as a solution to improve these limitations. By using an incompressible fluid as the main compliant element, the support stiffness becomes independent of rotation and buckling no longer limits the loading capability. This chapter analyses the fundamental working principle behind closed form pressure balancing and introduces a two-dimensional design model to determine stiffness properties. The design model is validated with a finite element model and used to construct an optimization strategy for optimum joint performance. Additionally, a conversion model and some practical considerations are presented for the transition to a three-dimensional design model.

As seen in the previous chapter, the performance of compliant joints can be crucial for the performance of compliant bearing systems. Compliant hinges have introduced elastic deformation of flexural elements as an alternative to sliding and rolling contacts in rigid-body hinges. As this rotation is based on deformation, the rotational degree of freedom (DOF) is characterised by a stiffness difference in the flexural elements instead of rigid body constraints between multiple parts [247]. Without clearances and friction between surfaces due to a monolithic design, significant advantages are the absence of wear, backlash, stick-slip behaviour and the need for lubrication [109]. This allows high repeatable motions, with high precision [123, 148]. General disadvantages include a limited range of motion due to stress concentrations [123] and an increased complexity in kinematics due to a moving center of rotation (COR), called axis drift [204]. Combinations of multiple leaf flexures in series and/or parallel have been proposed as solutions for these limitations. Examples are the cross-axis flexure [116], cartwheel hinge [123], X2-joint [151], butterfly hinge [102], trapezoidal hinges [246, 247] and CR-joints [204]. A different disadvantage to these types of joints, which also holds for the examples presented before, is the limited support stiffness and risk of buckling when the hinges are loaded in compression [92]. Although this effect depends on the design, it often worsens during rotation because leaf flexures lose their support stiffness when deflected [242]. As a result, there is often a trade-off between a low actuation stiffness and the disadvantages mentioned previously.

Due to this limited relation between support and rotation stiffness, the application range of compliant hinges is also limited. An improved axial support stiffness over a larger range of motion could thus increase the range of potential applications and aid in the development of deformable hydrostatic bearings. This chapter presents design models and performance details for an alternative type compliant joints using the principle of closed form pressure balancing.

8.1. DESIGN MODEL

The design principle analysed in this chapter uses an incompressible fluid as the main compliant element in a joint. The properties of this fluid fundamentally change the working principles behind the axial and rotation stiffness, as schematically seen in figure 8.1. The liquid state allows the fluid molecules to freely reorganize and thereby ac-
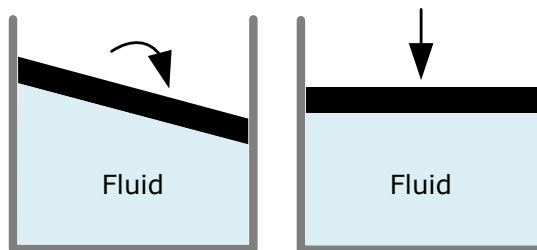

Figure 8.1: Schematic working principle of closed form pressure balancing. The liquid phase allows free shape changes for rotation (left) whereas the fluid incompressibility results in axial stiffness (right).

commodate a change in shape of the volume. Neglecting inertial and viscous effects,

this theoretically results in zero rotation stiffness. However, the incompressibility makes the fluid resist any volume changes when loaded in compression, resulting in a significant axial stiffness. The major advantage is that the working principle behind the axial stiffness is insensitive to the shape of the fluid volume, theoretically decoupling the axial and rotation stiffness. This prevents a decreasing axial stiffness during rotation and eliminates the trade-off between a high axial stiffness or low rotation stiffness. This characteristic behaviour, caused by the closed volume of incompressible fluid, is referred to as "closed form pressure balancing" [87]. However, performance will be influenced by the shape and stiffness of an elastic solid required to contain the fluid. This principle is elaborated on through the use of a 2D design model for analyzing performance.

8.1.1. CONCEPTUAL DESIGN

A cell is thus needed that optimally transfers the properties of the fluid to a physical joint. In this work, a cell with circular enclosures is proposed as seen in 8.2. When vertically
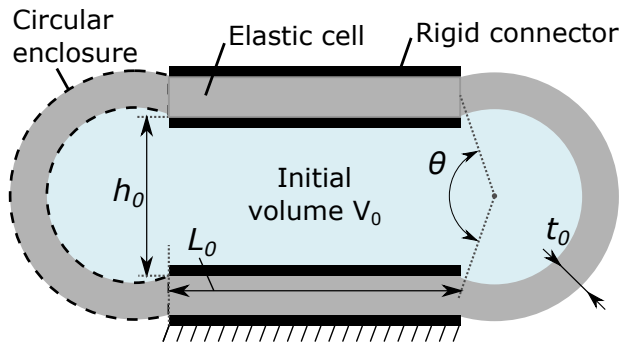

Figure 8.2: Embodiment of the pressure balanced compliant joint.

compressed, fluid is pushed sideways into the enclosure causing an internal pressure. During rotation, however, no pressure buildup is expected as the volume only needs to change shape, making the rotation stiffness fully dependent on the bending stiffness of the enclosures. The circular shape ensures an even distribution of stresses in the material under the internal pressure, whereas the curved geometry allows for a relative low bending stiffness.

The angle of the circular segment, indicated with θ in figure 8.2 and figure 8.3, is expected to influence both stiffness and range of motion. At smaller θ the segment length increases, which lowers both the elongation and bending stiffness of the enclosures. This translates to a decrease in both the axial and rotation stiffness of the joint as well. Furthermore, decreasing θ improves the rotation angle at which the enclosure transitions from bending to stretching. This effect is best explained through the schematic explanation of figure 8.3, where it is seen that the enclosure must elongate for an anticlockwise rotation when θ is larger than $\pi/2$ (rad). However, as the bending and elongation stiffness of the enclosures scale with $t_0{}^3$ and $t_0{}^1$ respectively, comparable to the basic static deformation of a beam, reducing thickness t_0 is expected to be most efficient to minimize rotation stiffness. Therefore, in this work the angle θ is increased to $\pi/2$ (rad) in

favor of axial stiffness. This allows for a co-linear connection between the horizontal and circular parts of the cell, which ensures a rotation of the top is translated into bending of the enclosure. The rigid connectors in figure 8.2 are added to clamp the horizontal segments. This is beneficial because the horizontal segments potentially provide additional compliance to the enclosures which would reduce the axial stiffness. Two ana-
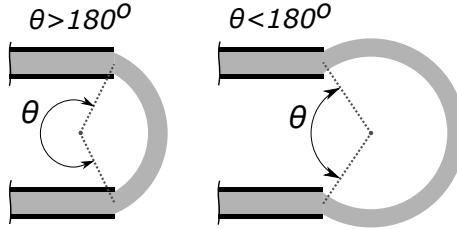

Figure 8.3: The assumption of a hinged connection in the enclosure.

lytical models are derived to predict the axial, rotation and shear stiffness. The goal of these models is to understand the characteristic behaviour and to provide a design tool for finding an initial set of design parameters. All models use a linear elastic material model and assume an out of plane width $b = 1(m)$. The fluid is assumed incompressible, requiring the initial volume V_0 to remain constant. Furthermore, the horizontal parts of the elastic cell are assumed rigid, due to the fact that they are clamped to a rigid connector.

8.1.2. AXIAL STIFFNESS

Axial stiffness can be modelled through some additional simplifications. The enclosures are assumed to maintain circular due to the internal pressure buildup. As this pressure buildup is also expected to be the main contributor to the axial stiffness, the bending stiffness from the enclosure is neglected and the enclosure is assumed to rotate free at its connections to the horizontal segments, as seen in figure 8.4.

8
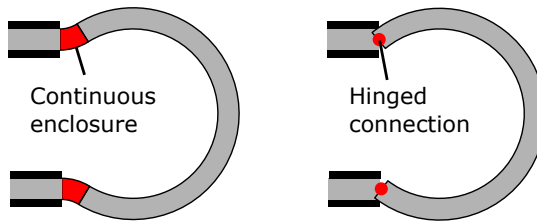
Figure 8.4: The assumption of a hinged connection in the enclosure.

The modelling approach itself consists of two parts. The first part is a geometrical description for the required deformation of the inner wall of the enclosure, as schematically seen in figure 8.5. A vertical displacement of the top causes fluid to move into the enclosures. The fluid in a single enclosure V_e after a compression dh is determined as:

$$V_e = (V_0 - bL_0(h_0 - dh))/2 \tag{8.1}$$

Figure 8.5: Geometric description of the inner wall of the enclosures both in undeformed (left) and deformed (right) configuration.

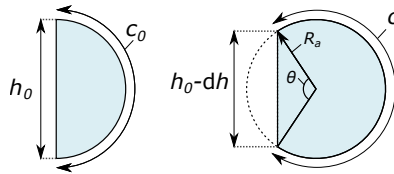where L_0 is the length of the horizontal segments, b the out of plane width as specified earlier and h_0 the initial height of the fluid, as seen in figure 8.2. The new geometry of the inner wall follows from two constraints. The first is the opening to the center volume of the joint, defined as:

$$h_0 - dh = 2R_a \sin(\theta/2) \tag{8.2}$$

where R_a is the radius and θ the opening angle of the inner wall as seen in figure 8.5. Secondly, the volume enclosed by the inner wall should comply with V_e from equation 8.1, defined as:

$$\pi R_a^2 - 0.5 R_a^2 (\theta - \sin(\theta)) = V_e \tag{8.3}$$

Together, equations 8.2 and 8.3 result in the geometry parameters R_a and θ for every compression dh, from which the required inner wall length c can be obtained by:

$$c = (2\pi - \theta)R_a \tag{8.4}$$

The second part of the model uses the derived deformation to determine the internal pressure increase and elastic force in the enclosure, leading to the axial stiffness of the joint. The steps described in this part are schematically depicted in 8.6. For this part,
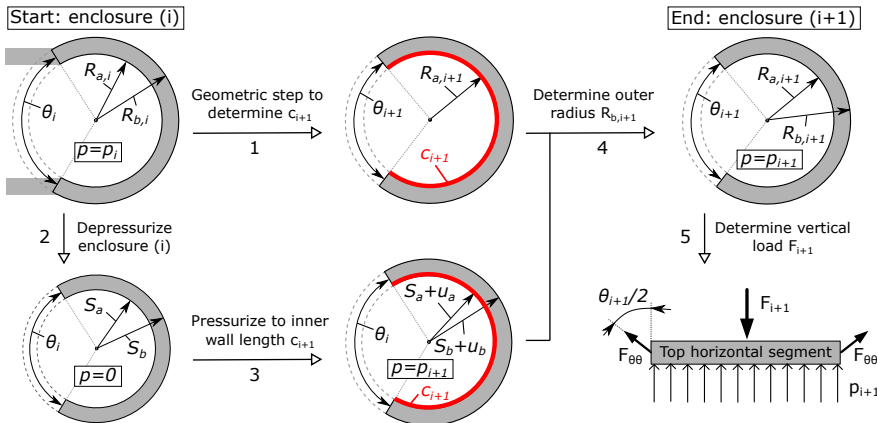

Figure 8.6: Flowchart for the calculation of a single inflation step in the enclosure and the corresponding compression force.

the enclosure is considered as a segment of a cylinder subjected to an internal pressure,

for which analytical models exist that describe its linear elastic expansion. As derived by [14], the radial displacement u of a material point at a center-distance r in a cylinder, subjected to an internal pressure p, can be described by:

$$u(S_A, S_B, p, r) = \frac{p(1+v)}{E(S_B^2 - S_A^2)}\left((1-2v)S_A^2 r + \frac{S_A^2 S_B^2}{r}\right) \tag{8.5}$$

where S_A and S_B are respectively the undeformed inner and outer radius of the cylinder, E the modulus of elasticity and v the Poisson's ratio. By neglecting bending stiffness, the stress distribution only depends on the geometry, which is unstressed as long as the pressure is zero. To implement equation 8.5, two additions to the model are required. Firstly, endpoints of the enclosure move inwards during inflation, due to the compression of the joint as seen in figure 8.4. To take this inward movement into account, the inflation of the enclosures is approached in multiple steps, where in each step equation 8.5 is applied to the updated geometry. The second addition to the model relates to the assumption of equation 8.5 that the initial internal pressure is zero. By using the step-wise approach for inflation, the initial pressure for subsequent steps is nonzero. Therefore, the geometry at the start of each step is projected back to a state of zero pressure before equation 8.5 is applied. This results in a sequence of computations for a single step. To determine the required compression force F_{i+1} for a compression dh_{i+1} of the joint, this sequence is as follows, as numbered in figure 8.6:

1. From the geometrical analysis, the updated inner radius $R_{a,i+1}$, angle θ_{i+1} and length of the inner wall c_{i+1} are determined based on the compression dh_{i+1}.

2. With the pressure p_i and both the inner and outer radius, $R_{a,i}$ & $R_{b,i}$, known from the previous step (i), equation 8.5 is applied twice to find the geometry of the enclosure from the previous step, with angle θ_i, for the case its internal pressure would be zero. This results in:

$$R_{a,i} = S_a + u(S_a, S_b, p_i, S_a) \tag{8.6}$$
$$R_{b,i} = S_b + u(S_a, S_b, p_i, S_b) \tag{8.7}$$

where both equations are solved simultaneously for S_a and S_b, respectively the inner and outer radius of the enclosure in the previous step under zero internal pressure.

3. For the depressurized enclosure from step 2, the required radial displacement u_a of the inner wall is determined that makes the length of the inner wall equal to c_{i+1}, by:

$$u_a = \frac{c_{i+1}}{2\pi - \theta_i} - S_a \tag{8.8}$$

Using equation 8.5, the required pressure p_{i+1} is then calculated to achieve this displacement u_a of the inner wall from the depressurized cylinder from step 2. Again using equation 8.5, the displacement u_b of the outer wall S_b is determined under the same pressure p_{i+1}.

4. From the displacements u_a and u_b, the enclosure thickness in the updated step $(i + 1)$ is determined and used to find the new outer radius $R_{b,i+1}$ by:

$$R_{b,i+1} = R_{a,i+1} + ((S_b + u_b) - (S_a + u_a)) \tag{8.9}$$

5. The pressure p_{i+1} is combined with the elastic force in the enclosure to determine the total vertical compression force. As derived by [14], the tangential stress distribution at position r in the enclosure is described by:

$$\sigma_{\theta\theta} = p \cdot \left(\frac{A^2}{B^2 - A^2} + \frac{A^2 B^2}{(B^2 - A^2) r^2} \right) \tag{8.10}$$

Integrating this equation over the enclosure in depressurized condition, defined by S_a and S_b, results in:

$$F_{\theta\theta,i+1} = \int_{S_a}^{S_b} \sigma_{\theta\theta} b \cdot dr = \frac{b}{S_b^2 - S_a^2} p_{i+1} (S_a S_b^2 - S_a^3) \tag{8.11}$$

Combined with the internal pressure on the top horizontal segment of the joint, the compression force F_{i+1} follows from:

$$F_{i+1} = p_{i+1} b L_0 + 2 F_{\theta\theta,i+1} \cos(\theta_{i+1}/2) \tag{8.12}$$

where the elastic force $F_{\theta\theta}$ is added as a tensile force on the top horizontal segment as seen in figure 8.6.

6. The axial secant stiffness K_y is then determined from:

$$K_y = \frac{F_{i+1}}{\mathrm{d}h_{i+1}} \tag{8.13}$$

8.1.3. ROTATION AND SHEAR STIFFNESS

For rotation or horizontal shearing motion of the upper rigid connector, no significant fluid flow from the center into the enclosures is expected. This prevents the buildup of internal pressure, making the rotation and shear stiffness depend only on the bending stiffness of the enclosures. To analyse this relatively large and non-linear motion, a pseudo-rigid-body (PRB) model [108] is used. The design model presented in this work is based on [217], which is based on modelling initially curved slender beams. A representation of the model can be seen in figure 8.7. Although [217] derived the model for a beam clamped on one side, the symmetry of the model is used to connect the links to both the upper and lower rigid connector by applying a fixed angle ζ_1 at both ends. With the angle of the enclosure known to be $\theta = \pi$ (rad), as derived previously, the parameters of the PRB model follow directly from [217] and are summarised in table 8.1.

To derive the rotation and shear stiffness, the principle of virtual work is applied to the motion of the upper rigid connector and torsion springs. Due to a similarity in derivation, only equations for the right enclosure are shown. This analysis requires the rotation of each torsion spring in terms of the position and orientation of the upper rigid
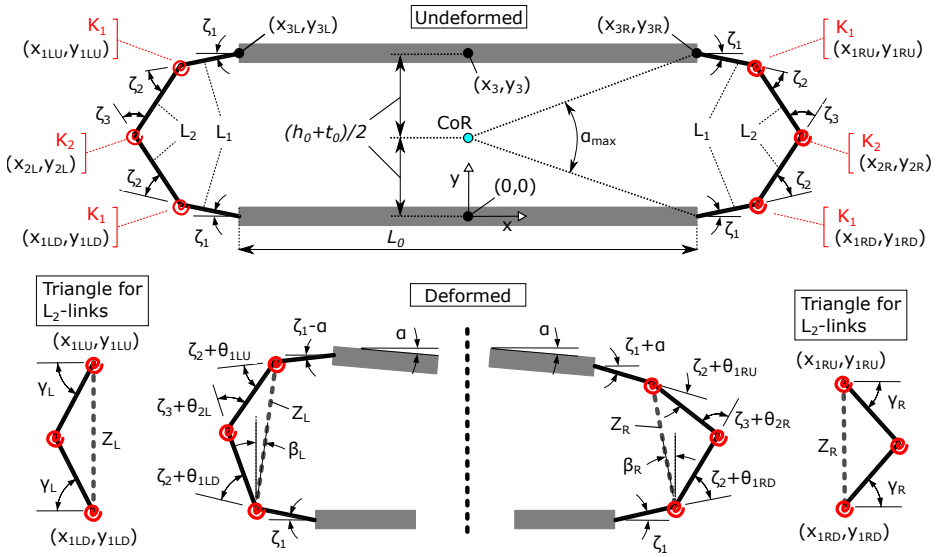
Figure 8.7: Model definition of the PRB model used to analyse both the rotation and shear stiffness.

connector, indicated by $[x_3, y_3, \alpha]$. For any joint configuration the positions $[x_{1QQ}, y_{1QQ}]$, with QQ specifying a specific torsion spring with stiffness K_1 as labelled in figure 8.7, are defined by:

$$x_{1RD} = \frac{1}{2} L_0 + L_1 \cos(\zeta_1) \tag{8.14}$$

$$y_{1RD} = L_1 \sin(\zeta_1) \tag{8.15}$$

$$x_{1RU} = x_3 + \frac{1}{2} L_0 \cos(\alpha) + L_1 \cos(\alpha + \zeta_1) \tag{8.16}$$

$$y_{1RU} = y_3 - \frac{1}{2} L_0 \sin(\alpha) - L_1 \sin(\alpha + \zeta_1) \tag{8.17}$$

Table 8.1: Parameters of the PRB model.

Parameter	Symbol	Value	Unit
Enclosure length	L_e	$\pi(h_0 + t_0)/2$	[m]
Moment of inertia	I	$bt_0^3/12$	[m^4]
Length 1	L_1	$0.1296 \cdot L_e$	[m]
Length 2	L_2	$0.3513 \cdot L_e$	[m]
Stiffness 1	K_1	$3.3546 \cdot EI/L_e$	[Nm]
Stiffness 2	K_2	$2.4764 \cdot EI/L_e$	[Nm]
Fixed angle 1	ζ_1	0.2008	[rad]
Initial angle 2	ζ_2	0.7854	[rad]
Initial angle 3	ζ_3	1.1692	[rad]

where L_0 is the previously mentioned length of the horizontal segments and L_1 and ζ_1 are respectively the length and angle of the links connected to the rigid connectors. With the coordinates of the top and bottom springs, the orientation of the middle links with length L_2 is determined using a triangle as seen in the bottom right of Figure 8.7. The distance Z_R between the top and bottom spring is determined by:

$$Z_R = \sqrt{(x_{1RD} - x_{1RU})^2 + (y_{1RD} - y_{1RU})^2} \tag{8.18}$$

The triangle orientation and relative angle of the middle links, indicated by β_R and γ_R in figure 8.7, are then given by:

$$\beta_R = \sin^{-1}\left(\frac{x_{1RD} - x_{1RU}}{Z_R}\right) \tag{8.19}$$

$$\gamma_R = \sin^{-1}\left(\frac{Z_R}{2L_2}\right) \tag{8.20}$$

The orientation of the middle links (L_2) can now be described both in terms of the triangle (β_R and γ_R) and the angles between the links (ζ_i and θ_i). Combining both options results in the rotation of the springs, described by:

$$\theta_{1RD} = \gamma_R + \beta_R - \zeta_1 - \zeta_2 \tag{8.21}$$

$$\theta_{1RU} = \gamma_R - \beta_R - \zeta_1 - \zeta_2 - \alpha \tag{8.22}$$

$$\theta_{2R} = -\theta_{1RD} - \theta_{1RU} - \alpha \tag{8.23}$$

For the rotation stiffness, the applied torque T is assumed to rotate the upper rigid connector around a COR in the middle of the fluid, as indicated in figure 8.8. For static equilibrium, the total virtual work W_t should be equal to zero, meaning:

$$W_{t,\text{rotation}} = T\delta\alpha - \sum_{i=1}^{6} K_i\theta_i\delta\theta_i = 0 \tag{8.24}$$

where i is the summation over all torsion springs and $\delta\alpha$ and $\delta\theta_i$ are respectively the virtual rotations of the upper rigid connector and the torsion springs. To evaluate torque T, all virtual rotations $\delta\theta_i$ need to be expressed in terms of $\delta\alpha$. With the COR not in the center of the connector, a virtual rotation $\delta\alpha$ also causes virtual displacements δx_3 and δy_3. This results in a description for $\delta\theta_i$ given by:

$$\delta\theta_i = \left[\frac{\partial\theta_i}{\partial x_3}\left(\frac{h_0 + t_0}{2}\cos\alpha\right) + \frac{\partial\theta_i}{\partial y_3}\left(\frac{h_0 + t_0}{-2}\sin\alpha\right) + \frac{\partial\theta_i}{\partial\alpha}\right]\delta\alpha \tag{8.25}$$

The secant rotation stiffness K_α is then determined by:

$$K_\alpha = \frac{T}{\alpha} = \frac{\left(\sum_{i=1}^{6} K_i\theta_i\delta\theta_i\right)/\delta\alpha}{\alpha} \tag{8.26}$$

For shear stiffness the same derivation is used, where a horizontal force F_x is assumed to translate the upper rigid connector in horizontal direction. Only equation 8.24 and equation 8.25 need to be changed for the shearing motion, resulting in:

$$W_{t,\text{shear}} = F_x\delta x_3 - \sum_{i=1}^{6} K_i\theta_i\delta\theta_i = 0 \tag{8.27}$$

where the virtual rotations $\delta\theta_i$ follow from:

$$\delta\theta_i = \frac{\partial\theta_i}{\partial x_3}\delta x_3 \tag{8.28}$$

The secant shear stiffness K_s is then determined by:

$$K_s = \frac{F_x}{x_3} = \frac{\left(\sum_{i=1}^{6} K_i\theta_i\delta\theta_i\right)/\delta x_3}{x_3} \tag{8.29}$$

8.2. FINITE ELEMENT MODEL AND VALIDATION

To verify the analytical stiffness models and investigate further performance behaviour, the pressure balanced joint is modeled in Comsol Multiphysics V5.5. The FEM model consists of a 2D geometry in which the horizontal segments are modeled as rigid domains, in accordance with the assumption of the analytical models. The bottom segment is given a fixed constraint while a prescribed displacement/rotation is imposed on the upper segment. The enclosures are modeled as a linear elastic material with $E = 1$(MPa) and $v − 0.49$(-). This simulates an incompressible silicon rubber, also used as reference material throughout the rest of this study. Fillets are added between the elastic enclosure and the rigid domains, with a radius $r = 0.20 \cdot t_0$ to limit stress peaks below a factor 2 compared to the stress in the enclosure [176]. To implement the internal pressure buildup, caused by the incompressibility of the fluid, a pressure p is added as boundary load on the inner boundary of the cell. The magnitude of p is defined in a global equation stating p is increased such that the inner volume V_{inner} equals the initial volume V_0, defined by:

$$\left(\frac{V_{\text{inner}}}{V_0} - 1\right) \cdot 10^5 = 0 \tag{8.30}$$

A constant 10^5, the order of number of elements, is added to increase the emphasis of this constraint in the overall system of equations and thereby ensure the constraint to be met when the model converges to a minimum relative error. The inner volume V_{inner} is evaluated using the divergence theorem on the inner boundary surface, as described in [87], by:

$$V_{inner} = -\int_A \frac{n_x \cdot x + n_y \cdot y}{2} dA \tag{8.31}$$

where x and y represent the position on the inner boundary and n_x and n_y the components of the inwards pointing normal vector $\vec{n}$ at that same position. After imposing a displacement, the solid mechanics module is used to determine the resulting deformations in the enclosure, with a physics controlled "extremely fine" mesh, a relative tolerance of $1 \cdot 10^{-6}$ and using nonlinear geometry and the fully coupled MUMPS solver. The resulting stiffness is obtained by evaluating the reaction force/torque from the upper rigid domain.

For a vertical compression, the upper rigid domain is prescribed a downward translation $u_{0y} = -\mathrm{d}h$. The horizontal translation (u_{0x}) and rotation (ϕ_0) are fixated as no movement is expected in these DOFs due to the symmetric load case. For rotation however, the exact COR is unknown. Therefore, the vertical and horizontal translations are

not prescribed, allowing the model to translate the upper rigid domain under an internal pressure increase to a state of equilibrium. Similarly for shear, the vertical translation is not prescribed although rotation is again constrained.

8.2.1. VALIDATION METHOD

The stiffness of the analytical models is compared to the FEM model for a range of design parameters. Two parameter ratios have been identified that influence the design: (L_0/h_0) and (t_0/h_0). To independently vary these ratios without scaling the design, a normalised height $h_0 = 1$(m) is used for validation. Although (L_0/h_0) significantly influences the stiffness, as confirmed in section 8.3.2, it does not alter the circular enclosure geometry, on which both analytical models are based. Therefore, different (L_0/h_0)-ratios are not considered. With the COR assumed in the center of the joint, the maximum rotation α_{max} before internal parts make contact, as indicated in figure 8.7, follows from:

$$\alpha_{max} = 2\tan^{-1}(h_0/L_0) \tag{8.32}$$

To analyse joint configurations able to reach state of the art ranges of motion [158], a maximum ratio $(L_0/h_0) = 4$ is allowed. Therefore, a range of $(L_0/h_0) = [2;4]$ is analysed in this work, of which the center $(L_0/h_0) = 3$ is used for validation. The (t_0/h_0) ratio is chosen as $(t_0/h_0) = [0.01;0.10]$ to account for thicknesses from a general plate ratio up to one order thicker enclosures. For axial stiffness, the compression is approached in $n = 25$ steps and a maximum compression ratio $C_{ratio} = 5\%$ is introduced, defined by:

$$C_{ratio} = \frac{dh}{h_0} = 0.05 \tag{8.33}$$

This maximum compression is chosen such that the strain of the enclosure, determined from the geometrical part of the axial model, remains below 10% as only a linear elastic material model is used [212]. Based on geometrical limitations of the PRB model, the rotation stiffness is evaluated up to 5° rotation and the shear stiffness up to a translation dx defined by a shear ratio S_{ratio} of 20%, given by:

$$S_{ratio} = \frac{dx}{h_0} = 0.20 \tag{8.34}$$

Figure 8.8 presents the comparison between the analytical and FEM model. Trend lines indicate the error of the analytical model relative to the FEM result. Different (t_0/h_0)-ratios are plotted to optimally present the encountered effects.

8.3. JOINT BEHAVIOUR AND IMPLEMENTATION

Both analytical and FEM models are used in this section to analyse the COR and characteristic stiffness behaviour and to introduce an optimization strategy. Additionally, a conversion model and some practical considerations are presented for 3D implementations.

8.3.1. CENTER OF ROTATION

Besides stiffness, the axis drift of the COR is an important characteristic of compliant joints [59, 204]. To determine the COR, several methods exist in literature [247] of which
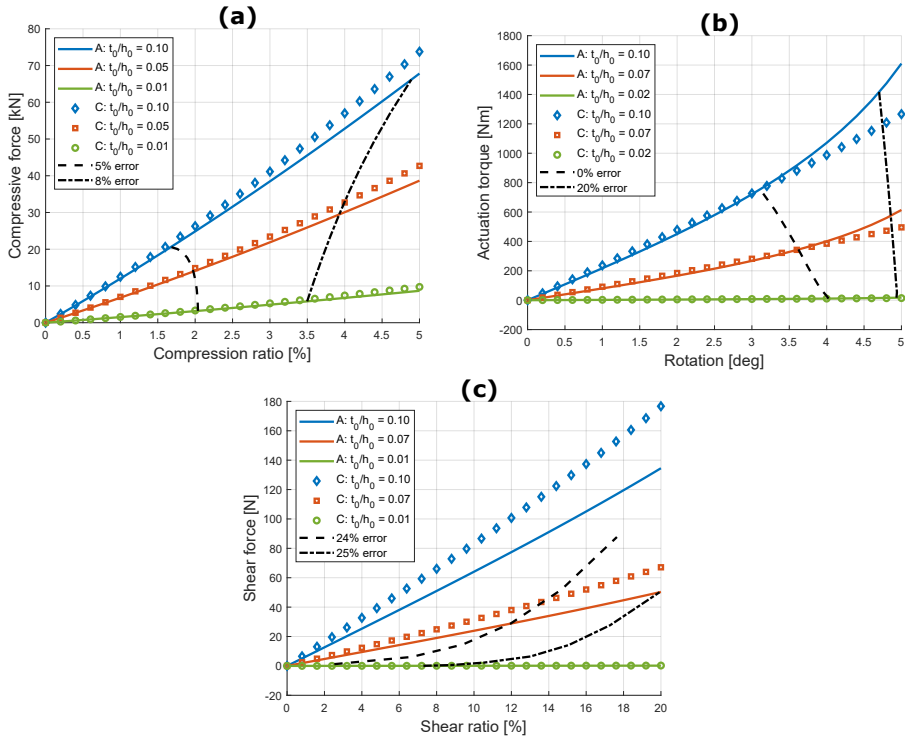
Figure 8.8: Comparison between the analytical models (A) and the Comsol model (C) for the (a) axial, (b) rotation and (c) shear stiffness, using $E = 1$(MPa), $v = 0.49$(-) and $h_0 = 1$(m). The error lines indicate the error of the analytical model relative to Comsol.

8

a construction of the instantaneous center is considered most accurate [247] and implemented in this work. To determine the COR, the displacements of two points on the upper rigid connector are tracked in the FEM model. For each displacement, a perpendicular bisector is constructed as seen in figure 8.9. The intersection point of both bisectors indicates the COR.

From simulations with multiple parameter combinations, only the (L_0/h_0)-ratio appeared to have a significant influence on the COR-movement. This is expected as the position of the upper rigid connector is related to the incompressibility constraint for a constant inner volume, and only the (L_0/h_0)-ratio influences the shape and magnitude of this volume. The COR starts for all parameters in the midpoint of the joint, as indicated in figure 8.7. When normalized to the length L_0, the drift of the COR for various (L_0/h_0)-ratios is relatively constant as seen in figure 8.10(a), showing a predominant translation to the right. To interpret the effect of this axis drift, the normalized displacement of the upper rigid connector, evaluated at its midpoint (x_3, y_3) as defined in figure 8.7, is shown in figure 8.10(b). As the COR appears to translate faster to the right, the rigid connector moves slightly upwards.
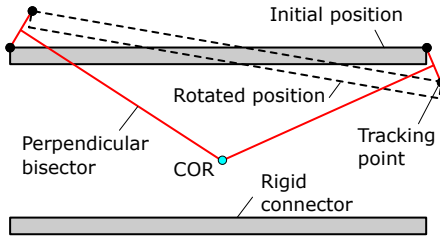
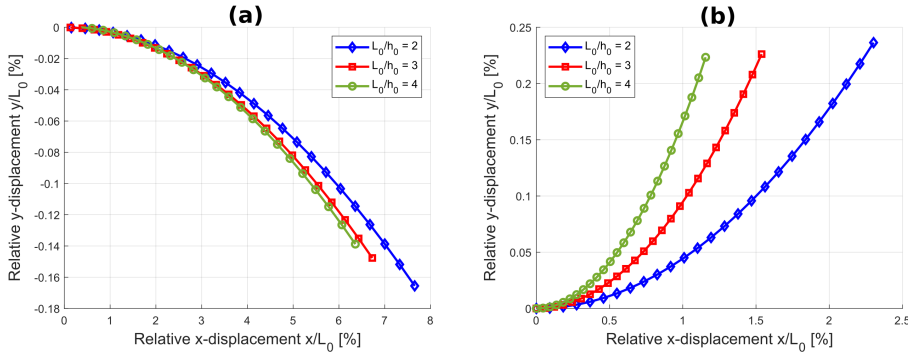Figure 8.9: Schematic construction of the instantaneous COR.

Figure 8.10: Normalized displacement of (a) the COR and (b) the midpoint (x_3, y_3) during a 5° anti-clockwise rotation, simulated for $(t_0/h_0) = 0.05$ and $h_0 = 1$(m).

8.3.2. PARAMETRIC ANALYSIS AND OPTIMIZATION

Using the analytical models, the influence of the design parameters on stiffness is analysed for the height $h_0 = 1$(m). In doing so, varying (L_0/h_0)-ratios are used that have not been verified in section 8.2. Therefore, a compression ratio $C_{ratio} = 1\%$ is used to minimize errors. For rotation stiffness, the analytical model showed most accurate around 3.5^o rotation for $(L_0/h_0) = 3$. As the vertical compression of the circular enclosure scales linearly with length L_0 for a given rotation, the optimum rotation α_{opt} used in the analytical stiffness model for other (L_0/h_0)-ratios is corrected by

$$\alpha_{\text{opt}} = 3.5^o \cdot \frac{3}{(L_0/h_0)} \tag{8.35}$$

With the focus on the use as axial stiff rotational joint, shear is not further considered in this work. If shear deformations cannot be allowed however, measures are needed as will be suggested in the discussion. The result of the stiffness analysis is seen in figure 8.11. The effect of the (t_0/h_0)-ratio on both stiffnesses corresponds with the assumption made in section 8.1.1 on the influence of t_0, making the axial and rotation stiffness scale with $(t_0/h_0)^1$ and $(t_0/h_0)^3$ respectively. With respect to the (L_0/h_0)-ratio, both stiffnesses scale quadratic. For a given compression, the fluid pushed sideways into the enclosures, and with it the pressure-buildup that is generated, increases with $L_0{}^1$. As the increased pressure acts on a larger surface area as well, related to $L_0{}^1$, the axial stiffness scales with $(L_0/h_0)^2$. For a given rotation, the vertical displacements at the edge of the rigid
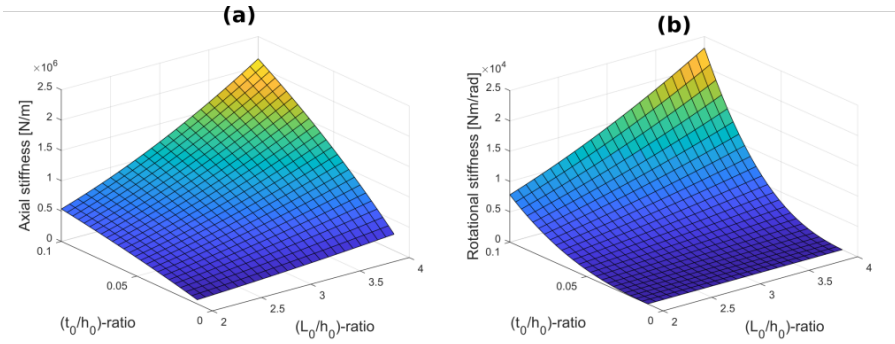
Figure 8.11: Parametric analysis on the (a) axial and (b) rotation stiffness for $h_0 = 1$(m).

connector increases with $L_0{}^1$, as does the resulting reaction force of the enclosure. With the moment-arm of this reaction force also related to $L_0{}^1$, the total rotation stiffness scales with $(L_0/h_0)^2$.

Additionally, the stiffness ratio K_{ratio} between the axial and rotation stiffness has been analysed, defined by:

$$K_{\text{ratio}} = \frac{K_y}{K_\alpha} \tag{8.36}$$

as suggested by [204]. This non-dimensionless ratio indicates the joints performance as an axially stiff rotational joint because the unconstrained rotational DOF should have a relatively low stiffness compared to the constrained axial DOF [247]. The result of this analysis is seen in figure 8.12(a). The (L_0/h_0)-ratio has no influence on the stiffness ra-
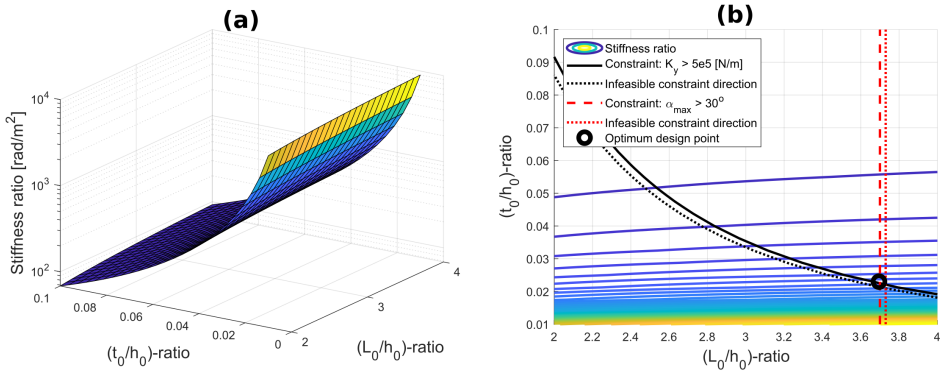
Figure 8.12: (a) Parametric analysis on the stiffness ratio for $h_0 = 1$(m) and (b) an example of an optimization strategy.

tio as both the axial and rotation stiffness scale with $(L_0/h_0)^2$. Although decreasing the thickness t_0 significantly improves the stiffness ratio, it also decreases the axial stiffness magnitude. To find the optimal design for a specific application, a basic strategy is introduced of which an example is seen in figure 8.12(b). Depending on the load case, a

minimum axial stiffness (e.g. $K_y > 5 \cdot 10^5 (\mathrm{N/m})$) can be defined as constraint. Additionally, equation 8.32 can be used to define the maximum (L_0/h_0)-ratio to reach a specified range of motion (e.g. $\alpha_{\max} > 30^o$). The intersection of both constraints then defines the optimum design point, as indicated in figure 8.12(b).

8.3.3. 2D to 3D Design Conversion

Although a 2D embodiment has been analysed for the characteristics of the new design principle, extruding the 2D geometry does not result in a feasible design as fluid will leak from the front and back. Therefore, potential embodiments for a 3D implementation are suggested in figure 8.13. It presents a rectangular design, functioning as single-DOF
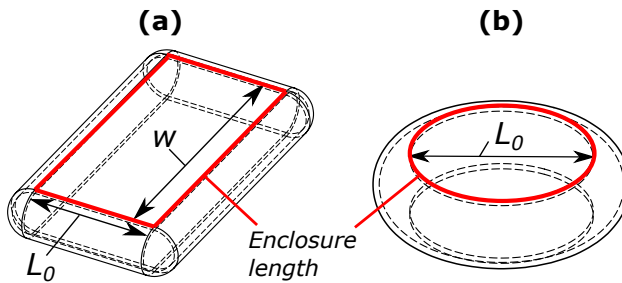

Figure 8.13: 3D embodiments of the pressure balanced joint as (a) a single-DOF rotational joint and (b) double-DOF universal joint.

hinge, and a circular design, functioning as double-DOF universal joint due to its axisymmetric topology. The double curvature in these embodiments indicates that a significant motion in the shearing direction is geometrically difficult to achieve. Therefore, only designs with rotational DOFs have been considered useful for implementation.

The step to a 3D design, however, will influence the stiffness properties. Taking the rectangular design as an example, the corners and added enclosure parts at the front and back are also compressed and stretched during rotation, which increases rotation stiffness. Due to a nonlinear behaviour and significant dependence on the shape of the 3D design, no correction factor for this effect is presented in this work. For axial stiffness, the added enclosure parts provide additional space for the fluid during compression. As this reduces the required inflation of the overall enclosure, the axial stiffness will decrease. This effect can be predicted through an analytical model independent of the 3D embodiment.

Predicting the 3D axial stiffness is based on the increase in enclosure length from the 2D to 3D design. This enclosure length is defined as the circumference of the rigid connector adjacent to an enclosure, as indicated in figure 8.13. With all segments of the enclosure in parallel, the axial stiffness is assumed to scale inversely proportional to the enclosure length. As shown with an example for both the rectangular and circular design, two steps define the stiffness prediction:

1. The out of plane width b in the 2D analytical model is scaled to equalize the top surface areas of the 2D and 3D design, as this results in an equal volume displace-

ment during compression. For the examples, this results in

$$b_{\text{rectangular}} = w \tag{8.37}$$

$$b_{\text{circular}} = \pi L_0 / 4 \tag{8.38}$$

where w is the width of the rectangular joint.

2. An axial stiffness correction factor $f_{\text{correction}}$, defined as

$$K_{y,\text{3D}} = f_{\text{correction}} \cdot K_{y,\text{2D}} \tag{8.39}$$

is then constructed using the ratio of enclosure lengths from the 2D (L_{2D}) and 3D (L_{3D}) design. Note that L_{2D} only consists of the two enclosure segments at the sides. For the examples, this results in

$$f_{\text{rectangular}} = \frac{L_{\text{2D}}}{L_{\text{3D}}} = \frac{2 b_{\text{rectangular}}}{2(w + L_0)} \tag{8.40}$$

$$f_{\text{circular}} = \frac{L_{\text{2D}}}{L_{\text{3D}}} = \frac{2 b_{\text{circular}}}{\pi L_0} = \frac{1}{2} \tag{8.41}$$

For a comparison, both designs have been implemented in a 3D Comsol model using the same approach as described in section 8.2. The only difference is the integral to evaluate the inner volume V_{inner}, in 3D defined by

$$V_{\text{inner,3D}} = -\int_A \frac{n_x \cdot x + n_y \cdot y + n_z \cdot z}{3} dA \tag{8.42}$$

Simultaneously, the analytical stiffness model and proposed correction factor are used to predict the axial stiffnesses. The design parameters used are $h_0 = 1$(m), $(L_0/h_0) = 3$, $(t_0/h_0) = 0.05$ and a width $w = 6$(m) for the rectangular shape. The results of this comparison, evaluated at a compression ratio $C_{\text{ratio}} = 1\%$, are given in table 8.2.

8.3.4. COMBINED LOADCASE

In the preceding sections, the axial and rotation stiffness have been analysed independently to identify the fundamental characteristics of the proposed design. However, a more common and realistic load case will be one where an axial load is present during rotation. The internal pressure, caused by the axial load, forces the enclosures into a circular shape. As this will negatively influence the bending stiffness of the enclosures, an increase in rotation stiffness is expected with increasing axial loads. It is therefore important to identify its effect on performance.

Table 8.2: Comparison between the predicted and simulated axial stiffness of the rectangular and circular 3D designs.

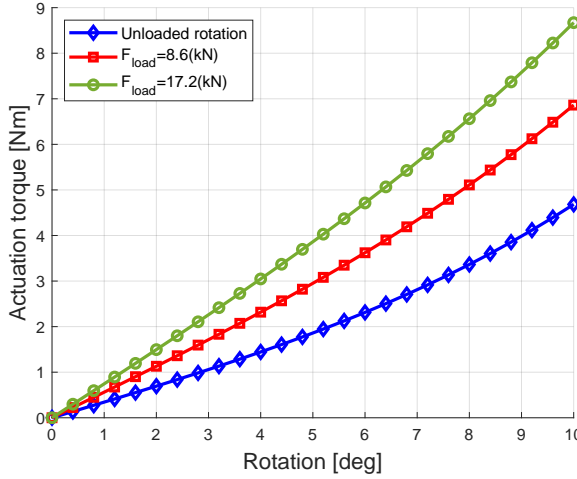| Joint type	Predicted K_y	Simulated K_y
Rectangular	$2.73 \cdot 10^6$ (N/m)	$2.74 \cdot 10^6$ (N/m)
Circular	$8.02 \cdot 10^5$ (N/m)	$8.61 \cdot 10^5$ (N/m)

Figure 8.14: Effect of varying axial loads on the rotation stiffness, simulated for $(L_0/h_0) = 3$, $(t_0/h_0) = 0.05$ and $h_0 = 1$(m).

Two types of simulations are compared for a rotation of the 3D circular design from section 8.3.3, using the same design parameters, of which the result is seen in figure 8.14. The first simulation rotates the upper rigid domain over 10° while it is free to translate, similar to the method described in section 8.2. For the second type, a constant vertical load F_{load} is applied on the upper rigid domain during rotation. A variable compression dz is prescribed to the upper rigid domain. Subsequently, this dz is defined in a global equation stating that the value of dz should increase such that the vertical reaction force F_z on the rigid domain equals F_{load} by:

$$\left(\frac{F_z}{F_{load}} - 1\right) = 0 \tag{8.43}$$

The axial loads used are 8.6(kN) and 17.2(kN), corresponding to a compression ratio of respectively 1% and 2%.

8.4. DISCUSSION

8.4.1. DESIGN MODEL
The design model presented in section 8.1, capable of estimating the initial axial and rotation stiffness within 10% error, shows to provide a design tool to find an initial parameter set for further optimization. However, there are a few limitations. Using a linear material model and PRB model limits the application of the design model to relative small deformations. Additionally the constraint for a constant inner volume can not be implemented in the PRB model, preventing analytical analyses of the COR. Thirdly, it is difficult to analyse embodiments with other angular segments (θ), as the parameters of the PRB model used only exist for specified flexure angles [217]. The embodiment proposed however, shows an additional characteristic advantage that compressive loads are

converted to a tensile load in the enclosure. As this removes the risk of buckling, it shows the potential for increased loading capability.

8.4.2. FEM MODEL AND VALIDATION

In section 8.2, FEM models of the pressure balanced joint were presented and used to validate the analytical models. Two notes apply to the method used. Firstly, for the validation and analyses a Young's Modulus $E = 1$(MPa) has been used as reference. As all stiffnesses scale linearly with the Young's Modulus however, this is not considered of influence on the results about the validity of the models or the performance of the proposed joint, except for the magnitude of the stiffnesses presented. Secondly, no experimental validation has been performed in this work. It is noted however, that an initial validation of a similar FEM model, using the same principal approach, has been performed in [87].

Comparing results in figure 8.8, a structural underestimation of the simulated axial stiffness is noted. This is caused by neglecting the bending stiffness of the enclosure and its connection points to the rigid connectors, as these these stiffnesses are in parallel with the inflation-stiffness. At smaller compressions, this effect is more significant for thicker enclosures, as expected. However, as seen in figure 8.8(a), at larger compressions the analytical model performs better for thicker enclosures. This is expected to be caused by an error in modelling the enclosure thickness (step 4 in figure 8.6), which is relatively more significant for thinner enclosures.

The rotation stiffness shows a decreasing underestimation before an increase is seen in the analytical stiffness. This underestimation is explained by the use of the PRB model. As the first links next to the horizontal segment are fixed under angle ζ_1, the required deformation is evenly distributed over all torsion springs. In the FEM model however, the enclosures maintain a more circular shape for a constant inner volume, resulting in a larger deformation closer to the rigid connectors which increases stiffness. At larger rotations, the PRB model approaches a singularity where the middle links start to align. This requires large rotations in the torsion springs, causing the increase in stiffness.

The analytical shear stiffness shows a structural underestimation as well. Similar to the rotation stiffness, the constraint on incompressibility causes larger deformations close to the rigid connectors in the FEM model, resulting in a larger stiffness. Additionally, it is noted from the figure 8.8 that the shear stiffness is relatively low compared to the axial stiffness. This is explained by the enclosures performing a rolling motion as result of the horizontal movement of the upper rigid connector, best compared to the motion seen in tape loops [216].

8.4.3. JOINT PERFORMANCE

The assumption of the central position of the COR has been verified in section 8.3.1. However, during rotation the COR moves predominantly sideways as seen in figure 8.10. This axis drift, relative to the joints dimensions, is significantly larger than in most conventional compliant joints [59]. The incompressibility constraint is responsible for the slight upwards motion of the rigid connector, to maintain an equal inner volume. Due to the relatively low shear stiffness however, additional loads during rotation are expected to dominate the horizontal translation and thus the COR. It is therefore recommended to

implement the pressure balanced joint in a parallel mechanism with elements improving the shear stiffness, like a set of internal cables for example.

The performance in terms of stiffnesses was presented in section 8.3.2. For this analysis, only secant stiffnesses have been used, which is assumed since figure 8.8 showed all stiffnesses to behave linearly. With respect to the stiffness ratio and optimization, two important remarks are made. Firstly, it is important to note that the stiffness ratio is not dimensionless and will improve for smaller designs. Secondly however, stresses and material failure have not been considered in this work, as only the characteristic stiffness behaviour is analysed. As stresses will increase for smaller designs subjected to the same loads, this will pose a limit on the minimal size and thus on the achievable stiffness ratio. Also with respect to the range of motion, it is recommended to analyse the material behaviour in these types of joints in future research.

8.4.4. CONVERSION TO 3D DESIGN

As described in section 8.3.3, the conversion from the 2D to a 3D design will negatively affect the axial and rotation stiffness. table 8.2 shows that the prediction method presented is able to estimate the 3D stiffness from the 2D model.The underestimation seen for the circular embodiment is likely caused by the circular shape, as the inflation requires the enclosure to expand both in the radial and circumferential direction. For the rectangular design, the straight segments only expand radially as in the 2D model. Although no prediction is yet available for the 3D rotation stiffness, it is noted that this stiffness is not required to set up the constraints needed for finding the design parameters of the optimal stiffness ratio, as described in section 8.3.2.

Another aspect for implementing this design, however, is the effect of combined load cases as presented in section 8.3.4. Figure 8.14 confirms that the rotation stiffness significantly increases when a compressive load is present during rotation. An additional explanation for this effect is a difference in deformation of the enclosure at opposite sides of the joint. On one side the rigid connector tips move apart resulting in an inward movement of the enclosure, while on the other side the tips move closer together resulting in an outward movement of the enclosure. As the internal pressure pushes equally on both enclosures, the shape difference causes an imbalance in the reaction forces, increasing the rotation stiffness. This effect should thus be taken into account when designing for a case with maximum rotation stiffness.

8.5. CONCLUSION

This work presents the characteristics of closed form pressure balancing, a design approach to improve axial performance in compliant rotational joints. By using an incompressible fluid, the axial and rotational stiffness become decoupled which prevents an axial stiffness decrease during rotation. Additionally, compressive forces are converted to tensile loads which prevents buckling and thus increases loading capability. Analytical and FEM models developed are capable to determine initial stiffnesses of a two-dimensional embodiment and provide a design tool to find optimum design parameters. With the proposed design, relative large ranges of motion can be achieved that only depend on joint length. Optimal joint performance in terms of stiffness is achieved

at smaller enclosure thicknesses, although a minimum axial stiffness should be maintained. The center of rotation, initially at the center of the joint, shows a horizontal drift up to 8% relative to the joints length during rotation. However, a relative low shear stiffness makes the COR susceptible to external loads, for which additional elements in parallel are recommended. Additionally, a conversion model is presented capable to predict the axial stiffness in three-dimensional designs from the two-dimensional model, showing a stiffness decrease up to 50% for circular embodiments. Finally, axial loads are shown to significantly increase the rotational stiffness, which needs to be taken into account in the design process.

8

III

IMPLEMENTATION

COMPLIANT PISTON-SLIPPER MECHANISMS FOR WOBBLE PLATE PISTON PUMPS

To motivate these conceptual principles, and show that the presented ideas and concepts can also be realized, more detailed design examples are required. This chapter presents an academic example which combines the principles of passive shape shifting and closed form pressure balancing into a scaled compliant bearing design. The principles are implemented in a piston-slipper mechanism designed for a scaled axial piston pump. The mechanism consists out of a universal joint based on the closed form pressure balancing principle, optimized for the specified design case.

Hydraulic systems are a key component in delivering effective supply power to various processes. One of the most common versions is the axial piston pump, which is used in an a spectrum of applications. This ranges from pitch control systems in wind turbines [35] to providing power in aircraft hydraulic systems [231]. They are also one of the most common components in various manufacturing processes [200], and come in various embodiements such as the wobble plate variant [98] or the swashplate variant [98, 128]. The wobble plate and its pressure profile, typical for piston pumps, can be seen in figure 9.1. Although various versions of these type of pumps exist, the general topology has not changed much during the years, and their functional components have not changed much.

The most common types of failure components within axial piston pumps are usually bearing elements that are loaded in partial or full contact. A common failure type is that caused by the lifting of the slipper [67]. This is inherent to the general ball joint design, which due to the predominantly mixed lubrication regime is still sensitive to some amount of wear. The back-and-forth reciprocating motion will drive the ball head to strike the socket [98, 200], causing deformation over its lifetime. This eventually causes relative motion between the surfaces, and thus wear. This wear further limits the lubrication performance of the ball joint. This type of failure potentially also damages the counter surface of the slipper as well as slipper retainer flanges. In wobble plate pumps, this effect is amplified through the relatively angle of the ball joints. Failure of these types of components is usually accompanied by tremendous costs created by downtime of the system [67]. It is therefore desired that these type of machine components function well, are well maintained and robust to different types of failure. A
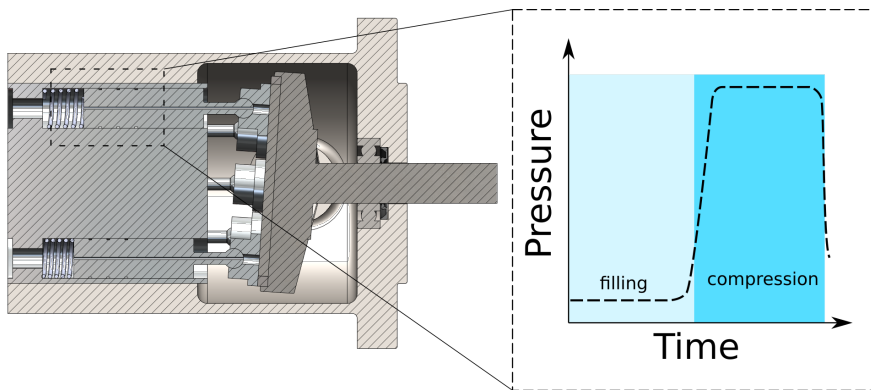

Figure 9.1: Typical embodiement of a wobble plate piston pump and its pressure characteristic, which is typical for piston pumps.

second aspect that has to be taken into account is the continuous search in engineering for sustainable machine design. Failure of machines is not only accompanied by downtime, but also the loss of hardware, which is not only cost but also eco-impact intensive. This can be seen for instance in conventional wind turbines, where downtime caused by gearbox failure heavily limits the effectiveness of this alternative energy source [36]. Again the most common type of failure here is caused by a system component failing

through some form of contact mechanics. The examples of failure shown above all have the element of contact mechanics in common. The question therefor arises if potential improvements in axial piston pumps could be made by the removal of this physical limitation. An alternative that is widely being investigated in other fields is the use of elasticity, or compliance. Instead of having contact-mechanics based joints, which also have the additional downsides such as stick-slip and hysteresis, compliant joints deform through the deformation of its elastic members [109]. For axial piston pumps, a different type of load case could be introduced for some of its system elements that could potentially create contact mechanics free alternatives. The main component of interest for this replacement is the ball-socket joint between the slipper and piston. This has a challenging load case which requires high support stiffness, while maintaining low rotational stiffness. The challenge for a compliant alternative is this previously mentioned ratio between support and rotation stiffness, in which compliant joints conventionally heavily underperform their contact-based counterparts [60]. Closed form pressure balancing, a compliant joint principle based on an enclosed fluid in an elastic body [87], has potentially a significantly improved stiffness ratio compared to other compliant joints. However, compliant mechanisms always have some form of coupling between rotation and support stiffness, which at higher load cases in the load cycle of piston pumps could cause the potential loss of full film lubrication. A significantly higher tilt stiffness of the bearing compared to the joint is thus desired. Increasing the tilt stiffness of conventional slipper designs used in axial piston pumps can be done through the use of additional pockets [185]. This however comes at the cost of increased volumetric losses, a characteristic highly undesired in hydraulic systems.

Also here, compliant mechanism implementation potentially provides alternatives to improve tilt stiffness at minimal cost of increased volumetric losses. By following the method of passive shape shifting as presented in chapter 6, compliant elements can be introduced into the slipper surface to obtain a different mechanism performance compared to its rigid alternative. This way both lower volumetric losses and higher tilt stiffness can be potentially obtained at different parts of the load case. The combined mechanism could therefor function as a fully contact-mechanics free alternative to the piston-slipper mechanisms used in the state of the art.

This paper presents the implementation and performance of a piston-slipper mechanism consisting of these two compliant alternatives: A compliant universal joint based on the principle of closed form pressure balancing, and a compliant slipper based on the principle of passive shape shifting. A case study is used to show the validity and potential of the new compliant piston-slipper mechanism alternative.

9.1. CONCEPT DESIGN

9.1.1. UNIVERSAL COMPLIANT JOINT

In a conventional piston-slipper mechanism such the one seen in figure 9.1, the spherical joint provides the degrees of freedom for the slipper to follow the motion of either the swash or wobble plate. In this work we focus solely on wobble plate based axial piston pumps. The angles typical for such a joint in a wobble plate piston pump can be quite significant, but do not require the axial rotation, making the joint effectively a universal

joint. The joint also transmits the compressive loads to the cylinder, for which a mini-
mum axial stiffness and load capacity are needed. This combination of requirements can
pose a challenge for using a compliant mechanism. The proposed design for the compli-
ant universal joint is based on the principle of closed form pressure balancing [87]. This
principle uses an incompressible fluid, encapsulated by an elastic body as seen in figure
9.2. As the fluid strongly resists any volume changes, high axial stiffness can be achieved
limited only by the elongation of the elastic body. Simultaneously, the liquid state allows
the molecules to freely reorganize for a change in shape, resulting in a low rotational
stiffness, only limited by bending of the elastic body. An axi-symmetric version of this
embodiment can be used to create a 2 degree of freedom rational joint. Although this
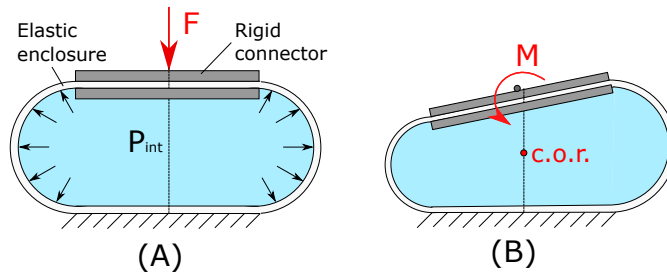

Figure 9.2: Schematic of a 2D closed form pressure balanced joint loaded in compression (A) and rotation (B).

topology satisfies the rotational compliance criteria, a limitation is the lack of shear stiff-
ness due to the rolling effect of the circular enclosure [191]. To remove this limitation,
a parallel combination with a set of wire flexures in the horizontal plane is proposed.
A set of three tension constraints is required to exactly constrain any horizontal trans-
lation. The horizontal setup of the wires is proposed as they maintain their stiffness in
horizontal direction during compression of the joint. The kinetostatic behaviour of this
combined mechanism is visualized using compliance ellipsoids [126]. Compliance el-
lipsoids visualize the linear rotation and translation compliance of a mechanism and
can be used for compliant mechanism concept design [163]. The individual mechanism
behaviour as well as its combined kinetostatic behaviour can be seen in figure 9.3. The
parallel mechanism thus behaves like a universal joint.

9.1.2. SHAPE SHIFTING SLIPPER
The second compliant implementation proposed in this work is the addition of a shape
shifting slipper. Since a compliant universal joint is used, there now exists a coupling
between its rotation and support stiffness. This will influence the full film lubrication
properties of the bearing when the tilt stiffness of the slipper is not significantly larger
than that of universal joint. A high tilt stiffness of the slipper with respect to the rotation
stiffness of the joint is therefore desired. The conventional topology used is a central re-
cess circular bearing pad, seen in figure 9.4B, directly fed by the cylinder its connected
to [128, 231]. The disadvantage of this configuration is that the slipper has to cope with
the dynamic pressure range seen in single pistons, and that this embodiment has a rel-
atively low tilt stiffness [185], which could prove problematic when combining it with
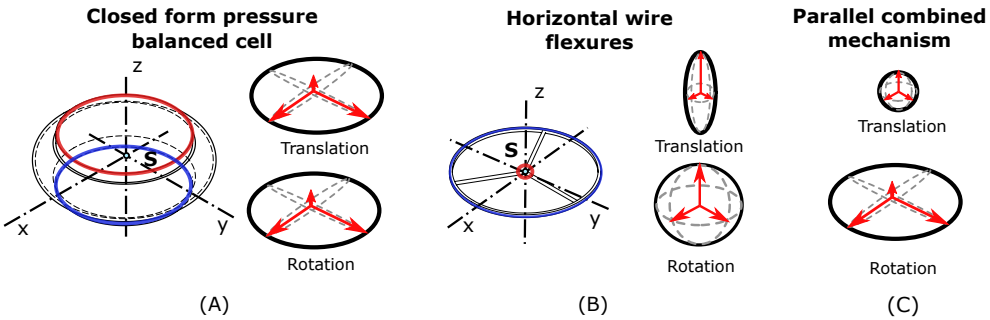
Figure 9.3: Compliance ellipsoids for the axi-symmetric topology of the closed form pressure balanced joint (A), the tension constraining wire-set (B) and a parallel combination of the two (C).

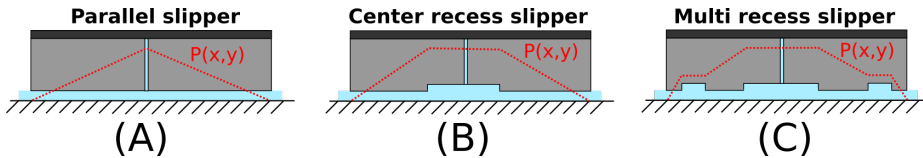the compliant universal joint. A different approach would be to feed the slippers with

Figure 9.4: Three conventional bearing topologies with (A) a parallel configuration, (B) a center recess configuration and (c) a multi-recess configuration. The pockets influence the pressure profile and therefor the bearings' load capacity and tilt-stiffness.

the constant pressure output from the pump, which is possible in a wobble plate piston pump since the pistons are stationary with respect to the plate. An additional advantage is that lubrication can still occur independent of any failures happening in any piston itself. During the filling stroke the pressure on the cylinder is low, as seen in figure 9.1, meaning the high available pressure source will result in higher then necessary film thickness and volumetric losses. A recessed bearing surface however, might still be required to obtain high enough load capacity or tilt stiffness at the compression stroke. In this case an improvement can be made through the implementation of passive shape shifting, presented in chapter 6. Passive shape shifting has been introduced as a bearing design approach for a variable operation range. In this case, the pump characteristics create a change in pressure and thus loads experienced by the slipper. This change in loads is significant and shows a stepwise variation between a low load in the filling stroke and a high load in the compression stroke. Using the principles presented in chapter 6, compliant elements are introduced into the slipper surface similar to that seen in self-adaptive bearings [64, 115], but now used to obtain two different bearing configurations for these load cases. The change in pressure and resulting load magnitude can be used to passively actuate the compliant pockets through the use of a compliant mechanism. The required displacement of these mechanisms is in the order of the film height and thus significantly smaller then the primary bearing dimensions [65]. In this work, shape shifting is utilized to obtain high load and tilt stiffness at high pressure, while simultaneously also exhibiting the desired low volumetric flow at low pressure. By adding multiple
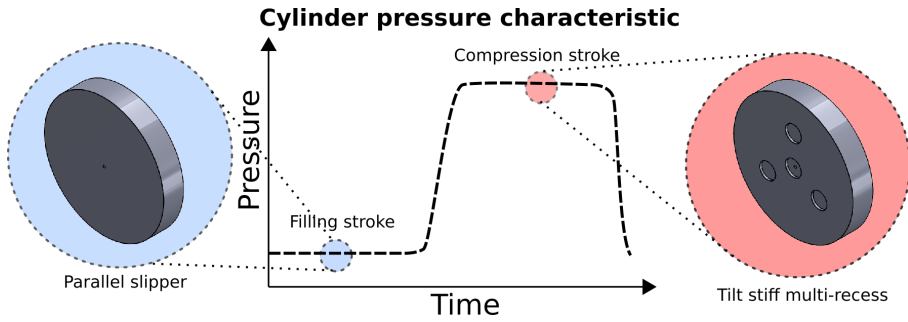
Figure 9.5: Visualization of pressure characteristic found in piston pumps. Because a pump almost has a step-like load case, it is proposed to switch between two different bearing geometries depending on this load case. In case of the filling stroke, a parallel topology will maintain low volumetric flow with a high pressure input source, while a multi-recess topology will guarantee a higher tilt stiffness and load capacity at higher loads.

compliant elements with a designed stiffness, a slipper can be obtained that functions as a parallel slipper at the lower loads, while functioning as a multi recess slipper at the higher loads. This switch can be seen in figure 9.5.

9.2. CASE STUDY

The potential of the proposed concept will be elaborated on through the use of a case study. This case study simulates a wobble plate with a single piston-slipper mechanism, seen in Figure 9.6. Here, the wobble plate defines angular rotations of the piston-slipper mechanism which, in a Cartesian system, can be defined as:

$$\alpha = A_{\mathrm{w}} \sin(\theta) \tag{9.1}$$

$$\beta = A_{\mathrm{w}} \cos(\theta) \tag{9.2}$$

Where A_{w} is the angle of the wobble plate with respect to the input axis. The input axis position can be defined by the angle θ [-]. The change in angles also affects the tangential shear loads present on the piston-slipper mechanism, which are of particular interest for designing the joint. Additionally, depending on the distance from the center of rotation of the universal joint to the wobble plate surface, the slipper 'drifts' over a certain area, which can be defined by:

$$B_{ly} = -H_b \tan(\beta) \tag{9.3}$$

$$B_{lx} = -H_b \tan(\alpha) \tag{9.4}$$

Where H_b is the distance from the center of rotation to the normal of the wobble plate. Besides the general kinematics of the mechanisms, there are several kinetostatic characteristics that define the general behaviour. The previously mentioned shear loads will be important for the design of the joint, and introduce the requirement of a sufficient shear stiffness. The magnitude of these loads depends on quasi-static equilibrium of the piston-slipper mechanism with respect to the slipper position on the wobble plate. Since this depends on the configuration of the mechanism, it relation needs to be defined. The
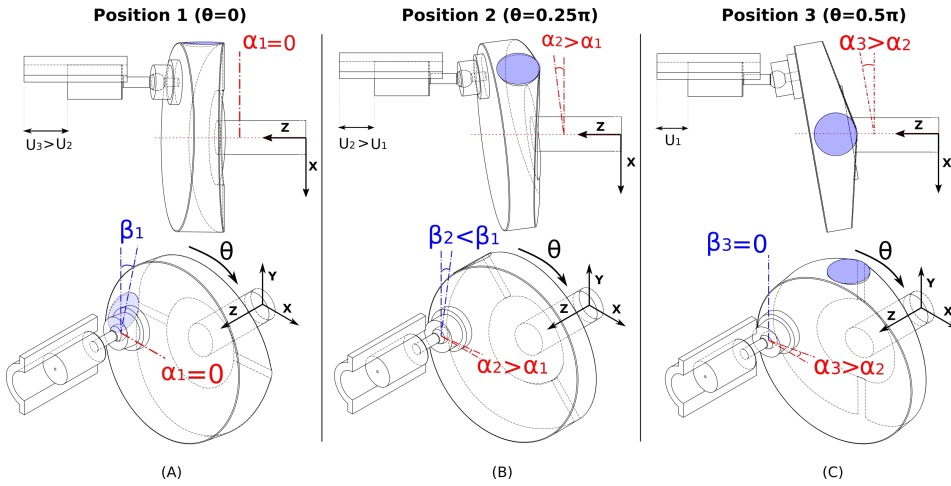
Figure 9.6: Half of the fill stroke depicted by three separate positions. All other positions occurring during operation are mirrored with respect to the presented positions.

piston-slipper mechanism system can be simplified as seen in Figure 9.7, where the constraint point C can be arbitrarily chosen along the piston for determining reaction forces. Since this system is decoupled, its reaction forces only depend on the bearing force F_b
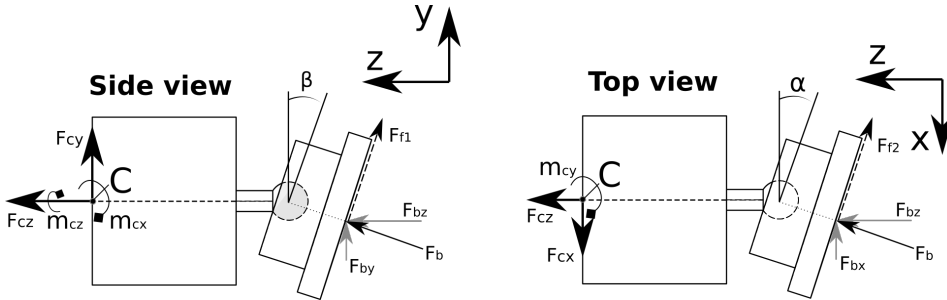
Figure 9.7: Load case of the basic piston-slipper mechanism topology used for this work.

and friction forces F_{f1}, F_{f2}. Secondly, since the cylinder applies a pressure on the cylinder in the z-direction, the model is based on knowing the force component F_{cz}. The shear forces F_{cy} and f_{cx} can be defined through the following relations:

$$F_{cx} = -F_{bz} \tan(\alpha) - F_{bz} \frac{\mu}{\cos(\beta)} V_x \tag{9.5}$$

$$F_{cy} = -F_{bz} \tan(\beta) - F_{bz} \frac{\mu}{\cos(\alpha)} V_y \tag{9.6}$$

Where μ is the friction coefficient [-], f_{bz} the z-direction bearing force component and $V_{x,y}$ the normalized velocity factor. The z-direction bearing force component is dependent on the cylinder force F_{cz} and friction force correction component, and can be de-

fined as:

$$F_{bz} = F_{cz}\left(1 + \frac{V_y \mu \tan(\beta)}{\cos(\alpha)} + \frac{V_x \mu \tan(\alpha)}{\cos(\beta)}\right)^{-1} \tag{9.7}$$

The velocity factor is required to determine the fraction of friction forces, since friction forces occur in the direction of motion. Since the bearing will drift over the wobble plate given a fixed distance between the wobble plate and the center of rotation, this will contribute to the relative velocity direction. These factors can be determined in the wobble plate frame, where the velocity components in the local x and y direction are defined as:

$$V_{wx} \quad = \quad \frac{dB_x(t)}{dt} \tag{9.8}$$

$$V_{wy} \quad = \quad \frac{dB_y(t)}{dt} + 2\pi r_b f_p \tag{9.9}$$

which is time dependent through the relation $\theta(t) = 2\pi f_p t$, with f_p being the rotation frequency of the pump. The resulting velocity factors are then determined by the following relation:

$$V_k = \frac{V_{wk}}{\sqrt{(V_{wx}^2 + V_{wy}^2)}} \tag{9.10}$$

Where k is equal to either x or y and V_{wk} is equal to either to V_{wx} or V_{wy} depending on which velocity factor is to be calculated. Finally, To fully identify all aspects of the case study, the serial stacking effects of the slipper and universal joint are described. To guarantee that the slipper remains in full film lubrication during the motion created by the wobble plate, the resulting rotation of the slipper should be small enough that it results in displacements smaller then the minimum allowable film height. The angular displacements of the system can be defined as:

$$\kappa = \frac{M_\kappa}{K_{RS}} + \frac{M_\kappa}{K_{RJ}} = \frac{M_\kappa}{\delta \cdot K_{RJ}} + \frac{M_\kappa}{K_{RJ}} \tag{9.11}$$

Here M_κ is the moment required to obtain the displacement controlled angles defined by κ, where κ is either $\alpha(\theta)$ or $\beta(\delta)$ and K_{RS} and K_{RJ} are the rotational stiffness of the slipper and joint respectively. Since these moments are equal for both components given the angular direction, it is the tilt stiffness relation of the joint and slipper expressed as parameter δ that defines the measure of slipper tilt. Therefor the following linearized design constraints can be defined, that define the allowable minimum tilt stiffness ratio:

$$h_{min} - \frac{\sin(\kappa)D_{slipper}}{2\delta} < h_c \tag{9.12}$$

Here h_{min} is the minimum present film thickness in the slipper film, $D_{slipper}$ the slipper diameter and h_c the film height constraint. For the presented design case this relation between the universal joint and slipper also extends to the rotational stiffness, defined as:

$$K_{RJ} = \frac{K_{RS}}{\delta} \tag{9.13}$$

Taking these principle kinematic and kinetostatic characteristics into account, several design statements can be made:

- All rotations need to be followed by the universal joint, defined by the position of the wobble plate θ and its angular orientation A_w.

- The distance from the wobble plate/slipper contact surface H_b to the joint center of rotation determines the slipper drift over the wobble plate.

- The joint will always undergo a changing shear load due to the orientation of the wobble plate A_w. The presence of sliding friction will influence this shear load.

- The ratio of joint rotation K_{RJ} to slipper rotation stiffness K_{RS} should be high in order to maintain a minimum acceptable film height defined by h_c.

9.3. Detail design

General parameters for this case study are defined in 9.1. The load ratio used in this

Table 9.1: Primary parameters used as load case in this work.

Parameter	symbol	value	unit
Compression load	F_c	65	[N]
Fill load	F_f	5	[N]
load ratio	ΔF	13	[−]
External pressure source	P_s	0.7E5	[Pa]
Wobble plate angle	A_w	10	[°]
Bearing diameter	D_S	70	[mm]
bearing x-position (w.r.t center wobble plate)	x_m	70	[mm]
bearing y-position (w.r.t center wobble plate)	y_m	0	[mm]
Pump rotation frequency	f_p	0.25	[Hz]
Stiffness coupling ratio	δ	100	[-]
Minimum allowable film thickness	h_c	10	[μm]

case study simulates a pump with a mechanical efficiency 92.3 %. Because the slipper and universal joint are stacked on top of each other, there is an effective serial coupling between the two machine components. This means that the performance of one will influence the other. In this work the design process is to first develop the slipper based on the general dimension constraints and case study parameters. The slipper performance, in combination with the case load and initial dimension set for the joint will determine the shear loads on the slipper. The slipper rotational stiffness, in combination with the shear loads and general dimension constraints will then determine the dimensions of the universal joint. This design process is depicted in detail in figure 9.8. In the flowchart several design statements are introduced that determine if the next step in the design process can be made. These steps will be further motivated throughout the following sections.

Detail design process
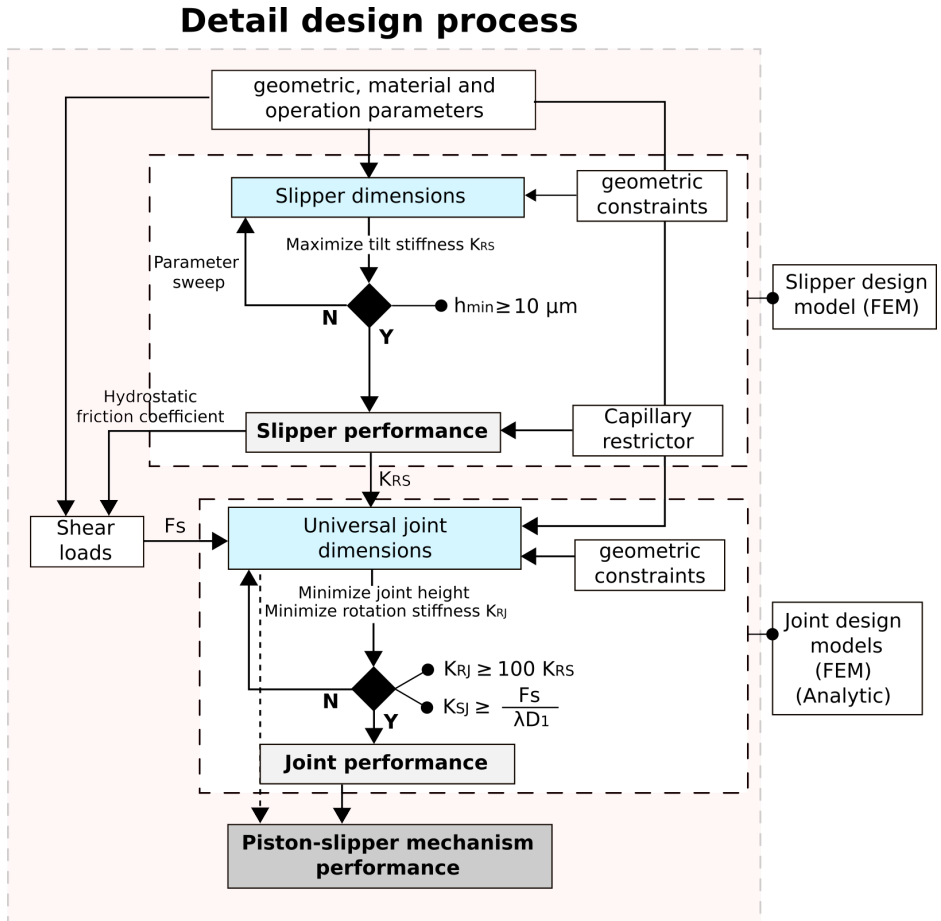

Figure 9.8: Design process of the piston slipper-mechanism depicted as a flow chart. The model consists of 2 main finite element method (FEM) models, which are both 3D models for the slipper and joint respectively. The the design process has 2 iteration processes in determining the dimensions and subsequent performance of the slipper and joint, but is sequential in its overall process.

9.3.1. Shape shifting slipper

Based on the design case, the slipper should:

- Function as a parallel bearing at the fill load of $F_f = 5$ [N] to obtain a low volumetric flow Q_{tot}

- Function as a multi-recess bearing at the compression load of $F_c = 65$ [N] to obtain the required load capacity and tilt stiffness K_{RS}.

To obtain a multi-recess geometry with high load capacity and tilt stiffness, a 5 pocket bearing is used. The central pocket is needed to increase the load carrying capacity, whereas the addition of radially spaced pockets significantly increase tilt stiffness. The radial placed pockets will be placed symmetrically, which is desired from the symmetric design case. A parallel combination of a compliant membrane functioning as a straight guide and seal, and a cantilever to provide the additional stiffness are used as the shape shifting elements. The general embodiment of the slipper can been seen in Figure 9.9. The slipper is modelled using Comsol Multiphysics V5.5. This model consists of a mem-
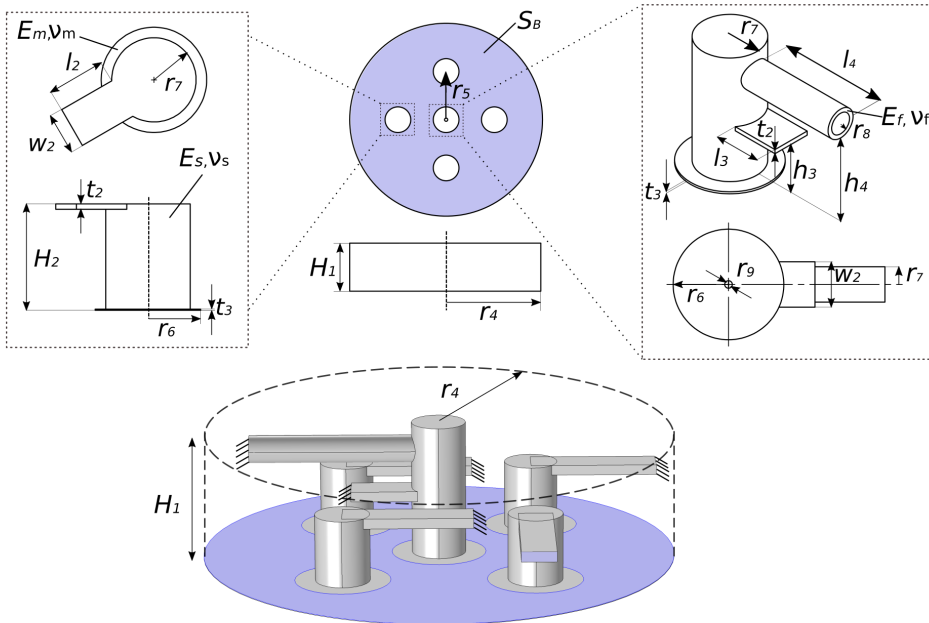
Figure 9.9: Geometry of the shape shifting slipper used in this work as well as the parameter set defining this topology. The coloured surfaces are constrained in the comsol model.

brane layer and a 3D embodiment of the cantilevers, supply feed and connection pylons. The membrane layer is divided into the parts that function as the rigid and plexible part of the bearing surface, together defining the full bearing surface. The solid mechanics module is used in Comsol Multiphysics to determine deformations. The geometry is

constrained at surface S_b as well as at the end of all cantilevers and the feedline tube, as seen in figure 9.9. The thin film is modeled using the general form boundary PDE module, defined on the bottom boundary of the membrane. Here, the Reynolds equation for a surface is defined as:

$$\frac{d}{dx}\left(-\frac{h_l^3}{12\eta}\frac{dP}{dx}\right) + \frac{d}{dy}\left(-\frac{h_l^3}{12\eta}\frac{dP}{dy}\right) = 0 \tag{9.14}$$

Where η is the viscosity of the lubricant and h_l the film height. The pressure profile is thus defined by the film height in this model. Figure 9.10 shows how the film height is defined over this boundary. The deformation of the pylons which are connected to the cantilevers is taking into account in the film height through its z-direction deformation component $w(x, Y)$. The film height at these membrane regions can thus be defined as:
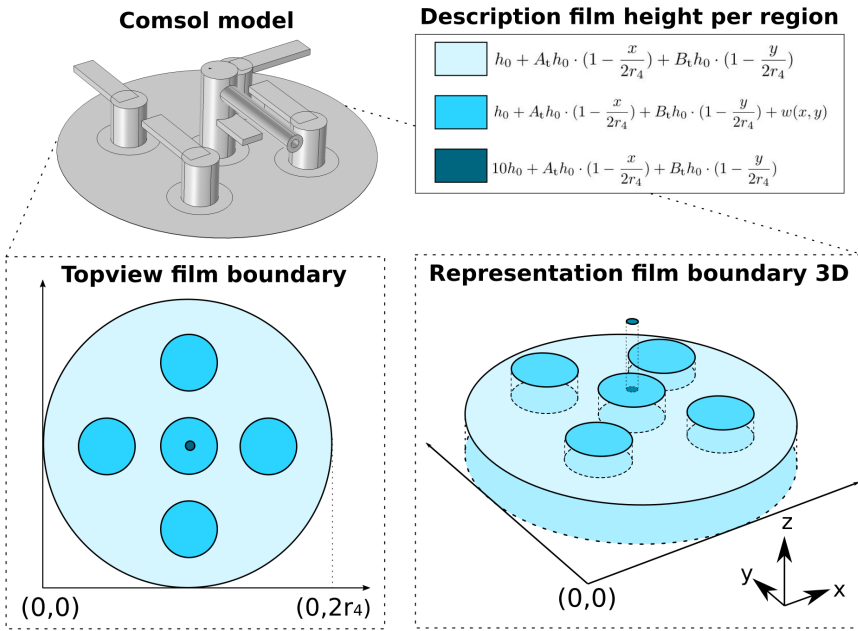
Figure 9.10: Description of the film height on the bottom boundary of the FEM model. Depending on the presence of the compliant elements, deformation $w(x, y)$ is taken into account or neglected.

$$h_l = h_0 + A_t h_0 \cdot (1 - \frac{x}{2r_4}) + B_t h_0 \cdot (1 - \frac{y}{2r_4}) + w(x, y) \tag{9.15}$$

Where A_t [-] and B_t [-] are tilt parameters used to define a rotated film in the x and y direction respectively. h_0 equals the minimum film height and r_4 is equal to the slipper radius, used to scale the tilting component. This deformation component is neglected at the rigid regions of the surface as well at the input channel. The film height at the input channel is modelled as being 10 times the minimum film height to guarantee the

input pressure remains uniform. Both these adaptations on the film height description of equation 9.15 can be seen in figure 9.10. The model makes use of a capillary restrictor to provide the bearing with stiffness, defined as:

$$Q_r = \frac{\pi r_{\mathrm{r}}^4}{128\eta} \frac{(P_{\mathrm{s}} - P_{\mathrm{r}})}{l_{\mathrm{r}}} \tag{9.16}$$

Where r_{r} is the restrictor radius and l_{r} the restrictor length. Tilt stiffness can be determined by solving two additional moment equilibria, around the x and y-axis respectively:

$$x_{\mathrm{T}} \int_A P(x, y) \mathrm{d}A = \int_A (P(x, y) \cdot x) \mathrm{d}A \tag{9.17}$$

$$y_{\mathrm{T}} \int_A P(x, y) \mathrm{d}A = \int_A (P(x, y) \cdot y) \mathrm{d}A + M_{\mathrm{ext}} \tag{9.18}$$

With M_{ext} an externally applied moment, and $x_{\mathrm{T}}, y_{\mathrm{T}}$ the position of the pivot point. By applying an external moment the resultant angle can be determined, meaning the tilt stiffness in N·m/rad can be acquired. To determine the desired dimensions of the bearing, a parameter sweep was performed. Certain parameters were chosen based on demonstrator production limitations. The leaf spring width w_2 and mechanism cylinder radius r_7 were also pre-defined since this was beneficial to limit design space, and other parameters could be adjusted to obtain stiffness change. The final dimensions of the bearing were determined through a parameter search of the pocket position r_5, thickness t_2 and membrane radius r_6. In the comsol model this membrane radius was decomposed into its x and y-components and modelled as $r_6 = \sqrt{\xi_1^2 + \xi_2^2}$, where ξ_1 and ξ_2 are the x- and y position respectively. The investigated range was equal to the $12 \geq \xi_1 \geq 18$, where $\xi_1 = \xi_2$ and the stepsize is equal to 1 [mm], $6.5 \geq r_6 \geq 8$ with a stepsize of 0.5 [mm], $1.2 \geq t_2 \geq 1.8$ with a stepsize of 0.1 [mm]. The search criteria for defining the parameter set were based on finding the highest tilt stiffness K_{RS}, while adhering to a minimum film height $h_{min} = 10$ [μm]. Table 9.2 shows resulting parameter values for this parameter sweep study. The proposed parameter set resulted in a minimum rotational stiffness $K_{RS} = 194.4$ Nm/rad and a minimum film thickness $h = 72.8$ μm.

SHAPE-SHIFTING SLIPPER PERFORMANCE

To show how shape shifting affects the performance, a comparison is provided between the shape shifting slipper and its equivalent rigid parallel bearing and multi-recess bearing. These rigid bearings are expected to outperform the shape shifting variant in different parts of the operation range. The dimensions of the rigid bearings are equal to their counterparts in the shape shifting version. This means the multi recess bearing will have all recesses equal to those of the shape shifting bearing. however, the depth of the features for the multi recess bearings are such that at low operational load the depth is equal to 4 times the minimum film height in accordance to [210]. The restrictor radius r_r used for all bearings topologies, making sure that the film height is equal at the low operational load, are equal to 0.5 [mm], 0.499 [mm] and 0.545 [mm] for the shape-shift, parallel and multi recess bearings. The load case is given through a combination of the bearing dimensions and external pressure and loads given in table 9.1. The

Table 9.2: Final parameter values for the shape shifting slipper used in this work.

Parameter	symbol	value	unit
Slipper Youngs modulus	E_s	1.2	[GPa]
Slipper poisson ratio	v_s	0.4	[-]
Slipper radius	r_4	35	[mm]
Slipper height	H_1	25	[mm]
Pocket position	r_5	19.8	[mm]
leaf spring length	l_2	15	[mm]
center leaf spring length	l_2	9	[mm]
leaf spring width	w_2	5	[mm]
leaf spring thickness	t_2	1.5	[mm]
Membrane radius	r_6	7	[mm]
Membrane thickness	t_3	100	[μm]
Membrane Youngs modulus	E_m	0.95	[GPa]
Membrane Youngs modulus	v_m	0.4	[-]
Membrane ratio	v_3	0.4	[-]
mechanism height	h_2	10	[mm]
Feedline length	l_4	28	[mm]
Feedline radius	r_8	2	[mm]
Feedline Youngs modulus	E_f	0.1	[GPa]
Feedline poisson ratio	v_f	0.4	[-]

performance, as expressed before, is defined by the volumetric flow and minimum film height. The comparison for this load case between all bearings can be seen in Figure 9.11. This shows the ability of the shape shift bearing to switch from behaviour similar to that of the parallel topology, to that of the multi-recess bearing. This can also be seen when comparing the tilt stiffness of the multi-recess bearing with that of the shape shifting concept. For the high end of the load case, the multi-recess bearing has a tilt stiffness $K_{RS} = 174.7$ Nm/rad with a minimum film height $h_{min} = 82.3$ μm, which means a lower tilt stiffness but at a higher minimum film height then the shape shifting concept. Finally the effect of slipper friction with respect to the shear load on the joint can be determined. Since a plastic-to-plastic archetype material combination will be used in this case study, the dynamic sliding friction is assumed to be equal to $\mu_d = 0.2$ [-]. The presented numerical model can also be used to determine the friction coefficient of the hydrostatic slipper during an average linear velocity of $U_b = 0.1$ [m/s], based on bearing position and pump frequency. This resulted in a friction coefficient of $\mu_{hl} = 7E-5$ [-] and $\mu_{hh} = 19E-5$ [-] for the high and low load case components respectively. Taking the respective friction coefficients into account resulted in the reaction shear forces seen in figure 9.12. The maximum occurring sliding shear force is equal to 24.5 N, which drops to 11.5 N in the hydrostatic shear force case. The drop in maximum shear load is one of benefits for implementing a hydrostatic bearing compared to sliding friction alternatives.
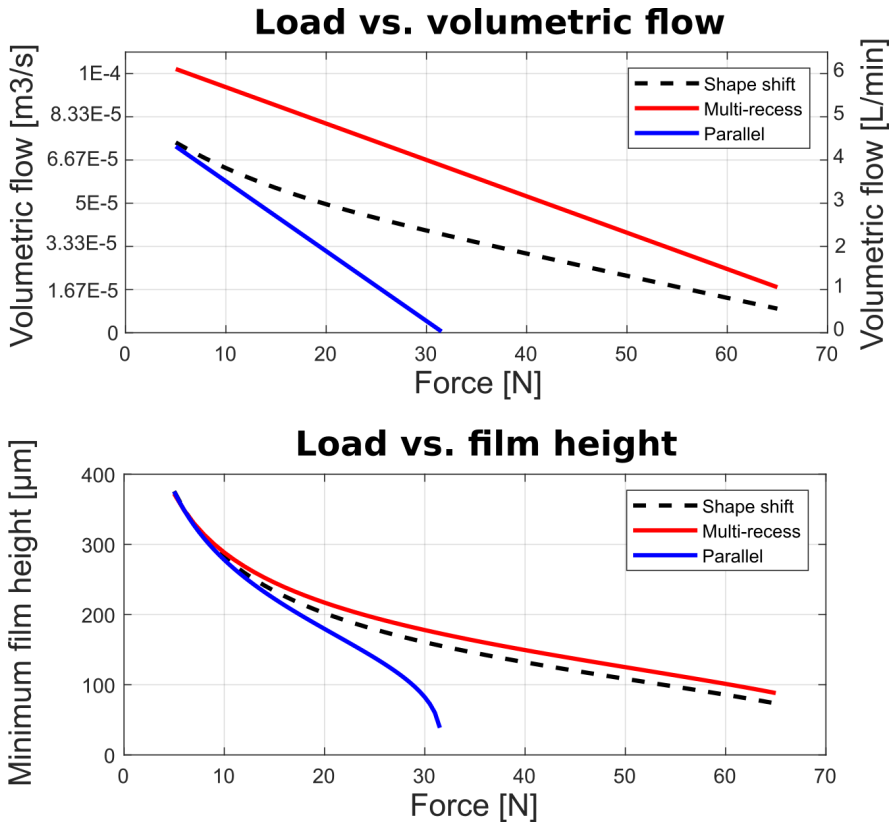
Figure 9.11: The performance of the shape shifting slipper in comparison to its rigid parallel and multi-recess counterparts. The performance is expressed through the volumetric flow vs. load and minimum film height vs. load. The key shape shifting characteristic is clearly visible in the volumetric flow comparison, where the trendline modes from the parallel comparison to its multi-recess counterpart.

9.3.2. UNIVERSAL COMPLIANT JOINT

For the detail design steps of the universal joints, two main objectives have been taken into account. First, a low total height of the joint is desired. Since the center of rotation is located a distance H_b from the central point of the slipper the wobble plate, it causes an axial displacement of the center of rotation when the slipper follows the wobble plate, reducing the cylinder compression stroke. More important however, is that the distance H_b causes the slipper to drift over the wobble plate during rotation of the joint. Therefore, minimizing the total joint height reduces the required movement space for the slipper. The second objective is to obtain rotational stiffness K_{RJ} below a factor $\delta = 100$ lower than the rotational stiffness K_{RS} of the slipper for its initial parameter set. Since the joint will be always loaded in compression during rotation, and this effects the rotational stiffness [191], its rotational stiffness is based on the combined compression and rotation case. In accordance with statements defined in previous sections, the compliant universal joint should adhere to the following design requirements:
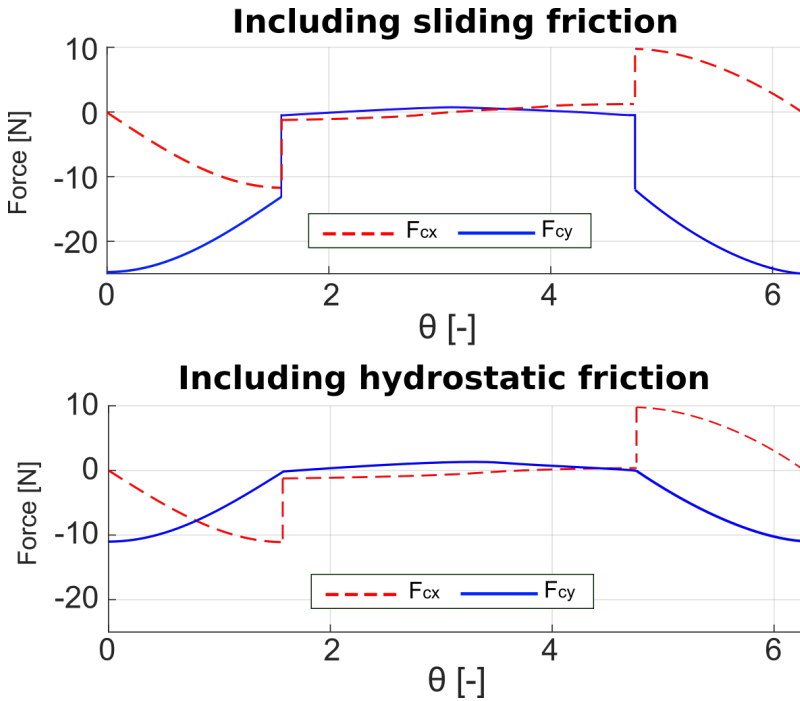
Figure 9.12: One load cycle expressed through the approximated shear loads that are design considerations for the universal joint. The reduction in maximum occuring load is due to the minimizing effect of switching from sliding friction to hydrostatic friction.

- The joint should allow 10° range of motion in any tip-tilt direction at the maximum compression load $F_c = 65$ [N].

- The joint should limit shear movement below $\lambda = 1\%$ of the slipper diameter at a maximum shear force $F_s = 25$ [N] to minimize drift of the slipper over the wobble plate surface.

- A minimum wall thickness of 1.5 [mm] is set for manufacturing of the prototype.

The maximum shear force is based on the modelled shear loads of figure 9.12. In determining the design parameters, the design of the elastic cell is decoupled from the internal wire design. This is done because the elastic body is assumed to have a negligible contribution to the shear stiffness while the wires are assumed to have a negligible contribution on the axial and rotational stiffness. This assumption that planar wire flexures have no initial out-of-plane stiffness. However, it is assumed that the wires geometrically constrain the center of rotation on the vertical symmetric axis of the elastic body. The general embodiment for the universal joint with the design parameters is seen in figure 9.13.

For the design of the pressure balanced cell, the effect of the maximum compression load $F_c = 65N$ on the range of motion needs to be taken into account. Due to the com-
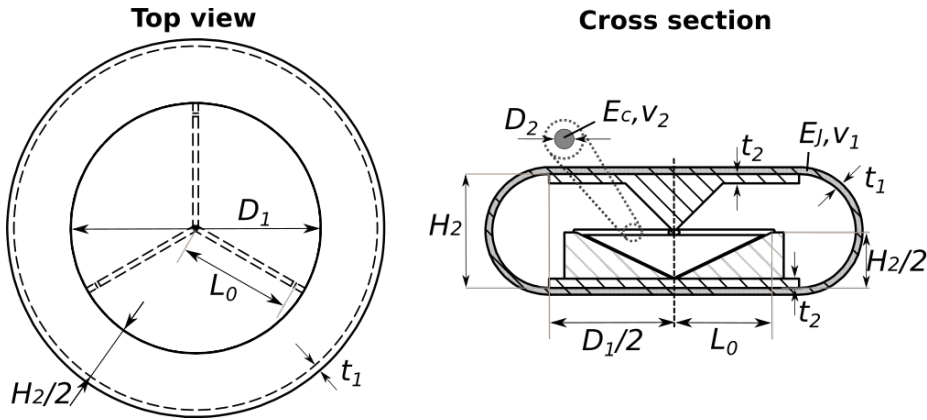
Figure 9.13: General embodiment of the compliant universal joint with design parameters. The white solid parts, within the elastic enclosure indicated with E_1, are assumed rigid in the design.

pression, internal parts that are used to clamp the end points of the wires in position can make contact at lower angles of rotation. This effect is translated to an axial stiffness constraint. A schematic of this situation with the parameters used is seen in 9.14. The distance from the center of rotation to the tip of the internal clamping plate, indicated as point A_J, is given by:

$$s_1 = \sqrt{\left(\frac{H_2}{2} - t_2\right)^2 + \left(\frac{D_1}{2}\right)^2} \tag{9.19}$$

To prevent internal contact between the clamping material and the wire pillar, point A is constrained to remain a minimum safety distance $d_{sf} = 1$ mm above the height of the wire pillar. Given a compression dH_2 of the joint, this results in a maximum range of motion ρ given by:

$$\rho = \arctan\left(\frac{H_2 - 2t_2}{D_1}\right) - \arcsin\left(\frac{dH_2 + d_{\text{sf}}}{s_1}\right) \tag{9.20}$$

As the required range of motion θ is known, equation 9.20 can be rewritten to the compression d_J. Combined with the maximum compression load and a safety factor $\Psi = 1.3$, based on possible stiffness variations due to manufacturing errors, the required linearised axial stiffness can be calculated for any set of design parameters by:

$$K_{AJ} = \frac{\Psi \cdot F_c}{\left(s_1 \cdot \sin\left(\arctan\left(\frac{H_2 - 2t_2}{D_1}\right) - \rho\right) - d_{sf}\right)} \tag{9.21}$$

To find suitable dimensions for the elastic body, both an analytical and finite element model is used. The analytical axial stiffness model from [191], for the 2D embodiment as seen in 9.13, is used to find an initial parameter set. The principle of this model is to calculate the fluid volume that is displaced into the semi circular enclosures when the horizontal top plate is compressed. Combined with the analytical solution for a cylindrical expanding tube from [14], the pressure buildup to accommodate the fluid displacement is determined. With this internal pressure, the reaction force on the top plate, and
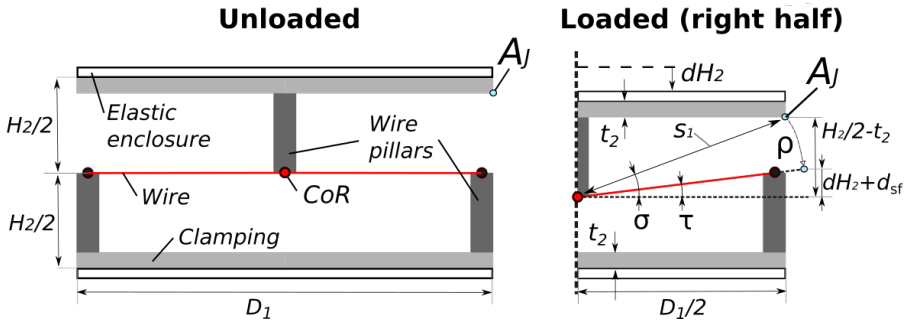
Figure 9.14: Influence of compressive load on the range of motion of the compliant universal joint.

thereby the axial stiffness, can be calculated. To use this 2D model for a 3D axial stiffness prediction, the proposed conversion method from [191] is also applied. This requires firstly scaling the out of plane dimension of the 2D model to create an equal surface area of the horizontal top surface. Secondly, a correction for the amount of edge length around this horizontal surface is applied, resulting in a total correction factor f_{cor} for the axial stiffness given by:

$$f_{cor} = \frac{\pi D_1}{4} \cdot \frac{2(\pi D_1/4)}{\pi D_1} \tag{9.22}$$

Using the analytical axial stiffness model from [191], a constraint line indicating feasible combinations of the enclosure parameters is created for different diameters D_1. For $D_1 = 55$ mm, this is seen in 9.15. The combination resulting in the lowest design height is selected as initial parameter set. Starting from this design point, the finite element model is used to explore parameter combinations that fulfill all constraints. The elas-
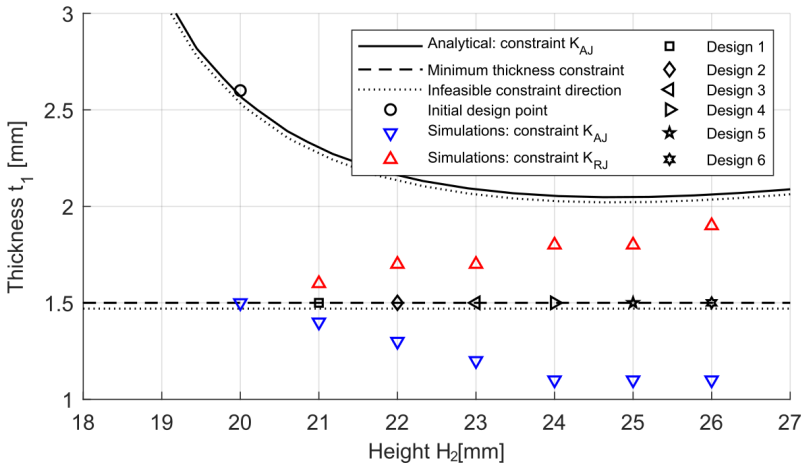

Figure 9.15: Evaluated design points for the universal joint. Both design points on the limit of the axial (K_{AJ}) and rotational (K_{RJ}) constraints have been explored, as well as feasible designs within these limits (designs 1-6).

tic enclosure is modelled using Comsol Multiphysics V5.5. The model consists of a 3D geometry where the horizontal parts of the elastic body are modelled as rigid bodies, as these parts are clamped in the physical design, similar to that seen in [87]. The bottom rigid body is made of a fixed constraint and the top part is given a prescribed rotation. Its center of rotation is fixated in x- and y-direction but given a vertical displacement dz, defined in a global equation stating dz is increased such that the vertical reaction force F_{rz} of the upper rigid body equals the maximum compression load F_c by:

$$\left(\frac{F_{rz}}{F_c} - 1\right) \cdot n_e = 0 \tag{9.23}$$

To implement the internal pressure buildup, a pressure p_{in} is added as boundary load to the inner boundary of the cell. The FEM system of equations describing the elastic deformation of the shell is enhanced by two additional equations. The first one describes the vertical load balance and is used to make sure that the vertical displacement of the joint is equal to the value that results in the maximum compression load. The second one expresses the incompressibility of the enclosed fluid in the cell, and calculates the internal pressure required to maintain the volume of the cell. Variable p_{in} is defined in a global equation stating it is increased such that the inner volume equals the original inner volume V_0, predefined from the geometry, to account for the incompressibility of the fluid by:

$$\left(\frac{V_{in}}{V_0} - 1\right) \cdot n_e = 0 \tag{9.24}$$

Both equations are multiplied with a factor $n_e = 10^5$, the order of number of elements, to increase their weight in the overall system of equations. The inner volume V_{in} is evaluated using an integral over the inner boundary A as described in [87] by:

$$V_{in} = -\int_A \frac{n_x \cdot x + n_y \cdot y + n_z \cdot z}{3} \, dA \tag{9.25}$$

Both the vertical compression dz and reaction torque on the upper rigid body are extracted for comparison. As the joint turns out to stiffen during compression, design parameters below the constraint line from the analytical model could be evaluated as well. The result of this search is shown in figure 9.15. Design points with a smaller wall thickness t_1 and larger height H show a lower rotational stiffness, although this generally increases the overall design height. As a compromise between both objectives, design 5 has been selected for implementation.

WIRE MECHANISM

The first step in designing the wires is to find the stiffness of the three wires combined. The stiffness K_c experienced when a force under an angle γ and at a displacement q_1 acts on a wire with initial length L_{c0}, as seen in figure 9.16, can be determined using the principle of virtual work. With respect to the initial stiffness K_{C0} of the wire, this results in:

$$K_C = K_{C0}\left[1 - \frac{L_{c0}}{\sqrt{L_{c0}^2 + q^2 + 2L_{c0}q\cos\gamma}} + \frac{L_{c0}(q + L_{c0}\cos\gamma)^2}{(L_{c0}^2 + q^2 + 2L_{c0}q\cos\gamma)^{3/2}}\right] \tag{9.26}$$

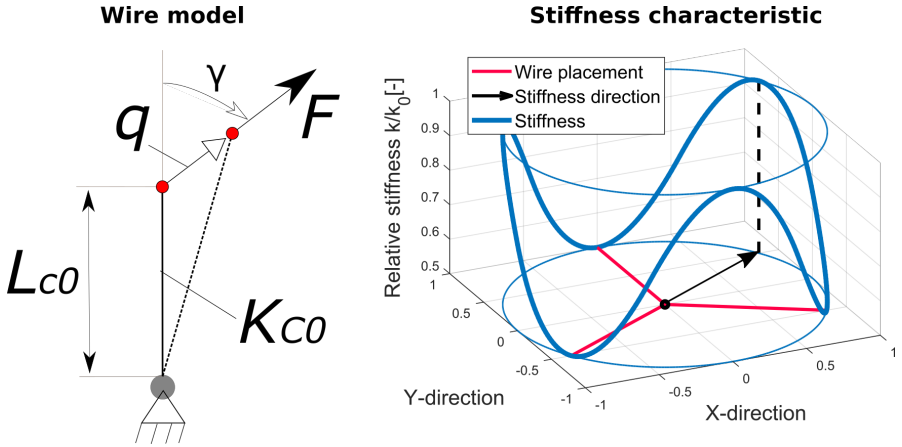**Wire model**   **Stiffness characteristic**

Figure 9.16: (left) The wire model used to determine stiffness of single cable. (right) The planar normalized stiffness which is caused by the position of the wires, causing a relatively lower shear stiffness in certain directions.

Two conclusions follow from equation 9.26. Firstly, the stiffness in any direction γ increases with increasing displacement q, indicating the wires can be designed based on the neutral configuration. Secondly, the stiffness in any direction in the initial configuration $q = 0$ reduces to:

$$K_{C,q=0} = \cos^2 \gamma K_{C0}, \qquad \gamma = [-\pi/2, \pi/2] \tag{9.27}$$

Combining the stiffness of each cable in the triangular configuration results in the directional shear stiffness as seen in figure 9.16. The minimum stiffness appears in a direction that relaxes one wire and equally loads the two other wires, with a total shear stiffness of $K_{CS} = K_{C0}/2$. To account for the possibility that one wire is not positioned well when the system is loaded in this minimum stiffness direction, a safety factor $\Psi_{CS} = 2$ is added so that the second wire still provides sufficient shear stiffness. Combined with the requirement on the maximum shear displacement, the required stiffness K_{C0} of each wire is determined by:

$$K_{C0} = 2 \frac{F_{CS}}{\lambda D_1} \Psi_{CS} \tag{9.28}$$

Where $\lambda = 1\%$ in this work. The resulting geometric and material parameters for both the elastic body and wire system of the final design on the compliant universal joint are presented in table 9.3.

UNIVERSAL JOINT PERFORMANCE
Based on these design parameters, the performance of the universal joint expressed as its stiffness characteristics, can be seen in table 9.4. two additional statements on this table have to be made. The first is that joint shear stiffness K_{SJ} is defined by its minimum occuring stiffness, meaning $K_{SJ} = K_{C0}/2$. The second is that rotational stiffness is presented twice, both as its combined load case K_{RJ} and as pure rotation K_{RJP}. The

Table 9.3: Design parameters of compliant universal joint, consisting of both the wire mechanism and the pressure balanced cell.

Parameter	Symbol	Value	Unit
Cell flat diameter	D_1	55	[mm]
Cell inner height	H	25	[mm]
Cell wall thickness	t_1	1.5	[mm]
Cell Youngs modulus	E_1	1.53	[MPa]
Cell poisson ratio	ν_1	0.49	[-]
Clamping thickness	t_2	2.0	[mm]
Wire diameter	D_2	1.15	[mm]
Wire initial length	L_0	23	[mm]
Wire Youngs modulus	E_2	4.0	[GPa]
Wire poisson ratio	ν_2	0.35	[-]

combined load case exist out of determining the rotation stiffness of the joint while its loaded with the compression load $F_c = 65$ [N]. This is the actual load case the joint will experience in the piston-slipper mechanism and is thus presented here. The pure rotation stiffness K_{RJP} will solely be used for experimental validation of the joint.

Table 9.4: Modelled performance of compliant universal joint.

Stiffness	Symbol	Value	Unit
Axial stiffness	K_{AJ}	22.1	[kN/m]
Rotational stiffness (combined case)	K_{RJ}	1.76	[Nm/rad]
Rotational stiffness (pure)	K_{RJP}	0.6	[Nm/rad]
Shear stiffness	K_{SJ}	90	[kN/m]

9.4. Experimental validation

Experimental validation has been performed to confirm the following properties of the compliant piston-slipper mechanism:

1. Stiffness properties of the universal joint.

2. Volumetric flow of the hydrostatic bearing over its load range.

3. Path-following properties of the universal joint during operation.

4. Friction reduction properties of the hydrostatic bearing.

The stiffness properties of the universal joint can be determined through the use of standard test bench setups, and is therefor first elaborated on. The universal joint is validated using a Zwick-Roell Z005 tensile test bench with the measurement setup for each stiffness configuration schematically shown in figure 9.17. For the shear stiffness, the joint is mounted under a 90° angle on a rigid support and clamped by a gripper to prevent rotation during the measurement. The shear stiffness is evaluated up to the maximum

shear load of 25[N] in two directions to measure the stiffness of a single cable and two cables combined, respectively the negative and positive y-direction in figure 9.16. The rotational stiffness is measured up to 10° using two L-shaped brackets to impose the axis of rotation through the middle of the joint. The load cells used are a Zwick Roell KAF-TC with a range up to 1000[N] and a relative accuracy of $< 0.21\%$ for translation and Zwick Roell HBM T20WN with a range of 0.500[Nm] and a relative accuracy of $< 0.15\%$ for rotation.
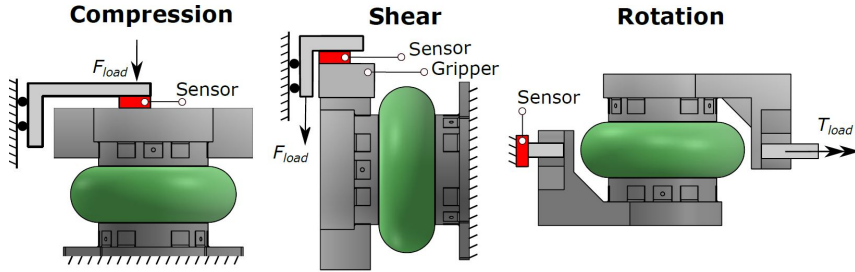

Figure 9.17: Schematic of the experimental setups for validating the universal joint.

The validation of full film bearings on the other hand is known to be more difficult to realize. This complexity increases significantly however when bearing surface elements are present that have variable depth, which influence the primary bearing performance characteristics. A conventional technique, and an implicit proof of performance, is measuring the volumetric flow of the bearing given a certain operation condition. The setup designed in this work uses this principle as its primary bearing validation measurement. The path following properties of the joint and friction reduction properties of the hydrostatic bearing will be determined by reproducing the load-case and measuring the X and Y shear forces, to determine if friction is minimized. These three criteria will be determined through the use of a self-designed setup, seen in Figure 9.18. Its a combination of a pneumatic cylinder as force generator, a linear guide for the piston-slipper mechanism and a wobble plate connected to a motor with reductor. The motor used is a 90 Nm, 750 W SEW eurodrive synchronous motor with a 1:18 straight line reductor. It is used to actuate a 260 mm diameter wobble plate with a wobble plate angle of $A_w = 10°$. The piston-slipper mechanism is placed on the wobble plate and is connected to the pneumatic cylinder through an Optoforce HEX-70-XH 6-axis load cell with an average resolution of ±245 [mN] for force and ±2.8 [mNm] for torque. The setup makes use of an external fluid pump, namely a 12V Seaflo membrane pump with a max output pressure of 0.28 [MPa]. The capillary restrictor is made from using a Prusa SL-1 3D printer and has a restrictor diameter of $r_r = 1$ [mm] and a length l_s of 25 [mm]. The hydraulic resistance of the capillary restrictor in combination with the hydraulic system is significantly higher then that of the restrictor taken into account in the mathematical model, and was found to be equal to $2.25E-10$ m^{4}s/kg. Since this resulted in a different load case for the bearing, the bearing input pressure was increased to 0.8E5 Pa to guarantee a stable input pressure source. Both were taken into account in the model for comparing the demonstrator with the proposed modelled design. In this proposed model used to
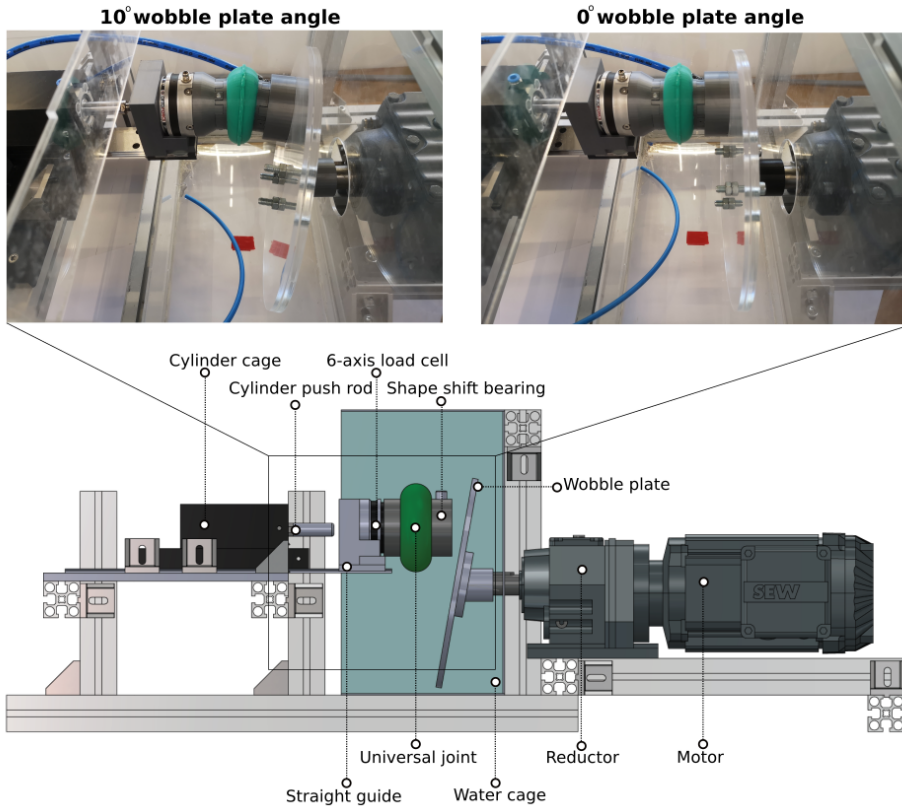
Figure 9.18: Overview of the test-setup developed for simulating the wobble plate motion. Both the volumetric flow measurements and shear force measurements are performed using this setup. For the volumetric flow the wobble plate angle configuration is depicted in the top left of the image, while for the volumetric flow measurement the top right configuration is used.

determine the shear forces seen in figure 9.12, the force generated on the piston slipper by the piston are idealized. However, due to compression of the air inside the pneumatic cylinder, the force generator in the setup instead exhibits a sinusoidal force characteristic. This effect was taken into account by modelling the force generator characteristic as:

$$F_{cz} = -F_A \cos(\theta + 0.5\theta) + F_{off} \tag{9.29}$$

Where $F_A = 30$ [N] and $F_{off} = 35$ [N]. Additionally, because of the design of the wobble plate connector, the position of the slipper with respect to the center of the wobble plate differs from that used in the concept design model. The x and y-position changed from from $x = 70$ [mm], $y = 0$ [mm] to $x = 65$ [mm], $y = 15$ [mm]. Taking these two aspects into account, a corrected shear force is used to compare the experimental results with. The corrected design model as function of these setup changes can be seen in figure 9.19.
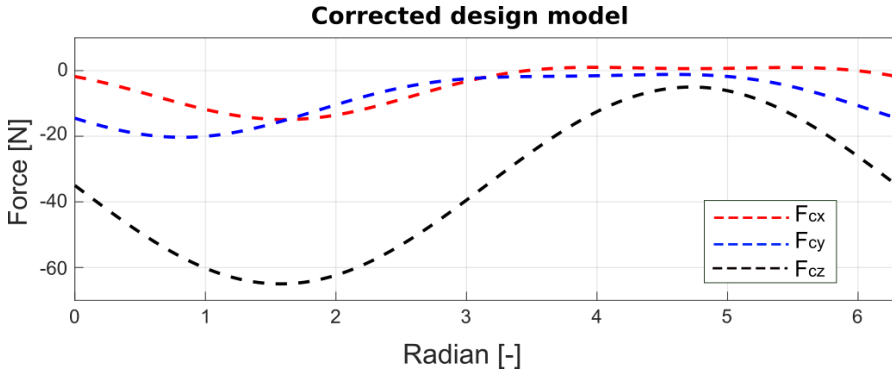
Figure 9.19: Corrected model results that determine the expected shear forces. This model assumes also the corrected friction coefficient found for the proposed material combination.

Table 9.5: Summary of known differences between design model and realised demonstrator as well as expected effect on mechanism performance for each parameter change. The membrane thickness t_3 and feedline radius r_7 are approximated based on determining the average thickness caused by the deposition of epoxy on the membrane.

Par.	Original design	Demonstrator	Expected effect on performance
E_s	1.2 [GPa]	2 [GPa]	decreasing load capacity slipper
E_m	0.95 [GPa]	2.8 [GPa]	decreasing load capacity slipper
D_2	1.15 [mm]	1.2 [mm]	increasing shear stiffness joint
l_4	28 [mm]	17 [mm]	decreasing load capacity slipper
μ_d	0.2 [-]	0.24 [-]	decreasing shear load
t_3	100 [μm]	170 [μm]	decreasing load capacity slipper
r_7	2 [mm]	2.1 [mm]	decreasing load capacity slipper

9.4.1. Demonstrator corrections

During production of the demonstrator a number of limitations were identified that would reduce its similarity to the proposed design. The main components of the demonstrator were built either using fused deposition 3D printing or silicon rubber casting. They were then assembled either by bolting components or, in the case of several components of the slippers, through adhesion. In total 3 slipper demonstrators are presented in this work. These are a parallel, multi-recess slipper as well as the shape-shifting slipper. The parallel and multi-recess bearing were produced out of one 3D printed part, and epoxy was used to seal the feedline tube. They are printed using low infill PLA (15 %). The shape-shfiting slippers are a combination of low infill PLA (15 %) and a 100 μm Mylar membrane. Since the majority of plastics produced in the required thickness have poor adhesion properties, mylar was used because of its relatively acceptable adhesion properties. Both materials have a higher expected material stiffness then that used in the design model. Based on [88], the Youngs modulus was corrected to $E_3 = 2$ [GPa] for all printed components, and the Youngs modulus for the mylar membrane was corrected to $E_m = 2.8$[GPa]. The use of Mylar and PMMA as the counter surface for the setup also influences the friction coefficient. Using the setup in figure 9.18, where the wobble plate

was placed at a 0 angle, the dynamic friction coefficient for the high load case $F_c = 65$ [N] was determined to be $\mu_d = 0.24$. This correction of friction coefficient has also been taken into account in figure 9.19. All corrections were taken into account for the final comparison. Table 9.5 shows a summary of all variations obtained through production on the demonstrator that would effect the original modelled mechanism as well as the expected result on performance. For the shape shifting demonstrator, the production process more significantly influences their performance. Epoxy is used to connect the membrane to the slipper body. The spilling of the bonding surfaces onto the membrane effectively increases the membrane thickness. This spilling also causes the feedline tube to increase in thickness, due to the spillage occuring when sealing the feedline. The increase in thickness was measured at several points using a micrometer screw gauge. The resulting approximated thickness has been taken into account for the result comparison of the shape shifting demonstrator as seen in table 9.5. The resulting demonstrator is seen in figure 9.20.
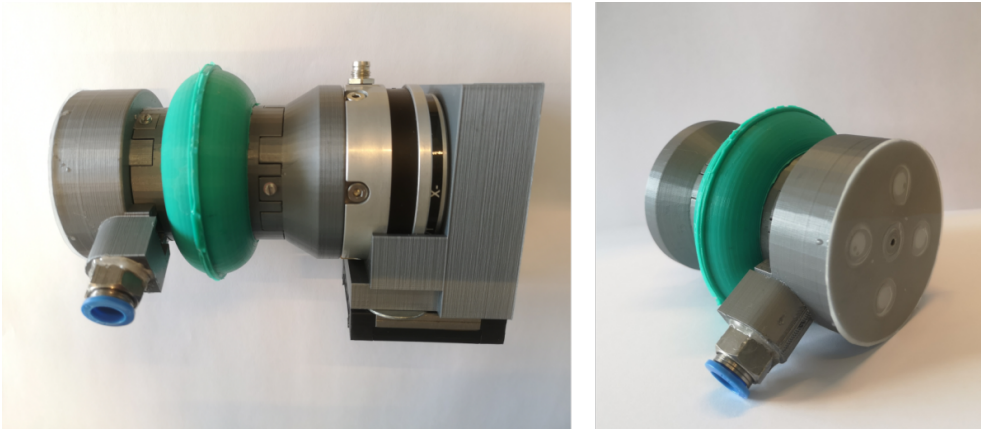

Figure 9.20: (left) The piston-slipper mechanism demonstrator, which is a combination of the shape shifting slipper, universal joint, 6-axis load cell and linear guide. (right) View of the pockets of the shape shifting slipper.

9.5. RESULTS

9.5.1. JOINT STIFFNESS

Figure 9.21 presents the comparison between the models and measurements for the universal joint. It is again noted that the rotational stiffness measurement is validated solely for pure rotation K_{RJP}. In addition to the original model, ss several significant deviations in stiffness are observed, a corrected model has also been included. These corrections consist of correcting the Young's Modulus (E), adding elasticity at the edge of the horizontal segments (FEL), correcting the initial fluid volume (V_0) and correcting the cable length (L_{cable}). The comparison between the modelled stiffness and measured stiffness can be seen in table 9.6. Using the updated joint model it was determined that the combined loading case rotation stiffness was equal to 1.56 Nm/rad for the universal joint.

Table 9.6: Modelled performance of compliant universal joint. For the adjusted error comparison the material parameters $E_J = 1.14$ [MPa], an addition of elasticity of the horizontal segments $FEL = 10$ [mm], effective wire length $L_{c0} = 50$ [mm] and $E_c = 0.97$ [GPa] are implemented. In all cases the secant stiffness is presented.

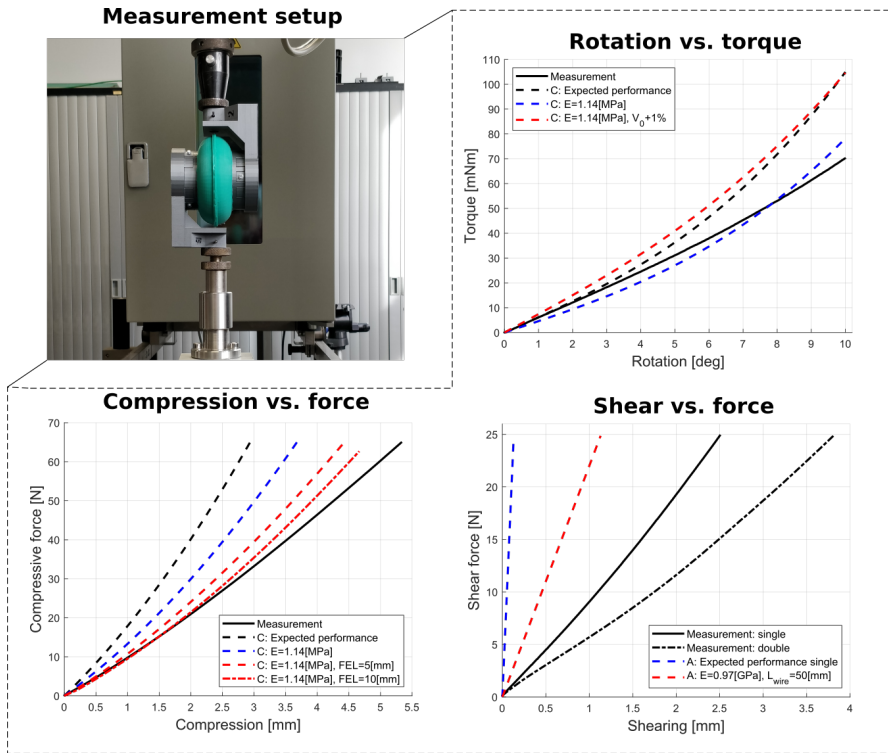| Stiffness	Symbol	Model	Corrected model	Measured	Unit	Error
Axial	K_{AJ}	22.1	13.4	12.2	[kN/m]	9.0 %
rotational	K_{RJP}	0.6	0.45	0.4	[Nm/rad]	11.1 %
Shear	K_{SJ}	98	11	6.7	[kN/m]	39.1 %

Figure 9.21: Experimental validation of the axial, rotational and shear stiffness using the Zwick test setup. The results of the measurements measurements, Comsol simulations and analytical predictions are shown.

9.5.2. VOLUMETRIC FLOW AND TILT STIFFNESS

The bearing flow measurement was performed on the setup depicted in figure 9.18, which was determined using a wobble plate $A_W = 0°$. The measurement was performed by actuating the system using the pneumatic cylinder, determining the load on the bearing through the 6-axis load cell, and measuring the time required to remove 2 Liters from the pump input reservoir. This was done for different loads during a cycle, which causes the measurement points to be unequal during a measurement cycle. In total 3 demonstrators have been validated, seen in figure 9.22, of which 1 possesses the shape-shifting characteristic. For all bearings 2 measurement sets are presented, which are performed

at different plate positions. To quantify the error between experimental and simulation
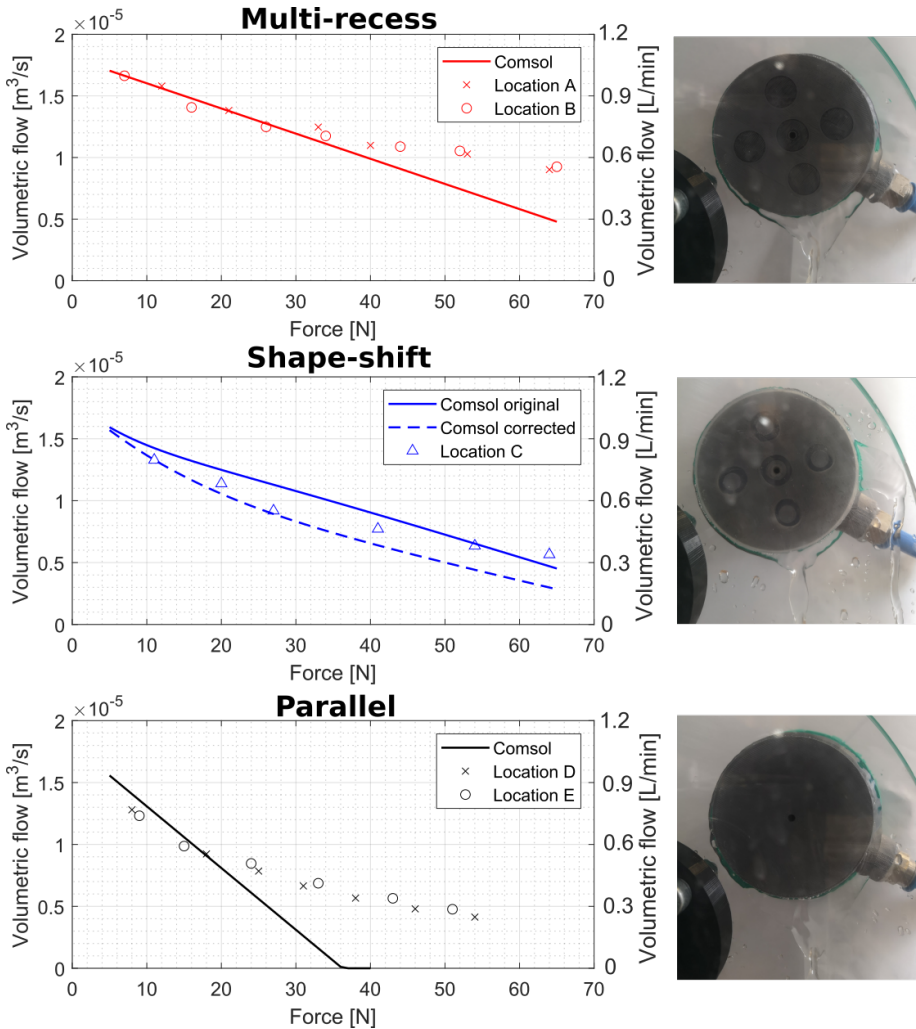

Figure 9.22: The volumetric flow vs. load for the shape shifting slipper and its rigid counterparts. Since the system is actuated through a pneumatic cylinder, a point wise measurement approach is performed. A front view of all slipper demonstrators at their initial load case can be seen for all bearings. The original design, with a membrane material stiffness $E_m = 0.95E9$ [GPa] is the added in the comparison and represents the best case shape-shifting design for this design case. For each slipper two experimental results have been presented.

results, the normalized mean absolute error (RMAE) is used, similar to [182]. For the multi-recess this error between the model and demonstrator is 10.05 % and 9.44 % for the first and and second measurement respectively. For the shape shifting bearing the error between the corrected model and the demonstrator is 14.76 % and 8.81 % for the first and second measurement respectively. For the Parallel bearing this error is 20.9 % and 19.49 %. Based on the corrected comsol model that approximates the shape-shift

demonstrator, its tilt stiffness K_{RS} = 273.3 Nm/rad at the F_c = 65 [N], with a minimum film height at this load of 51 μm. The combined rotational stiffness of the universal joint K_{RJ} determines the approximated remaining film height after rotation, based on the stiffness coupling ratio δ. This results in an stiffness coupling ratio of $\delta \approx 146$ between the shape-shift slipper and joint demonstrators.
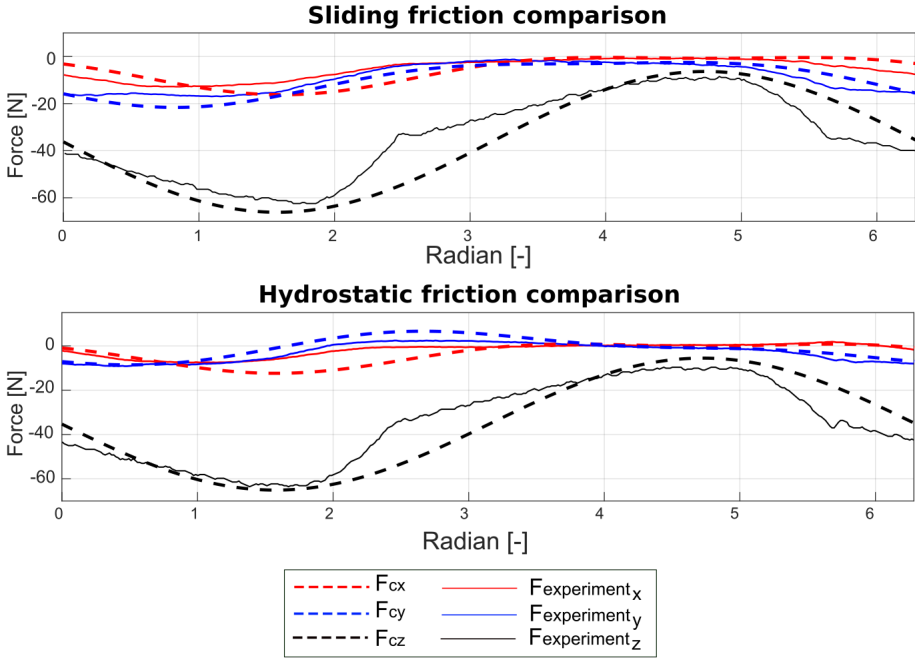

Figure 9.23: A comparison of the corrected model with the experimental results. In both cases the comparison for sliding friction and hydrostatic friction is made.

9.5.3. PATH FOLLOWING & FRICTION REDUCTION

Shear forces have been determined both for the case with and without hydrostatic lubrication, as can be seen in figure 9.23. These have been determined for the m.1 shape-shifting demonstrator presented in figure 9.22. The corrected model and experimental results are used to determine the error, again by using the RMAE. In case of the addition of sliding friction, the error equals 19.58 % for the shear forces in x-direction and 11.57 % for shear forces in the y-direction. With the addition of hydrostatic friction, the error is equal to 19.28 % for the shear force in x-direction and 31.77 % for shear force in the y-direction.

9.6. DISCUSSION

9.6.1. COMPLIANT UNIVERSAL JOINT

First, it is noted by the authors that an overestimation was made in the Young's Modulus of the elastic enclosure. Using the Shore-A hardness from the supplier ($S_A = 30$) a corrected Young's Modulus $E = 1.14$[MPa] was determined using the correlation from [75], resulting in a decrease in expected stiffnesses. The remaining overestimation of the true axial stiffness can be explained by the assumption of rigid horizontal segments. As the clamping of the top and bottom segments of the cell is not perfect, the edge of the elastic material in these segments stretches with the enclosure. The corrected models confirm that such as a $5 - 10$[mm] flexible edge can result in the lower stiffness measured. Additionally, remaining air bubbles within the joint can reduce the stiffness. Due to the corrected Young's Modulus, an underestimated rotational stiffness is seen in 9.21(b). The rotational stiffness, however, is known to be influenced by internal pressures from combined load cases. An excessive fluid volume due to production errors, also causing an initial pressure, can cause the measured stiffness as the corrected model already shows a significant stiffness increase for a volume error of 1%. From a separate measurement on the wires, the Young's Modulus of the nylon was corrected to $E = 0.97$[GPa]. With an additional correction for the true length between the connection points of each wire, the measured stiffness is overestimated by a factor 2.2. This effect is expected to be caused by an S-shaped curve in the wires due to their inability to perfectly curve around sharp corners. Additionally, the measurement on two cables shows a relative stiffness of 0.67[-] compared to the single cable, although a factor 0.5 was expected, which is attributed to inconsistencies in aligning each cable during manufacturing.

9.6.2. SHAPE SHIFTING SLIPPER

Similar to the universal joint, a number of differences can be observed in the comparison between the FEM model and demonstrator. The main comparison is made by looking at the load vs. volumetric flow of Figure 9.22. To give a more clear view on the effect of passive shape shifting and explaining the difference between model and experiment, the experimental results of the parallel and multi-recess bearing were also added. This additionally helps in identifying errors caused by the setup and errors between the demonstrators and their respective models. Firstly, there is deformation of the wobble plate counter surface at the higher loads, due its limited stiffness. This effect becomes especially noticeable in the difference between the parallel bearing demonstrator and model at higher loads, since it effectively guarantees a non-flat counter surface. This deformation causes a region through which leakage can occur and will become more dominant when this deformation becomes similar in magnitude to the film height. Performing the same measurement at a different radial positions on the plate also increases this effect. The second observable error is the drift between measurement points, which is primarily due to the timing of starting and stopping the flow measurement being done manually. This is limited by increasing the total measurable volume.

Besides the effects caused by the setup and load case, there are several differences that can be explained primarily through the production of the demonstrator. The fused

deposition printing method significantly changes the effective elastic modulus of the PLA printed component depending on the infill ratio and other print settings [2].This effect is heavily based on the shape of the printed part, thus making it hard to make general definitions on the material properties. Since the material properties of the membrane and slipper body are both approximated, a different combination of material specifications can yield similar results. These properties are also influenced by humidity and water absorption, which are both present variations in the setup. Secondly, as presented in table 9.5, the adhesion process between the mylar membrane and PLA bearing body leaves a residue of epoxy on the membrane. This effectively increasing its thickness, which for this demonstrator is approximated to be almost double its effective membrane thickness. The adhesion process also influenced the effective thickness of the feedline tube, which as also taken into account in table 9.5. Both parameters heavily influence the stiffness of the center recess mechanism and thereby its observable shape shifting behaviour. The adhesion process also makes it difficult to remain consistent during the production of different demonstrators. Due to heavy influence of the center recess stiffness on observable shape shifting behaviour, demonstrators with a higher center recess stiffness act similar to a parallel bearing in terms of volumetric loss, also observed in chapter 6. Other demonstrators built all had a significantly higher effective membrane thickness due to the production process, and as such performed poorly. Since these parameters significantly effect the performance as well as durability since the demonstrators destructively failed during the path following tests, it is proposed to focus on the monolithic production of future slippers. Finally, the stiffness of the feedline tube with respect to the center cantilever should also be designed to be low in respect, making sure the additional stiffness sealing methods create does not influence shape-shifting characteristics.

9.6.3. PISTON-SLIPPER MECHANISM

A number of limitations influence the quality of the measured results. The new position of the slipper causes the rotational velocity component, which is dominant over the small velocity components created by the slipper drift, to be split over the V_{lx} and V_{ly} components, therefor influencing the magnitude of shear forces in these direction. Secondly, the pneumatic cylinder used as force generator does not have a step-like characteristic when the setup switches from the filling to compression stroke, which has been accounted for by modelling the force characteristic using equation 9.29. This is however only an approximation of the compression behaviour of the pneumatic cylinder, which due to friction of the cylinder is seen to differ from the sinusoidal force generator assumption. Thirdly is the effect of sensor drift, which the model used in this work exhibited after loading. This drift was observed to be equal to 0.11 N and -0.56 N for the x- and y-forces respectively for the load case with sliding friction and -0.22 N and 0.41 N for the hydrostatic friction case. All drift values have been used as a correction on the experimental results. Taking these three effects onto account increases the similarity between the model and measurement, as observed in figure 9.23. One of the other characteristics that was not taken into account in the model, but does influence the result, is the stiffness of the feedline tube from the pump to the bearing. This component pulls the bearing, therefore generating a non-constant load during the load cycle depending on

the position of the wobble plate. A final simplification of the model is that the rotation stiffness of the joint has not been taken into account to determine equilibrium. This was motivated by the small magnitude of this respective stiffness. Taking these limitations into account, the effect of lubrication is however still clearly observable in the reduction of y-shear forces. Development of more advanced metrology setups that are able to determine the actual deformation of the pockets however are necessary to fully determine if the proposed behaviour is due to the shape-shifting aspect.

9.7. CONCLUSION

The compliant piston-slipper mechanism is presented in this work as an alternative to the contact-mechanics based mechanisms that can be found in the state of the art. The coupling in stiffness directions in compliant mechanisms creates the need for a combination of sub-systems that together are able to create a functional alternative to the state of the art. The case study presented in this work further builds on the potential of closed form pressure balancing and passive shape shifting, and shows how the combination can form a compliant alternative. The case study presented in this work only presents a simplified load case, which is however representative for industrial applications. Although the principles are further substantiated in this work, a more convincing future step needs to be made towards high load-cases found in industry. The presented concept shows is that the introduction of compliance into components that are traditionally high-stiffness can result in potentially desirable performance for next generation wobble plate piston pumps. To minimize the effects of production and further show the potential of shape-shifting slippers, it is suggested for future designs to be built and designed monolithically.

9

IV

CONCLUDING REMARKS

10

CONCLUSION

To conclude this dissertation, we first consider the research objective as stated in the introduction which was the implementation of compliance into water lubricated hydrostatic bearings resulting in improved performance and new design methodologies. The research objective embodies three common themes in this thesis: compliance, full film water bearings (and in particular hydrostatic bearings) and design methods. The thesis is divided in parts that were coupled to three sub-objectives that further motivated the structure and content of this thesis: Motivation, principles and implementation. These three sub-objectives are used to reflect on the content of this work and its contributions. The summary of all key statements per chapter can be seen in figure 10.1

10.1. MOTIVATION

The three aspects of motivation: engineering, environment and innovation, were presented in chapters 2, 3 and 4, each going further into detail on these objectives. Because of their superior operation range and performance, hydrostatic bearings remain important mechanical components in the development of next generation machines. This is especially true in hydraulic energy generation systems, where the requirements of lifetime and increased power output keep pushing the boundaries of what is possible with state of the art machine components. The field has been addressed in this thesis in more detail, i.e. water hydraulic wind turbine drive trains, could greatly benefit from the use of hydrostatic bearings. For future design solutions however, several key limitations of hydrostatic bearings have to be solved. A main finding is that a key limitation could be defined by the lack of deformability of full film bearings.

Simultaneously with the need for improved engineering characteristics, is the worldwide need for more sustainable machines. Since water is often suggested as *the* sustainable alternative to oil, chapter 3 was dedicated to identifying the state of the art of water lubricated bearings and developing a method for taking sustainability into account during concept design of full film bearings. The results of the developed anticipatory method are clear and show that the term sustainability should not automatically

be given to water lubricated systems and that, as with many engineering problems, it's very much situation dependent. For open systems, where lubricant is lost to the environment, water is most of the time the sustainable alternative. However, in closed systems, the impact of the more exotic materials used for water lubrication offsets the lower impact of the lubricant. A closed system might therefor be more sustainable when oil-based lubricants are used. Researchers should be aware of this and not by definition promote water lubrication as the de-facto sustainable alternative.

Innovation was the key subject in chapter 4, which discussed the types of innovation trends we see within the field. Here, we motivate that although elastic deformation of bearings in conventional engineering practise is seen as an error that has to be accounted for, the use of compliance can solve some of the limiting factors of full film bearings. The main design concept presented in this thesis was the introduction of large elastic deformations. This implementation has resulted in the concepts described in the chapters of the second part: principles.
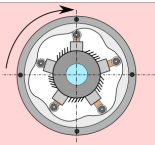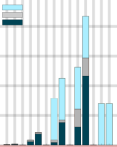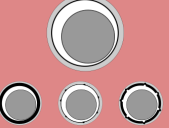
10.2. PRINCIPLES

Four principles were developed by looking at compliance and deformability as a design strategy rather then an error that has to be accounted for.

Chapter 5 discussed the principle of pressure profile matching. Basically, in this concept the pressure distribution in the lubricating film that is present in an ideal film geometry is matched with a nominal large scale deformation of the supporting structure of the bearing. The term 'Large scale' in this definition means, significantly larger than the elastic deformation required to track counter surface curvature variations. This concept is not limited to a single bearing topology, and can directly be implemented for any bearing topology. As long as the ideal pressure distribution is known, this principle can limit pre-loading effects of the support. To give an idea of this potential reduction in pre-loading effects we can look at the average and peak stresses and strain energy reductions of the example presented in chapter 5. Here the peak strain energy reduction was approximatly by a factor of 128, while the peak shear stress reduction was a factor of 569. Also a reduction of average strain energy and shear stress was observed, 16.1 % and 10.4 % respectively. Since these are limiting factors for these type of mechanisms the reduction is significant.
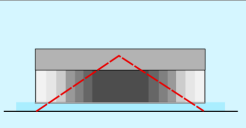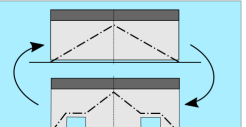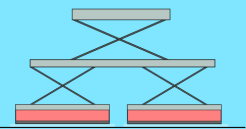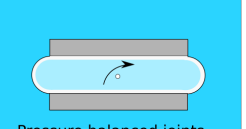
The second presented principle (chapter 6) is that of passive shape shifting. Passive shape shifting introduces the method of designing for 2 discrete points in the operation range, and using compliant elements to passively switch between them. The chapter shows that the use of compliant elements extends beyond coping with non-constant curvature counter surfaces, and presents several examples where the focus lies on other performance characteristics such as tilt stiffness, load capacity and limiting bearing leakage. This performance improvement can be understood by the fact that shape shifting bearings can have performance characteristics that are not obtainable by their rigid counterparts. By having elastic elements, the bearing can benefit from the properties of the two rigid bearing geometries it is based on. It can thus both have for instance a low

10

Figure 10.1: Key concluding statement for all chapters of this dissertation. They follow the structure used throughout this work and focus on a single overarching statement per chapter.

volumetric flow and a high tilt stiffness at different points in the operation range, where a rigid design would have to choose between these characteristics. This flexibility in performance, without the implementation of costly and complex mechatronic components is the value that passive shape shifting brings.

The third principle revisits one of the research objectives as presented in chapter 2: The development of a large deformable hydrostatic bearing. This chapter focuses on developing the general kinematics of a distributed bearing support which implements discrete elastic elements to deliver the desired load-carrying and deformability characteristics. This model presented two important design considerations that are required for future development of these supports. The first is that although increasing the number of mechanism layers decreases the bearing height, there is a functional limit to this trend. In the design case shown in chapter 7, this functional limit is obtained after only two whiffle tree layers, afterwhich any additional layers hardly influence the effective bearing footprint. The second is that its performance depends on the stiffness characteristics of its individual rotation joints that make up a large part of the mechanism. Since the magnitude of the angles do not change much over the different layers, the benefit of division mainly can be seen in the load division over the increasingly smaller joints and the decreased required compression for each slipper. The joints therefor should have a high support to rotation stiffness ratio, which is the desired specification for the whiffle-tree support.

The last chapter in the second part (chapter 8) provides a potential solution to this need of a high performing compliant joint. This chapter introduces a joint that funtions using the interaction of both solid and fluid. By encapsulating a fluid in a closed cell in an elastic body, a fundamentally different joint compared to the state of the art is developed. When compressed the elastic body is loaded in tension, while simultaneously the internal fluid is loaded in compression, providing the support stiffness. The compliant shape of the elastic body also creates a low rotation stiffness, uninfluenced by the internal liquid. Conceptually this creates a joint with a high support to rotation stiffness characteristic. The chapter provides the modelling tools that define the performance of such joints. Theoretical magntiude of the stiffness ratio predicted in the chapter is as high as 10^4 [rad/m^2], although this is coupled to a size dimension. Since the ratio is coupled to dimension, direct comparison between the state of the art and the introduced concept requires more extensive studies. Finally, conversion from 2D to 3D was investigated showing a negative influence on the support stiffness up to 50 %, thus reducing the theoretical obtainable stiffness ratio.

10

10.3. IMPLEMENTATION

The last part of this thesis consists of one chapter with one objective: A demonstration of several of the principles introduced in part 2. The case study combines the pressure balanced joint and a hydrostatic bearing designed with passive shape shifting. The specifications for the case study are inspired by the hydraulic piston pump design case of chapter 2, but now not in a radial but in an axial configuration. The results indicate that shape shifting is obtainable with an error between the model and measurement of 8.8

%, but also that stiffness variations of its compliant elements greatly impact the shifting ability. Since only a limited measurement set could be obtained, a re-iteration of the demonstrator production and additional measurements are required before concluding statements on the shape shifting behaviour can be made. The pressure balanced joint however shows its potential as a contact-mechanics free alternative with stiffness characteristics reminiscent to conventional ball-joints. This was validated by the path-following properties of the mechanisms. As was shown in the chapter, an average error between the model of 19.3 % and 31.8 % for the X and Y direction respectively was obtained. Finally, the design case strengthens the vision of bearing design in which compliance is used has a wide variety of implementation possibilities. Potential future implementation applications include hydraulics, pumps and motors, architectural components such as curved doors and rooftops and large milling machines.

10.4. COMPLIANT FULL FILM LUBRICATED BEARINGS

This brings us to reflection on the main objective of the thesis: *The implementation of compliance into water lubricated hydrostatic bearings resulting in improved performance and new methodologies.* This work has shown us that compliance can be used in different design strategies to improve the performance of full film bearings. This improvement can be found in the reduction of peak stresses for thrust bearing pads, the decreased footprint of a large deformation whiffletree based bearing support, an alternative for high support to rotation stiffness bearing supports or a design strategy that allows one single bearing pad to function as two different geometries. The fact that these principles can be combined into different bearing designs, reinforces their general use. Chapter 9 has provided a first example of this potential by combining two principles, resulting in a compliant based/contact mechanics free alternative to the current state of the art of piston-slipper mechanisms. The analyses performed show what kind of fundamental improvements can be obtained and how these bearings can be developed. To that end, the principles presented in this thesis are a valuable extension to the application range of full film bearings.

10.5. RECOMMENDATIONS

The main focus of this thesis is the introduction of new, innovative design concepts. These concepts have been introduced through the introduction and analysis of well-chosen specific examples or embodiments. A number of key potential research directions have been identified:

- The combination of the design principles of pressure profile matching and pressure balancing, into a single compliant hydrostatic bearing promises to be, to this authors knowledge, the best case development step for a monolithic large deforming hydrostatic bearings. This would be the first design direction that is suggested for the radial piston pump design case described in chapter 2. The main challenges would be to determine the performance under industrial load cases and the production process of the functionally graded part of the slipper.

- The production of a well defined pressure profile matched bearing support might

10

be more easily obtained when using meta-material structures. The main challenges to be overcome in these type of materials would then shift from the realization of gradient material properties such as Youngs' modulus, to buckling constraints and efficient footprints.

- The validation of deformable and shape shifting bearings requires new metrology approaches, since single point film height measurements or volumetric flow measurement can only provide a confirmation of global operating bearing parameters, such as load, volumetric total flow, and average or point measured fly height, and thus can only provide indirect proof of the deformation of the bearing. This limitation is also seen in chapter 9 in the determined error between model and demonstrator. The author believes that 2D film height measurements such as presented in [135] will be the best way of validating the local deformations of these bearing types.

- An iteration on the demonstrator of chapter 9 will improve the observed performance of shape shifting and decrease the error between model and demonstrator. The main proposed improvements are a monolithic design of the full slipper, and an improved counter surface design. These improvements should limit the effect of stiffness variation of the center compliant recesses, as well as the error the deformation of the wobble plate and its connector creates on measured volumetric flow. This unknown deformation and waviness of the used plate greatly influence the quality of the measurements, especially at lower film thickness where the deformation and film thickness are likely similar in magnitude. After this step, a switch to metal material archetypes for the slipper and joint and industrial flow restrictors should be made to move towards industrial performance characteristics.

BIBLIOGRAPHY

REFERENCES

[1] A. Abdelbary, M. N. Abouelwafa, I. M. El Fahham, and A. H. Hamdy. The effect of surface defects on the wear of Nylon 66 under dry and water lubricated sliding. *Tribology International*, 59:163–169, 2013.

[2] Chamil Abeykoon, Pimpisut Sri-Amphorn, and Anura Fernando. Optimization of fused deposition modeling parameters for improved PLA and ABS 3D printed structures. *International Journal of Lightweight Materials and Manufacture*, 3(3):284–297, 2020.

[3] Danish Energy Agency. Denmark's Energy and Climate Outlook 2019. Technical report, Danish Energy Agency, Copenhagen, 2019.

[4] Annas Bin Ali, M. Abdul Samad, and N. Merah. UHMWPE Hybrid Nanocomposites for Improved Tribological Performance Under Dry and Water-Lubricated Sliding Conditions. *Tribology Letters*, 65(3):1–10, 2017.

[5] Peter Andersson. Water-Lubricated and Dry-Running Properties of Ceramic Journal Bearings. *TriboTest*, 10(2):147–161, 2003.

[6] A Ansarifar and G Lake. On The Mechanics of Rubber-to-Metal Bond Failure. *The Journal of Adhesion*, 53:183–199, 1995.

[7] Fatun Aurelian and Dominique Bonneau. Finite Element Method for Fluid Film Bearings. In Q. jane Wang and Yip-Wah Chung, editors, *Encyclopedia of Tribology*, pages 34–109. Springer, 2013.

[8] Curtis Baffes, Terry Mast, Jerry Nelson, Eric Ponslet, Vince Stephens, Larry Stepp, and Eric Williams. Primary Mirror Segmentation Studies for the Thirty Meter Telescope - art. no. 70180S. *Proceedings of SPIE - The International Society for Optical Engineering 7018*, 2008.

[9] M. J. Balcerzak and S. Raynor. Solutions for several shapes of externally pressurized hydrostatic thrust bearing. *Applied Scientific Research, Section A*, 11(2):189–217, 1962.

[10] Anton Van Beek and Lubor Lepic. Rubber Supported Hydrostatic Thrust Bearing with Elastic Bearing Surfaces of Infinite Length. *Wear*, 201:45–50, 1996.

[11] H. Blok. Inverse Problems in Hydrodynamic Lubrication and Design Directives for Lubricated Flexure Surfaces. *Lubr and Wear*, 1963.

[12] Kittipong Boonlong and Puttha Jeenkour. Numerical study on axial vibration of water-lubricated small thrust bearing considering grooved pad. *Vibroengineering Procedia*, 16:13–18, 2017.

[13] Abdelkader Boulenouar, Noureddine Benseddiq, Mohamed Merzoug, Nabil Benamara, and Mohamed Mazari. A Strain Energy Density Theory for Mixed Mode Crack Propagation in Rubber-like Materials. *Journal of Theoretical and Applied Mechanics*, (mode I):1417, 2016.

[14] A.F. Bower. *Applied Mechanics of Solids*. CRC press, 2009.

[15] Michael Branagan, David Griffin, Christopher Goyne, and Alexandrina Untaroiu. Compliant Gas Foil Bearings and Analysis Tools. *Journal of Engineering for Gas Turbines and Power*, 138(5):054001, 2015.

[16] D. L. Cabrera, N. H. Woolley, D. R. Allanson, and Y. D. Tridimas. Film pressure distribution in water-lubricated rubber journal bearings. *Proceedings of the Institution of Mechanical Engineers, Part J: Journal of Engineering Tribology*, 219(2):125–132, 2005.

[17] James Carroll, Alasdair Mcdonald, and David Mcmillan. Reliability Comparison of Wind Turbines with DFIG and PMG Drive Trains. *IEEE Transaction on Energy Conversion*, 30(2):663–670, 2015.

[18] D. Cebon, M.F. Ashby, C. Bream, and L. Lee-Shothaman. CES EduPack software, 2009.

[19] Michail Chalkiopoulos, Anastassios Charitopoulos, Michel Fillon, and Christos I. Papadopoulos. Effects of thermal and mechanical deformations on textured thrust bearings optimally designed by a THD calculation method. *Tribology International*, 148(September 2019):106303, 2020.

[20] Tie Chang, Chengqing Yuan, and Zhiwei Guo. Tribological behavior of aged UHMWPE under water-lubricated condition. *Tribology International*, 133(September 2018):1–11, 2019.

[21] S R Chauhan, Bharti Gaur, and Kali Dass. Effect of Fiber Loading on Mechanical Properties , Friction and Wear Behaviour of Vinylester Composites under Dry and Water Lubricated Conditions. *International Journal of Material Science*, 1:1–8, 2011.

[22] S. R. Chauhan, Anoop Kumar, and I. Singh. Sliding friction and wear behaviour of vinylester and its composites under dry and water lubricated sliding conditions. *Materials and Design*, 31(6):2745–2751, 2010.

[23] Beibei Chen, Jianzhang Wang, Ning Liu, and Fengyuan Yan. Synergetic effect of lubricant additive and reinforcement additive on the tribological behaviors of PEEK-based composites under seawater lubrication. *Tribology Transactions*, 56(4):672–680, 2013.

[24] Beibei Chen, Jianzhang Wang, and Fengyuan Yan. Friction and wear behaviors of several polymers sliding against GCr15 and 316 steel under the lubrication of sea water. *Tribology Letters*, 42(1):17–25, 2011.

[25] Beibei Chen, Jianzhang Wang, and Fengyuan Yan. Comparative investigation on the tribological behaviors of CF/PEEK composites under sea water lubrication. *Tribology International*, 52:170–177, 2012.

[26] Beibei Chen, Jianzhang Wang, and Fengyuan Yan. Synergism of carbon fiber and polyimide in polytetrafluoroethylene-based composites: Friction and wear behavior under sea water lubrication. *Materials and Design*, 36:366–371, 2012.

[27] Beibei Chen, Jianzhang Wang, and Fengyuan Yan. Synergism of carbon fiber and polyimide in polytetrafluoroethylene-based composites: Friction and wear behavior under sea water lubrication. *Materials and Design*, 36:366–371, 2012.

[28] Chien Yu Chen, Bo Hsiung Wu, Chung Jen Chung, Wang Long Li, Chih Wei Chien, Ping Han Wu, and Chung Wei Cheng. Low-friction characteristics of nanostructured surfaces on silicon carbide for water-lubricated seals. *Tribology Letters*, 51(1):127–133, 2013.

[29] M. Chen, K. Kato, and K. Adachi. Friction and wear of self-mated SiC and Si3N4 sliding in water. *Wear*, 250(1-12):246–255, 2001.

[30] Ming Chen, Koji Kato, and Koshi Adachi. The difference in running-in period and friction coefficient between self-mated Si3N4 and SiC under water lubrication. *Tribology Letters*, 11(1):23–28, 2001.

[31] Song Chen, Jian Li, Lei Wei, Yongliang Jin, Hongfei Shang, Meng Hua, and Haitao Duan. Tribological properties of polyimide-modified UHMWPE for bushing materials of seawater lubricated sliding bearings. *Tribology International*, 115(126):470–476, 2017.

[32] Wei Chen, Yimin Gao, Faliang Ju, and Yong Wang. Tribochemical behavior of Si 3N 4-hBN ceramic materials with water lubrication. *Tribology Letters*, 37(2):229–238, 2010.

[33] Feng Cheng and Weixi Ji. Simultaneous identification of bearing dynamic coefficients in a water-gas lubricated hydrostatic spindle with a big thrust disc. *Journal of Mechanical Science and Technology*, 30(9):4095–4107, 2016.

[34] Shyang Ho Chi and Yen Ling Chung. Mechanical Behavior of Functionally Graded Material Plates under Transverse Load-Part II: Numerical Results. *International Journal of Solids and Structures*, 43(13):3675–3691, 2006.

[35] Mao Hsiung Chiang. A novel pitch control system for a wind turbine driven by a variable-speed pump-controlled hydraulic servo system. *Mechatronics*, 21(4):753–761, 2011.

[36] Bill Chun, Piu Lau, Eden Wai, and Man Ma. Review of Offshore Wind Turbine Failures and Fault Prognostic Methods. *Proceedings of the IEEE 2012 Prognostics and System Health Management Conference (PHM-2012 Beijing)*, pages 1–5, 2012.

[37] C. G. Clarke and C. Allen. The water lubricated, sliding wear behaviour of polymeric materials against steel. *Tribology International*, 24(2):109–118, 1991.

[38] R. C. Coy, Y. Michopoulos, and J. P.T. Wilkinson. Environmental Impact of Lubricants. *Tribology Series*, 30(C):15–23, 1995.

[39] A. B. Culaba and M. R.I. Purvis. A methodology for the life cycle and sustainability analysis of manufacturing processes. *Journal of Cleaner Production*, 7(6):435–445, 1999.

[40] L. Dabrowski and M. Wasilczuk. Evaluation of water turbine hydrodynamic thrust bearing performance on the basis of thermoelastohydrodynamic calculations and operational data. *Proceedings of the Institution of Mechanical Engineers, Part J: Journal of Engineering Tribology*, 218(5):413–421, 2004.

[41] J. Paulo Davim, Nuno Marques, and A. Monteiro Monteiro Baptista. Effect of carbon fibre reinforcement in the frictional behaviour of Peek in a water lubricated environment. *Wear*, 250(251):1100–1104, 2001.

[42] Lorena Deleanu and Constantin Georgescu. Water lubrication of PTFE composites. *Industrial Lubrication and Tribology*, 67(1):1–8, 2015.

[43] P Dierickx. The European extremely large telescope (E-ELT). In *Highlights of Spanish Astrophysics 4*, pages 15–28. Highlights of Spanish Astrophysics IV - Proceedings of the 7th Scientific Meeting of the Spanish Astronomical Society, SEA 2006, 2007.

[44] M. R. Doddamani and S. M. Kulkarni. Response of Fly Ash-Reinforced Functionally Graded Rubber Composites Subjected to Mechanical Loading. *Mechanics of Composite Materials*, 48(1):89–100, 2012.

[45] C. L. Dong, C. Q. Yuan, X. Q. Bai, Y. Yang, and X. P. Yan. Study on wear behaviours for NBR/stainless steel under sand water-lubricated conditions. *Wear*, 332-333:1012–1020, 2015.

[46] Conglin Dong, Lichun Shi, Lvzhou Li, Xiuqin Bai, Chengqing Yuan, and Yu Tian. Stick-slip behaviours of water lubrication polymer materials under low speed conditions. *Tribology International*, 106(October 2016):55–61, 2017.

[47] Conglin Dong, Chengqing Yuan, Xiuqin Bai, Xinping Yan, and Zhongxiao Peng. Study on wear behaviour and wear model of nitrile butadiene rubber under water lubricated conditions. *RSC Advances*, 4(36):19034–19042, 2014.

[48] Conglin Dong, Chengqing Yuan, Lei Wang, Wei Liu, Xiuqin Bai, and Xinping Yan. Tribological properties of water-lubricated rubber materials after modification by MoS2 nanoparticles. *Scientific Reports*, 6(October):1–12, 2016.

[49] Wutao Dong, Songlin Nie, and Anqing Zhang. Tribological behavior of PEEK filled with CF/PTFE/graphite sliding against stainless steel surface under water lubrication. *Proceedings of the Institution of Mechanical Engineers, Part J: Journal of Engineering Tribology*, 227(10):1130–1137, 2013.

[50] C A Douglas, G P Harrison, and J P Chick. Life cycle assessment of the Seagen marine current turbine. *Proc. IMechE Part M: J. Engineering for the Maritime Environment*, 222:1–12, 2007.

[51] D Downson. A generalized Reynolds equation for fluid-film lubrication. *Int. J. Mech. Sci.*, 4(4):159–170, 1962.

[52] Ravi S. Duvvuru, Robert L. Jackson, and Jong Wook Hong. Self-adapting microscale surface grooves for hydrodynamic lubrication. *Tribology Transactions*, 52(1):1–11, 2009.

[53] Asa Ekdahl. Life Cycle Assessment on SKF's Spherical Roller Bearing. Technical report, Chalmers University of Technology, 2001.

[54] Islam M. El-Galy, Bassiouny I. Saleh, and Mahmoud H. Ahmed. Functionally Graded Materials Classifications and Development Trends from Industrial Point of View. *SN Applied Sciences*, 1(11):1–23, 2019.

[55] Dagmar Schmidt Etkin. Worldwide analysis of in-port vessel operational lubricant discharges and leakages. *Proceedings of the 33rd AMOP Technical Seminar on Environmental Contamination and Response*, 1(2007):529–553, 2010.

[56] H. P. Evans and R. W. Snidle. Inverse Solution of Reynolds' Equation of Lubrication under Point-Contact Elastohydrodynamic Conditions. *Journal of Tribology*, 103(4):539–546, 1981.

[57] Ahmed Fadhil, Ammar Al-Kawaz, and Ahmed Ehsan. Numerical and Experimental Investigation of Functionally Graded Rubber-Nano-Composite Core for Sandwich Structure. *International Journal of Civil Engineering and Technology*, 9(13):199–206, 2018.

[58] Yajun Fan, Anle Mu, and Tao Ma. Study on the application of energy storage system in offshore wind turbine with hydraulic transmission. *Energy Conversion and Management*, 110:338–346, 2016.

[59] D Farhadi Machekposhti, N Tolou, and J L Herder. A Review on Compliant Joints and Rigid-Body Constant Velocity Universal Joints Toward the Design of Compliant Homokinetic Couplings. *Journal of Mechanical Design*, 137(3):1–12, 2015.

[60] D. Farhadi Machekposhti, N. Tolou, and J. L. Herder. A Review on Compliant Joints and Rigid-Body Constant Velocity Universal Joints Toward the Design of Compliant Homokinetic Couplings. *Journal of Mechanical Design*, 137(3):032301, 2015.

[61] Hui Hui Feng, Chun Dong Xu, and Jie Wan. Mathematical Model and Analysis of the Water-Lubricated Hydrostatic Journal Bearings considering the Translational and Tilting Motions. *Mathematical Problems in Engineering*, 2014, 2014.

[62] Huihui Feng, Shuyun Jiang, and Aimin Ji. Investigations of the static and dynamic characteristics of water-lubricated hydrodynamic journal bearing considering turbulent, thermohydrodynamic and misaligned effects. *Tribology International*, 130(May 2018):245–260, 2019.

[63] Wei Feng, Lei Yin, Yanfeng Han, Jiaxu Wang, Ke Xiao, and Junyang Li. Tribological and physical properties of PTFE-NBR self-lubricating composites under water lubrication. *Industrial Lubrication and Tribology*, 73(1):82–87, 2020.

[64] M. Fesanghary and M. M. Khonsari. On the shape optimization of self-adaptive grooves. *Tribology Transactions*, 54(2):256–264, 2011.

[65] M. Fesanghary and M. M. Khonsari. On the modeling and shape optimization of hydrodynamic flexible-pad thrust bearings. *Proceedings of the Institution of Mechanical Engineers, Part J: Journal of Engineering Tribology*, 227(6):548–558, 2013.

[66] M. Fesanghary and M. M. Khonsari. On the optimum groove shapes for load-carrying capacity enhancement in parallel flat surface bearings: Theory and experiment. *Tribology International*, 67:254–262, 2013.

[67] Charles G. Fey, George E. Totten, Roland J. Bishop, and A. Ashraf. Analysis of common failure modes of axial piston pumps. In *Internation Off-Highway & Powerplant congress & Exposition Milwaukee, Wisconsin*, Milwaukee, 2000. The Engineering Society for Advancing Mobility Land Sea Air and Space.

[68] Niels Frederik and Boudewijn Diepeveen. *On the Application of Fluid Power Transmission in O ff shore Wind Turbines door*. PhD thesis, Delft University of Technology, 2013.

[69] C. P. Gao, G. F. Guo, F. Y. Zhao, T. M. Wang, B. Jim, B. Wetzel, G. Zhang, and Q. H. Wang. Tribological behaviors of epoxy composites under water lubrication conditions. *Tribology International*, 95:333–341, 2016.

[70] Chuanping Gao, Shuguang Fan, Shengmao Zhang, Pingyu Zhang, and Qihua Wang. Enhancement of tribofilm formation from water lubricated PEEK composites by copper nanowires. *Applied Surface Science*, 444:364–376, 2018.

[71] Gengyuan Gao, Zhongwei Yin, Dan Jiang, and Xiuli Zhang. Numerical analysis of plain journal bearing under hydrodynamic lubrication by water. *Tribology International*, 75:31–38, 2014.

[72] Y F Gao, A F Bower, K S Kim, L Lev, and Y T Cheng. The behavior of an elastic-perfectly plastic sinusoidal surface under contact loading. *Wear*, 261(2):145–154, 2006.

[73] Andreas Gebhard, Thomas Bayerl, Alois K. Schlarb, and Klaus Friedrich. Increased wear of aqueous lubricated short carbon fiber reinforced polyetheretherketone (PEEK/SCF) composites due to galvanic fiber corrosion. *Wear*, 268(7-8):871–876, 2010.

[74] Gao Gengyuan, Yin Zhongwei, Jiang Dan, and Zhang Xiuli. CFD analysis of load-carrying capacity of hydrodynamic lubrication on a water-lubricated journal bearing. *Industrial Lubrication and Tribology*, 67(1):30–37, 2015.

[75] A. N. Gent. Crystallization in Natural Rubber. V. Chemically Modified Rubber. *Rubber Chemistry and Technology*, 31(3):519–525, 1958.

[76] B. M. Ginzburg, D. G. Tochil'nikov, V. E. Bakhareva, A. V. Anisimov, and O. F. Kireenko. Polymeric materials for water-lubricated plain bearings. *Russian Journal of Applied Chemistry*, 79(5):695–706, 2006.

[77] B. M. Ginzburg, D. G. Tochil'nikov, A. I. Lyashkov, P. A. Shiyan, V. M. Gaisin, I. V. Permyakov, and V. P. Ponimatkin. Tribological behavior of polyoxymethylene in water-lubricated friction against steel. *Journal of Friction and Wear*, 32(4):246–250, 2011.

[78] B. M. Ginzburg, D. G. Tochil'nikov, P. A. Shiyan, and A. O. Pozdnyakov. Carrying capacity of polymers and polymeric composites in water-lubricated friction against metals. *Journal of Friction and Wear*, 32(3):150–163, 2011.

[79] Sergei Glavatskih and Erik Höglund. Tribotronics-Towards active tribology. *Tribology International*, 41(9-10):934–939, 2008.

[80] D M Gleich, M J L Van Tooren, and Adriaan Beukers. A stress Singularity Approach to Failure Initiation in a Bonded Joint with Varying Bondline Thickness. *Journal of Adhesion Science and Technology*, 15(10):1247–1259, 2001.

[81] Mark Goedkoop, Reinout Heijungs, Mark Huijbregts, An De Schryver, Jaap Struijs, and Rosalie Van Zelm. ReCiPe 2008. *Potentials*, pages 1–44, 2009.

[82] Makoto Gohara, Kei Somaya, Masaaki Miyatake, and Shigeka Yoshimoto. Static characteristics of a water-lubricated hydrostatic thrust bearing using a membrane restrictor. *Tribology International*, 75:111–116, 2014.

[83] A. Golchin, G. F. Simmons, S. Glavatskih, and B. Prakash. Tribological behaviour of polymeric materials in water-lubricated contacts. *Proceedings of the Institution of Mechanical Engineers, Part J: Journal of Engineering Tribology*, 227(8):811–825, 2013.

[84] Arash Golchin, Tan Dat Nguyen, Patrick De Baets, Sergei Glavatskih, and Braham Prakash. Effect of shaft roughness and pressure on friction of polymer bearings in water. *Proceedings of the Institution of Mechanical Engineers, Part J: Journal of Engineering Tribology*, 228(4):371–381, 2014.

[85] Arash Golchin, Alexis Villain, and Nazanin Emami. Tribological behaviour of nanodiamond reinforced UHMWPE in water-lubricated contacts. *Tribology International*, 110(October 2016):195–200, 2017.

[86] Arash Golchin, Alfred Wikner, and Nazanin Emami. An investigation into tribological behaviour of multi-walled carbon nanotube/graphene oxide reinforced UHMWPE in water lubricated contacts. *Tribology International*, 95:156–161, 2016.

[87] R.F.P. Gomes, J.P.A. Nijssen, and R.A.J. van Ostayen. Design of a Compliant Joint Based on Closed Form Pressure Balancing. In *Proceedings of the ASME 2020 International Design Engineering Technical Conferences & Computers and Information in Engineering Conference IDETC/CIE 2020*, 2020.

[88] H. Gonabadi, A. Yadav, and S. J. Bull. The effect of processing parameters on the mechanical characteristics of PLA produced by a 3D FFF printer. *International Journal of Advanced Manufacturing Technology*, 111(3-4):695–709, 2020.

[89] Jiayu Gong, Yong Jin, Zhenglin Liu, Han Jiang, and Maohua Xiao. Study on influencing factors of lubrication performance of water-lubricated micro-groove bearing. *Tribology International*, 129(May 2018):390–397, 2019.

[90] H. L. Groth. Stress Singularities and Fracture at Interface Corners in Bonded Joints. *International Journal of Adhesion and Adhesives*, 8(2):107–113, 1988.

[91] Bosch Group. Radial piston hydraulic motor: Hägglunds CBm. Technical report, Bosch group, 2012.

[92] Alexandre E Guérinot, Spencer P Magleby, Larry L Howell, and Robert H Todd. Compliant Joint Design Principles for High Compressive Load Situations. *Journal of Mechanical Design*, 127(4):774–781, 2005.

[93] Begoña Guezuraga, Rudolf Zauner, and Werner Pölz. Life cycle assessment of two different 2 MW class wind turbines. *Renewable Energy*, 37(1):37–44, 2012.

[94] Zhiwei Guo, Chengqing Yuan, Aixue Liu, and Song Jiang. Study on tribological properties of novel biomimetic material for water-lubricated stern tube bearing. *Wear*, 376-377:911–919, 2017.

[95] A. Hamdi, M. Naït Abdelaziz, N. Aït Hocine, P. Heuillet, and N. Benseddiq. A fracture Criterion of Rubber-Like Materials under Plane Stress Conditions. *Polymer Testing*, 25(8):994–1005, 2006.

[96] B J Hamrock and W J Anderson. Rayleigh Step Journal Bearing, Part II—Incompressible Fluid. *Journal of Lubrication Technology*, 91(4):641–650, 1969.

[97] Naoki Hanawa, Masanori Kuniyoshi, Masaaki Miyatake, and Shigeka Yoshimoto. Static characteristics of a water-lubricated hydrostatic thrust bearing with a porous land region and a capillary restrictor. *Precision Engineering*, 50:293–307, 2017.

[98] R. M. Harris, K. A. Edge, and D. G. Tilley. Predicting the behavior of slipper pads in swashplate-type axial piston pumps. *Journal of Dynamic Systems, Measurement and Control, Transactions of the ASME*, 118(1):41–47, 1996.

[99] Tedric A Harris, Roger M Barnsby, and Tedric A Harris Member. Tribological Performance Prediction of Aircraft Gas Turbine Mainshaft Ball Bearings Tribological Performance Prediction of Aircraft Gas Turbine Mainshaft Ball Bearingso. *Tribology Transactions*, 41(1):60–68, 1998.

[100] Alan Hase, Hiroshi Mishina, and Masaki Wada. Fundamental study on early detection of seizure in journal bearing by using acoustic emission technique. *Wear*, 346-347:132–139, 2016.

[101] Niels Heinrichson. *On the Design of Tilting-Pad Thrust Bearings*. Phd dissertation, Technical University of Denmark, 2007.

[102] Simon Henein, Peter Spanoudakis, Serge Droz, Leif I Myklebust, and Emmanuel Onillon. Flexure pivot for aerospace mechanisms. *European Space Agency, (Special Publication) ESA SP*, pages 285–288, 2003.

[103] Harish Hirani and Manish Verma. Tribological study of elastomeric bearings for marine propeller shaft system. *Tribology International*, 42(2):378–390, 2009.

[104] Kenneth Holmberg and Ali Erdemir. Influence of tribology on global energy consumption, costs and emissions. *Friction*, 5(3):263–284, 2017.

[105] G.A. Holzapfel. *Nonlinear Solid Mechanics: A Continuum Approach for Engineering*. Wiley, 2000.

[106] C. O. Horgan and A. M. Chan. Pressurized Hollow Cylinder or Disk Problem for Functionally Graded Isotropic Linearly Elastic Materials. *Journal of Elasticity*, 55(1):43–59, 1999.

[107] S. Hother-Lushington. Water lubricated bearings. *Tribology International*, 9(6):257–260, 1976.

[108] L L Howell and A Midha. A Method for the Design of Compliant Mechanisms With Small-Length Flexural Pivots. *Journal of Mechanical Design*, 116(1):280–290, 1994.

[109] L.L. Howell. *Compliant Mechanisms*. Wiley & Sons, 2001.

[110] Xijin Hua, Jiaxu Wang, Juanjuan Zhu, and Wen Ji Liu. Study on tribological behavior of water-lubricated bearings. *Journal of Advanced Manufacturing Systems*, 7(1):115–121, 2008.

[111] L. Huanlong, K. Jian, W. Guozhi, and Y. Lanying. Research on the lubrication characteristics of water hydraulic slipper friction pairs. *Proceedings of the Institution of Mechanical Engineers, Part C: Journal of Mechanical Engineering Science*, 220(10):1559–1567, 2006.

[112] C. Iliev. On the wear behaviour of silicon nitride sliding against metals in water. *Industrial Lubrication and Tribology*, 62(1):32–36, 2010.

[113] Keita Ishizaki and Masaru Nakano. Reduction of CO2 emissions and cost analysis of ultra-low viscosity engine oil. *Lubricants*, 6(4):1–13, 2018.

[114] Robert Jackson and Jiang Lei. Hydrodynamically Lubricated and Grooved Biomimetic Self-Adapting Surfaces. *Journal of Functional Biomaterials*, 5(2):78–98, 2014.

[115] Robert L. Jackson. Self adapting mechanical step bearings for variations in load. *Tribology Letters*, 20(1):11–20, 2005.

[116] Brian D Jensen and Larry L Howell. The modeling of cross-axis flexural pivots. *Mechanism and Machine Theory*, 37(5):461–476, 2002.

[117] J. H. Jia, H. D. Zhou, S. Q. Gao, and J. M. Chen. A comparative investigation of the friction and wear behavior of polyimide composites under dry sliding and water-lubricated condition. *Materials Science and Engineering A*, 356(1-2):48–53, 2003.

[118] Jun Hong Jia, Jian Min Chen, Hui Di Zhou, Jing Bo Wang, and Hua Zhou. Friction and wear properties of bronze-graphite composite under water lubrication. *Tribology International*, 37(5):423–429, 2004.

[119] Junhong Jia, Jianmin Chen, Huidi Zhou, Litian Hu, and Lei Chen. Comparative investigation on the wear and transfer behaviors of carbon fiber reinforced polymer composites under dry sliding and water lubrication. *Composites Science and Technology*, 65(7-8):1139–1147, 2005.

[120] Y Jia. Gaussian and Mean Curvatures. Technical report, Iowa State University, 2018.

[121] Laurent Jordi, Christo Iliev, and Traugott E. Fischer. Lubrication of silicon nitride and silicon carbide by water: Running in, wear and operation of sliding bearings. *Tribology Letters*, 17(3):367–376, 2004.

[122] Kamat. Quintuplex Plungerpumpe K 120000 - 5G Maßzeichnung K 120000 - 5G Dimension drawing. Technical report, Kamat, 2018.

[123] Dongwoo Kang and Daegab Gweon. Analysis and design of a cartwheel-type flexure hinge. *Precision Engineering*, 37(1):33–43, 2013.

[124] Yuan Kang, Jian Lin Lee, Hua Chih Huang, Ching Yuan Lin, Hsing Han Lee, De Xing Peng, and Ching Chu Huang. Design for static stiffness of hydrostatic plain bearings: Constant compensations. *Industrial Lubrication and Tribology*, 63(3):178–191, 2011.

[125] T Kazama. Mixed Lubrication Simulation of Hydrostatic Spherical Bearings for Hydraulic Piston Pumps and Motors. *Journal of Advanced Mechanical Design, Systems, and Manufacturing*, 2(1):71–82, 2008.

[126] Charles J Kim, Yong-Mo Moon, and Sridhar Kota. A Building Block Approach to the Conceptual Synthesis of Compliant Mechanisms Utilizing Compliance and Stiffness Ellipsoids. *Journal of Mechanical Design*, 130(2):1–11, 2008.

[127] Raymond Kim, Stephen Balakirsky, Konrad Ahlin, Matthew Marcum, and Anirban Mazumdar. Enhancing Payload Capacity with Dual-Arm Manipulation and Adaptable Mechanical Intelligence. *ASME J Mech Robot*, 13(2), 2021.

[128] E. Koc, C. J. Hooke, and K. Y. Li. Slipper balance in axial piston pumps and motors. *Journal of Tribology*, 114(4):766–772, 1992.

[129] P. Reinier Kuppens, Just L. Herder, and Nima Tolou. Permanent Stiffness Reduction by Thermal Oxidation of Silicon. *Journal of Microelectromechanical Systems*, 28(5):900–909, 2019.

[130] C. A. Laukiavich, M. J. Braun, and A. J. Chandy. An Investigation into the Thermal Effects on a Hydrodynamic Bearing's Clearance. *Tribology Transactions*, 58(6):980–1001, 2015.

[131] Qiang Li, Shuo Zhang, Yujun Wang, Weiwei Xu, Zengli Wang, and Zhenbo Wang. Dynamic characteristics of water-lubricated journal bearings: Part 1: Full 3D transient hydrodynamic force models using structured mesh movement algorithm. *Mechanics and Industry*, 20(4):0–16, 2019.

[132] Q.M. Li. Strain Energy Density Failure Criterion. *International Journal of Solids and Structures*, 28:6997–7013, 2001.

[133] Xiuqing Li, Yimin Gao, Qingxia Yang, Wu Pan, Yefei Li, Zhichao Zhong, and Liancheng Song. Evaluation of tribological behavior of B4C-hBN ceramic composites under water-lubricated condition. *Ceramics International*, 41(6):7387–7393, 2015.

[134] Xingxin Liang, Zhenglin Liu, Chengqing Yuan, Wu Ouyang, and Xinping Yan. Design and performance analysis of a water lubricated tilting pad thrust bearing. *Proceedings of the International Offshore and Polar Engineering Conference*, 2016-Janua:908–913, 2016.

[135] Xingxin Liang, Xinping Yan, Wu Ouyang, Robert J.K. Wood, Fuming Kuang, Zhenglin Liu, and Xincong Zhou. Comparison of measured and calculated water film thickness of a water-lubricated elastically supported tilting pad thrust bearing. *Surface Topography: Metrology and Properties*, 7(4), 2019.

[136] Xingxin Liang, Xinping Yan, Wu Ouyang, Robert J.K. Wood, and Zhenglin Liu. Thermo-Elasto-Hydrodynamic Analysis and Optimization of Rubber-Supported Water-Lubricated Thrust Bearings with Polymer Coated Pads. *Tribology International*, 138:365–379, 2019.

[137] Zhong liang Xie, Na Ta, and Zhu shi Rao. The lubrication performance of water lubricated bearing with consideration of wall slip and inertial force. *Journal of Hydrodynamics*, 29(1):52–60, 2017.

[138] Xiaohui Lin, Shuyun Jiang, Chibin Zhang, and Xiang Liu. Thermohydrodynamic analysis of high speed water-lubricated spiral groove thrust bearing considering effects of cavitation, inertia and turbulence. *Tribology International*, 119(November 2017):645–658, 2018.

[139] Hong ling Qin, Xin cong Zhou, Xin ze Zhao, Jing tang Xing, and Zhi ming Yan. A new rubber/UHMWPE alloy for water-lubricated stern bearings. *Wear*, 328-329:257–261, 2015.

[140] Wojciech Litwin. Water-lubricated bearings of ship propeller shafts - Problems, experimental tests and theoretical investigations. *Polish Maritime Research*, 16(4):41–49, 2009.

[141] Wojciech Litwin. Influence of surface roughness topography on properties of water-lubricated polymer bearings: Experimental research. *Tribology Transactions*, 54(3):351–361, 2011.

[142] Wojciech Litwin and Artur Olszewski. Water-lubricated sintered bronze journal bearings-Theoretical and experimental research. *Tribology Transactions*, 57(1):114–122, 2013.

[143] Gang Liu and Ming Li. Lubrication Characteristics of Water-Lubricated Rubber Bearings With Partial Wear. *Journal of Fluids Engineering*, 142(February):1–10, 2020.

[144] Hong Liu, Tingmei Wang, and Qihua Wang. Tribological properties of thermosetting polyimide/TiO 2 nanocomposites under dry sliding and water-lubricated conditions. *Journal of Macromolecular Science, Part B: Physics*, 51(11):2284–2296, 2012.

[145] Shibing Liu and Bingen Yang. A new model of water-lubricated rubber bearings for vibration analysis of flexible multistage rotor systems. *Journal of Sound and Vibration*, 349(June):230–258, 2015.

[146] Z Liu, Y Wang, L Cai, Y Zhao, Q Cheng, and X Dong. A review of hydrostatic bearing system: Researches and applications. *Advances in Mechanical Engineering*, 9(10):1–27, 2017.

[147] Dun Lu, Kejia Liu, Wanhua Zhao, and Bingheng Lu. Thermal Characteristics of Water-Lubricated Ceramic Hydrostatic Hydrodynamic Hybrid Bearings. *Tribology Letters*, 63(2):1–10, 2016.

[148] Chris Lusty, Nicola Y Bailey, and Patrick S Keogh. A Comparison of the Capacity for Precise Motion Control Between Hinged Joints and Flexure Joints. In *Volume 4A: Dynamics, Vibration, and Control*, pages 1–8. American Society of Mechanical Engineers, 2017.

[149] Hatim Machrafi. *Green Energy and Technology*. Springer, 2012.

[150] Pai R Majumdar B. C. and Hargreaves D J. Analysis of water-lubricated journal bearings with. *Proc. Instn Mech. Engrs Vol. 218 Part J: J. Engineering tribology*, 218:135–146, 2003.

[151] Javier Martin and Mathieu Robert. Novel Flexible Pivot with Large Angular Range and Small Center Shift to be Integrated into a Bio-Inspired Robotic Hand. *Journal of Intelligent Material Systems and Structures*, 22(13):1431–1437, 2011.

[152] R. McKenna, P. Ostman v.d. Leye, and W. Fichtner. Key challenges and prospects for large wind turbines. *Renewable and Sustainable Energy Reviews*, 2015.

[153] Marcelle C. McManus, Geoffrey P. Hammond, and Clifford R. Burrows. Life-cycle assessment of mineral and rapeseed oil in mobile hydraulic systems. *Journal of Industrial Ecology*, 7(3-4):163–177, 2003.

[154] H. Meng, G. X. Sui, G. Y. Xie, and R. Yang. Friction and wear behavior of carbon nanotubes reinforced polyamide 6 composites under dry sliding and water lubricated condition. *Composites Science and Technology*, 69(5):606–611, 2009.

[155] A. Mimaroglu, H. Unal, and A. Ozel. Tribological performance of polyetheretherketone and its composites under water environment. *Macromolecular Symposia*, 327(1):108–113, 2013.

[156] S.P. Mulders. *Wind Turbine Control: Advances for Load Mitigations and Hydraulic Drivetrains*. PhD thesis, Delft University of Technology, 2020.

[157] Susumu Nakano, Tadaharu Kishibe, Tomoaki Inoue, and Hiroyuki Shiraiwa. An advanced microturbine system with water-lubricated bearings. *International Journal of Rotating Machinery*, 2009, 2009.

[158] M Naves, R.G.K.M. Aarts, and D M Brouwer. Large stroke high off-axis stiffness three degree of freedom spherical flexure joint. *Precision Engineering*, 56(November 2018):422–431, 2019.

[159] M.J. Neale. *Tribology Handbook*. The Butterworth group, 1 edition, 1973.

[160] T.D. Nguyen, J. Sukumaran, J. De Pauw, and P. De Baets. Tribological Behaviour of Polymer Bearings Under Dry and Water Lubrication. *International Journal Sustainable Construction & Design*, 4(2), 2013.

[161] S. L. Nie, G. H. Huang, and Y. P. Li. Tribological study on hydrostatic slipper bearing with annular orifice damper for water hydraulic axial piston motor. *Tribology International*, 39(11):1342–1354, 2006.

[162] J Nijenhuis, R Hamelinck, B Braam, and M Cayrel. Meeting highest performance requirements for lowest price and mass for the M1 segment support unit for E-ELT. *Ground-based and Airborne Telescopes III*, 7733, 2010.

[163] J.P.A. Nijssen, G. Radaelli, J.L. Herder, J.B. Ring, and C.J. Kim. Spatial Concept Synthesis of Compliant Mechanisms Utilizing Non-linear Eigentwist Characterization. In *Proceedings of the ASME Design Engineering Technical Conference*, volume 5A-2018, 2018.

[164] J.P.A. Nijssen and R.A.J. van Ostayen. Passive Shape Shifting: A Compliant Design Approach for Full Film Bearings. *Proceedings of the iMeche, part C: Journal of Mechanical Engineering Science*, 2021.

[165] Vlastimir Nikoli, Shahin Sajjadi, Dalibor Petkovi, Shahaboddin Shamshirband, Ž Ć, and Lip Yee. Design and state of art of innovative wind turbine systems. *Renewable and Sustainable Energy Reviews*, 61:258–265, 2016.

[166] Changxiong Ning. Simulation Analysis on Lubrication Performance of Water-lubricated Elastic Supported Tilting Pad Thrust Bearing. *2019 5th International Conference on Transportation Information and Safety (ICTIS)*, pages 437–445, 2019.

[167] Q. L. Niu, X. H. Zheng, W. W. Ming, and M. Chen. Friction and Wear Performance of Titanium Alloys against Tungsten Carbide under Dry Sliding and Water Lubrication. *Tribology Transactions*, 56(1):101–108, 2013.

[168] Michael Nosonosky and Bharat Bhushan. green tribology. *Phil. Trans. R. Soc. A*, 368:4677–4694, 2010.

[169] Paulina Nowak, Karolina Kucharska, and Marian Kamiński. Ecological and Health Effects of Lubricant Oils Emitted into the Environment. *International Journal of Environmental Research and Public Health*, 16(16):3002, 2019.

[170] R. Orndorff, L. Foster, and R. Sheppert. From lab to field: New high performance water lubricated. *Proceedings of the World Tribology Congress III - 2005*, pages 55–56, 2005.

[171] R.L. Orndorff. Water-lubricated rubber bearings, history and new developments. *Naval engineers journal*, pages 39–52, 1985.

[172] Rammohan S. Pai and R. Pai. Non-linear transient analysis of multiple axial groove water-lubricated journal bearings. *Proceedings of the Institution of Mechanical Engineers, Part J: Journal of Engineering Tribology*, 222(4):549–557, 2008.

[173] Rammohan S. Pai and R. Pai. Stability of four-axial and six-axial grooved water-lubricated journal bearings under dynamic load. *Proceedings of the Institution of Mechanical Engineers, Part J: Journal of Engineering Tribology*, 222(5):683–691, 2008.

[174] Sebastiaan Paul Mulders, Niels Frederik Boudewijn Diepeveen, and Jan Willem Van Wingerden. Control design, implementation, and evaluation for an in-field 500 kW wind turbine with a fixed-displacement hydraulic drivetrain. *Wind Energy Science*, 3(2):615–638, 2018.

[175] En Gao Peng, Zheng Lin Liu, Yu Zhong Tian, and Fang Lan. Experimental study on friction-induced vibration of water-lubricated rubber stern bearing at low speed. *Applied Mechanics and Materials*, 44-47:409–413, 2011.

[176] Walter D. Pilkey, Deborah F. Pilkey, and Zhuming Bi. *Peterson's Stress Concentration Factors*. Wiley, 4th edition, 2020.

[177] Henk Polinder, Frank F A Van Der Pijl, Gert-jan De Vilder, and Peter J Tavner. Comparison of Direct-Drive and Geared Generator Concepts for Wind Turbines. *IEEE Transaction on energy conversion*, 21(3):725–733, 2006.

[178] Franci Pusavec, Peter Krajnik, and Janez Kopac. Transitioning to sustainable production - Part I: application on machining technologies. *Journal of Cleaner Production*, 18(2):174–184, 2010.

[179] Z. Rasheva, G. Zhang, and Th Burkhart. A correlation between the tribological and mechanical properties of short carbon fibers reinforced PEEK materials with different fiber orientations. *Tribology International*, 43(8):1430–1437, 2010.

[180] Michael Rohmer, Luis San Andrés, and Scott Wilkinson. Static load performance of a water-lubricated hydrostatic thrust bearing. *Journal of Engineering for Gas Turbines and Power*, 140(6):1–11, 2018.

[181] Liane Roldo, Ivan Komar, and Nenad Vulić. Design and materials selection for environmentally friendly ship propulsion system. *Strojniski Vestnik/Journal of Mechanical Engineering*, 59(1):25–31, 2013.

[182] Jelle Rommers, Volkert van der Wijk, and Just L. Herder. A new type of spherical flexure joint based on tetrahedron elements. *Precision Engineering*, 71(February):130–140, 2021.

[183] Mink Ros. Triboregister: wrijvingscoëfficienten en slijtfactoren. Technical report, Ministerie van Verkeer en Waterstaat, 1996.

[184] Sabrina G.S.A. Rothausen and Declan Conway. Greenhouse-gas emissions from energy use in the water sector. *Nature Climate Change*, 1(4):210–219, 2011.

[185] W. B. Rowe. *Hydrostatic, Aerostatic and Hybrid Bearing Design*. Elsevier, 1st editio edition, 2013.

[186] J. Seabra and D. Bearthe. Elastohydrodynamic Point Contacts Part 1: Formulation and Numerical Solution. *Wear*, (130):301–318, 1989.

[187] Paolo Silva, Antonio Giuffrida, Nicola Fergnani, Ennio Macchi, Matteo Cantù, Roberto Suffredini, Massimo Schiavetti, and Gianluca Gigliucci. Performance prediction of a multi-MW wind turbine adopting an advanced hydrostatic transmission. *Energy*, 64:450–461, 2014.

[188] Varun Sivaram, John O Dabiri, David M Hart, and Nathaniel Austin. The Need for Continued Innovation in Solar , Wind , and Energy Storage. *Joule*, 2(9):1639–1642, 2018.

[189] W. V. SMITH. Material Selection Criteria for Water Lubrication. *wear*, 25((1973)):139–153, 1973.

[190] Zhixiang Song, Fei Guo, Ying Liu, Xiangfeng Liu, and Yuming Wang. Inertia Effect on the Load Capacity of Large Water-Lubricated Thrust Bearing. *Tribology Transactions*, 61(1):111–121, 2018.

[191] Dave Sonneveld, Joep Nijssen, and Ron van Ostayen. Compliant joints utilizing the principle of closed form pressure balancing. *Submitted to the Journal of Mechanisms and Machine Theory*, 2021.

[192] G.W. Stachowiak and A.W. Batchelor. *Engineering Tribology*. Elsevier, 1993.

[193] Gwidon W Stachowiak and Andrew W Batchelor. Engineering Tribology. In *Engineering Tribology (Fourth Edition)*. Butterworth-Heinemann, Boston, fourth edi edition, 2014.

[194] International Standard. International Standard Environmental management — Life cycle. Technical report, ISO, 2014.

[195] Jennifer R. Stokes and Arpad Horvath. Energy and air emission effects of water supply. *Environmental Science and Technology*, 43(8):2680–2687, 2009.

[196] Jacob Sukumaran, Vanessa Rodriguez Fereira, Yeczain Perez Delgado, Patrick De Baets, Mátyás Andó, H Dhieb, and Patric Neis. A review on water lubrication of polymers. *Sustainable Construction and Design*, 3(2):144, 2012.

[197] M. Sumer, H. Unal, and A. Mimaroglu. Evaluation of tribological behaviour of PEEK and glass fibre reinforced PEEK composite under dry sliding and water lubricated conditions. *Wear*, 265(7-8):1061–1065, 2008.

[198] A. Z. Syahir, N. W.M. Zulkifli, H. H. Masjuki, M. A. Kalam, Abdullah Alabdulkarem, M. Gulzar, L. S. Khuong, and M. H. Harith. A review on bio-based lubricants and their applications. *Journal of Cleaner Production*, 168:997–1016, 2017.

[199] Bruce L. Tai, David A. Stephenson, and Albert J. Shih. Improvement of surface flatness in face milling based on 3-D holographic laser metrology. *International Journal of Machine Tools and Manufacture*, 51(6):483–490, 2011.

[200] Hongbin Tang, Zichao Wang, and You Wu. A multi-fault diagnosis method for piston pump in construction machinery based on information fusion and PSO-SVM. *Journal of Vibroengineering*, 21(7):1904–1916, 2019.

[201] Qunguo Tang, Jingtian Chen, and Liping Liu. Tribological behaviours of carbon fibre reinforced PEEK sliding on silicon nitride lubricated with water. *Wear*, 269(7-8):541–546, 2010.

[202] Y Tian, B Shirinzadeh, D Zhang, and Y Zhong. Three flexure hinges for compliant mechanism designs based on dimensionless graph analysis. *Precision Engineering*, 34(1):92–100, 2010.

[203] S.P. Timoshenko and J.M. Gere. *Theory of Elastic Stability*. McGraw-Hill, second edi edition, 1981.

[204] Brian P Trease, Yong-Mo Moon, and Sridhar Kota. Design of Large-Displacement Compliant Joints. *Journal of Mechanical Design*, 127(4):788–798, 2005.

[205] I. Tzanakis, M. Hadfield, B. Thomas, S. M. Noya, I. Henshaw, and S. Austen. Future perspectives on sustainable tribology. *Renewable and Sustainable Energy Reviews*, 16(6):4126–4140, 2012.

[206] Gururaja Udupa, S. Shrikantha Rao, and K.V. Gangadharan. Functionally Graded Composite Materials: An Overview. *Procedia Materials Science*, 5:1291–1299, 2014.

[207] H. Unal and A. Mimaroglu. Friction and wear characteristics of PEEK and its composite under water lubrication. *Journal of Reinforced Plastics and Composites*, 25(16):1659–1667, 2006.

[208] Hari Shankar Vadivel, Arash Golchin, and Nazanin Emami. Tribological behaviour of carbon filled hybrid UHMWPE composites in water. *Tribology International*, 124(March):169–177, 2018.

[209] A. Van Beek and A. Segal. Rubber Supported Hydrostatic Thrust Bearings with Rigid Bearing Surfaces. *Tribology International*, 30(1):47–52, 1997.

[210] Anton van Beek. *Advanced Engineering Design Lifetime Performance and Reliability*. TU Delft, 6th editio edition, 2015.

[211] R A J van Ostayen, Anton van Beek, and Mink Ros. A mathematical model of the hydro-support: an elasto-hydrostatic thrust bearing with mixed lubrication. *Tribology International*, 37(8):607–616, 2004.

[212] Ron A J van Ostayen, Anton van Beek, and Alex de Kraker. Lift-Off of the Hydrostatic Thrust Bearing with Elastic Surfaces. In *2004 AIMETA International Tribology Conference*, pages 14–17, 2004.

[213] Ron A.J. Van Ostayen, Anton Van Beek, and Mink Ros. A mathematical model of the hydro-support: An elasto-hydrostatic thrust bearing with mixed lubrication. *Tribology International*, 37(8):607–616, 2004.

[214] Ron A.J. Van Ostayen, Anton Van Beek, and Mink Ros. A Parametric Study of the Hydro-Support. *Tribology International*, 37(8):617–625, 2004.

[215] Ron A.J. Van Ostayen, Anton Van Beek, and Mink Ros. A parametric study of the hydro-support. *Tribology International*, 37(8):617–625, 2004.

[216] Christine Vehar, Sridhar Kota, and Robert Dennis. Closed-loop tape springs as fully compliant mechanisms -preliminary investigations. *Proceedings of the ASME Design Engineering Technical Conference*, 2 B(January):1023–1032, 2004.

[217] Venkatasubramanian Kalpathy Venkiteswaran and Hai-Jun Su. A Versatile 3R Pseudo-Rigid-Body Model for Initially Curved and Straight Compliant Beams of Uniform Cross Section. *Journal of Mechanical Design*, 140(9):1–8, 2018.

[218] Centraal Bureau voor de Statistiek. Hernieuwbare energie in Nederland 2019. Technical report, CBS, 2019.

[219] Anying Wang, Shuai Yan, Bin Lin, Xiaofeng Zhang, and Xiaoxue Zhou. Aqueous lubrication and surface microstructures of engineering polymer materials (PEEK and PI) when sliding against Si3N4. *Friction*, 5(4):414–428, 2017.

[220] Jian Zhang Wang, Feng Yuan Yan, and Qun Ji Xue. Tribological behaviors of some polymeric materials in sea water. *Chinese Science Bulletin*, 54(24):4541–4548, 2009.

[221] Jianzhang Wang, Beibei Chen, Ning Liu, Gaofeng Han, and Fengyuan Yan. Combined effects of fiber/matrix interface and water absorption on the tribological behaviors of water-lubricated polytetrafluoroethylene-based composites reinforced with carbon and basalt fibers. *Composites Part A: Applied Science and Manufacturing*, 59:85–92, 2014.

[222] Jianzhang Wang, Fengyuan Yan, and Qunji Xue. Tribological behavior of PTFE sliding against steel in sea water. *Wear*, 267(9-10):1634–1641, 2009.

[223] Jiaxu Wang, Yanfeng Han, Guangwu Zhou, Xiao Ke, Yi Qin, and Song Wu. Numerical analysis of concave-slab type water lubricated rubber alloy bearings' lubrication. *Applied Mechanics and Materials*, 86:805–808, 2011.

[224] Lin Wang, Shiyuan Pei, Xianzhi Xiong, and Hua Xu. Investigation of the combined influence of turbulence and thermal effects on the performance of water-lubricated hybrid bearings with circumferential grooves and stepped recesses. *Proceedings of the Institution of Mechanical Engineers, Part J: Journal of Engineering Tribology*, 228(1):53–68, 2014.

[225] Nan Wang, Qingfeng Meng, Pengpeng Wang, Tao Geng, and Xiaoyang Yuan. Experimental research on film pressure distribution of water-lubricated rubber bearing with multiaxial grooves. *Journal of Fluids Engineering, Transactions of the ASME*, 135(8):1–6, 2013.

[226] Ruyi Wang, Zhenglin Liu, and Yong Jin. Research on lubrication properties of water-lubricated rubber bearing based on fluid structure interaction. *Applied Mechanics and Materials*, 79:159–165, 2011.

[227] Shiwei Wang, Xiaoniu Yang, Wanli Su, and Yunhui Li. Fabrication of polyurethane-based composites used in water-lubricated bearings. *Advances in Polymer Technology*, 33(4):1–6, 2014.

[228] X. Wang, K. Kato, and K. Adachi. Running-in effect on the load-carrying capacity of a water-lubricated SiC thrust bearing. *Proceedings of the Institution of Mechanical Engineers, Part J: Journal of Engineering Tribology*, 219(2):117–124, 2005.

[229] Xiaolei Wang, Koshi Adachi, Katsunori Otsuka, and Koji Kato. Optimization of the surface texture for silicon carbide sliding in water. *Applied Surface Science*, 253(3):1282–1286, 2006.

[230] Xiaolei Wang, Koji Kato, and Koshi Adachi. The critical condition for the transition from HL to ML in water-lubricated SiC. *Tribology Letters*, 16(4):253–258, 2004.

[231] Xingjian Wang, Siru Lin, Shaoping Wang, Zhaomin He, and Chao Zhang. Remaining useful life prediction based on the Wiener process for an aviation axial piston pump. *Chinese Journal of Aeronautics*, 29(3):779–788, 2016.

[232] Yanzhen Wang, Zhongwei Yin, Hulin Li, Gengyuan Gao, and Xiuli Zhang. Friction and wear characteristics of ultrahigh molecular weight polyethylene (UHMWPE) composites containing glass fibers and carbon fibers under dry and water-lubricated conditions. *Wear*, 380-381:42–51, 2017.

[233] Yongxin Wang, Liping Wang, and Qunji Xue. Improvement in the tribological performances of Si3N4, SiC and WC by graphite-like carbon films under dry and water-lubricated sliding conditions. *Surface and Coatings Technology*, 205(8-9):2770–2777, 2011.

[234] You Qiang Wang, Xiu Jiang Shi, and Li Jing Zhang. Experimental and numerical study on water-lubricated rubber bearings. *Industrial Lubrication and Tribology*, 66(2):282–288, 2014.

[235] You Qiang Wang and Li Jing Zhang. Characteristics and outline of water-lubricated thordon bearing. *Advanced Materials Research*, 496:355–358, 2012.

[236] Zhiqiang Wang and Dianrong Gao. Comparative investigation on the tribological behavior of reinforced plastic composite under natural seawater lubrication. *Materials and Design*, 51:983–988, 2013.

[237] Zhiqiang Wang and Dianrong Gao. Friction and wear properties of stainless steel sliding against polyetheretherketone and carbon-fiber-reinforced polyetheretherketone under natural seawater lubrication. *Materials and Design*, 53:881–887, 2014.

[238] Zhiqiang Wang and Dianrong Gao. Friction and wear properties of stainless steel sliding against polyetheretherketone and carbon-fiber-reinforced polyetheretherketone under natural seawater lubrication. *Materials and Design*, 53:881–887, 2014.

[239] Zhiqiang Wang, Jing Ni, and Dianrong Gao. Combined effect of the use of carbon fiber and seawater and the molecular structure on the tribological behavior of polymer materials. *Friction*, 6(2):183–194, 2018.

[240] Ben A. Wender, Rider W. Foley, Troy A. Hottle, Jathan Sadowski, Valentina Prado-Lopez, Daniel A. Eisenberg, Lise Laurin, and Thomas P. Seager. Anticipatory life-cycle assessment for responsible research and innovation. *Journal of Responsible Innovation*, 1(2):200–207, 2014.

[241] G. Wernet, C. Bauer, B. Steuging, J. Reinhard, E. Moreno-Ruiz, and B. Weidema. The ecoinvent database version 3 (part 1): overview and methodology. *The international Journal of Life Cycle Assessment,*, 21(21):1218–1230, 2016.

[242] D H Wiersma, S E Boer, R G K M Aarts, and D M Brouwer. Design and Performance Optimization of Large Stroke Spatial Flexures. *Journal of Computational and Nonlinear Dynamics*, 9(1), 2014.

[243] J. Wu and X. H. Cheng. The tribological properties of Kevlar pulp reinforced epoxy composites under dry sliding and water lubricated condition. *Wear*, 261(11-12):1293–1297, 2006.

[244] Guo Xiang, Yanfeng Han, Renxiang Chen, Jiaxu Wang, Xiaokang Ni, and Ke Xiao. A hydrodynamic lubrication model and comparative analysis for coupled microgroove journal-thrust bearings lubricated with water. *Proceedings of the Institution of Mechanical Engineers, Part J: Journal of Engineering Tribology*, 0(0):1–16, 2019.

[245] Enle Xu, Yue Wang, Jianeng Wu, Shichang Xu, Yuxin Wang, and Shichang Wang. Investigations on the applicability of hydrostatic bearing technology in a rotary energy recovery device through CFD simulation and validating experiment. *Desalination*, 383:60–67, 2016.

[246] Pei Xu, Yu Jingjun, Zong Guanghua, and Bi Shusheng. The Stiffness Model of Leaf-Type Isosceles-Trapezoidal Flexural Pivots. *Journal of Mechanical Design*, 130(8):823031–823036, 2008.

[247] Pei Xu, Yu Jingjun, Zong Guanghua, Bi Shusheng, and Yu Zhiwei. Analysis of Rotational Precision for an Isosceles-Trapezoidal Flexural Pivot. *Journal of Mechanical Design*, 130(5), 2008.

[248] Yuji Yamamoto and Masaaki Hashimoto. Friction and wear of water lubricated PEEK and PPS sliding contacts Part 2. Composites with carbon or glass fibre. *Wear*, 257(1-2):181–189, 2004.

[249] Yuji Yamamoto and Masaaki Hashimoto. Friction and wear of water lubricated PEEK and PPS sliding contacts Part 2. Composites with carbon or glass fibre. *Wear*, 257(1-2):181–189, 2004.

[250] Jun Yang, Zhenglin Liu, Xingxin Liang, Jian Wang, and Qichao Cheng. Research on friction vibration of marine water lubricated rubber bearing. *Tribology Online*, 13(3):108–118, 2018.

[251] V A Yastrebov, G Anciaux, and J F Molinari. The contact of elastic regular wavy surfaces revisited. *Tribology Letters*, 56:171–183, 2014.

[252] Xiaoyan Ye, Jing Wang, Desheng Zhang, Lanqian Hu, and Xunan She. Experimental research of journal orbit for water-lubricated bearing. *Mathematical Problems in Engineering*, 2016, 2016.

[253] Fanglong Yin, Songlin Nie, Zhenghua Zhang, and Xiaojun Zhang. Research on the sliding bearing pair of water hydraulic axial piston pump. *Proceedings of the Institution of Mechanical Engineers, Part C: Journal of Mechanical Engineering Science*, 227(9):2049–2063, 2013.

[254] S. Yoshimoto, S. Oshima, S. Danbara, and T. Shitara. Stability of water-lubricated, hydrostatic, conical bearings with spiral grooves for high-speed spindles. *Journal of Tribology*, 124(2):398–405, 2002.

[255] Sirong Yu, Haixia Hu, and Jian Yin. Effect of rubber on tribological behaviors of polyamide 66 under dry and water lubricated sliding. *Wear*, 265(3-4):361–366, 2008.

[256] Xiuli Zhang, Gengyuan Gao, Zhongwei Yin, Yanzhen Wang, and Chao Gao. Numerical analysis and experimental research on load carrying capacity of water-lubricated tilting-pad thrust bearings. *Mechanics and Industry*, 19(2), 2018.

[257] Xiuli Zhang, Zhongwei Yin, Gengyuan Gao, and Zheng Li. Determination of stiffness coefficients of hydrodynamic water-lubricated plain journal bearings. *Tribology International*, 85:37–47, 2015.

[258] Xiuli Zhang, Zhongwei Yin, Dan Jiang, and Gengyuan Gao. The design of hydrodynamic water-lubricated step thrust bearings using CFD method. *Mechanics and Industry*, 15(3):197–206, 2014.

[259] Xiuli Zhang, Zhongwei Yin, Dan Jiang, Gengyuan Gao, Yanzhen Wang, and Xinbo Wang. Load carrying capacity of misaligned hydrodynamic water-lubricated plain journal bearings with rigid bush materials. *Tribology International*, 99(March):1–13, 2016.

[260] Y Zhang, S Finger, and S Behrens. *Introduction to Mechanisms*. Carnegie Mellon University, Pennsylvania, 2010.

[261] Gai Zhao, Tingmei Wang, and Qihua Wang. Friction and wear behavior of the polyurethane composites reinforced with potassium titanate whiskers under dry sliding and water lubrication. *Journal of Materials Science*, 46(20):6673–6681, 2011.

[262] Shengdun Zhao, Tong Guo, Yanghuiwen Yu, Peng Dong, Chen Liu, and Wanqiang Chen. Design and experimental studies of a novel double-row radial piston pump. *Proc ImMechE part C: J. Mechanical Engineering Science*, 231(28):1884–1896, 2017.

[263] Guangwu Zhou, Xiongwei Mi, Jiaxu Wang, and Rukang Hu. Experimental comparison between the Stribeck curves of water lubricated rubber bearing with straight and spiral grooves. *Industrial Lubrication and Tribology*, 70(7):1326–1330, 2018.

[264] Guangwu Zhou, Jiaxu Wang, Yanfeng Han, Bo Wei, Baoping Tang, and Ping Zhong. An Experimental Study on Film Pressure Circumferential Distribution of Water-Lubricated Rubber Bearings with Multiple Grooves. *Tribology Transactions*, 60(3):385–391, 2017.

CURRICULUM VITÆ

Joep Peter Abram Nijssen

08-01-1992   Born in Groningen, The Netherlands.

EDUCATION

2004–2010   VWO Nature & Health
              Maartenscollege voor Lyceum Havo Mavo
              Haren, The Netherlands

2010–2014   WO Bachelor Industrial Design Engineering
              Delft University of Technology
              Delft, The Netherlands

2014–2017   WO Master Mechanical Engineering
              Delft University of Technology
              Delft, The Netherlands

2017-2021   PhD. Mechanical Engineering
              Delft University of Technology
              Thesis: Compliant Full Film Water Lubricated Bearings:
                             Concept Design & Development
              Promotor: Dr.ir. R.A.J van Ostayen
              Promotor: Prof.dr.ir. J.L. Herder

AWARDS

2019   Best student paper award at the 15th IFToMM World Congress

LIST OF PUBLICATIONS

Journal Publications

8. **J.P.A. Nijssen**, R.A.J. van Ostayen, J. Faludi, *An Eco-impact Design Metric for Water Lubricated Bearings based on Anticipatory Life Cycle Assessment*, Journal of Cleaner Production, Volume 321, (2021).

7. V.A. van Parijs, **J.P.A. Nijssen**, R.A.J. van Ostayen, *Whiffletree Based Supports for Self-Adjustable Hydrostatic Bearings*, Advances in Mechanical Engineering (2021).

6. D. Sonneveld, **J.P.A. Nijssen**, R.A.J. van Ostayen, *Compliant joints utilizing the principle of closed form pressure balancing*, To be submitted to Mechanism and Machine Theory (2022).

5. **J.P.A. Nijssen**, R.A.J. van Ostayen, *Passive Shape Shifting: A Compliant Design Approach for Full Film Bearings*, Proceedings of the Institution of Mechanical Engineers, Part C: Journal of Mechanical Engineering Science (2021).

4. **J.P.A. Nijssen**, R.A.J. van Ostayen, *Compliant Hydrostatic Bearings Utilizing Functionally Graded materials*, Journal of Tribology **11**, 142 (2020).

3. **J.P.A. Nijssen**, G. Radaelli, C.J. Kim, J.L. Herder, *Overview and Kinetostatic Characterization of Compliant Shell Mechanism Building Blocks*, Journal of Mechanisms and Robotics **6**, 12 (2020).

2. **J.P.A. Nijssen**, T.W.A. Blad, F. Broeren, S.G.E. Lampaert, S. van den Toorn, J. van den Dobbelsteen, *A Rapidly Deployable Test Suite for Respiratory Protective Devices in the COVID-19 Pandemic*, Applied Biosafety **3**, 25 (2020).

1. B. Boogaard, A. Tas, **J.P.A. Nijssen**, F. Broeren, J. van den Dobbelsteen, V. Verhoeven, J. Pluim, S. Dekker, E.J. Snijder, M.J. van Hemert, S. Herfst, *Efficacy assessment of newly-designed filtering facemasks during the SARS-CoV-2 pandemic*, Aerosol and Air Quality Research, 21 (2020).

Conference Publications

5. R.F.P. Gomes, **J.P.A. Nijssen**, R.A.J. van Ostayen, *Design of a Compliant Hinge Based on Closed Form Pressure Balancing*, Proc. ASME. IDETC-CIE2020, Volume 10: 44th Mechanisms and Robotics Conference (MR), V010T10A003, August 17-19, (2020).

4. **J.P.A. Nijssen**, R.A.J. van Ostayen, *Open Form Pressure Balancing for compliant Hydrostatic Thrust Bearings*, Advances in Mechanism and Machine Science. IFToMM WC 2019. Mechanisms and Machine Science, vol 73. Springer (2019).

3. **J.P.A. Nijssen**, A. kempenaar, N. Diepeveen, *Development of an Interface between a Plunger and an Eccentric Running Track for a Low-speed Seawater Pump*, 11th International Fluid Power Conference Aachen (2018).

2. **J.P.A. Nijssen**, G. Radaelli, J.L. herder, JB Ring, C.J. Kim, *Spatial Concept Synthesis of Compliant Mechanisms Utilizing Non-Linear Eigentwist Characterization*, Proc. ASME. IDETC-CIE2018, Volume 5A: 42nd Mechanisms and Robotics Conference, V05AT07A004, August 26–29 (2018).

1. **J.P.A. Nijssen**, G. Radaelli, J.L. Herder, C.J. Kim, JB Ring, *Design and Analysis of a Shell Mechanism Based Two-Fold Force Controlled Scoliosis Brace*, Proc. ASME. IDETC-CIE2017, Volume 5A: 41st Mechanisms and Robotics Conference, V05AT08A014, August 6–9 (2017).